Jon Are Suul

Control of Grid Integrated Voltage Source Converters under Unbalanced Conditions

Development of an On-line Frequency-adaptive Virtual Flux-based Approach

Thesis for the degree of Philosophiae Doctor

Trondheim, March 2012

Norwegian University of Science and Technology
Faculty of Information Technology, Mathematics and Electrical Engineering
Department of Electric Power Engineering

NTNU – Trondheim
Norwegian University of
Science and Technology

NTNU
Norwegian University of Science and Technology

Thesis for the degree of Philosophiae Doctor

Faculty of Information Technology, Mathematics and Electrical Engineering
Department of Electric Power Engineering

ISBN 978-82-471-3455-9 (printed ver.)
ISBN 978-82-471-3457-3 (electronic ver.)
ISSN 1503-8181

Doctoral theses at NTNU, 2012:90

Printed by NTNU-trykk

Abstract

Three-Phase Voltage Source Converters (VSCs) are finding widespread applications in grid integrated power conversion systems. The control systems of such VSCs are in an increasing number of these applications required to operate during voltage disturbances and unbalanced conditions. Control systems designed for grid side voltage-sensor-less operation are at the same time becoming attractive due to the continuous drive for cost reduction and increased reliability of VSCs, but are not commonly applied for operation during unbalanced conditions. Methods for voltage-sensor-less grid synchronization and control of VSCs under unbalanced grid voltage conditions will therefore be the main focus of this Thesis.

Estimation methods based on the concept of Virtual Flux, considering the integral of the converter voltage in analogy to the flux of an electric machine, are among the simplest and most well known techniques for achieving voltage-sensor-less grid synchronization. Most of the established techniques for Virtual Flux estimation are, however, either sensitive to grid frequency variations or they are not easily adaptable for operation under unbalanced grid voltage conditions. This Thesis addresses both these issues by proposing a simple approach for Virtual Flux estimation by utilizing a frequency-adaptive filter based on a Second Order Generalized Integrator (SOGI). The proposed approach can be used to achieve on-line frequency-adaptive varieties of conventional strategies for Virtual Flux estimation. The main advantage is, however, that the SOGI-based Virtual Flux estimation can be arranged in a structure that achieves inherent symmetrical component sequence separation under unbalanced conditions.

The proposed method for Virtual Flux estimation can be used as a general basis for voltage-sensor-less grid synchronization and control during unbalanced conditions. In this Thesis, the estimated Virtual Flux signals are used to develop a flexible strategy for control of active and reactive power flow, formulated as generalized equations for current reference calculation. A simple, but general, implementation is therefore achieved, where the control objective and the power flow characteristics can be selected according to the requirements of any particular application. Thus, the same control structure can be used to achieve for instance balanced sinusoidal currents or elimination of double frequency active power oscillations during unbalanced conditions.

In case of voltage sags, current references corresponding to a specified active or reactive power flow might exceed the current capability of the converter. The limits for active and reactive power transfer during unbalanced conditions have therefore been analyzed, and generalized strategies for current reference calculation when operating under current limitations have been derived. The specified objectives for active and reactive power flow characteristics can therefore be maintained during unbalanced grid conditions, while the average active and reactive power flow is limited to keep the current references within safe values.

All concepts and techniques proposed in this Thesis have been verified by simulations and laboratory experiments. The SOGI-based method for Virtual Flux estimation and the strategies for active and reactive power control with current limitation can also be easily adapted for a wide range of applications and can be combined with various types of inner loop control structures. Therefore, the proposed approach can potentially be used as a general basis for Virtual Flux-based voltage-sensor-less operation of VSCs under unbalanced grid voltage conditions.

Keywords: Grid Synchronization, Voltage-sensor-less Operation, Virtual Flux Estimation, Unbalanced Grid Voltage Conditions, Grid Frequency Variations, Active and Reactive Power Control, Current Limitation

Preface

This Thesis presents the main results from my time as a PhD student at the Department of Electric Power Engineering at NTNU, funded by an open grant from the Faculty of Information Technology, Mathematics and Electrical Engineering. I am grateful to NTNU for providing such an opportunity to freely pursue technical and academic topics. My supervisor at the Department of Electric Power Engineering during the grant period has been Professor Tore Undeland.

During these years of studies, I have enjoyed technical discussions and cooperation with fellow students and researchers, both at the Department and other institutions, which have been the source of valuable learning and interesting experiences both in life and science. Especially Professor Marta Molinas, who was a post doc. researcher at the Department when we first worked together, has been a continuous inspiration in striving for academic and scientific ideals. She has been always present to give help and advices, and to point me in a good direction when facing critical moments. My closest family and friends have also been a continuous support.

During my studies, I have been working on several topics and considered several lines of research. Some of the attempted efforts have shown interesting implications, and have been documented by publications. In most cases, the possibilities for achieving relevant and significant results in the context of this Thesis have, however, been out of reach within the timeframe of my studies. The breakthrough with respect to preparing this Thesis came after I was invited by Professor Pedro Rodríguez to visit his research group on Renewable Electrical Energy Systems (REES) at the Technical University of Catalonia (UPC) in Terrassa, Spain. This invitation resulted in two short stays in Terrassa during 2010, where the basis for the concepts and ideas presented in this Thesis were developed. While staying in Terrassa, I also received support by the researchers and PhD students of the REES group for working in their laboratories, making it possible to test some of the developed concepts in short time. Thus, all experimental results presented in this Thesis are originating from my visits to Terrassa. The support from Professor Rodríguez and the members of his research group is therefore highly valued, and has been crucial for the completion of this work in its current form.

Trondheim, January 2012

Jon Are Suul

Content

List of Figures

List of Tables

Nomenclature and Abbreviations

Symbols
In general, uppercase symbols are expressing physical, un-scaled, variables or parameters, while lowercase symbols are expressing per unit variables or parameters. There are a few exceptions from this rule, corresponding to well-established nomenclature in relevant literature. In these cases, per unit variables are denoted with "pu" as subscript. Bold symbols are representing vector quantities corresponding to voltages, currents and Virtual Flux signals.

V,v	Voltage [V, pu]
Ψ, ψ	Flux [Wb, pu]
X, χ	Virtual Flux scaled with grid frequency [Wb/s, pu] = [V, pu]
I,i	Current [A, pu]
ϑ	Charge, corresponding to integral of current [pu]
S	Apparent power [VA] (Only used in the definition of per unit systems)
ω	Angular frequency [rad/s]
f	Grid frequency [Hz]
δ	Fault angle, describing the graphical orientation of the voltage or Virtual Flux trajectory in the stationary reference frame under unbalanced conditions [rad]
ϕ	Phase angle of positive or negative sequence voltage components [rad]
P,p	Active power [W, pu]
Q,q	Reactive power [VAr, pu]
t	Time [s]
T	Period-time of periodic signal [s]
L/l	Inductance [H, pu]
R/r	*R*esistance [Ω, pu]
C/c	Capacitance [F, pu]
a	Representation of phase shift of 120° on complex form
b	Suseptance (used for both voltage and Virtual Flux-based suseptance)
g	Conductance (used for both voltage and Virtual Flux-based conductance)
h	Denotes a generic transfer function
m	Modulation index for PWM algorithm

q	Phase shifting operator corresponding to −90° phase shift
θ	Phase angle of voltage
γ	Phase angle of estimated Virtual Flux
τ	Time constant [s]

Subscripts

abc	Three-phase quantities in the natural reference frame
αβ	Quantities in the stationary αβ reference frame
c	Variables at converter output
DC	Variable associated with the DC-link of the converter
b	Base value for per unit system
N	Nominal value
C	Capacitor values in case of LCL filter configuration
f	Variables at the grid side of the filter inductor
g	Variables at connection point to a grid equivalent source
1	Parameters of filter inductor connected to converter terminals
2	Parameters of grid side filter inductor in LCL filter configuration
2ω	Indicates active or reactive power component oscillating at twice the grid frequency
p	Indicates active current components or oscillating active or reactive power components originating from average active power flow
q	Indicates reactive current component, or oscillating active or reactive power component originating from average reactive power flow
d-t	Dead-time
sw	Semiconductor switch
th	Semiconductor threshold voltage
r	Resistance
BP	Band-Pass filter
LP	Low-Pass filter
LP2	Second Order Low-Pass filter
ref	Reference signal for PWM
samp	Sampling in case of digital control system implementation

tot	Total – used in case of equivalent paramters for resistance and inductance
ph	Phase variables
lim	Limitation specified for peack value of active or reactive phase current or current vector component
max	Maximum values of current vector amplitude or active or reactive power flow associated with an imposed current limitation

Superscripts

+	Positive Sequence quantity
−	Negative Sequence quantity
0	Zero Sequence quantity
‘	Values estimated by SOGI and/or FLL
¯	Denotes average values of active and reactive power components
~	Denotes active and reactive power components oscillating at twice the grid frequency
⌣	Defines estimated values during start-up procedures
*	Reference value for currents or power components
^	Peak values
∫	Indicate input and output variables from Virtual Flux estimation
∫,ideal	Denotes ideal integration

Abbreviations

AARC	Average-Active-Reactive Control
BPSC	Balanced Positive Sequence Control
DPC	Direct Power Control
DSC	Delayed Signal Cancellation
DSOGI	Dual Second Order Generalized Integrator
DSOGI-VF	Dual Second Order Generalized Integrator-based Virtual Flux
EMI	Electro-Magnetic Interference
FLL	Frequency-Locked Loop
PLL	Phase-Locked Loop
PNS	Positive and Negative Sequence
PNSC	Positive-Negative-Sequence Compensation
QSG	Quadrature Signal Generator
RMS	Root Mean Square
SOGI	Second Order Generalized Integrator
THD	Total Harmonic Distortion
VF	Virtual Flux

1 Introduction

The utilization of power electronic technology in power system applications has been steadily increasing during the last decades. The continuous improvement of semiconductor device technology and the availability of digital control systems with continuously increasing performance have reinforced this development. Power electronic converter technology has also been an important enabling factor for the recent developments in distributed generation and renewable energy systems, especially with respect to wind power and photovoltaic systems.

A large variety of controllable power electronic converter topologies are currently being utilized in grid connected applications. The range of well known applications span from large thyristor-based line-commutated converters for classical high-voltage DC (HVDC) transmission systems, to small single-phase power-factor-correction circuits used for low power domestic loads. In between these examples, a wide range of topologies have been developed and optimized for various applications. However, only a few of the available three-phase topologies have reached widespread deployment and mass production.

During the last couple of decades, the Voltage Source Converter (VSC) has emerged as the dominant topology for actively controlled three-phase applications. This development has been supported by the widespread use of VSCs in variable speed electric drive systems. VSCs operating as active rectifiers have also become a relevant option for replacing diode rectifiers or line-commutated converters due to the Pulse Width Modulated (PWM) operation, which ensures limited current distortion and reduced harmonic filter requirements together with the ability to control power factor and DC-link voltage [1]-[3]. Thus, almost identical VSC modules connected in a back-to-back configurations have become the most common solution for regenerative motor drives and variable speed generator systems [1], [4]-[6]. Various configurations based on three-phase VSCs are also used for distributed energy resources like photovoltaic's and fuel cell systems which naturally provide a DC output and depend on power electronic converters for integration to the AC grid [4], [6]-[8]. Other well-known applications of grid integrated VSCs include operation as grid interfaces of energy storage systems, reactive power compensation when configured as a Static Synchronous Compensators (STATCOM), and active filter systems [4], [6], [7], [9]-[13].

Large scale deployment of VSCs has until now been most common in low voltage AC systems (below 1 kV), based on the two-level VSC topology. The power ratings of such converter units are usually limited to about 5 MW, due to the high currents. However, multi-level VSC topologies are currently finding numerous applications in the medium voltage (kV) range, and are commercially available with power ratings up to about 50 MW [14]-[17]. Medium-voltage grid integrated multi-level VSCs have until now

mainly been used in regenerative motor drives, but similar converter units are also expected to be utilized for wind power applications approaching 10 MW [5], [16].

High voltage, high power VSC topologies have also been developed for High Voltage DC (HVDC) transmission systems and for power system applications within the Flexible AC Transmission System (FACTS) concept [18]-[22]. The largest VSC HVDC converters currently in operation are in the range of 400 MW, but systems reaching 1000 MW with ± 300 kV DC voltage are considered within the reach of available technology. Two- or three-level VSC topologies implemented by series connection of a large number of high voltage semiconductors has been used for most of the existing VSC HVDC systems, illustrating that the same topology as for low voltage applications can be used even in the high voltage range.

This brief overview demonstrates how the three-phase VSC is a very flexible topology that can be designed and implemented for a wide range of applications and voltage levels, spanning the power range from a few kW to hundreds of MWs. The main difference between the basic two-level topology compared to the varieties of multi-level converters will be the PWM technique used to control the operation of the individual switches. Therefore, the main principles of operation as well as the general structure and functionality of the control system are usually the same for most applications of grid connected VSCs. Thus, the further discussions will be limited to the basic three-phase, three-wire two-level VSC topology.

1.1 Overview of Conventional Control Systems for Grid Connected Voltage Source Converters

There has been an intense research effort on development and analysis of control systems for grid connected VSCs during the last couple of decades. A large variety of techniques and methods for grid synchronization and control have therefore been proposed and analyzed. The main principles of operation for VSCs in grid integrated applications are, however, similar to what has been well known for control of VSC-based electric drives. Many of the control techniques and traditions developed for implementation of machine drive systems have therefore been successfully adapted to operation of grid connected VSCs.

When operated in grid integrated applications, the VSC will be exposed to disturbances, transients and interruptions that propagate through the electric power system. A large share of such disturbances and transients are likely to introduce temporary unbalanced grid voltage conditions [23]-[25]. In an increasing number of grid connected applications, the VSC is also required to operate during such voltage disturbances and grid voltage unbalance, while the conventional approach has been to disconnect from the power system to protect the converter [26]-[34]. Such requirements have become well known under the general term of Low-Voltage Ride-Through (LVRT) for wind power systems, and are becoming increasingly relevant for other distributed generation systems as well as for compensation systems, regenerative loads and energy storage applications. Safe operation during severe voltage transients and grid voltage unbalance will usually require added functionality and increased complexity of the control system, since the performance of conventional control strategies inspired by electrical drives systems will deteriorate under unbalanced conditions [35]-[38]. Research and development related to VSC control systems for

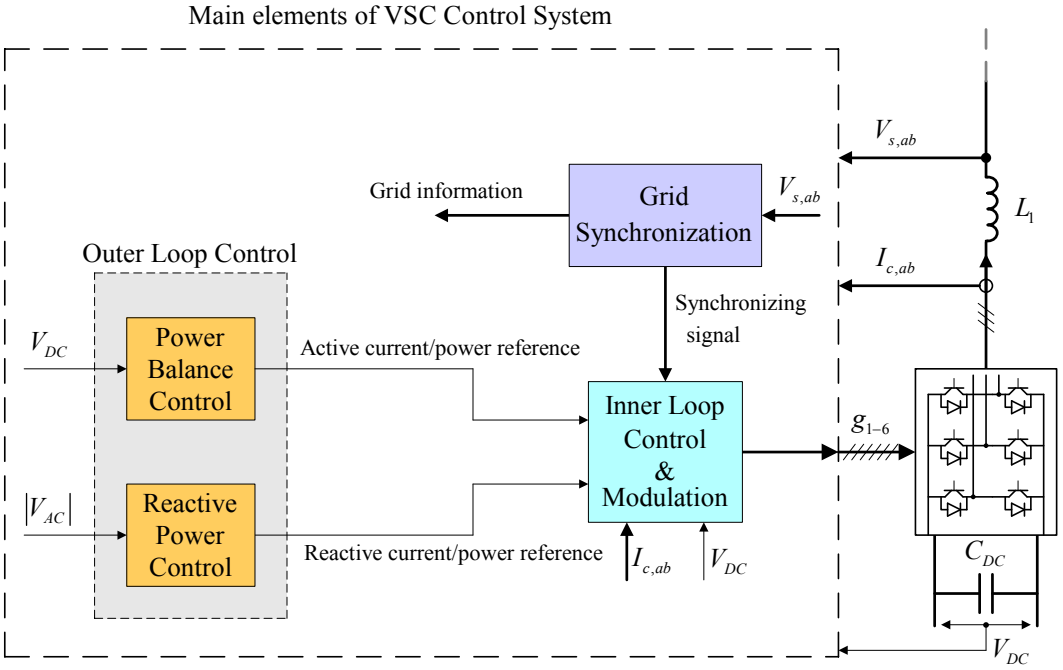

Fig. 1-1 Overview of main elements in conventional VSC control system with cascaded control loops

operation during unbalanced conditions have therefore received significant attention during the last few years.

Although there is a wide range of possible control techniques that can be applied to a grid connected VSC, most of the available proposals share a general structure, with three main elements as indicated in Fig. 1-1. Assuming a VSC converter that will always be connected to an external grid without the need for stand-alone operation, these three elements can be listed and briefly described as:

1. Grid Synchronization:
   - Information about the phase angle, amplitude and/or frequency of the grid voltage is of vital importance for the converter control system to be able to accurately control the flow of active and reactive power. The main purpose of the grid synchronization technique is therefore to identify the information needed by the rest of the control system. Although a wide range of synchronization methods have been proposed, the most common and well known synchronization technique for three-phase VSCs is the Synchronous Reference Frame (SRF) Phase Locked Loop (PLL) [39]-[44].
   - In case of operation during unbalanced grid voltage conditions, the grid synchronization method is usually required to identify the phase angle and amplitude of the positive sequence (and sometimes also the negative sequence) component of the grid voltage. Adding functionality to the conventional SRF PLL, or implementing techniques for symmetrical component sequence separation in the stationary reference frame are among the most common strategies for grid synchronization under unbalanced conditions [26], [28], [45]-[57].

- The grid synchronization is usually based on voltage measurements, but voltage-sensor-less techniques for grid synchronization are gaining interest due to potential cost reduction and improvement of reliability [58]-[65]. Voltage-sensor-less grid synchronization based on the concept of Virtual Flux, where the integral of the converter output voltage is considered in analogy to the flux of an electrical machine, has for instance become relatively well known [66]-[68]. However, voltage-sensor-less control systems are not yet commonly applied for converters required to have the capability for operating under unbalanced conditions.

2. Inner loop control and modulation:
   - The inner control loops of the converter control system must be fast and accurate, since they will control the PWM switching operation of the converter and determine the performance limits for the outer loops [69].
   - Traditionally, the inner control loops are controlling the currents in the filter inductor L_1 indicated in Fig. 1-1 [69]-[79]. The inner control loops can also be designed to control the active and reactive power flow directly, according to the concept known as Direct Power Control (DPC) [59], [60], [66], [67], [80].
   - Depending on the type of controller, the inner control loop control can directly provide the switching signals controlling the VSC operation, or the switching signals can be provided by a separate PWM mechanism. Inner control loops acting directly on the switching states of the converter are usually associated with nonlinear control and variable switching frequency, while PWM mechanisms with a voltage reference input will be operating at fixed switching frequency. In case of fixed frequency PWM, the inner loop current or power controllers are therefore providing a voltage reference, or a modulation index, which corresponds to the desired average output voltage of the converter within one switching period [69], [81]. For three-phase three-wire VSCs, the fixed frequency PWM mechanisms must be specifically adapted for maximizing the utilization of the available DC-link voltage [82]-[84], while this is usually inherently achieved with nonlinear control loops acting directly on the switching signals.
   - The performance of traditional Proportional-Integral (PI) current control loops implemented in the Synchronous Reference Frame, as well known from vector oriented control of electric drives, will usually deteriorate during unbalanced conditions. This problem is usually solved by either duplicating the current controller implementation in both the positive and negative sequence SRFs, or by utilizing controllers which are capable of achieving negligible steady state errors when operating with sinusoidal reference values [31], [34], [75]-[79], [85]-[90].

3. Outer loop control:
   - In a traditional cascaded control structure as indicated in Fig. 1-1, there are usually a set of outer loop controllers providing the reference values to the inner control loops.

- The reference signal influencing the active power flow of the converter is usually provided by a control loop operating on the power balance of the converter. Usually, this control loop is a PI-controller operating on the DC-link voltage or the energy stored in the DC-link capacitor, but also more advanced methods for controller designs are used [91]-[93].
- The reference signal influencing the reactive power flow of the converter usually originates from a control loop designed to follow a reference for either the reactive power flow, the power factor of the converter or the voltage in the AC grid [39], [94]-[97].
- Under unbalanced conditions, the active and reactive power flow in the converter will be characterized by an average value and an oscillating component at twice the grid frequency [89], [96], [98], [99]. The outer loop controllers in a cascaded control system must however be slower than the inner loops, and are usually controlling only the average values of the active and reactive power flow. Therefore, an intermediate level between the outer and inner control loops is usually required for operation under unbalanced conditions, where the intended characteristics of active and reactive power flow of the converter should be specified.
- The type and purpose of the outer loop controllers, as well as the relevant methods for design and analysis of these control loops will depend on the application. The outer loop controllers will therefore not be further investigated.

1.2 Identification of Research Question

Grid synchronization and control of VSCs, as briefly outlined in the previous section, have received significant attention during the last decades, and most issues related to conventional control of VSCs during both balanced and unbalanced conditions have therefore been thoroughly addressed. Voltage-sensor-less operation during unbalanced conditions is, however, a relatively new topic, and the studies available in the scientific literature have been mainly focused on achieving particular, application specific objectives. The presented techniques and methods have therefore not yet converged towards a generally valid approach for voltage-sensor-less grid synchronization and control of the active and reactive power flow during unbalanced conditions. One of the main goals for this Thesis has therefore been to address these issues in a way that should be valid for a wide range of applications, control objectives and operating conditions.

The desired features that should be fulfilled for control and operation of a grid connected VSC considered in this Thesis can be summarized by the following points:

- Ability to operate in voltage-sensor-less mode:
  - The method for grid synchronization should still be relatively simple and easily understandable. The concept of Virtual Flux-based grid synchronization and control has therefore been considered as a suitable starting point, since it can be easily understood in analogy to the flux of an electrical machine.

    - The applied method for voltage-sensor-less grid synchronization should be generally valid for unbalanced grid voltage conditions.
    - The accuracy and dynamic response of the grid synchronization method should not be significantly influenced by variations in the grid frequency.
- The converter control system should be able to control both average active and average reactive power flow, as well as the double frequency oscillating components of the active and reactive power flow during unbalanced conditions. The control strategy should be generally valid for both balanced and unbalanced conditions, and it should be possible to determine the active and reactive power flow characteristics in a flexible manner.
- The converter control system should be able to limit the current references during balanced and unbalanced disturbances in the grid voltage to safe values, while still maintaining the requested power flow characteristics

From the few examples given in the previous sections it can be seen that current controllers for VSCs have been exhaustively studied in the available literature, both for operation under balanced and unbalanced conditions. The design, operation and performance of the current controllers can also to some extent be considered independently from to the grid synchronization method. Current controllers for VSCs will therefore not be further investigated. Similarly, the outer loop controllers for maintaining the active and reactive power balance of the converter are usually not depending on the implementation of the inner loop controllers or the grid synchronization method.

The focus of this Thesis will therefore be limited to two main parts of a general control system of a current controlled VSC intended for operation under unbalanced conditions, as illustrated in Fig. 1-2. First, synchronization methods with potential for voltage-sensor-less operation will be investigated, starting from the concept of Virtual Flux. Secondly, the issue of current reference calculation will be addressed with the purpose of achieving generalized strategies for voltage-sensor-less control of active and reactive power flow and power flow characteristics under voltage-sensor-less operation.

The general research question behind the results and analysis that will be presented in this Thesis can therefore be defined as:

> ***How to develop and analyze a general approach for Virtual Flux-based voltage-sensor-less grid synchronization and control of a grid integrated three-phase Voltage Source Converter?***
>
> *It is taken as a condition that the VSC control system should be able to fulfil all the desired features listed above when operating in voltage-sensor-less mode. It should also be possible to easily adapt the control system to operation based on available voltage measurements.*

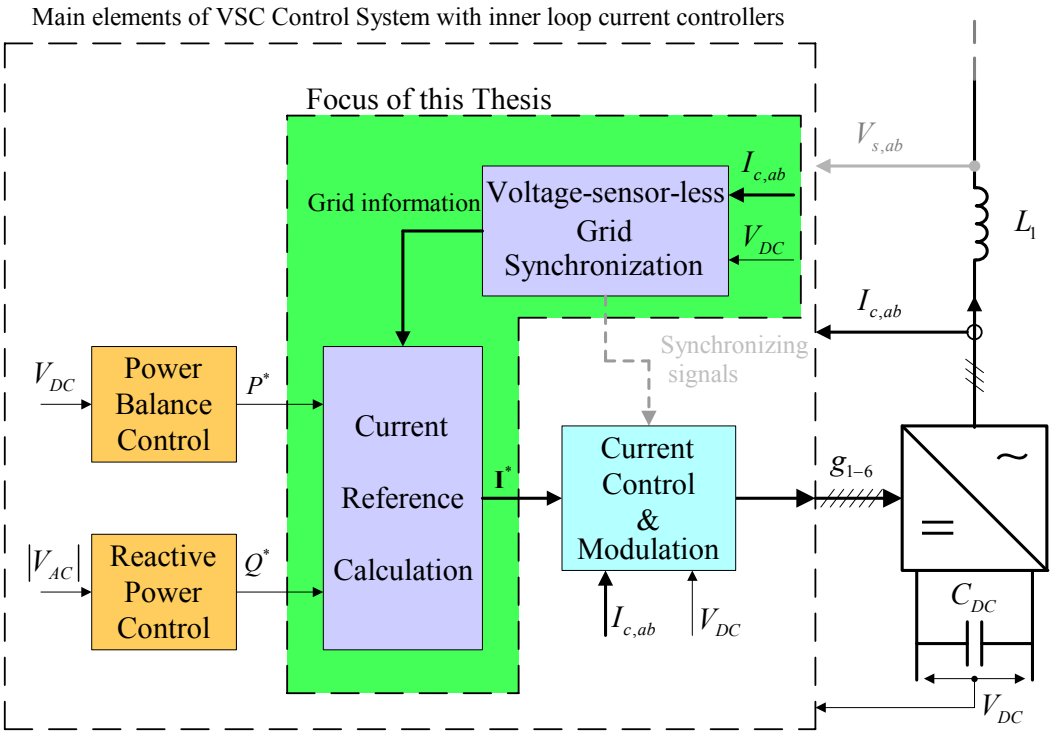

Fig. 1-2 Overview of control system for operation under unbalanced grid voltage conditions with indication of the focus area of this Thesis

1.3 Overview of Earlier Contributions

From the previous discussions, it can be noted that a wide range of literature is available on various aspects of grid connected voltage source converters. This section is intended to give a brief outline of the previous contributions that constitute the main basis for the results achieved in this Thesis.

The methods for voltage-sensor-less grid synchronization that will be discussed in this Thesis are based on the concept of Virtual Flux. The most important previous contributions that have been used as basis for developing this concept are listed in the following:

- The fist example of flux-based control for a three-phase grid connected VSC was presented by Weinhold in 1991 [100]. Another example of flux-based control was presented by Chandorkar et al. later in the same year [101], and a filter-based method for implementation of the flux estimation was subsequently discussed by Bhattacharya et al. in 1995 [102]. The concept of flux-based control, and the benefits of using the flux instead of the grid voltage to establish a Synchronous Reference Frame for vector oriented control of grid connected VSCs, was discussed in a general way by Duarte et al. in 1999 [103].
- Voltage-sensor-less control based on the converter flux was first explicitly discussed by Manninen in 1995, in combination with a modulation method based on the Direct Torque Control for controlling the active and reactive power flow of a VSC [104].

- The term “Virtual Flux” and its application for voltage-sensor-less grid synchronization and control of VSCs was established by the work of Malinowski et al. published from year 2000 and onwards [66], [67]. This approach was based on utilizing the converter output voltages, the measured currents and the filter parameters to estimate the Virtual Flux at the grid side of the filter inductor.
- The first explicit investigation of Virtual Flux-based voltage-sensor-less operation under unbalanced grid voltage conditions was presented by Malinowski et al in 2003 [105]. Later, utilization of a Synchronous Double Reference Frame (SDRF) PLL for estimation of the positive and negative sequence components of the Virtual Flux and the phase angle of the positive sequence component was proposed by Chicowlas et al. in 2005 [106].
- Explicit estimation of the positive and negative sequence Virtual Flux components in the stationary reference frame was first proposed by Kulka in 2009 [107].

The method for Virtual Flux estimation that will be proposed in this Thesis is based on techniques that have been previously introduced and analyzed for voltage-based grid synchronization:

- The specific configuration of the Second Order Generalized Integrator (SOGI) and Quadrature Signal Generator (QSG) that is utilized in the proposed method for Virtual Flux estimation was first introduced by Rodríguez et al. in 2006 [51].
- The approach for sequence separation in the stationary reference frame applied in this Thesis is also based on SOGI-QSGs in a similar way as the proposal by Rodríguez et al. from 2006 [51].

The approach followed when deriving Virtual Flux-based equations for current reference calculation under unbalanced conditions presented in this Thesis can be considered as a Virtual Flux-based equivalent to the voltage-based approach analyzed in several publications.

- The notation and the classifications of different power control objectives and strategies for current reference calculation followed in this Thesis are based on work by Rodríguez et al., presented from 2006 an onwards [108]-[110].
- The approach for generalizing the equations for current reference calculation is inspired by the work of Wang et al. starting from 2009 [111]-[114].
- The presented approach for current reference calculation for active and reactive power control when operating under phase current limitation is inspired by the approach presented for current limitation of a STATCOM by Rodríguez et al. in 2010 [115].

Also other previous publications have been used as important background information and as basis for analysis and discussions, as can be seen from the references that will be given continuously in the text.

1.4 Contributions of this Thesis

In the opinion of the author, the main contributions presented in this Thesis are:

- Development, analysis and experimental verification of a method for explicitly frequency-adaptive Virtual Flux estimation with inherent sequence separation in the stationary reference frame:
  - The proposed method is designed to merge the functions of Virtual Flux estimation and sequence separation under unbalanced conditions. Thus, the delays associated with the conventional approach of cascading techniques for sequence separation and Virtual Flux estimation is avoided.
  - The transient response and general characteristics of the proposed method for estimation of positive and negative sequence Virtual Flux components is analyzed in comparison to similar techniques for grid synchronization. The proposed method is demonstrated to achieve similar features and dynamic response for voltage-sensor-less operation as associated with conventional methods for grid synchronization based on sequence separation of voltage measurements.
  - The proposed method for Virtual Flux estimation is flexible in the sence that it can be easily adapted for grid synchronization based on voltage measurements. It can also be configured for synchronization to positive and negative sequence components at different points in a radial AC grid by selecting corresponding values for resistance and inductance used for the Virtual Flux estimation.
- Derivation, analysis and experimental verification of generalized expressions for Virtual Flux-based current reference calculation and control of active and reactive power flow under unbalanced conditions:
  - The presented approach for Virtual Flux based derivation of current references corresponding to different objectives for control of active and reactive power flow characteristics during unbalanced conditions is generally valid. The same approach can therefore be followed to fulfil other control objectives than investigated in this Thesis, and can be adapted to various categories of control systems for VSCs.
  - The presented approach shows how the same flexibility in selecting control objectives for operation under unbalanced conditions can be achieved with the Virtual Flux-based approach as when the grid synchronization is based on measured grid voltages.
  - The Virtual Flux-based approach for active and reactive power control under unbalanced conditions can be applied for voltage-sensor-less operation of VSCs, as well as for operation based on available voltage measurements.
- Derivation, analysis and verification of strategies for current limitation under unbalanced grid voltage conditions:
  - The theoretical differences between strategies for limitation of the individual phase currents of the converter compared to the conventional

approach for limitation of the maximum current vector amplitude have been analyzed.

- General expressions for the maximum active and reactive powers that can be transferred under unbalanced conditions, within a specified active and reactive current limitation, have been derived and analyzed. By applying the developed strategies, the converter can be operated with the maximum allowable current under severe voltage sags, while at the same time controlling the active and reactive power flow characteristics.

1.5 Outline of the Thesis

Chapter 1 of this Thesis presented a brief introduction to application and control of voltage source converters. This served as a basis for identifying the research question presented in section 1.2 and for defining the focus area of this Thesis within Virtual Flux-based voltage-sensor-less grid synchronization and control of VSCs.

A review of methods for voltage-sensor-less control of VSCs, with specific focus on state-of-the art in implementation of Virtual Flux estimation as well as methods for Virtual Flux-based control is presented in chapter 2. This chapter also serves as a basis for identifying the limitations of existing methods for Virtual Flux estimation.

Chapter 3 presents a general method for frequency-adaptive, filter-based Virtual Flux estimation. This method can be used as a general building block for achieving on-line frequency-adaptive operation of traditional strategies for Virtual Flux estimation. The main advantage of the proposed estimation method is, however, that it can be configured to achieve Virtual Flux estimation with inherent sequence separation. The operation of the resulting method for Virtual Flux estimation under unbalanced conditions is then analyzed and verified by simulation results and laboratory experiments. The performance and complexity of the proposed method is also compared to conventional configurations for Virtual Flux estimation, showing that it is a relatively simple structure with improved dynamic response.

In chapter 4, the method from chapter 3 for estimation of positive and negative sequence Virtual Flux components under unbalanced conditions is used as a basis for developing strategies for current reference calculation. The active and reactive power flow characteristics under unbalanced conditions are investigated, and current reference equations corresponding to different power control objectives are derived. The resulting current reference equations and the corresponding power flow characteristics are synthesized into generalized expressions that can be used for simple implementation and analysis of different power control objectives under unbalanced conditions.

Chapter 5 is focused on methods for protecting the converter against over-currents during unbalanced grid faults by limiting the current references. The difference between approaches for limiting the current vector amplitude and for limiting the actual phase currents of the converter is investigated analytically. Then, expressions for current reference calculation under phase current limitation, as well as under current vector amplitude limitation, are derived with the purpose of maintaining the specified power control objectives. Thus, the converter can be protected against over-currents and requested power flow characteristics can be maintained during unbalanced conditions, while the average active and/or reactive power flow can be kept at the maximum levels

achievable with the specified requirements and the actual grid conditions. The derived expressions for current reference calculation under phase current and current vector amplitude limitation are verified and analyzed by simulations and laboratory experiments.

A summary of the Thesis with concluding remarks and an outline of possible topics for further research based on the presented results is given in chapter 6.

Appendix A presents the applied conventions for reference frame transformation and per unit scaling applied in this Thesis. Frequency-domain analysis of some relevant strategies for sequence separation and Virtual Flux estimation under unbalanced conditions is presented in Appendix B, as a basis for the comparisons in chapter 3. The discrete time equations used for practical implementation of the converter control system are presented In Appendix C. The applied conventions for voltages and Virtual Flux signals are presented in Appendix D, together with the derivations required to arrive at the results presented in chapter 4 and 5.

1.6 Scientific Publications

This section presents an overview of the scientific manuscripts that have been prepared during the PhD studies. However, this Thesis is focused on presenting an approach for Virtual Flux-based grid synchronization and control under unbalanced conditions. The list of publications presented below is therefore divided in two parts, whereof the conference publication [C1] and the two journal publications [J1] and [J2] are containing some of the main contributions of this Thesis.

The remaining publications, not directly related to the proposed approach for Virtual Flux-based operation under unbalanced conditions, are listed in section 1.6.2. Among these publications, manuscript [C2] and [C3] are discussing Virtual Flux-based control of VSCs in weak, high-impedance grids, but based on a different method for Virtual Flux estimation than the frequency-adaptive method proposed in this Thesis. These manuscripts are also considering the interaction between the VSC and the grid, and the possible flexibility of the Virtual Flux concept in utilizing the grid synchronization to influence the performance and stability of the converter. The results presented in this Thesis can also be used as starting point for further investigations of these issues, with a more power system oriented approach. Implications of the results presented in manuscripts [C2] and [C3] with respect to the stability of VSCs in high-impedance grids and the corresponding interaction with the power system are however not investigated in depth or by any systematic or analytical approach in this Thesis.

The publications listed as [J3]-[C13] are also related to grid synchronization, control and utilization of VSCs in grid connected applications. They are however not related to voltage-sensor-less control and will therefore not be further commented or discussed.

1.6.1 Publications Containing Results Defended as Parts of this Thesis

The following manuscripts are containing contributions presented in this Thesis:

[J1] **Jon Are Suul**, Alvaro Luna, Pedro Rodríguez, Tore Undeland: "Voltage Sensor-less Synchronization to Unbalanced Grids by Frequency-Adaptive Virtual Flux Estimation," in *IEEE Transactions on Industrial Electronics*, Vol. 59, No. 7, July 2012, pp. 2910-2923

[J2] **Jon Are Suul**, Alvaro Luna, Pedro Rodríguez, Tore Undeland: "Virtual Flux-based Voltage-Sensor-Less Power Control in Unbalanced Grids," accepted for publication in *IEEE Transactions on Power Electronics*, February 2012

[C1] **Jon Are Suul**, Alvaro Luna, Pedro Rodríguez, Tore Undeland: "Frequency-adaptive Virtual Flux Estimation for Grid Synchronization under Unbalanced Conditions," in *Proceedings of the 36th Annual Conference of the IEEE Industrial Electronics Society*, IECON 2010, 7-10 November 2010, Glendale, Arizona, USA, pp. 486-492

1.6.2 Other Publications Prepared During the PhD-studies

The following publications have been prepared during the PhD-studies, but the obtained results are not explicitly included in this Thesis.

1.6.2.1 Publications related to Virtual Flux-based control of VSCs

These publications are discussing voltage-sensor-less control based on another approach for Virtual Flux estimation than the method presented in [C1], [J1] and [J2]:

[C2] Jon Are Suul, Tore Undeland; "Flexible Reference Frame Orientation of Virtual Flux-based Dual Frame Current Controllers for Operation in Weak Grids," in *Proceedings of the 2011 IEEE Trondheim PowerTech*, 19-23 June 2011, Trondheim, Norway, 8 pp

[C3] Jon Are Suul, Tore Undeland: "Impact of Virtual Flux Reference Frame Orientation on Voltage Source Inverters in Weak Grids," *Proceedings of the 2010 International Power Electronics Conference – ECCE Asia –*, IPEC-Sapporo 2010, Sapporo, Japan, 21-24 June 2010, pp. 368-375

1.6.2.2 Publications concerning various topics related to control of VSCs

The following publications are not related to voltage-sensor-less control of VSCs. Some of the investigated topics can however be relevant for further investigation together with the main contributions presented in this Thesis. Publications with contributions as co-author are also included in the following list:

[J3] **Jon Are Suul**, Kjell Ljøkelsøy, Tarjei Midtsund, Tore Undeland: "Synchronous Reference Frame Hysteresis Current Control for Grid Converter Applications," in *IEEE Transactions on Industry Applications*, Vol. 47, No. 5, September/October 2011, pp. 2183-2194

[J4] **Jon Are Suul**, Marta Molinas, Tore Undeland; "STATCOM-Based Indirect Torque Control of Induction Machines During Voltage Recovery After Grid Faults," in *IEEE Transactions on Power Electronics*, Vol. 25, No. 5, May 2010, pp. 1240-1250

[J5] Marta Molinas, **Jon Are Suul**, Tore Undeland: "Extending the Life of Gear Box in Wind Generators by Smoothing Transient Torques With STATCOM," *IEEE Transactions on Industrial Electronics*, Vol. 57, No. 2, February 2010, pp. 476-484

[J6] Steinar Danielsen, Olav B. Fosso, Marta Molinas, **Jon Are Suul**, Trond Toftevaag: "Simplified models of single-phase power electronic inverter for railway power system stability analysis – Development and evaluation," *Electric Power System Research*, Vol. 80, No. 2, February 2010, pp. 204-214

[J7] **Jon Are Suul**: "Variable speed pumped storage hydropower plants for grid integration of wind power in isolated grids," in *Renewable Energy*, Hammons, T. J., Ed., pp. 553-580, INTECH, Vukovar, Croatia, December 2009, ISBN 978-953-7619-52-7

[J8] Marta Molinas, **Jon Are Suul**, Tore Undeland: "Low Voltage Ride Through of Wind Farms With Cage Generators: STATCOM Versus SVC", *IEEE Transactions on Power Electronics*, Vol. 23, No. 3, May 2008, pp. 1104-1117

[C4] **Jon Are Suul**, Kjell Ljøkelsøy, Tarjei Midtsund, Tore Undeland: "Synchronous Reference Frame Hysteresis Current Control for Grid Converter Applications," in *Proceedings of the 14th International Power Electronics and Motion Control Conference*, EPE-PEMC 2010, Ohrid, Republic of Macedonia, 6-8 September 2010, pp T3-111–T3-119

[C5] Tarjei Midtsund, **Jon Are Suul**, Tore Undeland: "*Evaluation of Current Controller Performance and Stability for Voltage Source Converters Connected to a Weak Grid*," in Proceedings of the 2nd International Symposium on Power Electronics for Distributed Generation Systems, Hefei, China, 16-18 June 2010, 7 pp.

[C6] **Jon Are Suul**, Kjell Ljøkelsøy, Tore Undeland; "Design, tuning and testing of a flexible PLL for grid synchronization of three-phase power converters," *Proceedings of the 13th European Conference on Power Electronics and Applications*, EPE'09, Barcelona, Spain, 8-10 September 2009, 10 pp.

[C7] **Jon Are Suul**, Marta Molinas, Lars Norum, Tore Undeland: "Tuning of Control Loops for Grid Connected Voltage Source Converters," *Proceedings of the 2nd IEEE International Power and Energy Conference*, PECon 2008, Johor Bahru, Malaysia, 1-3 December, 2008, pp. 797-802

[C8] **Jon Are Suul**, Kjetil Uhlen, Tore Undeland: "Wind Power Integration in Isolated Grids enabled by Variable Speed Pumped Storage Hydropower Plant, "*Proceedings of the IEEE International Conference on Sustainable Energy Technologies*, ICSET 2008, Singapore, 24-27 November 2008, pp. 399-404

[C9] Marta Molinas, **Jon Are Suul**, Tore Undeland: "*Torque Transient Alleviation in Fixed Speed Wind Generators by Indirect Torque Control with STATCOM*," Proceedings of the 13th International Power Electronics and Motion Control Conference, EPE-PEMC 2008, Poznań, Poland, 1-3 September 2008, pp. 2318-2324

[C10] Marta Molinas, Duilio Moltoni, Gabrielle Fascendini, **Jon Are Suul**, Tore Undeland: "*Constant Power Loads in AC Distribution Systems: an investigation of Stability,*" Proceedings of the 2008 IEEE International Symposium on Industrial Electronics, ISIE'08, Cambridge, UK, 30 June – 2 July, 2008, pp. 1531-1536

[C11] Marta Molinas, Duilio Moltoni, Gabrielle Fascendini, **Jon Are Suul**, Roberto Ferranda, Tore Undeland: "*Investigation on the role of power electronic controlled constant power loads for voltage support in AC systems,*" Proceedings of the IEEE 39th Power Electronics Specialists Conference, PESC'08, Rhodes, Greece, 15-19 June, 2008, pp. 3597-3602

[C12] Chandra Bajracharya, Marta Molinas, **Jon Are Suul**, Tore M. Undeland: "*Understanding of tuning techniques of converter controllers for VSC-HVDC,*" Proceedings of Nordic Workshop on Power and Industrial Electronics, NORPIE 2008, Espoo, Finland, 9-11 June, 2008, 8 pp.

[C13] **Jon Are Suul**, Kjetil Uhlen, Tore Undeland: "Variable speed pumped hydropower for integration of wind energy in isolated grids – case description and control strategies," *Proceedings of the Nordic Workshop on Power and Industrial Electronics*, NORPIE 2008, Espoo, Finland, 9-11 June, 2008, 8 pp.

2 State-of-the art for Voltage-sensor-less Operation and Virtual Flux-based Control of VSCs

This chapter presents a technical introduction to voltage-sensor-less grid synchronization and the concept of Virtual Flux. The chapter starts with an outline of the main motivations for implementing voltage-sensor-less control systems in grid connected Voltage Source Converters, followed by a brief review of control methods presented in the scientific literature. The concept of Virtual Flux is then presented in detail. The background of flux-based methods for grid synchronization and control is reviewed, and an overview of the current state-of-the-art in implementation and utilization of voltage-sensor-less control of VSCs is presented. This will show that the available methods for Virtual Flux estimation either have limited ability to follow grid frequency variations or are not easily adaptable for operation under unbalanced grid voltage conditions. It is also pointed out that previously presented studies of Virtual Flux-based grid synchronization under unbalanced conditions are based on cascading techniques for symmetrical components sequence detection with conventional methods for Virtual Flux estimation. The transient response is therefore relatively slow. These limitations of the conventional methods for Virtual Flux estimation are identified as a basis for developing an alternative approach that will be presented in the following chapter.

2.1 Introduction to Voltage-Sensor-Less Grid Synchronization and Control

Conventional control methods for three-phase three-wire VSCs utilize at least 5 sensors; two current sensors for measuring the AC currents, one sensor for measuring the DC-link voltage and two voltage sensors for measuring the AC voltage at the grid side of the filter inductor [61], [116], [117]. Parallel operation of several converter modules on the same DC-link will require three current sensors, to control zero-sequence currents. In four-wire systems, also three voltage sensors will also be required resulting in a total number of seven sensors. However, it is possible to operate a converter with reduced number of sensors and during the last two decades, there has been an increasing effort on research and development of different “sensor-less” control methods.

2.1.1 Motivation for Voltage-sensor-less Operation of VSCs

There are several possibilities to design control systems with a reduced number of sensors. Some of the proposed control methods reported in the literature include:

- Grid voltage-sensor-less operation [58]-[61], [117].
- AC-side current-sensor-less operation [118], [119].
- Operation with a single current sensor in the DC-link together with AC voltage sensors and a DC-link voltage sensor [120].
- Operation with only DC-link voltage and DC-link current sensors [121].
- Operation with only AC current measurements [122].

However, the AC current sensors are usually an important part of the over-current protection of the converter, and designers of converter systems are therefore more reluctant to remove the current sensors than the grid voltage sensors [60], [62]. Additionally, the current sensors are usually an integrated part of the VSC converter module, while the grid voltage sensors have to be installed at the grid side of the filter inductor, implying longer wires for the feedback signals due to the physical distance between the converter module and the control electronics. The AC voltage measurements therefore have a higher risk of electromagnetic interference (EMI) and physical damage [60]. Thus, AC voltage-sensor-less operation is the simplest and most common approach for reducing the number of sensors, with the least disadvantageous consequences regarding protection of the converter, implementation complexity and control system performance.

The main motivations for implementing AC voltage-sensor-less control systems for VSCs can be summarized by the following considerations.

- Cost reduction;
  - With voltage-sensor-less design, the cost of at least two AC-voltage sensors, with corresponding wiring, signal conditioning and integration to the digital control system can be avoided [58], [61], [62], [117], [123].
- Possibilities for increased hardware modularity;
  - For back-to-back VSCs, for instance for renewable energy generation systems or regenerative motor drive systems, AC voltage-sensor-less control of the grid side inverter and position-sensor-less control of the machine side converter will allow for exactly the same configuration of the two converter modules [63]. Thus, both converter modules can be identical, with AC current sensors and a DC-link voltage sensor as integrated parts of the VSC hardware module. In addition, the hardware for the control electronics can be identical, using only the same measurement inputs [63]-[65]. The only difference between the grid side and the machine side of such a back-to-back configuration will then be in the software, but even modular parts of the software can be applied in similar ways for both converter modules.
- Potential for increased reliability of the converter system;

  - Voltage-sensor-less control will reduce the number of components that can fail. The reliability of the converter system with respect to interruption of operation due to component failure can be increased [62], [117], [123], [124].
  - AC-voltage measurements are usually considered to be more exposed to risks of malfunction or disruption than the current measurements, since they have to be installed at some distance from the converter module. Although the actual distance between the converter and the voltage sensor will depend on the application, the system configuration and the voltage level, the voltage measurements are considered to be more exposed to EMI and even risk of physical damage to the signal wires between the sensors and the control electronics [60].
  - It can also be relevant to develop control systems with the ability for voltage-sensor-less operation, even if voltage sensors are installed as part of the hardware configuration. Thus, the benefits of available voltage measurements can be utilized in normal operation, while the voltage-sensor-less control algorithms can allow the converter to continue operation in case of voltage sensor failure.
- Increased flexibility and performance improvement of converter control system;
  - In some cases, the estimation methods needed for voltage-sensor-less control can be utilized to avoid errors caused by delays and disturbances in voltage measurements used for feed-forward compensation in the converter control system [117], [123]. Voltage-sensor-less control methods have also been claimed to improve the robustness with respect to operation of paralleled converters when using open-loop power sharing mechanisms [117], [123].
  - Estimation techniques used to replace voltage measurements can also be used to estimate grid conditions at points that are not easily available for real time measurements. This can be utilized for monitoring relevant points in the grid, and provide useful information for operation of the converter. The same approach can also be used to introduce flexibility in selecting the point where the converter is synchronized to the grid, and thus to influence the performance and operation of the converter as indicated by the results presented in the publications [C2] and [C3].

2.1.2 Review of Methods for Voltage-Sensor-less Grid Synchronization

Since the beginning of the 1990s, the topic of voltage-sensor-less control of VSCs has started receiving significant attention. An approach based on a discrete time mathematical observer for estimating the grid voltages was presented in English in 1994 [58], but similar methods had already been presented in local Japanese conferences. Application of the Direct Torque Control (DTC) modulation technique for control of grid connected converter was presented in 1995 [104], implying voltage-sensor-less operation based on estimation of converter “Flux” and “electromagnetic torque“ considered in analogy to the control of induction machines.

In a conference publication from 1996, [59], followed by a transaction paper published in 1998, [60], the concept of Direct Power Control (DPC) was presented for two-level grid connected VSCs based on voltage-sensor-less grid synchronization. The estimation of the grid voltage was based on the derivative of the currents in the filter inductor to calculate the active and reactive power at the grid side of the filter inductor, and then estimating the grid side voltages from the calculated powers and the measured currents. The same method for grid voltage estimation has also been investigated in control systems based on vector oriented current control [62]. Voltage estimation based on current derivatives will, however, be sensitive to noise and disturbances. A high value of the filter inductance and a high sampling frequency is therefore needed to achieve good accuracy. Another disadvantage of the method used in [59]-[62] is that the voltage estimation is obtained from a division by the current vector amplitude, making the estimation method unsuitable for operation with low or zero current flowing in the filter inductors. Therefore, voltage sensor-less control based on the concept of "Virtual Flux" was proposed in [66]-[68], as will be discussed in detail in the following sections. Several other concepts for grid voltage estimation and voltage-sensor-less operation of VSCs have also been proposed, as briefly outlined in the following.

In [124], a voltage-sensor-less control method was proposed on the basis of using the output of the converter DC-link voltage controller to estimate the grid frequency and phase angle. By this approach, the power balance of the converter was used to synchronize to the grid voltage and thus to achieve voltage-sensor-less control. A voltage-sensor-less concept labeled "indirect voltage sensing" was later proposed in [63]. In this case, the grid synchronization was based on the output of Synchronous Reference Frame PI-current controllers represented in polar coordinates. The resulting phase angle in the *dq*-reference frame was used as an input to a Phase-Locked Loop providing the angular signal used for transforming the current measurements into the synchronous reference frame and for the Space Vector Modulation of the converter output voltage. A variety of the same approach was proposed by [64], [65], [125], where the output of the synchronous frame PI-current controllers, including feed-forward of the grid voltage nominal voltage was used to estimate the grid voltage phase angle in a similar way. Using the output of the PI-current controllers before adding the decoupling terms compensating the inductive voltage drop, the converter was effectively synchronized to the grid side of the filter inductor. The methods proposed in [63]-[65], [125] also included considerations about initialization and start-up of voltage-sensor-less control systems, based on estimating the grid voltage angular position and the grid frequency from current measurements taken when applying two short duration zero voltage vectors.

Other synchronization methods, based on the estimated converter output voltage or the voltage reference output of the current controllers combined with different ways of compensating for the resistive and inductive voltage drop in the filter inductor have been proposed in [126]-[129]. A method for voltage-sensor-less operation based on another principle was however proposed by [130], [131], for the specific case of resistance emulation as the control objective of a VSC operating as an active rectifier. The voltage-sensor-less operation was based on utilizing information from the calculation of converter duty cycles to achieve "self-synchronization" of the voltage pulses of the converter with the grid voltage,

A simple observer for voltage estimation, partly integrated with a current controller in the synchronous reference frame was proposed by [116]. Later, techniques for voltage estimation based on more advanced control theory have been proposed. For instance, a sliding-mode voltage observer for grid voltage-sensor-less synchronization was proposed by [132], while voltage estimation based on the Kalman filter was investigated in [133]. Various methods to achieve parameter-adaptive voltage estimation by using modified Kalman filters and mathematical optimization methods have for instance been proposed in [134]-[136], while adaptive techniques based on neural networks have been investigated in [137], [138].

Although a relatively wide range of methods for voltage-sensor-less grid synchronization and control have been proposed in scientific literature, only a few of them are explicitly adapted for operation under unbalanced grid voltage conditions. The voltage estimation method proposed in [128], [129] was, however, investigated for low values of unbalance in the grid voltage. The first thorough approach to grid voltage estimation under unbalanced conditions was presented in [139], [140], where full-order and reduced order estimators for tracking the positive and negative sequence components of the grid voltage were investigated. A reduced order observer for estimating positive and negative sequence grid voltage components was later proposed in [141]. Mathematical observers for estimating positive and negative sequence components, and also harmonic components, of the grid voltage have been further investigated in [142]-[145]. The Kalman filter-based approach from [133] was also used to estimate sequence components and harmonic components of the grid voltage, while estimation of and compensation for unbalance and distortion in the grid voltage has been investigated recently in [146]. The voltage-sensor-less control method from [130], [131], based on resistance emulation for a VSC operating in rectifier mode, has also been adapted for operation under unbalanced conditions with the objective of maintaining balanced three-phase currents [147], [148]. Some examples of voltage-sensor-less grid synchronization based on Virtual Flux estimation have also been proposed, as will be discussed in the one of the following subsections.

2.2 Introduction to Virtual Flux Estimation for Voltage-Sensor-less Grid Synchronization

The starting point for the concept of Virtual Flux is the definition of the "Flux," Ψ, corresponding to the integral of the voltage, V, as given in (2.1).

$$\Psi = \int V \cdot dt + \Psi_0 \tag{2.1}$$

This "flux" integral has been used for long time in analysis and control of converters and electric drive systems [149]-[152], and has also been used to implement "flux-based" control of grid connected converters where the flux calculation has been based on measured voltages [100]-[103], [118], [153].

As voltage-sensor-less control of grid connected converters has gained increasing interest, the "flux-based" approach has become well-known due to the easy interpretation in analogy to the flux of an electrical machine. Thus, the flux integral is usually based on the output voltage of the converter in a similar way as for flux estimation in electric drives. The voltage to be integrated is usually calculated from the converter DC-link voltage and the switching states of the semiconductors as discussed

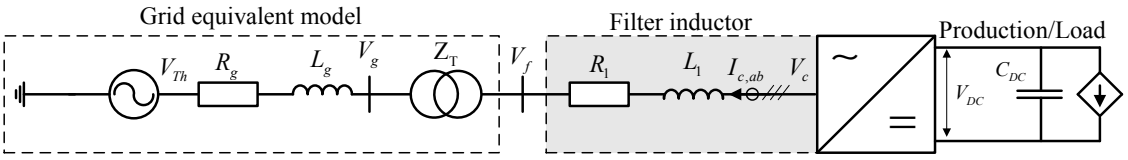

Fig. 2-1 Grid connected VSC with inductive filter

in [66]-[68], [80], [107]. Control methods with variable switching frequency will require the control system to operate on a significantly higher sampling frequency than the average switching frequency of the converter [154], [155]. For fixed frequency PWM operation of the converter, the converter output voltage can more easily be found from the PWM reference signals, and the Virtual Flux estimation can be operated with sampling frequency equal to (or twice) the switching frequency, as for standard PWM modulation with synchronized sampling [81], [154], [155],. For voltage-sensor-less operation, the Virtual Flux estimation must, however, be adapted to the intended point of synchronization to the grid.

2.2.1 Ideal Virtual Flux Estimation for Grid Synchronization

In a system configuration as shown in Fig. 2-1, the Virtual Flux estimation method is usually designed to replace voltage measurements at the grid side of the filter inductor. The corresponding estimation strategy is easily found by combining the definition from (2.1) with the voltage equation for the filter inductor as given by (2.2). Assuming PWM operation of the converter, the converter output voltage V_c can be estimated from the PWM reference signals and the measured DC-link voltage according to (2.3). The Virtual Flux, Ψ_f, at the grid side of the filter inductor can then be found by (2.4) [3], [68], [107]. The resistance R_1 represents the internal resistance of the filter inductor and is often small enough to be neglected, but it will be included in all following discussions to maintain general validity. The initial value of the flux integral is needed for initialization of the estimation, but will be omitted in the most of the following discussions.

$$V_{f,\alpha\beta} = V_{c,\alpha\beta} - R_1 \cdot I_{c,\alpha\beta} - L_1 \cdot \frac{dI_{c,\alpha\beta}}{dt} \tag{2.2}$$

$$V_{c,\alpha\beta} \approx m_{ref,\alpha\beta} \cdot \frac{1}{2} V_{DC} \tag{2.3}$$

$$\Psi_{f,\alpha\beta} = \int \underbrace{\left(m_{ref,\alpha\beta} \cdot \frac{1}{2} V_{DC} - R_1 \cdot I_{c,\alpha\beta} \right)}_{V_{\alpha\beta}^{\int}} dt - L_1 \cdot I_{c,\alpha\beta} \tag{2.4}$$

Introducing per unit values, according to the conventions described in Appendix A, the Virtual Flux estimation can be expressed by (2.5) as illustrated by a block diagram in Fig. 2-2. The figure shows clearly how the resistive voltage drop ($r_1 \cdot i_c$) is subtracted from the effective output voltage of the converter, while the inductive flux drop ($l_1 \cdot i_c$) is subtracted from the integrated voltage, to result in the Virtual Flux at the grid side of the filter inductor.

$$\psi_{f,\alpha\beta} = \omega_b \int \underbrace{\left(m_{ref,\alpha\beta} \cdot v_{DC} - r_1 \cdot i_{c,\alpha\beta} \right)}_{v_{\alpha\beta}^{\int}} dt - l_1 \cdot i_{c,\alpha\beta} \tag{2.5}$$

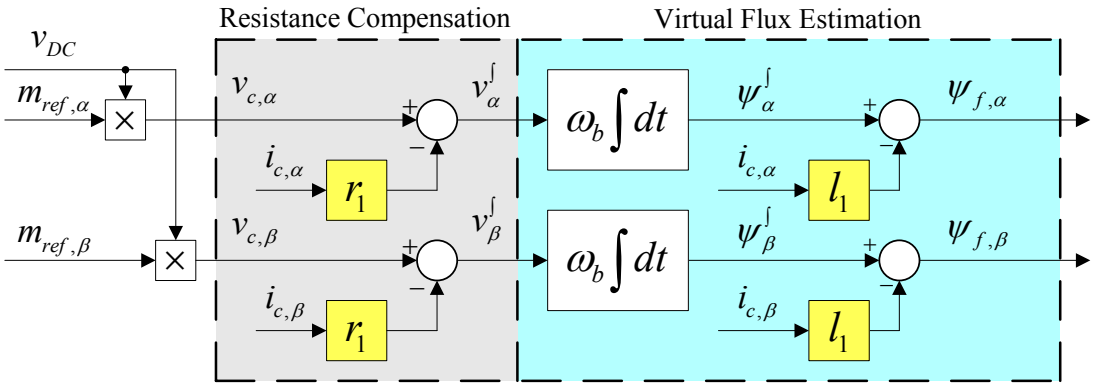

Fig. 2-2 Basic concept of ideal Virtual Flux estimation

A vector diagram illustrating the estimation in (2.5) and the relationship between voltage and Virtual Flux vectors, when assuming negligible resistance in the filter inductor, is shown in Fig. 2-3. Since the Virtual Flux corresponds to the integral of the voltage, its instantaneous phase angle γ lags the voltage phase angle by 90º for fundamental frequency signals. Therefore, the voltage phase angle θ_f can be easily estimated by (2.6). Since the integration required for Virtual Flux estimation implies a filtering effect, the instantaneous phase angle for synchronization can usually be calculated directly from (2.6), but it can also be tracked by a Phase Locked Loop [41].

$$\gamma_f = \arctan\left(\frac{\psi_{f,\beta}}{\psi_{f,\alpha}}\right) \qquad \theta_f = \gamma_f + 90° \tag{2.6}$$

2.2.2 Implementation Issues Regarding Virtual Flux Estimation

There are several issues that need to be considered for practical implementation of Virtual Flux estimation. The switching characteristics of the VSC might for instance be taken into consideration when estimating the converter output voltage, if accurate estimation of the Virtual Flux should be achieved. Possible drift and saturation of the estimated Virtual Flux, for instance due to DC-offset in the integrated signals, must also be avoided. In case of voltage-sensor-less converter operation, the strategy for start-up of the system and initialization of the Virtual Flux estimation should also be considered.

2.2.2.1 Influence of semiconductor characteristics and converter dead-time

Estimation of the converter output voltage directly from (2.3) will only be valid in case of PWM modulation of the VSC with negligible influence of the converter switching characteristics. If the switching characteristics have non-negligible influence on the converter operation and on the accuracy of the Virtual Flux estimation, the two dominant factors will be [107]:

- The conduction characteristics of the semiconductor switches.
- Converter dead-time implemented to avoid shoot-through of the DC-link voltage through one converter leg

The switching characteristics of the semiconductors are usually approximated by a piecewise linear characteristics described by a threshold voltage and a resistive conduction region. If the values of the threshold voltage and equivalent resistances can

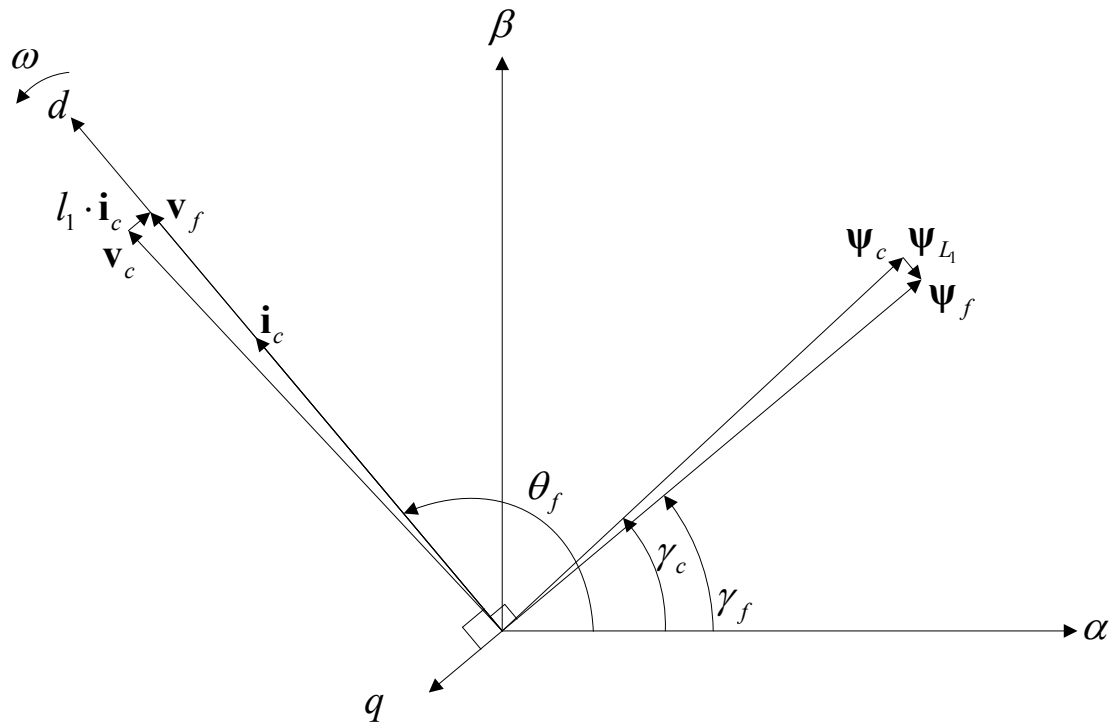

Fig. 2-3 Vector diagram showing voltage and Virtual Flux at the converter terminals and at the grid side of the filter inductor

be assumed equal for the controlled semiconductor switch and the anti-parallel diode, the voltage drop due to the conduction characteristics can be approximated by (2.7).

$$v_{sw} \approx \underbrace{\mathrm{Sign}(i_c) \cdot \left| v_{sw,th} \right|}_{v_{sw,th}} + \underbrace{r_{sw} \cdot i_c}_{v_{sw,r}} \tag{2.7}$$

The accuracy of the Virtual Flux estimation can thus be improved by subtracting the voltage v_{sw} from the ideal converter output voltage v_c before carrying out the integration of (2.5). The resistive voltage drop $v_{sw,r}$ can however be easily included in the Virtual Flux estimation by adding the semiconductor equivalent resistance r_{sw} to the equivalent resistance r_1 of the filter inductor in (2.5). The voltage drop $v_{sw,th}$ caused by the threshold voltage of the semiconductor switches can then be subtracted, as a separate term, from the ideal converter output voltage, v_c, before carrying out the integration of (2.5). In some cases, the converter threshold voltage can be compensated as part of the PWM mechanism, and the uncompensated modulation signals can then be used in the Virtual Flux estimation without loosing accuracy [107].

Compensation for the converter dead-time can also be included in the PWM operation of the converter, or in the Virtual Flux estimation. The implementation and the influence on the Virtual Flux estimation will depend on the applied modulation strategy as briefly outlined below.

i. Fixed frequency PWM operation with synchronized sampling

For fixed frequency PWM operation of the converter, with synchronized sampling of the control system, the influence of the dead-time averaged over one switching period, on the converter output voltage, can be described by (2.8) [107]. This equation can be used to implement dead-time compensation as a part of the PWM algorithm applied to

the VSC, either by adding the voltage in (2.8) to the reference signals or by adding/subtracting the dead-time to/from the length of the converter output voltage pulses [68], [107].

$$v_{sw,d-t} = \mathrm{Sign}\left(i_c\right)\frac{\Delta t_{d-t}}{T_{sw}}v_{DC} \tag{2.8}$$

If dead-time compensation is included in the PWM algorithm of the VSC, the uncompensated modulation can be used to estimate the converter output voltage as given by (2.5). Dead-time compensation can also be included in the Virtual Flux estimation by subtracting the equivalent voltage according to (2.8) from the estimated converter output voltage.

ii. Hysteresis-based modulation and control systems based on over-sampling

In case of nonlinear control methods like hysteresis current control or hysteresis-based Direct Power Control, the influence of the converter dead-time will be handled by the modulation itself and not by an explicit compensation method as described by (2.8). For such control methods, the Virtual Flux must be estimated from the actual switching states of the converter or from the gate signals. A relatively high ratio of control system oversampling with respect to the average switching frequency of the converter will then be needed. Still, the Virtual Flux-based approach will usually allow for applying a lower sampling frequency than other approaches for voltage-sensor-less grid synchronization [154], [155].

If compensation for the influence of converter dead-time on the estimated Virtual Flux should be included, either the real gate signals to the semiconductor switches has to be used for the Virtual Flux integration, or a turn-on/off delay has to be included in output from the hysteresis elements before these signals are used for integration of the converter output voltage pulses. Similar approaches should be used in case of predictive control methods with variable switching frequency, and in case of fixed switching frequency control methods where the control system is operated with a high degree of oversampling.

2.2.3 Practical Implementation of Virtual Flux Estimation

Ideal integration according to (2.4) or (2.5) can not be used for practical implementation of Virtual Flux estimation, since even apparently negligible DC-offset in the integrated signals will cause drift and saturation of the estimated signals. Such DC-offsets can for instance be caused by the converter dead-time and the characteristics of the semiconductor switches as discussed in the previous section, but can also be caused by current sensor off-sets, non-ideal characteristics or inaccuracies of analogue and digital signal conditioning, and by noise in the integrated signals [107]. Therefore, several different methods for practical implementation of Virtual Flux estimation have been proposed, with the purpose of avoiding drift and saturation of the estimated signals. The simplest methods for Virtual Flux estimation are using analogue or digital filters with phase characteristics designed to emulate integration at the fundamental grid frequency, but also more advanced, adaptive, integration methods have been applied.

2.2.3.1 Filter-based implementation of Virtual Flux estimation

The simplest method for filter-based Virtual Flux estimation is to use a first order low-pass filter with a crossover frequency significantly below the grid frequency. This

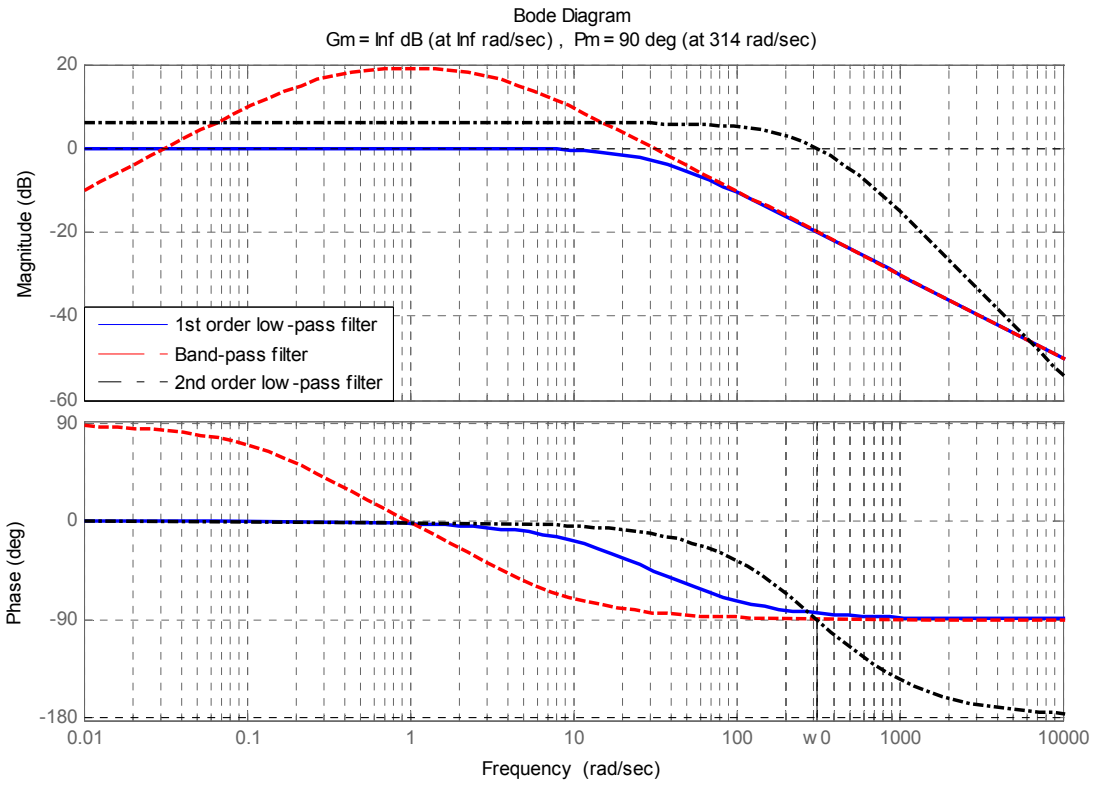

Fig. 2-4 Frequency response of filter-based methods for Virtual Flux estimation

approach has been commonly used for Virtual Flux-based voltage-sensor-less grid synchronization, and the crossover frequency is then usually specified to be one decade below the nominal angular frequency of the power system [66]-[68], [80], [107], [156]. The corresponding transfer function is given in (2.9), and the frequency characteristics verifying a phase shift close to 90° for fundamental frequency signals are shown by blue lines in Fig. 2-4. There will, however, be a small phase error in the estimated Virtual Flux signals, and significant attenuation of the amplitude. Possible problems with drift and saturation can be avoided by the low-pass-filter characteristics, but the amplitude attenuation will imply that dc-components in the input signals are magnified with respect to the fundamental frequency signals.

$$\psi_{LP}^{\int}(s) = \frac{\omega_{LP}}{s+\omega_{LP}} \cdot v^{\int}(s) \qquad \omega_{LP} = \frac{\omega_b}{10} \tag{2.9}$$

In order to eliminate DC-components in the estimated Virtual Flux signals, different varieties of band-pass filters have been used instead of the first order low-pass filter in (2.9) [102], [103], [156]. This approach gives more freedom to shape the frequency characteristics of the transfer function used for Virtual Flux estimation, but there will still be small phase errors in the estimated Virtual Flux and significant amplitude attenuation. A band-pass filter with similar frequency characteristics as described in [102], [103] is given by the transfer function and parameters of (2.10), and the resulting frequency response is plotted with red dashed lines in Fig. 2-4. With this estimation method, zero gain for dc-components is achieved and the phase characteristics result in approximately −90° phase shift for frequencies above a few Hz. There will, however, be significant amplitude attenuation in the estimated Virtual Flux signals, and in this

particular case, the amplitude characteristics is identical to that of the first order low-pass-filter in the frequency range corresponding to integrator emulation.

$$\psi_{BP}^{\int}(s) = \frac{\tau_a \cdot s}{(1+\tau_b \cdot s)\cdot(1+\tau_c \cdot s)} \cdot v^{\int}(s), \qquad \tau_a = \frac{1}{0.0001 \cdot \omega_b}, \quad \tau_b = \frac{1}{0.001 \cdot \omega_b}, \quad \tau_c = \frac{1}{0.01 \cdot \omega_b} \tag{2.10}$$

Another simple filter-based method for Virtual Flux estimation is described by the transfer function in (2.11), with the corresponding frequency response plotted by black dashed lines in Fig. 2-4 [107], [157], [158]. This method is based on two cascaded low-pass filters with crossover frequency equal to the nominal angular frequency of the grid. With this strategy, the amplitude and phase characteristics are analytically corresponding to unity gain and −90º phase shift at the fundamental frequency. This corresponds to a phase margin of 90º at the crossover frequency, as indicated in the figure. This method has the advantage of a relatively fast transient response but there will be a gain factor of 2 for DC-components [107].

$$\psi_{LP2}^{\int}(s) = \frac{2 \cdot \omega_b^2}{(s+\omega_b)^2} \cdot v^{\int}(s) \tag{2.11}$$

The filter-based methods with frequency responses plotted in Fig. 2-4, and several other varieties, can be used for Virtual Flux estimation with good results in strong grids. The accuracy of the phase angle and amplitude of the estimated Virtual Flux, will however be influenced by deviations from the nominal grid frequency unless special measures are taken to make the implementation frequency-adaptive.

2.2.3.2 Adaptive integration and advanced estimation techniques

Flux estimation methods for application in electric drive systems are usually required to handle large frequency variations. Therefore, several different approaches have been proposed to achieve flux estimation algorithms with integrator characteristics at a variable operating frequency while at the same time avoiding drift and saturation of the estimated flux signals.

A method for amplitude and phase compensation of flux estimation based on first-order low-pass-filters was for instance proposed by [159]. The compensation terms of this method is based on the ratio between the angular operation frequency ω and the crossover frequency ω_{LP} selected for the low-pass-filter, as given by (2.12). The same method has later been utilized for Virtual Flux estimation in a grid connected converter by [160], [161], and a slight modification to the structure from [159] has been applied for Virtual Flux estimation in [162].

$$\psi_{\alpha}^{\int} = \psi_{\alpha,LP} + \frac{\omega_{LP}}{\omega}\psi_{\beta,LP}$$
$$\psi_{\beta}^{\int} = \psi_{\beta,LP} - \frac{\omega_{LP}}{\omega}\psi_{\alpha,LP} \tag{2.12}$$

Estimation methods based on low-pass filters combined with feedback signals based on the vector amplitude of the estimated flux have also been proposed for drive systems in [163], and recently applied to grid connected converters in [164].

Adaptive methods for flux estimation have also been designed on basis of ideal integrators combined with different types of feedback from the estimated flux signals [156]-[166]. The basic consideration behind these methods is to use the feedback signal to maintain centricity of the trajectory of the estimated flux in the $\alpha\beta$ stationary reference frame. The resulting flux estimation can for instance be given by (2.13), with $\psi_{\alpha\beta}$ being a result of ideal integration, while different adaptation strategies are used to determine the gain k_ψ. Several different varieties of this approach, with different adaptive ways of calculating the correction term $\psi_{corr,\alpha\beta}$ have been investigated and applied in [3], [156], [165], [166] with [156] and [3] considering application to Virtual Flux estimation for grid connected converters.

$$\psi_{\alpha\beta}^{\int} = \psi_{\alpha\beta}^{\int,ideal} + \underbrace{k_\psi \left(\left| \psi_{filt,\alpha\beta}^{\int,ideal} \right|^2 - \left| \psi_{\alpha\beta}^{\int,ideal} \right|^2 \right) \cdot \psi_{\alpha\beta}^{\int,ideal}}_{\psi_{corr,\alpha\beta}} \tag{2.13}$$

The estimation methods mentioned above are implying correction terms found from the estimated $\alpha\beta$-components or from the vector amplitude of the estimated flux signals, and are based on the assumption of balanced three-phase voltages and fluxes. Although these methods will provide Virtual Flux estimation with good performance in case of frequency variations and eliminate the problem of drift and saturation, they will not be directly applicable to single phase systems or unbalanced operation of three-phase systems.

It can be noted that sliding mode observers for individual estimation of the Virtual Flux corresponding to each phase of the converter have been investigated in [167], [168]. Under unbalanced conditions, the Virtual Flux signals that will be estimated by this method will, however, have different amplitudes for each phase, just like the pure filter-based methods for Virtual Flux estimation described in the previous subsection.

2.2.4 Initialization and Start-up of Virtual Flux-based Grid Synchronization

As can be understood from the voltage integral in (2.1), the initial value of the Virtual Flux integral should be used for initialization of the estimation, and thus for voltage-sensor-less start-up of a VSC. This is usually achieved by applying two short zero-voltage-vector pulses from the converter and measuring the resulting current [3], [63], [64], [107], [156],. Considering that the zero-voltage pulse from the converter is short enough to assume constant grid voltage during the switching cycle, the expression for the resulting current can be approximated by (2.14) where T_p is the length of the zero-voltage pulse. Thus, the grid side voltage at the time of the zero-voltage pulse can be approximated by (2.15), with corresponding Virtual Flux values given by (2.16). The phase angle of the grid voltage, or the corresponding Virtual Flux, can be estimated according to (2.17), and the grid frequency can be estimated according to (2.18), where Δt is the time difference between the two zero-voltage pulses.

$$i_{\alpha\beta} \approx \frac{1}{l_1} \cdot \omega_b \cdot v_{\alpha\beta} \cdot T_p \tag{2.14}$$

$$\breve{v}_{\alpha\beta} = i_{\alpha\beta} \cdot \frac{l_1}{T_p \cdot \omega_b} \qquad \left| \breve{\mathbf{v}} \right| = \sqrt{\breve{v}_\alpha^2 + \breve{v}_\beta^2} = \frac{l_1}{T_p \cdot \omega_b} \sqrt{i_\alpha^2 + i_\beta^2} \tag{2.15}$$

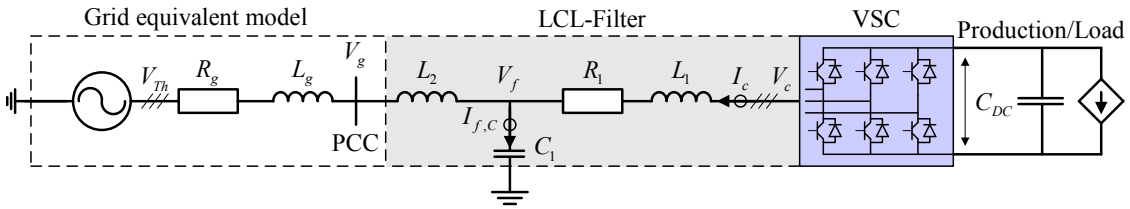

Fig. 2-5 Configuration with VSC and LCL-filter

$$\breve{\psi}_\alpha = \breve{v}_\beta = \frac{l_1}{T_p \cdot \omega_b} \cdot i_\beta \qquad \breve{\psi}_\beta = -\breve{v}_\alpha = -\frac{l_1}{T_p \cdot \omega_b} \cdot i_\alpha \qquad \left|\breve{\boldsymbol{\psi}}\right| = \left|\breve{\mathbf{v}}\right| \tag{2.16}$$

$$\breve{\theta}_1 = \tan^{-1}\left(\frac{i_{\beta,1}}{i_{\alpha,1}}\right) \qquad \breve{\gamma}_1 = \theta_1 - 90° \tag{2.17}$$

$$\breve{f} = \frac{\breve{\theta}_2 - \breve{\theta}_1}{\Delta t} \tag{2.18}$$

The grid frequency estimated from (2.18) can be used to predict the phase angle of the grid voltage and Virtual Flux at the time when regular switching of the VSC is enabled and the control system is allowed to start normal operation. More details regarding start-up procedures are discussed in [3], [107]. The possibility for start-up of a VSC without the estimation procedure outlined above, with corresponding initialization of the control system, has also been investigated in [107]. However, techniques for initialization of the Virtual Flux estimation and voltage-sensor-less start-up of VSCs will not be further discussed here.

2.2.5 Virtual Flux-based Grid Synchronization and Control in Case of LCL-filters

In Fig. 2-1, the VSC was connected to the grid through an inductive filter, but in most cases a capacitive branch will also be included in the filter, either in the form of an LC-filter or in the form of an LCL-filter as shown in Fig. 2-5 [2], [39], [169]. Depending on the application and the power system configuration, the grid side inductance, L_2, can be a separate inductor as indicated in Fig. 2-5, or it can be the leakage inductance of a transformer. The point where the power factor or the reactive power exchange with the grid is controlled and/or the point of synchronization to the grid should however be carefully considered in configurations with LC- or LCL-filters. Depending on the filter design, it can also be necessary to implement strategies for active damping of LC-oscillations. These issues are well known from traditional voltage-based grid synchronization and control of VSCs, but need additional attention in the case of Virtual Flux-based voltage-sensor-less control.

2.2.5.1 Virtual Flux estimation and power control at the grid side of an LCL-filter

In most cases, a VSC is required to have the ability to control the power factor or the flow of reactive power at the point of connection to the grid. There are several ways to address this issue, depending on the design and parameters of the filter and the converter control system.

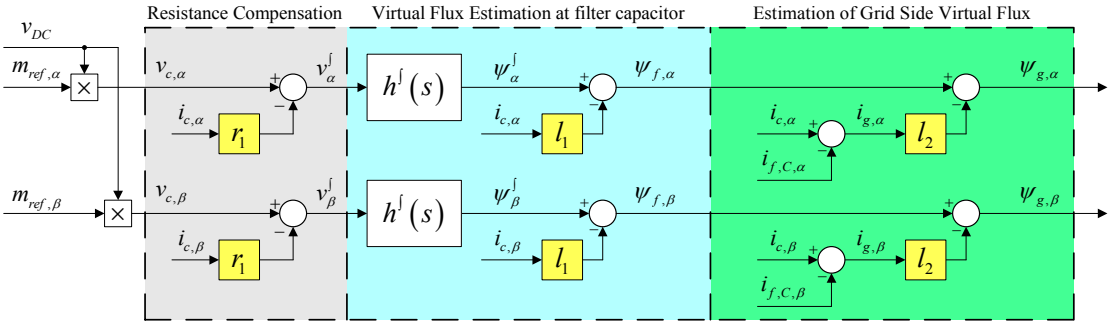

Fig. 2-6 Estimation of Virtual Flux at grid side of LCL-filter

The simplest approach to voltage-sensor-less grid synchronization and control in case of LCL filters can be applied if the fundamental frequency current component $i_{f,c}$ in the filter capacitor C_1 can be considered negligible. If the resistance of the grid side filter inductor is also negligible, the Virtual Flux at the grid side of the LCL-filter can then be easily estimated according to (2.19) [170], [171]. In this equation, $h^\int(s)$ is denoting a generic transfer function for estimation of the Virtual Flux, and any of the methods discussed in the previous section could be applied. As the current in the filter capacitor, and thus the corresponding reactive power, is considered negligible, the control of active and reactive power flow at the grid side of the LCL-filter can be based on the estimated Virtual Flux, just as for the case with a pure L-filter.

$$\psi_{g,\alpha\beta} \approx h^\int(s)\cdot v^\int(s) - (l_1+l_2)\cdot i_{c,\alpha\beta} \qquad \text{for} \qquad i_{f,C,\alpha\beta} \approx 0 \tag{2.19}$$

When the fundamental frequency component of the current in the filter capacitor is non-negligible, it has to be taken into account in the Virtual Flux estimation and in the control of the active and reactive power flow. If the resistance of the grid side filer inductor L_2 is negligible, the resulting structure for estimation of the Virtual Flux at the filter capacitor and at the grid side of the LCL-filter is described by (2.20) and illustrated by Fig. 2-6. If the resistance in the grid side inductor can not be neglected, the Virtual Flux estimation will have to include the integral of the grid current multiplied by the grid side resistance r_2 as expressed by (2.21).

$$\psi_{g,\alpha\beta} = h^\int(s)\cdot v_{\alpha\beta}^\int - l_1\cdot i_{c,\alpha\beta}(s) - l_2\cdot \underbrace{\left(i_{c,\alpha\beta}(s) - i_{f,C,\alpha\beta}(s)\right)}_{i_{g,\alpha\beta}(s)} s \tag{2.20}$$

$$\begin{aligned} \psi_{g,\alpha\beta} &= h^\int(s)\cdot v_{\alpha\beta}^\int(s) - l_1\cdot i_{c,\alpha\beta}(s) - r_2\cdot h^\int(s)\cdot i_{g,\alpha\beta}(s) - l_2\cdot i_{g,\alpha\beta}(s) \\ i_{g,\alpha\beta}(s) &= \left(i_{c,\alpha\beta}(s) - i_{f,C,\alpha\beta}(s)\right) \end{aligned} \tag{2.21}$$

The Virtual Flux estimation according to Fig. 2-6 or (2.21) is dependent on the current in the filter capacitor for estimating the Virtual Flux at the grid side of the filter inductor L_2. In [160], the capacitor current is measured and used for implementation of the estimation structure shown in Fig. 2-6, but it is also possible to estimate the capacitor current as described in [3], [172].

Another approach for controlling the reactive power at the grid side of L and LCL-filters is proposed in [156], [173], where the control system of the VSC is synchronized to the Virtual Flux estimated at the converter terminals. Thus, the reactive power flow at the grid side of the filter was controlled by using the filter parameters for specifying current references resulting in the specified reactive power flow at the grid side of the

filter. The investigations presented in [156], [173] included strategies based on open loop calculation of the appropriate current references. Also closed loop strategies where the current references were partly determined by a feedback-loop based on the estimated active and reactive power flow at the grid side of the filter were considered. In this way, unity power factor or a specified flow of reactive power could be achieved at the point of connection to the grid.

2.2.5.2 Active damping of LC-oscillations

When LC- or LCL-filters are used for grid connection of VSCs, there might be a need for implementing algorithms for active damping of LC-oscillations as part of the converter control system. The active damping is usually based on feedback from either the voltage over the filter capacitors or from the current in the filter capacitor. It is also possible to implement active damping as a part of the current controllers based only on the converter current feedback.

When active damping is integrated as a part of the current controllers, as analyzed in [174]-[176], there will be no need for additional feedback signals, and the active damping mechanism can be designed without consideration of the method used for synchronization to the grid. In such cases there will not be any additional challenges related to application of active damping, apart from the issues related to the Virtual Flux estimation discussed in the previous subsection. With active damping is based on the measured currents in the filter capacitors, there will neither be additional challenges in the active damping. The additional current measurement will however ease the estimation of the Virtual Flux at the grid side of the LCL filter, as described in the previous subsection [160], [177].

Active damping of LC-oscillations can also be implemented on basis of estimated values for the voltages at the filter capacitors. This estimation can be a part of the algorithms needed for estimating the Virtual Flux at the grid side of the LCL-filter, since the Virtual Flux and the voltage at the filter capacitor is needed for estimation of the capacitor currents and by that the total current in the grid side inductor [3], [172]. To apply conventional techniques for active damping from for instance [169], [178], the Virtual Flux estimation at the filter capacitor should be capable of capturing the dynamics in the frequency range of the LC-oscillations, since the capacitor voltage and the current must be found by differentiation of the estimated Virtual Flux. Thus, adaptive integration techniques with drift compensation as outlined in section 2.2.3 were used for the Virtual Flux estimation in [3], [172], since the filter-based estimation methods provide significant attenuation of the high frequency oscillations.

Another approach for estimation of the filter capacitor voltages for the purpose of active damping was applied in [170], [179], based on the instantaneous power theory discussed in [59], [60], [62]. This approach was especially convenient in [170] and [171] where the current in the filter capacitor was considered negligible with respect to the Virtual Flux estimation used for grid synchronization. Thus, the voltage estimation according to [59], [60], [62], which is more sensitive to noise, was used only for the active damping, while the grid synchronization could be based on simple structure for Virtual Flux estimation.

As understood from this discussion, a high bandwidth is required in the estimation of the capacitor current if this estimate is used as a part of an active damping algorithm. If the current estimate is mainly needed for Virtual Flux estimation with the purpose of

grid synchronization, estimation of the fundamental frequency component will however be the main objective. Thus, the influence of high frequency noise as well as LC-oscillations should be attenuated in the Virtual Flux estimate used for grid synchronization. The Virtual Flux estimation methods achieving a suitable compromise between these two considerations can be expected to receive further attention. Active damping will however not be a main issue in the following discussions, but can be a relevant issue for further investigation together with some of the issues that will be analysed in more detail.

2.2.6 Parameter Sensitivity of Virtual Flux Estimation

From the presented strategies for Virtual Flux estimation, it is obvious that the accuracy of the estimated Virtual Flux at the grid side of L-, LC- or LCL-filter will depend on the accuracy of the available filter parameters. From the diagrams in Fig. 2-2 and Fig. 2-6, it can be seen that resistive and inductive terms of the Virtual Flux estimation are only involved in arithmetic operations, and parameter deviations should therefore not influence the stability of the estimation structure. Parameter deviations will, however, influence the accuracy of the grid synchronization, and therefore also the accuracy of active and reactive power control or power factor control at the point where the converter is intended to be synchronized to the grid [154], [155]. When the active power flow is resulting from a closed loop controller, usually operating on the DC-link voltage of the VSC, the influence of parameter deviations will be compensated by the controller, and only the power factor or the reactive power exchange with the grid will be influenced. If the converter control system is based on the Direct Power Control (DPC) principle with a look-up table, parameter deviations can however have some influence on the THD of the resulting currents [154], [155].

The reactive power error at the point of connection to the grid has been systematically investigated as a function of parameter deviations for L- and LCL-filters in [156], [173], showing acceptable accuracy for relatively large variations in the values of L_1, C_1, and L_2. Some simple analytical approximations for the reactive power deviation caused by parameter errors were also introduced. Active and reactive power deviations from the reference values were further investigated with respect to variations in the inductance values for L-filters in [160] and for LCL-filters in [180], showing similar results.

The influence of deviations in the converter side filter inductance on the operation of a particular control strategy based on Predictive Direct Power Control has also been investigated in [181] and [182]. In this case, the sensitivity with respect to the inductance of the filter is higher, and a method for on-line inductance estimation was therefore proposed as part of the control system. Until now, [181] and [182] have been the only examples of Virtual Flux estimation strategies with on-line parameter estimation, but parameter identification techniques similar to the methods applied in combination with strategies for grid voltage estimation in [134]-[138], could also be further investigated together with Virtual Flux-based voltage-sensor-less synchronization strategies.

2.3 Virtual Flux-based Grid Synchronization under Unbalanced Grid Voltage Conditions

Considering the relatively large number of publications discussing voltage-sensor-less operation of VSCs, it is remarkable that so few studies until now have systematically considered Virtual Flux-based voltage-sensor-less grid synchronization and control under unbalanced grid voltage conditions. The majority of the available publications related to voltage-sensor-less operation under unbalanced conditions are based on mathematical observers, as briefly reviewed in section 2.1.2, without considering the inherent simplicity of the Virtual Flux concept.

2.3.1 Methods Based on Synchronous Reference Frames for Identification of Positive Sequence Virtual Flux Components

The first study of Virtual Flux-based voltage-sensor-less control designed for operation under significant grid voltage unbalance was presented in [105]. In this study, the Virtual Flux was estimated by first-order low-pass filters according to (2.9), and a simple PLL with low bandwidth was used to track the positive sequence phase angle of the estimated Virtual Flux. In addition, a low-pass filter operating on the Virtual Flux vector amplitude was used to estimate the amplitude of the positive sequence component and to reconstruct the positive sequence Virtual Flux signals in the stationary reference frame. The control of the VSC was in this case based on Direct Power Control with Space Vector Modulation (DPC-SVM), using the positive sequence Virtual Flux components for the power estimation and the corresponding phase angle for transformation of voltage references into the stationary reference frame for SVM. Thus balanced, sinusoidal currents were achieved with the Virtual Flux-based DPC-SVM under unbalanced and distorted conditions.

More advanced PLL strategies based on different varieties of the Double Decoupled Synchronous Reference Frame- (DDSRF) PLL described by [45], have also been applied for estimating the amplitudes and phase angles of positive and negative sequence Virtual Flux components as presented in [106], [183], [184]. These methods are improving the speed of response and the accuracy of the synchronization under unbalanced conditions by using decoupling networks to remove the influence of negative sequence components on the positive sequence components represented in the positive sequence Synchronous Reference Frame (SRF), and vice versa,

Another approach for voltage-sensor-less operation based on Virtual Flux estimation under unbalanced conditions has been investigated in [185]-[188]. In this case, the output voltage from the converter is first estimated from the DC-link voltage and the PWM reference signals. The voltages, estimated in the stationary $\alpha\beta$-Reference Frame, are then transformed into the positive and negative sequence SRFs. A notch-filter followed by a low-pass-filter is used to remove the second harmonic oscillations in the positive sequence dq-components caused by the negative sequence components and vice versa. A simple PLL, operating on the estimated positive sequence voltage, is then detecting the phase angle needed for the dq-transformations. The estimated positive and negative sequence voltage components in the corresponding SRFs are transformed back to the stationary $\alpha\beta$-Reference Frame, and the positive sequence voltage components are used to estimate the positive sequence Virtual Flux components. The phase angle of the estimated positive sequence Virtual Flux is used to transform the voltage references

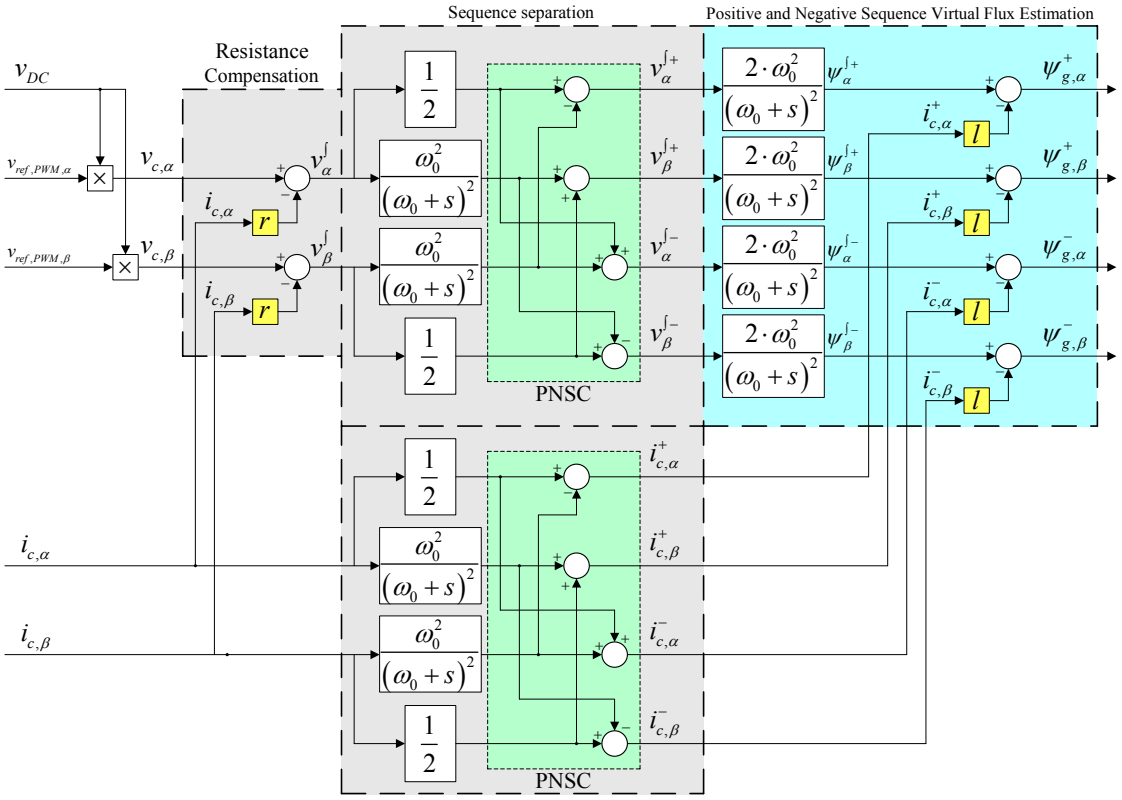

Fig. 2-7 Method for estimation of Positive and Negative Sequence Virtual Flux components proposed by Kulka in [107]

from the control system into the stationary $\alpha\beta$-reference frame, where the negative sequence voltage components are added as feed-forward terms.

2.3.2 Estimation of Positive and Negative Sequence Virtual Flux Components in the Stationary Reference Frame

The synchronization methods mentioned above are based on identification of positive and negative sequence components in the corresponding Synchronous Reference Frames. A different approach for Virtual Flux-based estimation has however been proposed by [107], based on explicit estimation of Positive and Negative Sequence (PNS) Virtual Flux components in the stationary reference frame.

The total structure of the voltage-sensor-less grid synchronization method proposed in [107] is shown in Fig. 2-7. It can be seen from the figure that positive and negative sequence components of the converter output voltage are estimated in the stationary reference frame by using second-order low-pass filters as phase shifting operators for achieving sequence separation in the time domain [50], [51], [189], [190]. The Positive and Negative sequence Virtual Flux components are then estimated separately. A further analysis of the synchronization method and control system proposed in [107] has later been presented in publication [C2] listed in the introduction. Additional analysis of the sequence separation method and the Virtual Flux estimation strategy from [107] is also presented and compared to the characteristics of other possible configurations in Appendix B.

2.3.3 General Features of Available Methods for Virtual Flux-based Grid Synchronization under Unbalanced Conditions

The common feature of all the presented studies of Virtual Flux-based grid synchronization under unbalanced conditions is that they are considering the Virtual Flux estimation and the separation of PNS components as separate problems. The methods in [105], [106], [183], [184] are, for instance, first estimating the Virtual Flux according to traditional filter-based methods before applying different SRF-based PLL structures for identifying the positive and negative sequence Virtual Flux components. The synchronization methods in [107], [185]-[188] are on the other side identifying positive and negative sequence voltage components before estimating the individual PNS Virtual Flux components. Both these approaches imply that a strategy for sequence separation is cascaded to the Virtual Flux estimation, causing cascaded delays resulting in relatively slow transient response.

2.4 Summary of Chapter

This chapter has presented an overview of the state-of-the-art for voltage-sensor-less control with particular focus on estimation strategies and implementation issues for Virtual Flux-based voltage-sensor-less control. It has been shown how the concept of Virtual Flux-based grid synchronization is well established for voltage-sensor-less operation under balanced three-phase conditions. However, only few studies have presented methods for Virtual Flux-based voltage-sensor-less grid synchronization and control during unbalanced conditions.

Main purpose of Chapter:

- Review of state-of-the-art in Virtual Flux-based voltage-sensor-less grid synchronization and control, presented as a background for the following chapters.

.

3 Voltage-sensor-less Grid Synchronization by Frequency-adaptive Virtual Flux Estimation

This chapter is presenting a method for explicitly frequency-adaptive implementation of Virtual Flux estimation, utilizing a Second Order Generalized Integrator (SOGI) configured for simultaneous band-pass filtering and Quadrature Signal Generation (QSG). This method can be applied in different configurations for both single-phase and three-phase applications. However, the main advantage of the proposed method for Virtual Flux estimation is that it can be configured to achieve Virtual Flux estimation with inherent sequence separation during unbalanced conditions, thus achieving a simpler structure with faster dynamic response compared to conventional techniques presented in the previous literature. The proposed method for Virtual Flux estimation with inherent sequence separation is labeled as DSOGI-VF estimation, since it is based on two parallel SOGI-QSGs. This new method has been tested by simulation studies and experimental verification in a small-scale laboratory setup, and has been analyzed in comparison to conventional approaches for Virtual Flux estimation. The main contributions and results in this chapter have been published in the manuscripts [C1] and [J1], although more details and additional results are included in this chapter. A few variations of the proposed methods, adapted for various applications, are outlined at the end of the chapter, together with suggestions for potential extensions and possible ideas for further investigations.

3.1 Frequency-adaptive Implementation of Conventional Strategies for Virtual Flux Estimation

From the existing scientific literature related to Virtual Flux estimation and Virtual Flux-based voltage-sensor-less control, two main limitations can be identified:

i. The simple and commonly applied filter-based methods for Virtual Flux estimation can result in inaccurate estimation of phase angle and/or amplitude, and they can be sensitive to grid frequency variations.
ii. The available techniques for Virtual Flux-based grid synchronization under unbalanced conditions are based on cascading filter-based methods for Virtual Flux estimation with different techniques for sequence separation. This results in complex structures with relatively slow transient response.

Considering the inherent simplicity of the filter-based approaches for Virtual Flux estimation, utilization of an explicitly frequency-adaptive filter structure with

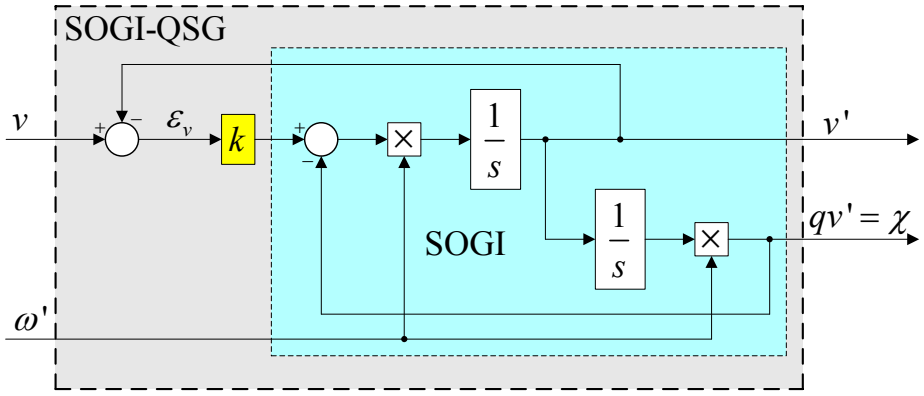

Fig. 3-1 Explicitly frequency-adaptive Second Order Generalized Integrator configured as a Quadrature Signal Generator (SOGI-QSG) with the in-quadrature output signal *qv'* representing the scaled Virtual Flux χ

characteristic features suitable for overcoming the mentioned limitations is proposed in the following sub-sections. The applied filter structure can be used as a basic building block for Virtual Flux estimation in single-phase or multi-phase systems, and will be shown to have characteristics suitable for designing grid synchronization methods for unbalanced three-phase conditions.

3.1.1 The Second Order Generalized Integrator Configured as a Quadrature Signal Generator (SOGI-QSG) for On-line Frequency-adaptive Virtual Flux Estimation

The Second Order Generalized Integrator (SOGI) has become well known as a building block used for sinusoidal signal integration in converter control systems and grid synchronization methods [51], [52], [77], [191]. Configured as an on-line frequency-adaptive Quadrature Signal Generator (QSG), as shown in Fig. 3-1, the SOGI can provides two output signals where the direct output signal, *v'*, will be in phase with the input for signals for fundamental frequency components, while the in-quadrature output signal, *qv'*, will be always be phase shifted by -90° with respect to *v'* [51], [52], [191]. This configuration, labeled SOGI-QSG, has found widespread applications in grid synchronization methods, where 90° phase shifting can be utilized for implementing SRF PLLs in single-phase systems and for symmetrical component sequence separation under unbalanced three-phase conditions.

The characteristics of the in-quadrature output signal, *qv'*, with -90° phase shift at the fundamental frequency, is corresponding to the frequency characteristics required for filter-based Virtual Flux estimation as described in section 2.2.3. The SOGI-QSG, based on the configuration in Fig. 3-1, can therefore be used as a basic building block for implementing explicitly frequency-adaptive Virtual Flux estimation as proposed in [C1] and [J1].

3.1.1.1 Steady-state characteristics and tuning of SOGI-QSG

Assuming a constant resonance frequency ω', the transfer functions of the SOGI-QSG in Fig. 3-1 can be established as given by (3.1) and (3.2). The transfer function from *v* to *v'* in (3.1) can be seen to describe a band-pass filter while the transfer function from *v* to *qv'* in (3.2) corresponds to a second-order low-pass filter [51], [52].

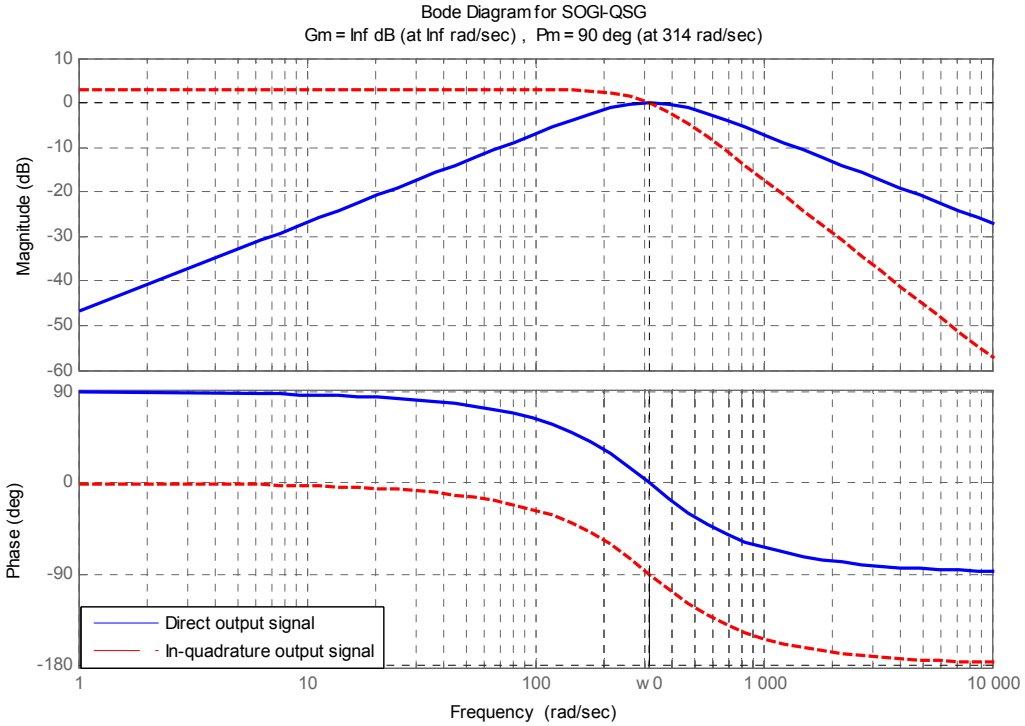

Fig. 3-2 Frequency response of SOGI-QSG

$$\frac{v'(s)}{v(s)} = \frac{k \cdot \omega' \cdot s}{s^2 + k \cdot \omega' \cdot s + \omega'^2} \tag{3.1}$$

$$\frac{qv'(s)}{v(s)} = \frac{k \cdot \omega'^2}{s^2 + k \cdot \omega' \cdot s + \omega'^2} \tag{3.2}$$

The frequency responses of transfer functions in (3.1) and (3.2) are shaped by the value of the gain constant k. Selecting k equal to $\sqrt{2}$ will result in a critically damped second order system, providing a good compromise between overshoot, settling time and rejection of high frequency harmonic components, as discussed in [51], [192]. The value of k will therefore be kept equal to $\sqrt{2}$ for all following investigation, and the resulting frequency characteristics of the SOGI-QSG is are shown in the Bode-diagram of Fig. 3-2 for a resonance frequency equal to 50 Hz, indicated by ω_0 in the figure. The frequency responses clearly shows that the direct output signal v' has band-pass characteristics with unity gain and zero phase shift at the fundamental angular frequency ω_0, while the in-quadrature signal qv' has low-pass characteristics with unity gain and −90° phase shift at the fundamental angular frequency.

From the frequency response in Fig. 3-2 and the transfer function in (3.2), it can be noticed that the DC-gain of the in-quadrature signal will be equal to the gain constant k. As this DC-component will usually be small and slowly varying, it can be removed by additional high-pass filtering as discussed in [107]. However, the DC-component can also be removed from the in-quadrature output signal by adding another state variable for estimating the DC-component in the structure of the SOGI-QSG, as proposed in [193]. For the following discussions the magnitude of the DC-component will be assumed negligible, so that the low-pass filter characteristics of the SOGI-QSG will provide sufficient accuracy in quadrature signal generation and Virtual Flux estimation.

It can also be noted that the frequency response of the transfer function in (3.2) shown in Fig. 3-2 is only marginally different from the frequency response of the second-order low-pass-filter in (2.11), as they are both providing unity gain and −90° phase-shift for fundamental frequency signals. However, the main functional difference is that the implementation according to Fig. 3-1 will be inherently frequency-adaptive as long as an estimate of the grid angular frequency ω' is available. This frequency information can for instance be provided by a Phase Locked Loop (PLL) as discussed in [51] or by a Frequency Locked Loop (FLL) as proposed and discussed in [52], [192], [194]-[196]. In the following, either a simple SRF PLL or a FLL with the structure and tuning described in [195], [196], will be used.

3.1.1.2 Approximated transient response of SOGI-QSG

Considering the transfer function of (3.2), traditional approximations for the transient response described by the rise-time, t_r and the settling time t_s, can be approximated by (3.3) where ζ is the damping ratio of the transfer function and T' is the period-time of the grid frequency [197].

$$\begin{aligned} t_r &\approx \frac{1.8}{\omega'} = \frac{1.8}{2\pi \cdot f'} = \frac{1.8}{2\pi} T' \approx \frac{1}{4} T' \\ t_s &\approx \frac{1}{\zeta} \cdot \frac{4.6}{\omega'} = \frac{2}{k} \cdot \frac{4.6}{2\pi \cdot f'} = \frac{\sqrt{2} \cdot 4.6}{2\pi} T' \approx T' \end{aligned} \tag{3.3}$$

From (3.3), a rise time in the range of a quarter of a period, and a settling time in the range of one period should be expected for the amplitude of the Virtual Flux estimated by the SOGI-QSG. More detailed analysis of the transient response of the SOGI-QSG in case of a sinusoidal input was presented in [192], [195], [196], resulting in an approximation for the settling time given by (3.4), that is corresponding well to the more simplified approximation in (3.3).

$$t_s \approx 5 \frac{2}{k \cdot \omega'} = \frac{5}{\sqrt{2} \cdot \pi \cdot f'} = \frac{5}{\sqrt{2} \cdot \pi} T' \approx 1.1 \cdot T' \tag{3.4}$$

The presented expressions will be useful for evaluating the transient response of different methods for grid synchronization and Virtual Flux estimation in the following investigations. However, the steady-state operation and the transient response of the SOGI-QSG is well documented in [51], [52], [191], [192], and no further analysis will be presented here.

3.1.1.3 Discrete time implementation of SOGIs and SOGI-QSGs

The structure of the SOGI and the SOGI-QSG, with two separate integrators in a resonance structure as shown in Fig. 3-1, is designed to provide as simple way of achieving frequency-adaptive operation. Discrete time implementation of the SOGI resonance structure based on two separately discretized integrators will, however, be sensitive to stability problems and performance degradation due to numerical errors [191], [198]. For simulation studies with very small time-steps, implementation of SOGI-QSGs according to Fig. 3-1 can still provide acceptable accuracy based on trapezoidal integration, and this approach will therefore be used for most of the simulations presented in this Thesis. For implementation in real-time experimental systems, as well as for simulations with increased time-step or accurate emulation of

digital control systems, the numerical accuracy must, however, be addressed more carefully. One possible approach is to establish state-space difference equations describing the entire SOGI-QSG. The approach followed in this Thesis is based on [194], [199], with state-space difference equations established by trapezoidal integration. These difference equations will be non-linear, since the terms depending on the grid frequency must be continuously updated to keep the system frequency adaptive. The resulting state-space model of the SOGI-QSG and the derivation of the difference equations used for discrete time implementation are documented in Appendix C.

3.1.2 Definition of Frequency-scaled Virtual Flux based on SOGI-QSG

Considering the block diagram of Fig. 3-1 and the transfer functions in (3.1) and (3.2), it is clearly seen that the in-quadrature output signal labeled *qv'* is the integral of the in-phase output *v'* multiplied with the resonance frequency *ω'*, as given by (3.5). Therefore, this signal will have the same amplitude as the voltage, and can with reference to the expression for per-unit Virtual Flux in (2.5) be considered to represent the Virtual Flux scaled with the per unit value of the fundamental frequency. This quantity can be defined as the "frequency-scaled Virtual Flux," and is labeled χ as also indicated in Fig. 3-1 and shown in (3.5).

$$qv' = \omega' \int \left[v^{\int} \right]' dt = \omega_{pu}' \cdot \omega_b \int \left[v^{\int} \right]' dt = \omega_{pu}' \cdot \psi^{\int}_{SOGI-QSG} \equiv \chi \tag{3.5}$$

Applying the definition from (3.5), the scaled Virtual Flux at the grid side of the filter inductor in Fig. 2-1 can be expressed by (3.6). As the transfer function of the Virtual Flux estimation based on the SOGI-QSG is given by (3.7), the scaled Virtual Flux, χ_f, at the filter terminals can then be expressed in the Laplace domain by (3.8).

$$\chi_f = \omega' \int \left[v^{\int} \right]' dt - \omega'_{pu} \cdot l_1 \cdot i_c \tag{3.6}$$

$$\chi(s) = qv'(s) = \underbrace{\frac{k \cdot \omega'^2}{s^2 + k \cdot \omega' \cdot s + \omega'^2}}_{h^{\int}_{SOGI-QSG}} v(s) \tag{3.7}$$

$$\chi_f(s) = \frac{k \cdot \omega'^2}{s^2 + k \cdot \omega' \cdot s + \omega'^2} \cdot \left[v_c(s) - r_1 \cdot i_c(s) \right] - \omega_{pu}' \cdot l_1 \cdot i_c(s) \tag{3.8}$$

This definition of "frequency scaled Virtual Flux" estimated by a SOGI-QSG is generic, and can be applied to both single-phase and multi-phase systems. This method for Virtual Flux estimation can therefore be used to straightforward to implement explicitly frequency-adaptive Virtual Flux estimation in any configuration, for grid synchronization based in either voltage-sensor-less operation or voltage measurements. A block diagram describing the resulting structure for Virtual Flux-based voltage-sensor-less grid synchronization in the three-phase system from Fig. 2-1, based on the SOGI-QSG and the presented definition of frequency-scaled Virtual Flux is shown in Fig. 3-3.

It can be noticed that the configuration in Fig. 3-3 is only utilizing the in-quadrature output signals from the SOGI-QSG. Full utilization of the features of the SOGI-QSG is however only achieved when both the output signals are utilized, for instance for the purpose of symmetrical component sequence separation as proposed in [51], [52].

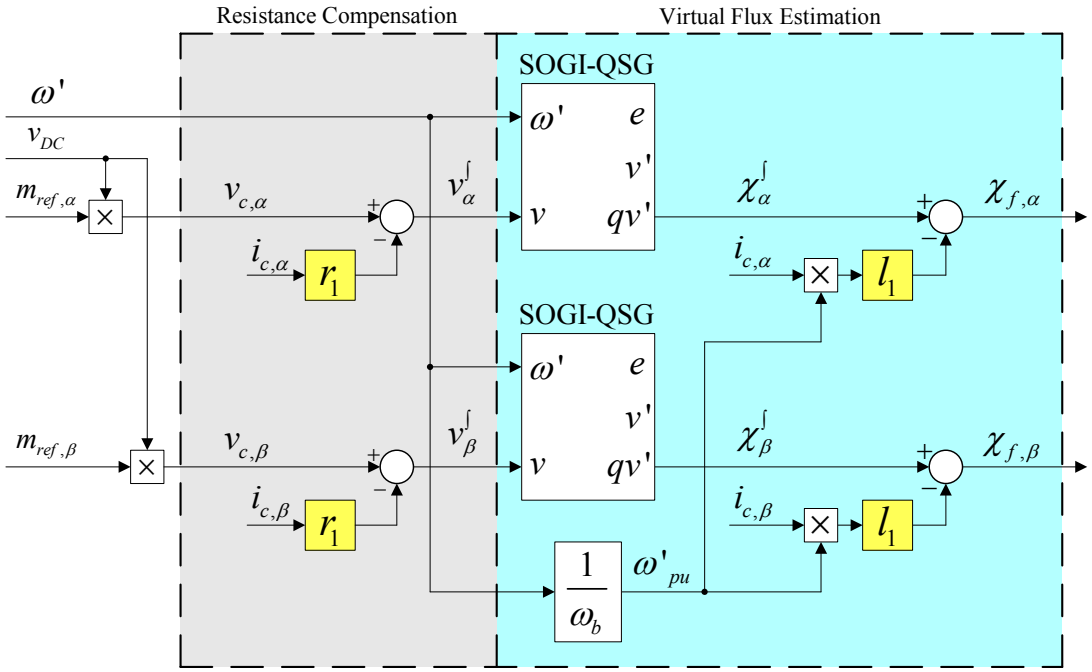

Fig. 3-3 Estimation of frequency-scaled Virtual Flux based on SOGI-QSGs

3.2 *Utilization of SOGI-QSGs for On-line Frequency-adaptive Virtual Flux Estimation and Sequence Separation under Unbalanced Conditions*

As mentioned, only a limited number of studies have until now considered Virtual Flux-based voltage-sensor-less grid synchronization under unbalanced conditions. From the studies, reported in [105]-[107], [183]-[188], it can also be noticed that the applied strategies for Virtual Flux estimation and the sensitivity to grid frequency variations are not discussed in detail. However, all the presented estimation strategies are based on cascaded operation of methods for Virtual Flux estimation and sequence separation organized in different ways. This section will show how the main strategies presented in the literature can be implemented in the stationary reference frame on basis of the DSOGI-QSG as a building block, to achieve on-line frequency-adaptive operation. Following the approaches presented in the literature, there are two ways to organize Virtual Flux-based grid synchronization under unbalanced conditions.

3.2.1 Sequence Separation of Estimated Virtual Flux

The most obvious and common approach is to first estimate the Virtual Flux, and then apply a filtering technique, a PLL, or a sequence separation technique for tracking the corresponding PNS components, as reported in [105], [106], [183], [184]. If measures are not taken to obtain frequency-adaptive operation of the Virtual Flux estimation, the performance of such strategies will however degenerate during frequency variations, even if a fully frequency-adaptive method like the DDSRF-PLL from [45] is used to track the positive sequence of the estimated Virtual Flux. Frequency-adaptive operation must also be ensured in case of sequence separation methods implemented in the

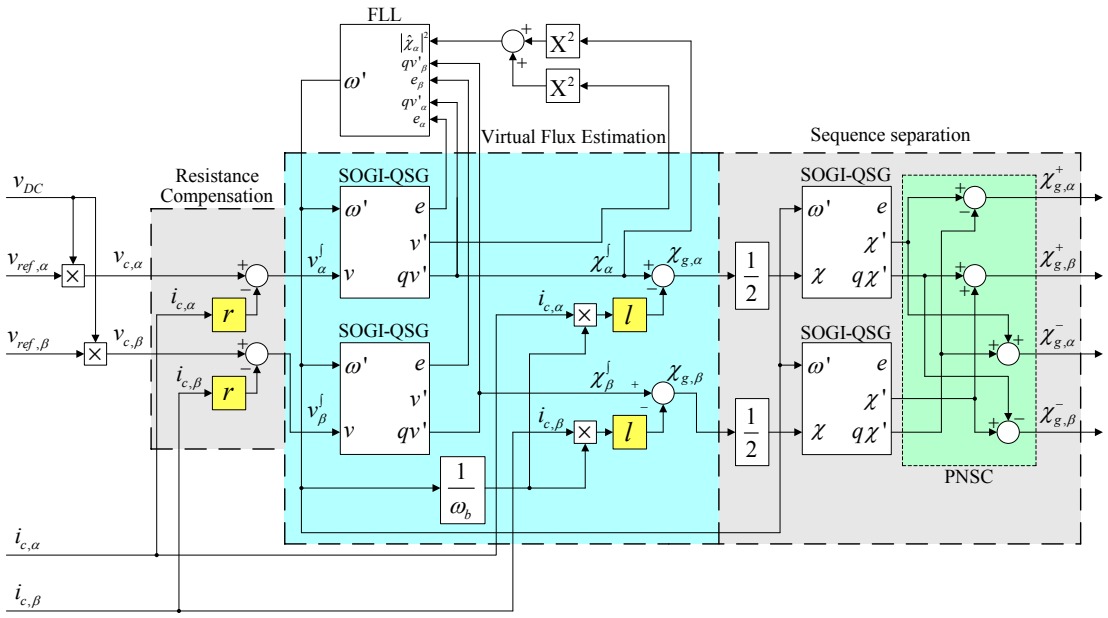

Fig. 3-4 Frequency adaptive Virtual Flux estimation cascaded with SOGI-QSG-based Sequence Separation of the estimated Virtual Flux

stationary reference frame, for the system to maintain its performance during grid frequency variations.

Following this approach, explicitly on-line frequency-adaptive voltage-sensor-less grid synchronization can be obtained in a simple way by utilizing the DSOGI-QSG for both Virtual Flux estimation and sequence separation in the stationary reference frame. The resulting structure is shown in Fig. 3-4, where it can be seen that the scaled Virtual Flux, $\chi_{g,\alpha\beta}$, at the point of connection to the grid is first estimated according to the definition and the descriptions from section 3.1.2. Then, the Virtual Flux sequence components are estimated in the stationary $\alpha\beta$-reference frame by using the output signals from two SOGI-QSGs (usually labeled as DSOGI-PLL or DSOGI-FLL depending on the source of the frequency information) according to [51], [52].The Positive and Negative Sequence Calculation (PNSC) marked in the figure is the SOGI-QSG-based implementation of (B.1) as explained in Appendix B.1, and this is exactly the same application of the SOGI-QSG as for the sequence separation of voltage measurements in [51], [52].

As demonstrated in [96], the implementation of sequence separation based on DSOGI-QSGs in the stationary frame is equivalent to detection of positive and negative sequence components in the synchronous reference frames by the DDSRF-PLL from [45]. The methods for PNS Virtual Flux estimation proposed in [106], [183], [184] can therefore be expected to have similar features and dynamic performance as the structure shown in Fig. 3-4, but with a less demanding practical implementation [96], [54]. The further analysis will therefore be limited to the implementation in the stationary reference frame according to Fig. 3-4.

In Fig. 3-4, a Frequency Locked Loop (FLL) with the structure and tuning proposed in [195], [196] is used to provide the grid frequency estimate to the SOGI-QSGs, but the source of the frequency information is of minor importance in this context.

Considering Fig. 3-4, it can be observed that the estimation of PNS Virtual Flux components is achieved by using 4 SOGI-QSG blocks. However, if the PNS components of the measured currents are needed in the control system of the converter, another 2 SOGI-QSG-blocks would be required. It can also be noticed that the filtering effect of the Virtual Flux estimation is cascaded with the filtering effect of the SOGI-QSGs used for the sequence separation, and that this will slow down the dynamic response of the PNS-VF estimation. The performance characteristics of this configuration for PNS Virtual Flux estimation will be further investigated and compared to other synchronization methods in a following section.

3.2.2 Sequence Separation of Converter Output Voltages Followed by Individual Estimation of PNS-VF Components

The other possible configuration for PNS-VF estimation is to first carry out sequence separation of the converter output voltage, before estimating the Virtual Flux signals. This approach has been partly followed by [185]-[188], where the positive sequence component of the converter voltage was found by notch-filtering and low-pass-filtering in the synchronous reference frame before the positive sequence Virtual Flux was estimated. The same approach was also followed by [107] that presented the first systematic proposal for PNS Virtual Flux estimation in the stationary reference frame. The implementation of the Virtual Flux estimation and the in-quadrature signal generation for sequence separation in [107] was based on to (2.11), but an explicitly frequency-adaptive implementation can easily be achieved by using the SOGI-QSG to replace the 2^{nd} order low-pass filters. The resulting structure is shown in Fig. 3-5, where a FLL with the structure and tuning from [195], [196] is providing the grid frequency estimate to the SOGI-QSGs.

Considering the block diagram of Fig. 3-5, it is seen that this structure is more complex than the structure from Fig. 3-4, and a total number of 8 SOGI-QSG-blocks are needed for the implementation. The same number of 2^{nd} order filters was also needed in the original implementation proposed in [107], since two sets of 2^{nd} order filters were needed for sequence separation of voltages and currents, while four 2^{nd} order filters were needed for estimating the individual PNS-VF components.

It can be noticed that the main difference between Fig. 3-5 and Fig. 3-4 is that the sequence separation and the Virtual Flux estimation are cascaded in the opposite order with respect to Fig. 3-4. The transfer functions from the converter voltage to the estimated PNS Virtual Flux sequence components will however be the same in both cases, and the dynamic response of the two different structures should therefore be the same.

For the PNS Virtual Flux estimation method proposed in [107] based on (2.11), only 90º phase shifted values are available at the outputs the filters. Therefore, the un-filtered input values were used for the PNSC network. This should result in higher bandwidth and faster transient response, but also reduced attenuation of high frequency harmonics. The bandwidth of the estimation methods shown in Fig. 3-4 and Fig. 3-5 can also be increased by using the un-filtered input values instead of the direct output signals from the SOGI-QSGs in the PNSC network, but the difference in transient response will not be significant. A further comparative analysis of different possible configurations for sequence separation and Virtual Flux estimation is however provided in Appendix B.

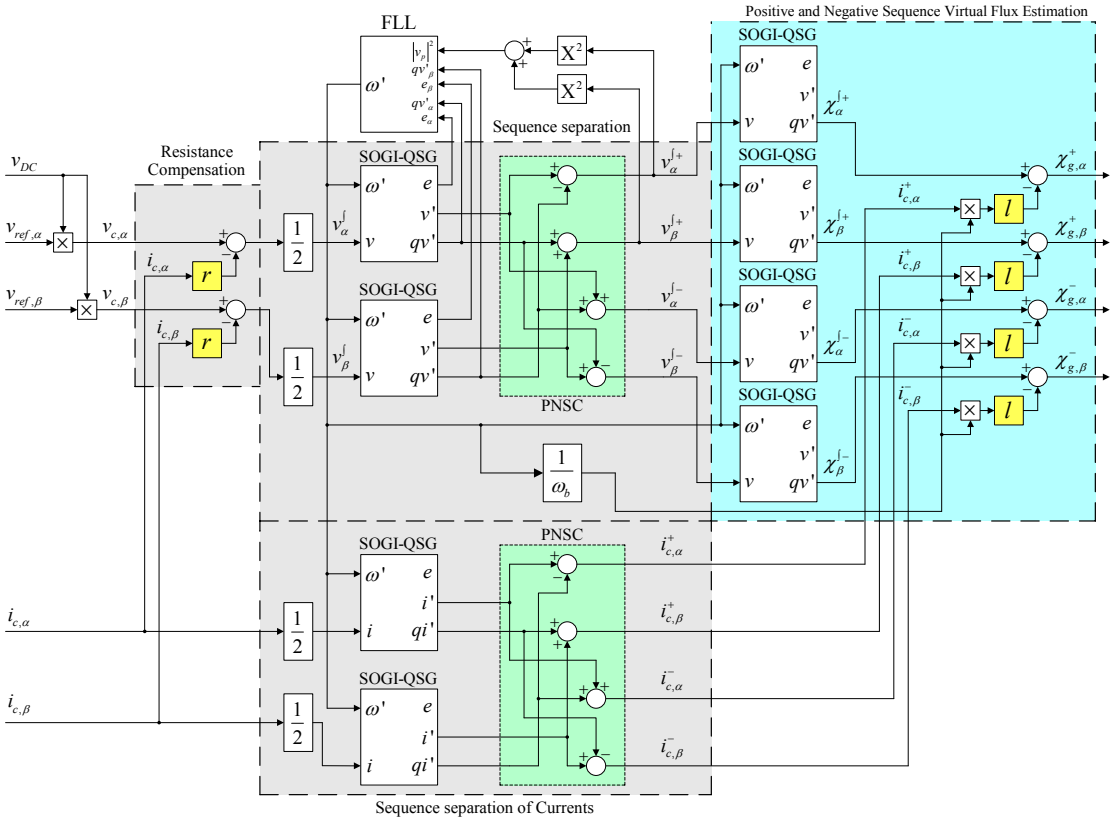

Fig. 3-5 Frequency-adaptive Sequence Separation of voltages cascaded with separate estimation of PNS-VF components

An interesting feature of the structure presented in Fig. 3-5, and the structure from [107] is however that they allow for using different inductance values in the estimation of the positive and negative sequence components of the Virtual Flux. This possibility for different characteristic could be a relevant issue for further investigations related multi-functional and flexible control systems for operation under unbalanced conditions.

3.3 Frequency-adaptive Virtual Flux Estimation with Inherent Sequence Separation

From the information presented in the previous sections, it should be clear that the SOGI-QSG has all the features needed for Virtual Flux estimation band-pass filtering and generation of in-quadrature signals needed for sequence separation in the stationary reference frame. It is therefore possible to merge all these functions together to achieve a structure for explicitly frequency-adaptive Virtual Flux estimation with inherent sequence separation in the stationary reference frame.

3.3.1 Proposed Approach for achieving Virtual Flux Estimation with Inherent Sequence Separation

Considering that the in-quadrature output signal, *qv'*, of the SOGI-QSG in Fig. 3-1 represents the Virtual Flux χ, a signal phase-shifted by 90º is needed for sequence

separation. This is already available from the same SOGI-QSG in the form of the band-pass-filtered output signal *v'*, that is leading the Virtual Flux signal by 90º. Considering that the band-pass-filtered signal is the derivative of the Virtual Flux, the positive and negative sequence components can be calculated according to the approach presented in [200]. However, changing the sign of the band-pass-filtered signal will make it correspond to a 90º phase-lag, and the same Positive and Negative Sequence Calculation (PNSC) network as presented in the figures above can be applied. Independent of how the output signals of a SOGI-QSG is considered, the main advantage is that sequence separation of the estimated Virtual Flux can be based directly on the outputs from the two SOGI-QSGs used for the Virtual Flux estimation. Therefore, the cascaded structures from Fig. 3-4 and Fig. 3-5 can be avoided.

3.3.1.1 Structure of the proposed method for Virtual Flux estimation

The proposed structure for PNS Virtual Flux estimation, based on simple considerations of the output signals from two SOGI-QSGs is shown in Fig. 3-6. Since the Virtual Flux integration with sequence separation is based on two single SOGI-QSGs, this structure has been labeled as Dual SOGI-based Virtual Flux (DSOGI-VF) estimation.

When PNS-VF components are estimated by the method shown in Fig. 3-6, the current induced fluxes have to be subtracted separately for all sequence components. Sequence separation of the current measurements is therefore necessary as shown in the figure. However, only 4 SOGI-QSGs are needed for the total implementation, and there are no cascaded filtering effects in the Virtual Flux estimation. Therefore, this model will have faster dynamic response than techniques based on conventional approaches for PNS Virtual Flux estimation, like the methods shown in Fig. 3-4 and Fig. 3-5.

Compared to the strategies for grid synchronization, it can be noted that DSOGI-based sequence separation of measured voltages requires two SOGI-QSGs in an almost identical configuration as described in [51], [52]. The dynamic response of the proposed estimation method should therefore be similar to that of DSOGI-based grid synchronization under unbalanced conditions. It can also be noted that frequency-adaptive implementation of conventional Virtual Flux estimation under balanced conditions, as illustrated by Fig. 3-3, will require two SOGI-QSGs, and should have similar dynamic response.

In Fig. 3-6, a FLL with the structure and tuning from [195], [196] is used to keep the PNS-VF estimation inherently frequency-adaptive, although any other technique for frequency estimation could be used. As for the structure shown in Fig. 3-5, different points of synchronization to the grid can be selected for the PNS-VF components.

3.3.1.2 Properties of the Proposed Estimation Method

The characteristics of the SOGI-QSG for Virtual Flux estimation has already been discussed in section 3.1.1, but the influence of the sequence separation must be included to study the performance of the DSOGI-VF estimation from Fig. 3-6. Thus, the transfer function from the voltage inputs to the sequence separated flux signals should be investigated.

In balanced conditions, the α- and β- voltage components have equal amplitude and the β-component is lagging the α-component by 90º in time. For the steady state frequency response, this phase displacement can be described by (3.9) [52].

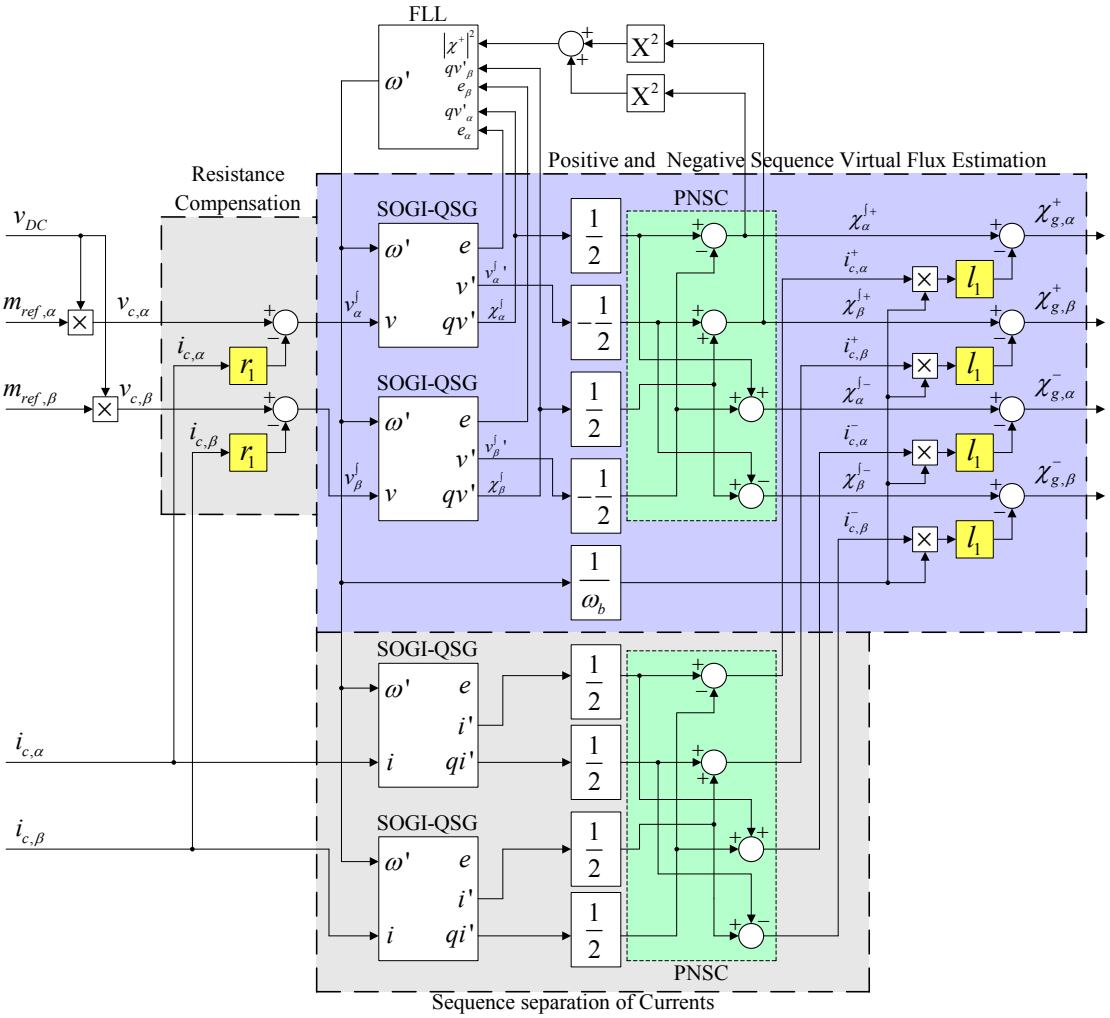

Fig. 3-6 Frequency Adaptive Dual SOGI-based Virtual Flux Estimation with Inherent Sequence Separation

$$v_\beta^{\int}(s) = -\frac{s}{\omega} v_\alpha^{\int}(s) \tag{3.9}$$

Considering the previous discussion of the SOGI-QSG and the block diagram of Fig. 3-6, the positive sequence flux component can be described by (3.10). Substituting the expression from (3.9) into this equation results in (3.11) that can be further expanded, by using equation (3.1), into the full expression given by (3.12).

$$\chi_\alpha^{\int+}(s) = \frac{1}{2}\left(\chi_\alpha^{\int}(s) - q \cdot \chi_\beta^{\int+}(s)\right) = \frac{1}{2}\left(\frac{\omega'}{s} v_\alpha^{\int}{}'(s) + v_\beta^{\int}{}'(s)\right) \tag{3.10}$$

$$\chi_\alpha^{\int+}(s) = \frac{1}{2}\left(\frac{\omega'}{s} v_\alpha^{\int}{}'(s) - \frac{s}{\omega} v_\alpha^{\int}{}'(s)\right) \tag{3.11}$$

$$\chi_\alpha^{\int+}(s) = \frac{1}{2}\left(\frac{k \cdot \omega'^2}{s^2 + k \cdot \omega' \cdot s + \omega'^2} - \frac{s}{\omega} \cdot \frac{k \cdot \omega' \cdot s}{s^2 + k \cdot \omega' \cdot s + \omega'^2}\right) v_\alpha^{\int}(s) \tag{3.12}$$

Analyzing the steady state frequency response results in (3.13).

$$\frac{\chi_\alpha^{\int+}(j\omega)}{v_\alpha^{\int}(j\omega)} = \frac{1}{2}\left(\frac{k\cdot\omega'\cdot(\omega'+\omega)}{\omega'^2-\omega^2+j\cdot k\cdot\omega'\cdot\omega}\right) \tag{3.13}$$

It can be easily be verified that (3.13) results in unity gain and −90º phase shift when the fundamental frequency ω is equal to the resonance frequency, ω' of the SOGI-QSGs. For negative sequence fundamental frequency components, corresponding to ω being negative but with the same numeric value as ω', (3.13) results in zero amplitude. This will effectively eliminate the influence of negative sequence components on the estimated positive sequence Virtual Flux.

The derivation above can also be generalized and expressed on matrix form, resulting in (3.14) describing the DSOGI-VF estimation in the Laplace domain. It can be noticed that this expression has the same form as derived in [96] to describe both DSOGI-based sequence separation and the DDSRF-PLL expressed in the stationary reference frame, with the only difference that the diagonal and cross-diagonal terms have changed place. This corresponds to a phase shift of 90°, coinciding with the expected characteristics of Virtual Flux estimation

$$\begin{bmatrix}\chi_\alpha^{\int+}(s)\\ \chi_\beta^{\int+}(s)\end{bmatrix} = \frac{1}{2}\cdot\frac{k\cdot\omega'}{s^2+k\cdot\omega'\cdot s+\omega'^2}\cdot\begin{bmatrix}\omega' & s\\ -s & \omega'\end{bmatrix}\cdot\begin{bmatrix}v_\alpha^{\int}(s)\\ v_\beta^{\int}(s)\end{bmatrix}$$
$$\begin{bmatrix}\chi_\alpha^{\int-}(s)\\ \chi_\beta^{\int-}(s)\end{bmatrix} = \frac{1}{2}\cdot\frac{k\cdot\omega'}{s^2+k\cdot\omega'\cdot s+\omega'^2}\cdot\begin{bmatrix}\omega' & -s\\ s & \omega'\end{bmatrix}\cdot\begin{bmatrix}v_\alpha^{\int}(s)\\ v_\beta^{\int}(s)\end{bmatrix} \tag{3.14}$$

When investigating the steady-state frequency characteristics, and by using (3.9), equation (3.14) is reduced to (3.15). The resulting frequency characteristics for estimation of PNS Virtual Flux components are shown in Fig. 3-7 a) and b) respectively for a case when the resonance frequency ω' of the SOGI-QSGs corresponds to the fundamental grid frequency ω_0 of a 50 Hz system.

$$\begin{bmatrix}\chi_\alpha^{\int+}(j\omega)\\ \chi_\beta^{\int+}(j\omega)\end{bmatrix} = \frac{1}{2}\left(\frac{k\cdot\omega'\cdot(\omega'+\omega)}{\omega'^2-\omega^2+j\cdot k\cdot\omega'\cdot\omega}\right)\cdot\begin{bmatrix}v_\alpha^{\int}(j\omega)\\ v_\beta^{\int}(j\omega)\end{bmatrix}$$
$$\begin{bmatrix}\chi_\alpha^{\int-}(j\omega)\\ \chi_\beta^{\int-}(j\omega)\end{bmatrix} = \frac{1}{2}\left(\frac{k\cdot\omega'\cdot(\omega'-\omega)}{\omega'^2-\omega^2+j\cdot k\cdot\omega'\cdot\omega}\right)\cdot\begin{bmatrix}v_\alpha^{\int}(j\omega)\\ v_\beta^{\int}(j\omega)\end{bmatrix} \tag{3.15}$$

From Fig. 3-7 it can clearly be seen that any negative sequence components in the input voltage signals are eliminated in the estimated positive sequence Virtual Flux, while positive sequence voltage components are eliminated in the estimated negative sequence Virtual Flux. It can also be noted that the phase shift is −90° for estimated fundamental frequency positive sequence Virtual Flux components, while it is +90° for estimated fundamental frequency negative sequence Virtual Flux components. This is in line with the definition of the Virtual Flux as the integral of the voltage, since positive sequence components can be described by a clockwise rotating vector, while negative sequence components can be described by a vector rotating in the counterclockwise direction. The estimation Virtual Flux components should therefore always lag the voltage by 90° in the direction of rotation, as verified by the frequency responses at the fundamental grid frequency in Fig. 3-7.

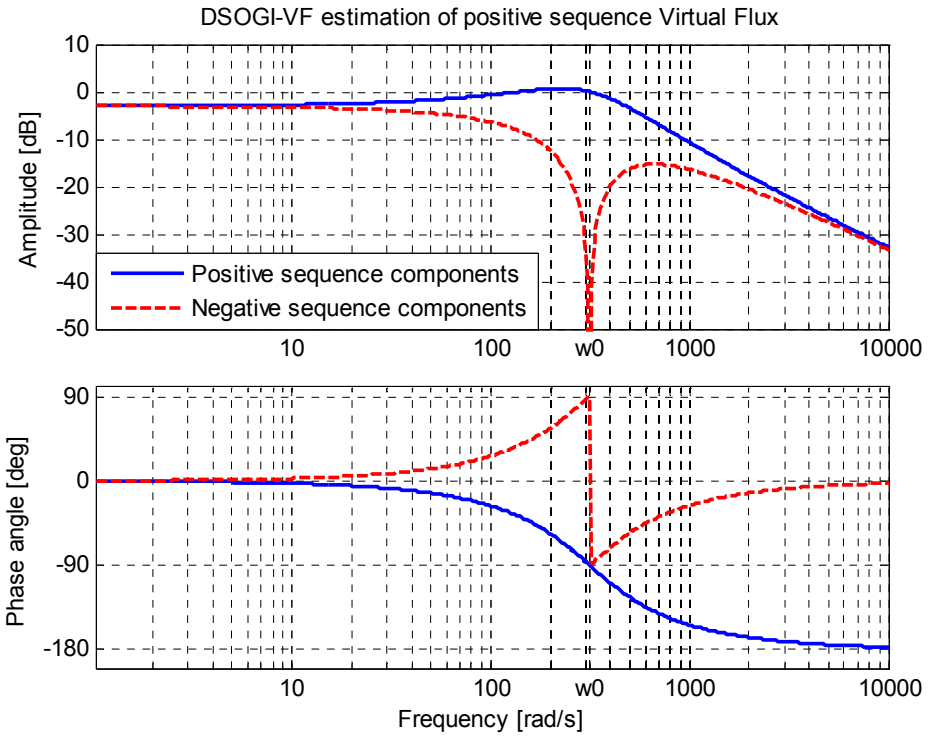

a)

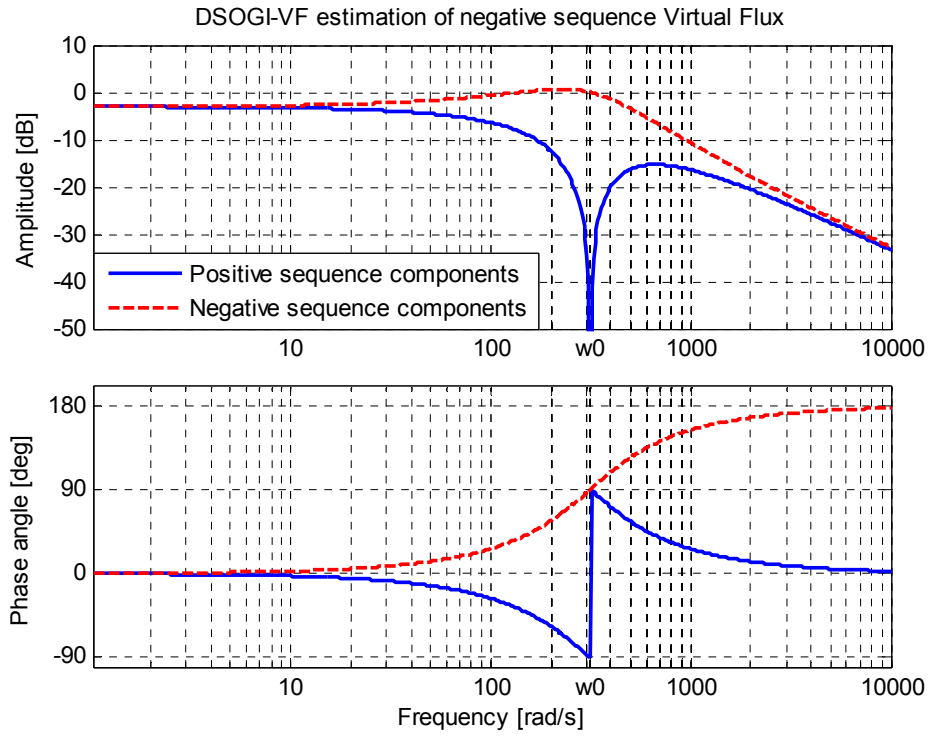

b)

Fig. 3-7 Frequency response of DSOGI-VF Estimation; a) positive sequence Virtual Flux components, and b) negative sequence Virtual Flux components

Considering the characteristics of (3.15) plotted in Fig. 3-7, it is clear that both Virtual Flux estimation and sequence separation will be achieved with the proposed DSOGI-VF estimation method under steady state operation, as long as the estimated frequency ω' is equal to the fundamental frequency of the grid. Correct steady state operation will also be the achieved with the estimation strategies shown in Fig. 3-4 and Fig. 3-5, but with a slower transient response as will be demonstrated in the following section.

3.3.2 Simulation Studies of DSOGI-VF estimation

The operation of the DSOGI-VF estimation has been investigated by simulating a converter operating in the simple grid configuration from Fig. 2-1. The converter is simulated by an average model neglecting the semiconductor switching, with the main parameters and characteristics summarized in Table 3-1.

For these particular simulations, the converter is controlled by a DC-link voltage controller and balanced three-phase currents are achieved by using Dual Frame PI-current controllers according to [89]. Sequence separation of currents needed for the current controllers is implemented by using un-filtered values together with the in-quadrature signals, to increase the bandwidth, as analyzed in Appendix B. The sequence separation of the currents, needed for the flux-calculations of the DSOGI-VF estimation, is however implemented according to Fig. 3-6. The DSOGI-VF estimation is in this cased designed to synchronize the converter control system to the high voltage side of the transformer. This is achieved by specifying the resistance and inductance used for the Virtual Flux estimation to be given by the series connection of the

Table 3-1 Parameters for simulation study

Converter modelling	Sinusoidal average model with maximum output voltages limited by DC-link voltage
Simulation tool	PSCAD/EMTDC
Power rating	S_N = 2.26 MVA
Rated line voltage	$V_{N,LL}$ = 690 V_{RMS}
Grid frequency	f_N = 50 Hz (tested also for 60 Hz)
Filter inductor	l_1 =0.05 pu
Transformer leakage inductance	l_T =0.07 pu
Total inductance used for Virtual Flux estimation	l_{tot} = 0.12 pu
Total resistance used for Virtual Flux estimation	r_{tot} = 0.006 pu
Pre-fault voltage	v^+ = 1.0 pu, v^- = 0.01 pu
Voltage during grid fault	v^+ = 0.733 pu, v^- = 0.210 pu
Power flow	$\bar{p}$ = 0.5 pu injected to the DC-link
Frequency tracking	Frequency Locked Loop (FLL)
Control principle	Balanced sinusoidal currents
Point of synchronization	Grid side of the transformer

parameters for the filter inductor and the series equivalent leakage inductance and conduction losses of the transformer. Thus, the estimated Virtual Flux values $\chi_{g,}{}^{+-}{}_{\alpha\beta}$ in Fig. 3-6 will be corresponding to the voltage V_g in Fig. 2-1.

3.3.2.1 Transient response of the DSOGI-VF Estimation in case of an unbalanced grid voltage sag

The transient response of the DSOGI-VF estimation method to grid voltage unbalance has been investigated by imposing an unbalanced voltage dip in the grid at the high voltage side of the transformer in the simulation model. When the fault occurs, the positive sequence voltage is stepped down to 0.733 pu and the phase angle is shifted by 5º. At the same time the negative sequence component of the voltage is set to 0.210 pu while the phase angle is shifted by 50.4º. This is the same fault sequence as used to investigate grid synchronization based on voltage measurements in [51] where the DSOGI-PLL was first proposed, and corresponds to a common fault in a distribution grid.

The main simulation results are shown in Fig. 3-8, where the fault is applied at t = 0.04 s, while the system is operating under steady state conditions. From Fig. 3-8 (a), it can be seen how the voltage references for generation of PWM signals become unbalanced, as the converter is injecting balanced currents during the unbalanced conditions. From these unbalanced voltage references and the measured currents, positive and negative sequence Virtual Flux signals are estimated by the proposed strategy as shown in Fig. 3-8 (b) and (c), respectively. In Fig. 3-8 (d), the amplitudes of the positive and negative sequence Virtual Flux components are calculated and compared to the amplitudes of the grid voltage imposed to the system. It can be seen that the Virtual Flux estimation is relatively fast and accurate, with about 5 ms rise time, very little overshoot and a settling time around 20 ms. This is corresponding well with the approximations for the SOGI-QSG presented in section 3.1.1.2. It can also be noted that the transient response is the same as for DSOGI-based grid synchronization by using voltage measurements, and also similar to the response time of other methods for sequence separation based on voltage measurements [51]-[53].

The phase angles $\theta_{\chi}{}^{+}$ and $\theta_{\chi}{}^{-}$, calculated directly from the PNS-VF components, are shown in Fig. 3-8 (e) and (f) respectively, phase shifted by ±90º for comparison to the phase angles $\theta_{v}{}^{+}$ and $\theta_{v}-$ of the voltage components. The phase angles of the PNS voltage components are obtained by DSOGI-based sequence separation of voltages measured at the point of synchronization, according to [51], [52]. The curves show that the values obtained from the Virtual Flux estimation are closely corresponding to the values obtained from the voltage measurements. This verifies that the proposed DSOGI-VF estimation method can achieve the same transient response as conventional grid synchronization based on measured voltages.

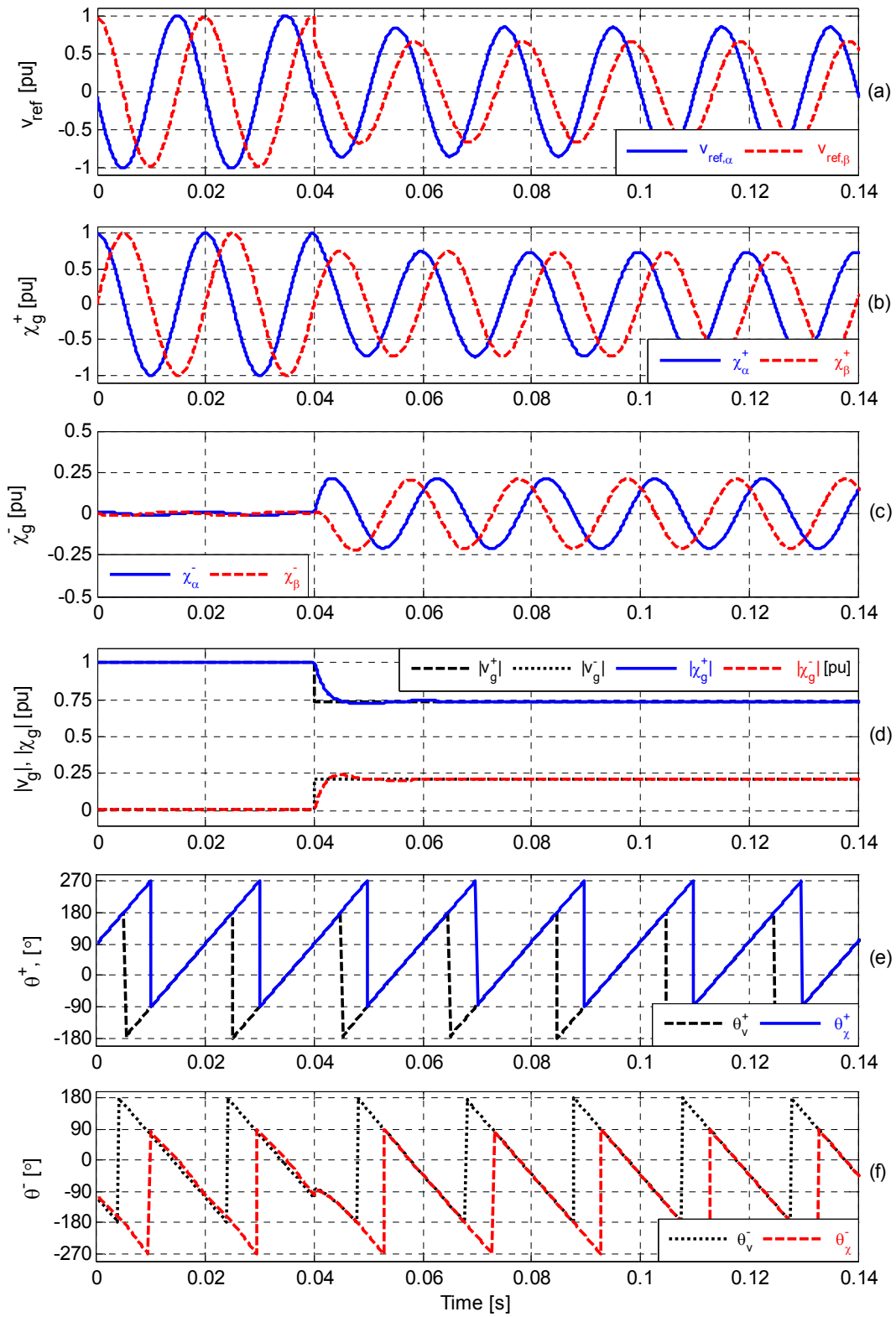

Fig. 3-8 Simulation results showing the operation of the DSOGI-VF estimation in case of an unbalanced sag in the grid voltage

3.3.2.2 Transient response of the DSOGI-VF Estimation in case of large variations in the grid frequency

To demonstrate the frequency-adaptive operation of the DSOGI-VF estimation, an extreme case of a step in grid frequency from 50Hz to 60Hz has been simulated. The step in the grid frequency was imposed during unbalanced conditions characterized by the voltage dip described for the simulations presented in the previous subsection. Although not a realistic case, the large step in grid frequency is a challenging test to the grid synchronization strategy, and is therefore used to demonstrate how the DSOGI-VF is capable responding to frequency changes in the grid while maintaining its performance.

The change in frequency is imposed after the system has reached steady state in the unbalanced conditions, and the main results are shown in Fig. 3-9, where the time-axis is shifted so the frequency step occurs at t = 0.04s.

Since the change of frequency is not introducing any change of voltage amplitude or power flow, the influence on the frequency change is barely noticeable in the plots of the $\alpha\beta$-components. However, in can be noticed that there is a disturbance in the amplitude of the estimated positive and negative sequence components. The estimated phase angles are also influenced, and the relative influence of the frequency step is larger for the negative sequence Virtual Flux since the amplitudes is smaller.

The grid frequency estimated from the Virtual Flux model is shown in the last plot of Fig. 3-9, and here it can be seen that the Frequency Locked Loop used in these simulations is tracking the frequency within a time-period in the range of 100ms. When the frequency is correctly tracked by the FLL, so that the SOGI-QSGs are provided with the correct value of the grid frequency, the system reaches a new steady state condition where the disturbances in the estimation are eliminated. This verifies how the proposed system is inherently frequency adaptive. For realistic frequency variations in the grid, the response time of the frequency tracking is expected to have negligible influence on the performance.

3.3.2.3 Main observations from simulation of DSOGI-VF estimation

From the presented simulation results, is should be clear that the DSOGI-VF estimation is performing as expected. The estimated frequency-scaled Virtual Flux sequence components have the same amplitude as the corresponding voltage components, and the phase angles estimated from the Virtual Flux signals are corresponding to the phase angle of the voltage components, just 90° phase delayed in the direction of rotation. The transient response is also as expected from the simplified considerations in section 3.1.1.2.

The results also verify that the grid frequency can be estimated from the Virtual Flux signals, in this case by a FLL, and how the estimated frequency can be used to keep the DSOGI-VF estimation frequency adaptive.

A brief experimental investigation of the DSOGI-VF estimation is however provided in the following section, to verify the operability of the concept and to evaluate the validity of the presented simulation results.

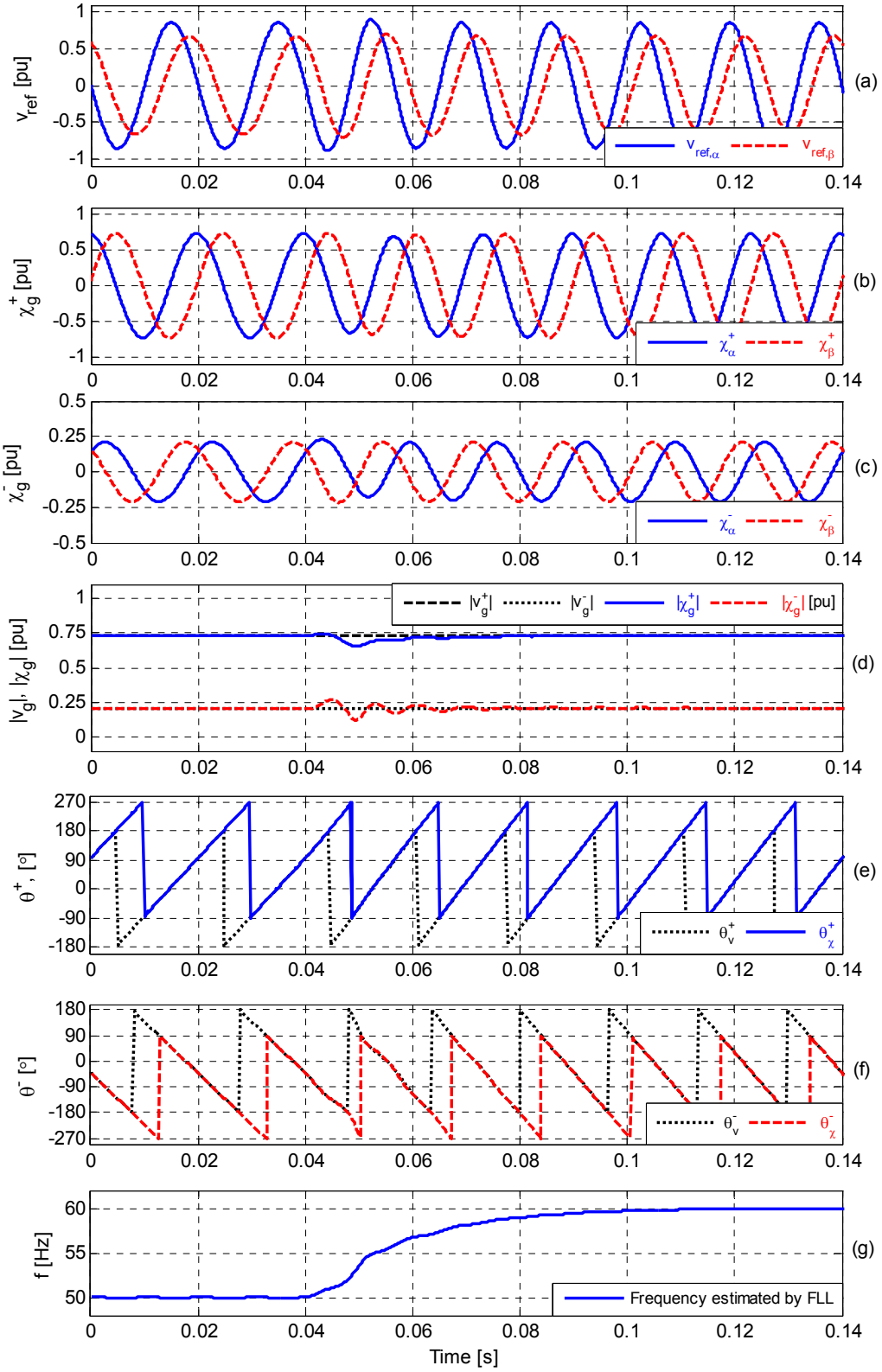

Fig. 3-9 Simulation results showing the response of the proposed Virtual Flux estimation when a large step in grid frequency occurs

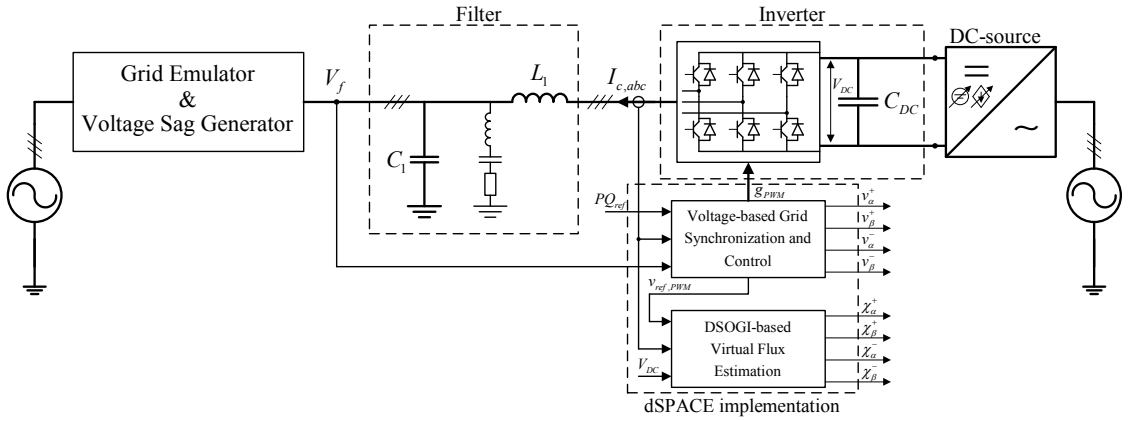

Fig. 3-10 Overview of laboratory setup for verification of DSOGI-VF estimation

3.3.3 Experimental Verification of the DSOGI-VF Estimation Method

The experimental setup for verification of the DSOGI-VF estimation method consisted of a grid connected 5 kVA power converter module with an LC-filter on the AC-side. Power to the DC-capacitor of the converter was provided by a controllable DC-source. The AC grid voltage was controlled by a grid emulator based on adjustable transformers and contactors that could be configured to generate balanced or unbalanced voltage sags. For this study, the grid emulator was operated with a pre-fault line-to-line voltage of 110 VRMS.

The DSOGI-VF estimation was implemented on a dSPACE DS1103 platform together with the control algorithms needed to operate the converter. In this case, the sampling interval was set to 100 μs, and the control system was generating duty-cycles for PWM operation of the converter with 10 kHz switching frequency. The duty-cycle signals were transmitted from the dSPACE platform to the converter module by fiber-optic connections. The layout of the laboratory setup and the implemented control system is shown in Fig. 3-10, with the main parameters listed in Table 3-2.

3.3.3.1 Control system and fault sequence

In these experiments, the converter was operated with grid synchronization based on the DSOGI-FLL operating on voltage measurements as described in [52], and the

Table 3-2 Details of Laboratory Setup

Converter module	5.5 kVA, 400 V VLT5005 Danfoss converter
Switching frequency	f_{sw} = 10 kHz
Filter inductor	L_1 = 2.46 mH (Losses corresponding to $R_1 \approx 4\Omega$)
Filter capacitor	C_1 = 5 μF (Y-connected)
Trap filter	RLC-circuit tuned for 10 kHz (Y-connected)
Grid voltage (pre-fault)	V_{LL} = 110 V_{RMS} (V_b = 89.8 V for per unit phase voltages)
DC-link voltage	V_{DC} = 350 V ($v_{DC} \approx$ 1.9 pu)
Grid connection	Transformer-based voltage sag generator
Control system	Operated on the dSPACE DS1103 platform
Sampling frequency	f_{samp} = 10 kHz

converter was controlled according to the strategies described in [109]. For the presented results, the setup was configured to inject a constant average power of 350 W to the grid by balanced three-phase currents. To impose an unbalanced disturbance to the system, the voltage-sag generator was controlled to generate a voltage drop of about 50% in two of the phases, while the converter was operating in steady-state conditions.

The DSOGI-VF estimation was implemented in parallel to the voltage-based synchronization strategy, and was not used in the closed loop control of the converter as indicated in Fig. 3-10. This parallel operation of the two synchronization strategies allowed for direct comparison of signals obtained from measurements and from the Virtual Flux estimation.

3.3.3.2 Experimental results

A set of results comparing signals obtained from the voltage measurements and from the Virtual Flux estimation is shown in Fig. 3-11 for the case when the unbalanced voltage-sag occurs. Fig. 3-11 (a) shows the measured three-phase voltages while Fig. 3-11 (b) and (c) show the positive and negative sequence components of the measured voltage as detected by the DSOGI-based method from [52]. Fig. 3-11 (d) and (e) show the positive and negative sequence components of the estimated Virtual Flux. The 90° phase shift between voltage and flux signals can be easily identified by studying the curves.

The phase angles of the positive and negative sequence components of voltage and Virtual Flux signals are calculated by post-processing of the data logged by the dSPACE interface to the converter. The resulting angles are plotted in Fig. 3-11 (f) and (g), where the phase angles of the Virtual Flux components are shifted by +90° and −90° for positive and negative sequence components, respectively, in order to simplify the comparison.

The results show that the phase angle of the positive sequence grid voltage component is well estimated by the DSOGI-VF estimation, both under balanced and unbalanced conditions. In the normal operating condition before and after the fault, the negative sequence components of the grid voltage and the corresponding Virtual Flux signals are fluctuating around zero, and the phase angles of these signals are therefore not containing relevant information. When the fault occurs, it is however seen that the phase angle calculated from the negative sequence Virtual Flux component is quickly tracking the negative sequence phase angle found from the voltage measurements.

In Fig. 3-12, the amplitudes of the positive and negative sequence components of the measured voltage and the estimated Virtual Flux are compared for a time period of 0.5 s including the unbalanced dip in the grid voltage. These signals are also found by post-processing voltage and Virtual Flux signals logged by the dSPACE interface to the converter. It can be seen from this figure that the amplitudes are matching reasonably well, and that there is no additional delay in the estimation of the PNS-VF components compared to the sequence separation of the measured voltages. There is however a slight deviation in the amplitudes that is originating from parameter mismatch in the Virtual Flux estimation, since nominal values for inductance and resistance of the filter inductor are used without further measurements or identification routines. The sensitivity to parameter variations is however the same as for other methods for Virtual Flux estimation as commented in section 2.2.6.

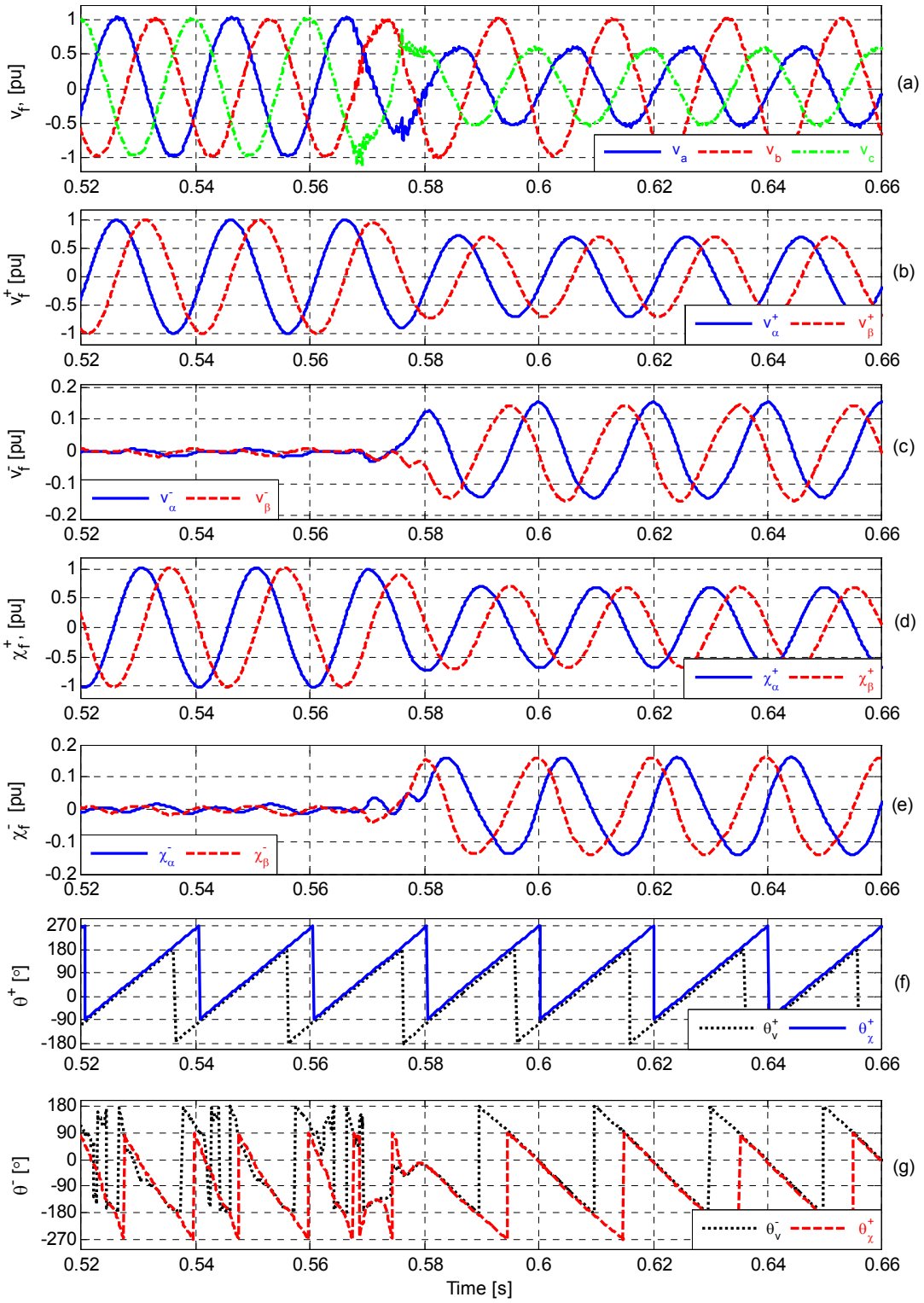

Fig. 3-11 Laboratory results showing measured three-phase voltages, PNS components of measured voltage and PNS components of the estimated Virtual Flux, with corresponding phase angles

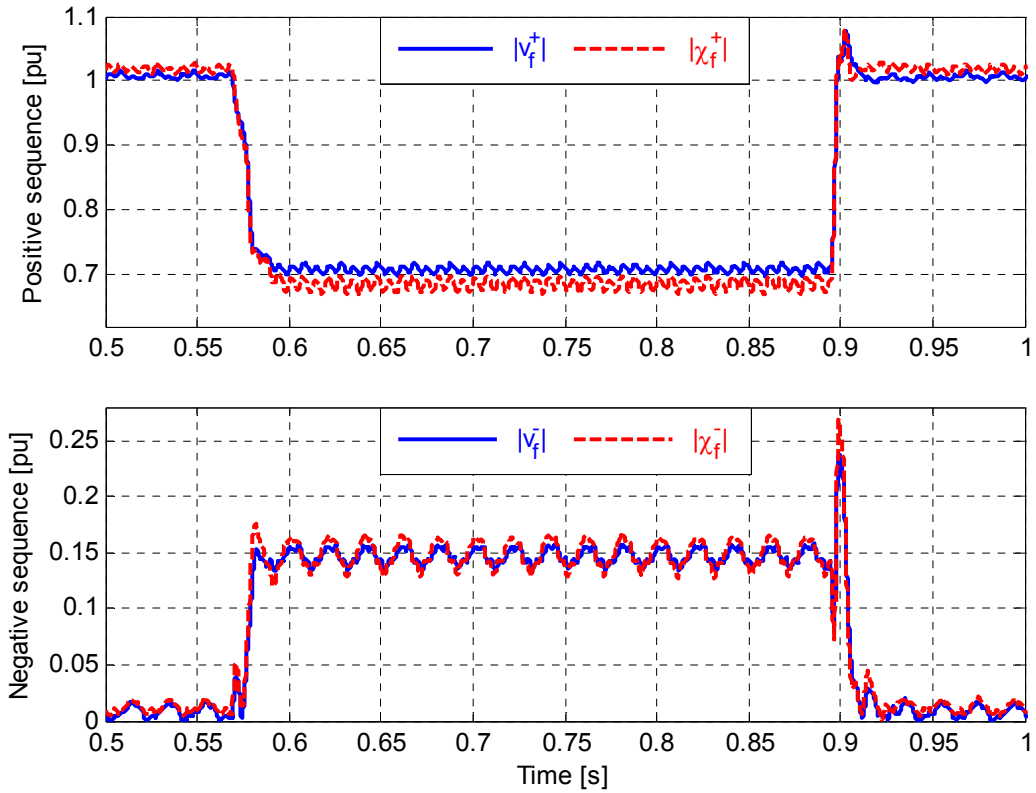

Fig. 3-12 Laboratory results showing amplitudes calculated from the PNS components of voltage and estimated Virtual Flux before, during and after the voltage sag

Fig. 3-12 also shows that there is more ripple in the amplitudes of the estimated Virtual Flux components than in the amplitude of the PNS components of the voltage. This additional ripple is mainly appearing due to the parameter deviations and because compensation for converter dead-time and for the threshold voltage of the IGBTs, as described in section 2.2.2.1, was not included in the laboratory implementation.

The overall result from the experimental test is however that the DSOGI-VF estimation is operating as expected. The steady-state and transient response is corresponding well to the results from the simulations and the analytical approximations in the previous subsections. Further analysis of the DSOGI-VF estimation method in comparison to other methods for grid synchronization will therefore be based on theoretical considerations and simulation studies.

3.4 Evaluation and Comparison of Methods for Virtual Flux Estimation under Unbalanced Conditions

In this section, the DSOGI-VF estimation method will further compared to the more conventional configurations for Virtual Flux estimation under unbalanced described in section 3.2. The comparison will mainly be based on the estimation method described in section 3.1.1.1, to easily achieve a fair comparison of different configurations without influence from the tuning and implementation of the different strategies as they have been proposed in the literature. This approach is justifiable since the structures

described in section 3.2 can be considered as explicitly frequency-adaptive stationary reference frame implementations of the two main approaches for Virtual Flux estimation presented in [105], [106], [183]-[188]. Simulation results and characteristics of the method proposed in [107] will however be included as another point of reference, since this was the first approach explicitly proposed for systematic estimation of PNS Virtual Flux components in the stationary reference frame, based on a particular implementation with clearly defined parameters.

3.4.1 Comparison of Transient Response based on Simulation

To compare the transient response of the different methods for PNS Virtual Flux estimation, they have all been simulated by the PSCAD/EMTDC software in the simple grid configuration shown in Fig. 2-1, with the same parameters and conditions as listed in Table 3-1 and described in section 3.3.2. To limit the amount of results, only the amplitudes of the PNS Virtual Flux components, found by vector summation of the $\alpha\beta$-quantities will be compared. The PNS grid voltage components, $|v_g^+|$ and $|v_g^-|$, imposed in the simulation model will be used as a reference to evaluate the transient response of the estimated Virtual Flux.

The simulations are, as expected, resulting in identical transient response for the structures from Fig. 3-4 and Fig. 3-5. Therefore, only results from the structure in Fig. 3-4 with DSOGI-based sequence separation of estimated Virtual Flux signals will be shown in the figures, labeled as $|\chi^+|_{VF\text{-}PNS}$. Simulation results obtained with the structure proposed in [107] and shown in Fig. 2-7 will also be shown in the figures, labeled as $|\psi^+|_{PNS\text{-}VF,LP2}$, to represent a configuration with sequence separation of voltage followed by individual estimation of PNS Virtual Flux components. It can be noted that the simulations showed identical transient response in the positive and negative sequence amplitudes resulting from DSOGI-VF estimation, labeled as $|\chi^+|_{DSOGI\text{-}VF}$ in the figurer as for DSOGI-based sequence separation of measured voltages. Thus, results from DSOGI-based synchronization to measured voltage are not included in the figures.

3.4.1.1 Comparison of transient response to unbalanced voltage sags for different PNS Virtual Flux Estimation methods

The resulting amplitudes of the PNS-VF components compared to the amplitude of the PNS voltages imposed to the simulation model are shown in Fig. 3-13 for the case when the voltage sag listed in Table 3-1 occurs. The figure shows that the PNS components of the Virtual Flux estimated by the structure from Fig. 3-4, plotted by blue lines in Fig. 3-13 have a significant overshoot and a settling time in the range of 30-40 ms. The method proposed in [107], plotted by green dashed lines, shows a slightly more damped response, due to the higher damping factor of the second order low-pass-filter from (2.11), and the speed of response is slightly increased by using un-filtered input signals together with the phase-shifted signals when carrying out the sequence separation. However, the speed of response for the estimation methods in Fig. 3-4 and Fig. 3-5 can also be improved in a similar way by using un-filtered signals instead of the band-pass filtered signals in the sequence separation, and the damping can be increased by increasing the gain parameter k in Fig. 3-1. However, the overshoot and relatively long settling time of these methods is mainly a consequence of the conventional approach of cascading 2nd order filters used for both sequence separation and Virtual Flux estimation.

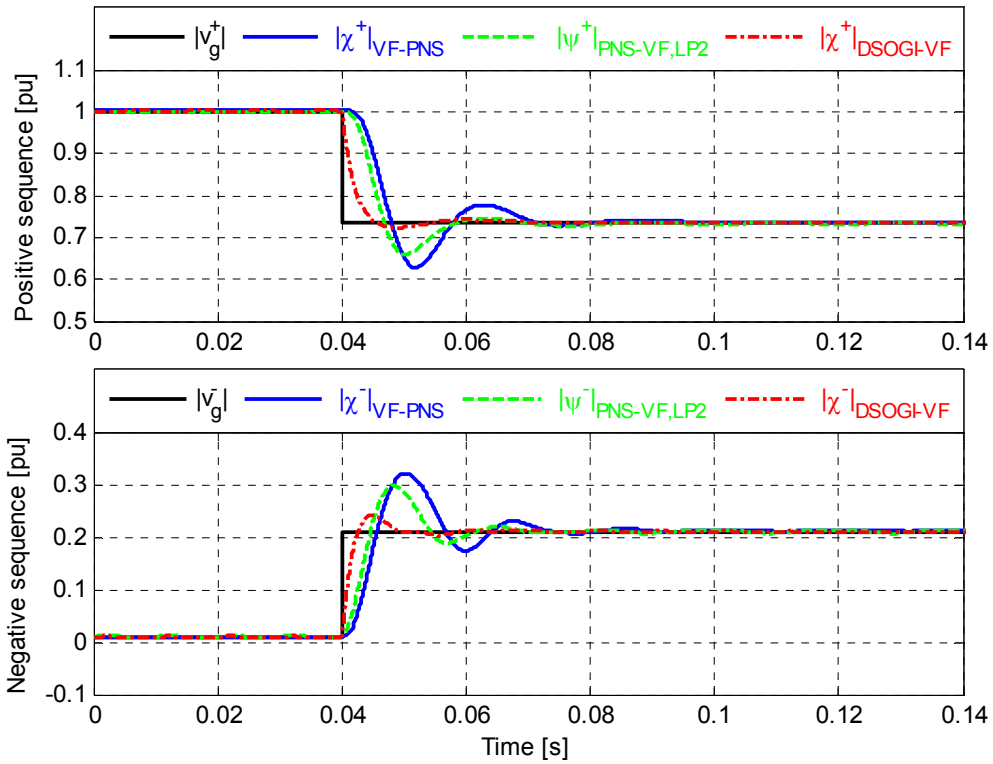

Fig. 3-13 Transient response of PNS Virtual Flux amplitudes for different estimation methods when exposed to an unbalanced drop in grid voltage

A faster and more damped response of both the positive and negative sequence amplitudes is clearly achieved with the proposed DSOGI-VF estimation method from Fig. 3-6 as plotted by red dashed lines in Fig. 3-13. The observed rise time of about 5 ms, and the settling time around 20 ms, is in accordance with the characteristics of the SOGI-QSG as discussed in section 3.1.1.2. This is because the DSOGI-VF estimation method effectively reduces the positive and negative sequence Virtual Flux estimation to a second order system, as long as the grid frequency is constant.

As mentioned, the DSOGI-VF estimation shows exactly the same amplitude response as DSOGI-based sequence separation of measured voltages according to [52], as long as the parameters for the flux estimation are accurately identified and the input signals are purely sinusoidal. This is the case for both voltage-based and voltage-sensor-less operation of the DSOGI-VF estimation, since the sequence separation of the measured currents has the same dynamic response as the DSOGI-VF estimation, and since the subtraction of the current induced fluxes corresponds to an arithmetic operation without introducing additional dynamics.

3.4.1.2 Comparison of transient response in case of grid frequency variations for different Virtual Flux estimation methods

Fig. 3-14 shows the results when the estimation methods compared in Fig. 3-13 are exposed to a step in the grid frequency from 50 to 60 Hz during the unbalanced conditions. Although an unrealistic frequency change for real grid conditions, this case gives useful illustration of the properties of the different estimation methods.

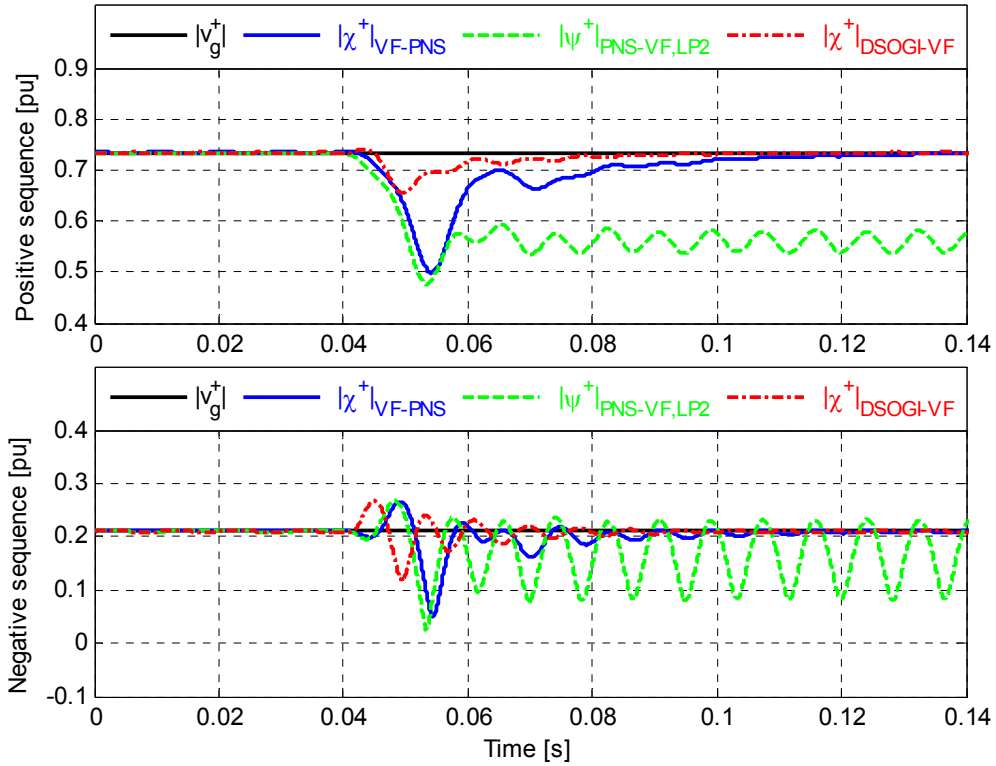

Fig. 3-14 Amplitudes of estimated PNS-VF components for different VF estimation methods when exposed to a step in the grid frequency

From the curves in Fig. 3-14, it can be clearly seen how the filter-based method for sequence separation and Virtual Flux estimation based directly on (2.11) is unable to estimate the correct amplitude when the grid frequency is different from the nominal frequency. This is because the filter will result in a gain unequal to unity and a phase shift unequal to −90° for signals with angular frequencies unequal to the nominal value ω_b used in the design of the filter. As mentioned in [107], it is also possible to make the implementation of this estimation structure frequency-adaptive either by introducing a correction factor based on the deviation from the nominal grid frequency, or by updating the parameters of the digital implementation according to the variations in the grid frequency. This will however be more complicated than for the SOGI-QSG that is based on a structure specifically designed to be frequency-adaptive.

Since all the methods for Virtual Flux estimation and sequence separation based on SOGI-QSGs will be explicitly frequency-adaptive, the estimation method from Fig. 3-4 is reaching a new steady state after a transient period of about 120 ms. The settling time is however mainly influence by the dynamics of the grid frequency tracking and its interaction with the VF estimation.

The DSOGI-VF estimation from Fig. 3-6 shows a faster response and a significantly lower maximum deviation from the real grid voltage amplitude compared to what can be obtained with the methods from Fig. 3-4 and Fig. 3-5. This improvement in the dynamical response is mainly because cascaded operation of sequence separation and Virtual Flux estimation is avoided, since the reduced settling time of the DSOGI-VF estimation makes the FLL operate on signals that are reaching steady-state faster than for the cases with cascaded structures.

3.4.2 Comparative Summary of Characteristics and Implementation Complexity of Different Methods for Grid Synchronization

Information characterizing different strategies for Virtual Flux-based voltage-sensor-less grid synchronization is collected in Table 3-3 as a basis for discussion and comparison. Corresponding information about grid synchronization by DSOGI-based sequence separation of measured voltages, based on [52], is included in the table as a point of reference.

The first column of the table is concerning the possibility for frequency-adaptive operation. As already mentioned, this is not automatically achieved with traditional filter-based methods for sequence separation and Virtual Flux estimation, but will be an inherent feature if SOGI-QSGs are used for implementation of the synchronization method.

The next column of the table is summarizing how the different synchronization methods behave during unbalanced conditions. As implied by the previous descriptions, conventional methods for Virtual Flux estimation based on the structure from Fig. 2-2 or Fig. 3-3 will not be able to maintain the intended performance during unbalanced conditions without including additional functionality for sequence separations. This issue is addressed in different ways by the methods discussed in section 3.2, while the DSOGI-VF estimation is designed to achieve PNS Virtual Flux estimation without the need of cascading functionality for sequence separation and Virtual Flux estimation. Table 3-3 is therefore summarizing the order of signal processing in cascade and the asymptotic frequency response for the different synchronization methods, based on the discussions in section 3.1, 3.2 and 3.3, and on the additional analysis presented in Appendix B.

Considering the transient response of the different synchronization methods, it is confirmed that the DSOGI-VF estimation achieves the same rise time and settling time as the voltage-based synchronization method from [52] and as conventional Virtual Flux estimation implemented by SOGI-QSGs. This is because the DSOGI-VF estimation is configured to achieve sequence separation and Virtual Flux estimation in one single operation and therefore exhibits predominantly 2^{nd} order dynamics. The PNS-VF estimation methods based on cascaded operation of Virtual Flux estimation and sequence separation exhibits 4^{th} order dynamics due to the series connection of two 2^{nd} order structures, and the transient response will therefore be slower and more oscillatory as already demonstrated by the presented simulation results. The transient response of such cascaded methods will however depend on the implementation and tuning, and therefore only values for implementations based on SOGI-QSGs with the tuning discussed in section are given in Table 3-3.

The last columns of Table 3-3 are giving details regarding the complexity of implementation for the different synchronization methods, based on the diagrams shown in Fig. 3-1, Fig. 3-3 Fig. 3-4, Fig. 3-5 and Fig. 3-6. The state variables and the mathematical operations related to tracking of the grid frequency are not included in the table since they can be the same for all the different methods.

Table 3-3 Summary of Performance Characteristics and Implementation Complexity for Different Synchronization Methods

Synchronization method	General characteristics				Transient response with SOGI-QSGs		Implementation details based on block diagrams from [52], Fig. 3-1, Fig. 3-3, Fig. 3-4, Fig. 3-5 and Fig. 3-6				
	Frequency-adaptive operation	Operation under unbalanced conditions	Order of signal processing in cascade	High frequency characteristics	Rise Time	Settling Time	State variables / integrations: Total number	State variables / integrations: Utilized variables	Total number of signals / variables	Multiplications / scaling operations	Additions / subtractions
DSOGI-based Sequence Separation of measured Voltages (Ref [52]).	**Inherent**	**Inherent**	**2**	**- 20 dB/decade**	**~5 ms**	**~20 ms**	**4**	**4**	7	8	8
Conventional Virtual Flux estimation for balanced three-phase conditions (Fig. 3-3)	Depends on implementation – Inherent with SOGI-QSGs	Not without introducing additional techniques	2 (1 in [66]-[68])	Depends on implementation – 40 dB/decade with SOGI-QSG and with (2.10) or (2.11) – 20 dB/decade with (2.9) and in [66]-[68]	~5 ms	~20 ms	4	2	8	12	8
Virtual Flux estimation followed by Sequence Separation (Fig. 3-4)	Depends on Implementation – Inherent with SOGI-QSGs	Achieved by cascading of functionality	4	Depends on implementation – 60 dB/decade for Fig. 3-4	~10 ms	~40 ms	8	6	12	23	16
Sequence Separation followed by PNS Virtual Flux estimation (Fig. 3-5)	Depends on Implementation – Inherent with SOGI-QSGs	Achieved by cascading of functionality	4	Depends on implementation – 60 dB/decade for Fig. 3-5 – 40 dB/decade for [107]	~10 ms	~40 ms	16	12	18	41	30
DSOGI-based Virtual Flux estimation with inherent Sequence Separation (Fig. 3-6)	**Inherent**	**Inherent**	**2**	**- 20 dB/decade**	**~5 ms**	**~20 ms**	**8**	**8**	14	29 (can be reduced to 25)	22

From Table 3-3, it is seen that all the methods for PNS-VF estimation requires a significantly higher number of mathematical operations than the DSOGI-based sequence separation from [52], but this is mainly due to the flux estimation according to (2.5). The lowest number of mathematical operations is required by the method from Fig. 3-4, since this method does not include sequence separation of the currents. However, the transient response is significantly slower than for the proposed DSOGI-VF estimation due to the cascaded operation of Virtual Flux estimation and sequence separation, and it can be noticed that two of the state variables are not directly utilized. The DSOGI-VF estimation is resulting in a slightly higher number of mathematical operations, because the PNS Virtual Flux components are calculated individually. However, since this method implies parallel operation of SOGI-based sequence separation of Virtual Flux and currents, all the 8 state variables are utilized and as already discussed, the transient response is predominantly showing 2^{nd} order characteristics. The PNS-VF estimation from Fig. 3-5 results in a significantly more complex implementation, while achieving the same dynamic response as the method from Fig. 3-4.

From this information, it is clear that the proposed DSOGI-VF estimation can be an effective method for voltage-sensor-less grid synchronization with good dynamic performance and inherent ability to operate under unbalanced conditions as well as grid frequency variations. The method adds little to the complexity of the grid synchronization while achieving fast transient response and effective utilization of the computational efforts. It should also be noticed that in case sequence separation of the current measurements is needed in other parts of the converter control system, the computational efforts of the DSOGI-VF estimation can be utilized even more effectively.

3.5 Other Possible Configurations and Implementations of DSOGI-based Virtual Flux Estimation

The structure of the DSOGI-VF estimation presented in specifically Fig. 3-6 is specifically designed for voltage-sensor-less grid synchronization, following the conventional approach where the Virtual Flux estimation is used to replace voltage measurements at the grid side of the filter inductor. Depending on the control system configuration and the main control objectives for operation of the VSC, it is however possible to design different varieties of the DSOGI-VF estimation method that can be adapted to the application. The structure can also be extended to other application areas then three-phase three-wire converters used. Some examples of varieties of the DSOGI-VF estimation intended to fulfill different purposes, and some topics that can be relevant for future investigations are outlined below.

3.5.1 Simplified DSOGI-VF Structure for Synchronization to Converter Terminals or Available Voltage Measurements

In some cases it can be relevant to synchronize the VSC control system directly to the terminals of the converter, as for instance investigated in [156]. This can be achieved with all the methods for Virtual Flux estimation discussed in the previous sections, simply by specifying the values of r_1 and l_1 equal to zero. Such an approach for grid

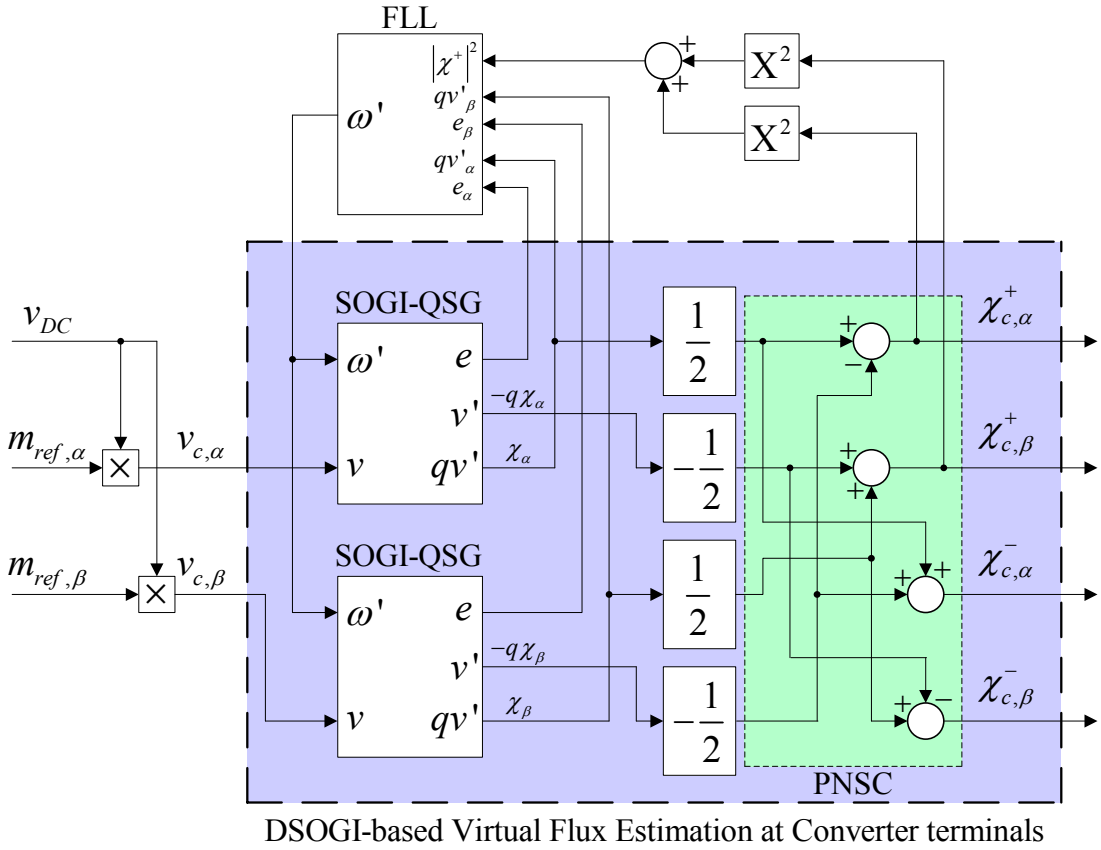

Fig. 3-15 Structure of DSOGI-based estimation of Virtual Flux at converter terminals

synchronization of a VSC has been labeled "Converter Flux Orientation," and has been discussed and analyzed with respect to current control based on the Direct Torque Control (DTC) modulation algorithm in [156], [173], [201], [202].

Considering the DSOGI-VF estimation from Fig. 3-6, it can be noticed that this structure will be significantly simplified if the resistive and inductive terms are cancelled. The resulting structure is shown in Fig. 3-15, where the same FLL as in previous figures is included for keeping the Virtual Flux estimation frequency adaptive. If necessary, compensation for the converter characteristics can be included as discussed in section 2.2.2.1 before the converter voltages is used as input to the SOGI-QSGs. Since the organization of the SOGI-QSGs and the Positive and Negative Sequence Calculation (PNSC) network is the same as in Fig. 3-6, the operational characteristics will the same as already analyzed for the complete DSOGI-VF estimation.

The structure shown in Fig. 3-6 can also be used for explicitly frequency-adaptive estimation of PNS Virtual Flux components based on available voltage measurements. In such cases, the estimated converter voltage $v_{c,\alpha\beta}$ shown as the input to the DSOGI-based structure in Fig. 3-15, can be simply replaced by the available voltage measurements. This can for instance be relevant in cases where both voltage-based and voltage-sensor-less operation is desirable due to reliability requirements.

3.5.2 Configuration with Separate Integration of Converter Output Voltage and Resistive Voltage Drop

The strategies for Virtual Flux estimation presented in the previous sections are limited to the possibility of estimating the Virtual Flux at one specified point, unless the resistive terms are negligible. The simple expression for Virtual Flux estimation according to (2.5) can however be easily expanded into (3.16) where υ_c represents the current integral corresponding to the per unit charge passed through the converter terminals and by that through the resistance r_1 [149]. By organizing the estimation in this way, the Virtual Fluxes, ψ_c, at the converter terminals and ψ_f, at the grid side of the filter inductor are explicitly estimated. Compensation for the converter characteristics can be included before estimating the converter Virtual Flux as ψ_c, discussed in section 2.2.2.1 if necessary to improve the accuracy of the estimation.

$$\begin{aligned}\psi_{f,\alpha\beta} &= \omega_b \int \left(v_{ref,\alpha\beta} \cdot v_{DC} - r_1 \cdot i_{c,\alpha\beta} \right) dt - l_1 \cdot i_{c,\alpha\beta} \\ &= \underbrace{\omega_b \int \left(v_{ref,\alpha\beta} \cdot v_{DC} \right) dt}_{\psi_{c,\alpha\beta}} - r_1 \cdot \underbrace{\omega_b \int \left(i_{c,\alpha\beta} \right) dt}_{\upsilon_{c,\alpha\beta}} - \underbrace{l_1 \cdot i_{c,\alpha\beta}}_{\psi_{l_1,\alpha\beta}} \\ &= \psi_{c,\alpha\beta} - r_1 \cdot \upsilon_{c,\alpha\beta} - l_1 \cdot i_{c,\alpha\beta}\end{aligned} \tag{3.16}$$

Utilizing the SOGI-QSG for emulating the integration of the Virtual Flux estimation and applying the definition of the frequency-scaled Virtual Flux according to section 3.1.2, the Virtual Flux estimation can be expressed in the Laplace domain by (3.17). Here, the symbol ϑ_c is introduced to represent the current integral, or the charge, scaled by the per unit angular frequency ω_{pu}. Equation (3.17) is shown for three-phase systems represented in αβ reference frame, but could also be adapted for single-phase systems or any other circuit configuration.

$$\begin{aligned}\chi_{f,\alpha\beta}(s) = &\underbrace{\frac{k \cdot \omega'^2}{s^2 + k \cdot \omega' \cdot s + \omega'^2} \cdot v_{c,\alpha\beta}(s)}_{\chi_c} \\ &- r_1 \cdot \underbrace{\frac{k \cdot \omega'^2}{s^2 + k \cdot \omega' \cdot s + \omega'^2} \cdot i_{c,\alpha\beta}(s)}_{\vartheta_c} - \omega_{pu}' \cdot l_1 \cdot i_{c,\alpha\beta}(s)\end{aligned} \tag{3.17}$$

The reformulation of the Virtual Flux estimation according to (3.17) can also be applied for estimation of Positive and Negative Sequence (PNS) Virtual Flux components based on the DSOGI-VF strategy from Fig. 3-6. The resulting structure is shown in Fig. 3-16, where it can be seen that the Virtual Flux χ_c^{+-} the converter terminals are first estimated separately according to the simplified structure from Fig. 3-15. Then, sequence separation of the currents and of the charge signals is carried out on basis of two SOGI-QSGs so that the resistive and inductive terms can be subtracted separately fore the PNS Virtual Flux components to result in the grid side Virtual Flux χ_g^{+-}.

Because the compensation for the resistive term is decoupled from the initial Virtual Flux integration, the structure in figure Fig. 3-16 allows for simultaneous estimation of the Virtual Flux at the converter terminals and at any other point specified by the resistance r and inductance l. This can for instance allow for synchronizing the converter to one point in the grid while the active and reactive power flow in another point can be estimated from the Virtual Flux and the current measurements for the

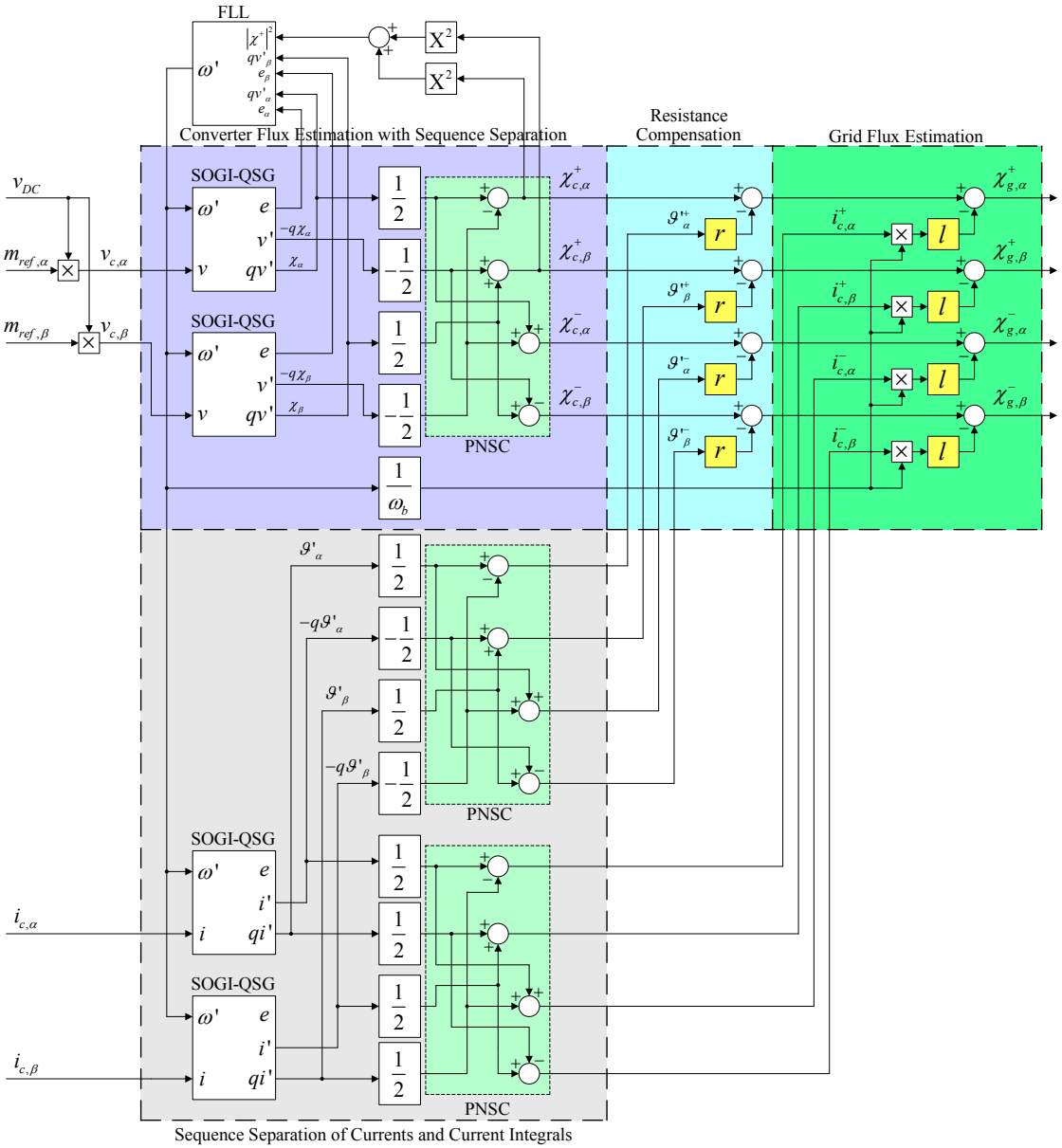

Fig. 3-16 DSOGI-based Virtual Flux estimation with inherent sequence separation and simultaneous estimation of converter Virtual Flux and grid-side Virtual Flux

purpose of monitoring or as a basis for internal feedback signals in the control system. Some further indications on how this can be utilized will be provided towards the end of chapter 4.

It can also be noted that different values for r and l can be selected for the positive and negative sequence components when utilizing estimation methods based on the DSOGI-VF structure. This can allow for synchronization to the positive sequence component in one point and to the negative sequence component in another point in the grid.

It should be noted that SOGI-QSGs used for sequence separation of the currents and the current integrals will have the same characteristics as the SOGI-QSGs for the Virtual Flux estimation. Therefore, the dynamic response of the structure in Fig. 3-16 should be equivalent to that of the DSOGI-VF estimation from Fig. 3-6.

3.5.3 Possible Extensions of the Presented Approaches for Virtual Flux Estimation based on SOGI-QSGs and Indications of Possible Topics of Future Investigations

From the presented discussions of different strategies for Virtual Flux estimation based on the SOGI-QSG in various configurations, it is possible to identify several issues for relevant future investigations outside the scope of this work. Some of these issues are listed below without presenting any further detailed studies:

- Virtual Flux estimation under generalized unbalanced three-phase conditions with unbalanced impedances
  - The DSOIG-VF estimation in Fig. 3-6 and Fig. 3-15 can allow for specifying different resistance and inductance values in the α- and β-axis. Thus, the correct Virtual Flux could be estimated even with unequal inductances or resistances in the different phases.
  - This could allow for extending previous investigations into operation with unbalanced impedances, as discussed for voltage-based control in [203]-[205], towards voltage-sensor-less operation
- The DSOGI-VF estimation could be extended for application to different converter topologies, including single-phase converters and three-phase four-wire converters
  - Single-phase Virtual Flux estimation based on one SOGI-QSG can also be used to establish a virtual in-quadrature system as commonly applied for voltage-based grid synchronization in single-phase systems
  - The Virtual Flux estimation for the zero-sequence component in a three-phase four-wire converter would also be similar to the single-phase application.
- The DSOGI-VF estimation structure could be further investigated with respect to Virtual Flux estimation in the case of LCL-filters
  - This could require estimation of the capacitor current for estimating the Virtual Flux at the grid side of the LCL-filter. Special care should also be taken with respect to the bandwidth of possible strategies for active damping
- Virtual Flux estimation in case of high degrees of harmonic distortion, and in the case of converter over-modulation could be further investigated.
  - The DSOGI-VF estimation could for instance be extended to include harmonic estimation in a similar way to the synchronization strategies proposed in [192], [194], [195].
- Based on the equivalence between DSOGI-based sequence separation and the DDSRF-PLL, as analyzed in [96], it could be possible to implement the DSOGI-VF estimation in the positive and negative sequence synchronous reference frames.
  - This approach should be simpler than previous investigations based on Virtual Flux estimation in the stationary reference frame followed by

applying the DDSRF-PLL for synchronizing to the positive and negative sequence components, as proposed in [106], [183], [184].

- As DSOGI-based sequence separation is simpler to implement than the DDSRF-PLL, Virtual Flux estimation in the synchronous reference frames in a structure similar to the DDSRF-PLL will also require a more demanding digital implementation than the DSOGI-VF estimation.

3.6 Summary of Chapter

To overcome the limitations of existing methods for Virtual Flux estimation with respect to grid frequency variations and operation under unbalanced conditions, a method for explicitly frequency-adaptive Virtual Flux estimation based on the SOGI-QSG has been proposed. This method has been demonstrated to be a suitable building block for achieving inherently frequency-adaptive implementation of different configurations for Virtual Flux estimation under balanced and unbalanced conditions.

To avoid the slow transient response associated with traditional strategies for Virtual Flux estimation under unbalanced conditions, a new Virtual Flux estimation method that merges the functions of frequency-adaptive band-pass filtering, Virtual Flux estimation and sequence separation into one operation has been proposed and analyzed. This method has been labeled as DSOIG-VF estimation, since the implementation is based on two parallel SOGI-QSGs for estimating the Positive and Negative Sequence Virtual Flux (PNS-VF) components.

The proposed DSOGI-VF estimation has been investigated by theoretical analysis, simulation studies and experimental verification, and it has been proved to have faster dynamic response compared to other comparable methods. In fact, the transient response has been proved to be in the same range as the transient response of voltage-based synchronization methods.

Based on the presented analysis, the DSOGI-VF estimation has shown to have all the features required for further investigations into Virtual Flux-based voltage-sensor-less control under unbalanced conditions, and will therefore be used as a basis for the following chapters. Some possible modifications and adaptations of the DSOGI-VF structure have been outlined at the end of the chapter, and a range of issues that are relevant for further investigations have been identified at the end of the chapter.

Main contributions of Chapter:

- Introduction of the Second Order Generalized Integrator (SOGI) configured as a Quadrature Signal Generator (QSG) as a basic building block for explicitly on-line frequency-adaptive Virtual Flux estimation.
- Development and analysis of a new method for frequency-adaptive Virtual Flux estimation with inherent sequence separation, labeled DSOGI-VF estimation.
- Comparative analysis of methods for estimation of Positive and Negative Sequence Virtual Flux components under unbalanced conditions

4 Virtual Flux-based Power Control Strategies under Unbalanced Conditions

This chapter will discuss strategies for voltage-sensor-less control of active and reactive power under unbalanced conditions based on grid synchronization by the DSOGI-VF estimation method presented in the previous chapter. The proposed approach is assuming a traditional cascaded control structure with inner loop current controllers, and the power control is therefore achieved by calculating current references corresponding to specific power control objectives, in a similar way as for conventional control strategies based on voltage measurements. All derivations of the current reference calculation will be presented in the stationary αβ reference frame, but can easily be adapted to any other reference frame used for implementation of the current controllers. The investigated control objectives will be to achieve balances three-phase currents, elimination of double frequency active power oscillations or elimination of double frequency reactive power oscillations, and only power control strategies resulting in sinusoidal current references will be considered to limit the investigations. To achieve a simple implementation of flexible, Virtual Flux-based, control of active and reactive power flow under unbalanced grid voltage conditions, the derived expressions for current reference calculation will be synthesized into generalized equations allowing for The different power control strategies and the corresponding expressions for Virtual Flux-based current reference calculation have been investigated by experiments on a small-scale converter setup, to verify that the intended power control objectives are achieved. Most of the contributions presented in this chapter have been published in manuscript [J2], although organized differently. Some additional examples of potential applications and some further implications of the presented results are outlined at the end of the chapter.

4.1 Introduction to Power Control Strategies and Current Reference Calculation under Unbalanced Conditions

As the application of Voltage Source Converters in grid connected applications has become more widespread, there has been increased attention towards the challenges of operation during transient and unbalanced conditions. Therefore, a wide range of methods and techniques for control and analysis of VSC operation during unbalanced conditions have been presented during the last two decades.

Assuming a converter control structure based on inner loop current controllers, where the grid synchronization and the current controllers are designed for satisfactory

performance during both balanced and unbalanced conditions, the operational characteristics of the converter will mainly be influenced by the objectives and techniques used for specifying the current reference values. In most of the early publications related to control of VSCs during unbalanced conditions, the attention was focused on eliminating 2nd harmonic oscillations in the active power flow of the converter during operation with a limited degree of voltage unbalance, and by that limiting the oscillations in the DC-link voltage of the converter [35], [98], [206], [207]. In other cases, the priority has been to assure balanced sinusoidal currents from the converter [208]. With the increased use of VSCs in renewable energy systems and the emergence of Grid Codes requiring capability for delivering reactive power to the grid, also different control objectives for controlling the reactive power flow under unbalanced conditions have become relevant [39]. Several recent publications have therefore presented generalized discussions on how to derive current references corresponding to different objectives for control of active and reactive power during unbalanced conditions, as well as comparative studies investigating converter operation with different control objectives [34], [39], [96], [108]-[114], [209]-[213].

The available studies of generalized and flexible methods for control of VSCs during unbalanced conditions are however based on utilizing measured voltages to fulfill the specified control objectives, without considering voltage-sensor-less operation. Although some studies of observer-based voltage-sensor-less operation under unbalanced conditions have been presented, as reviewed in section 2.1.2, these publications have until now only considered case-specific objectives of achieving either balanced currents or elimination of second harmonic oscillations in the active power flow during unbalanced conditions. The same is the case for Virtual Flux-based voltage-sensor-less control, as discussed in section 2.3.

This chapter will follow a general approach for Virtual Flux-based power control during unbalanced conditions and will present expressions for current reference calculation corresponding to selectable objectives for control of active and reactive power flow. The analysis will be based on the DSOGI-VF estimation method from section 3.3, and will result in Virtual Flux-based power control strategies, analogous to the voltage-based strategies presented in [108]-[110], [113], [114].

4.2 Active and Reactive Power Equations based on Virtual Flux

The starting point for the following derivations will be the formulation of instantaneous active and reactive powers, well known from the work of Akagi et al. [214]-[216]. Only three-phase three-wire systems will be considered, and vector notation based on the representation introduced in [217]-[219] will be used for the derivations, following most of the conventions applied in [108]-[110], [113], [114]. The instantaneous active and reactive power components are accordingly expressed by (4.1) and (4.2), where "•" denotes the inner-product while "×" represents the cross-product of two vectors. The vector operation "⊥" is in this cased defined to represent a vector that is a 90° lagging version of the original vector.

$$p = v_\alpha \cdot i_\alpha + v_\beta \cdot i_\beta = \mathbf{v} \cdot \mathbf{i} \tag{4.1}$$

$$q = v_\beta \cdot i_\alpha - v_\alpha \cdot i_\beta = -\left|\mathbf{v} \times \mathbf{i}\right| = \mathbf{v}_\perp \cdot \mathbf{i} \tag{4.2}$$

4.2.1 Virtual Flux-based Power Equations under Balanced Conditions

Starting from the definition of the Virtual Flux from (2.1), the voltage vector needed for the power equations of (4.1) and (4.2) can be found by differentiation according to (4.3). As supported by the results and discussions presented in [67], [68], [80], sufficient accuracy of power calculations under balanced three-phase conditions is usually achieved by neglecting the derivative of the Virtual Flux vector amplitude, as given by the approximation shown in (4.3). Utilizing the definition of the scaled Virtual Flux according to (3.5), and introducing the results from (4.3) into (4.1) and (4.2), the active and reactive power can be expressed by (4.4) and (4.5).

$$\mathbf{v} = \frac{d}{dt}\boldsymbol{\psi} = \frac{d}{dt}\left(|\boldsymbol{\psi}| \cdot e^{j\omega t}\right) = \frac{d|\boldsymbol{\psi}|}{dt} + j\omega \cdot \boldsymbol{\psi} = \begin{bmatrix} \left.\frac{d|\boldsymbol{\psi}|}{dt}\right|_{\alpha} - \omega \cdot \psi_{\beta} \\ \left.\frac{d|\boldsymbol{\psi}|}{dt}\right|_{\beta} + \omega \cdot \psi_{\alpha} \end{bmatrix} \approx \begin{bmatrix} -\omega \cdot \psi_{\beta} \\ \omega \cdot \psi_{\alpha} \end{bmatrix} = \begin{bmatrix} -\chi_{\beta} \\ \chi_{\alpha} \end{bmatrix} = -\boldsymbol{\chi}_{\perp} \tag{4.3}$$

$$p \approx \chi_{\alpha} \cdot i_{\beta} - \chi_{\beta} \cdot i_{\alpha} = -\boldsymbol{\chi}_{\perp} \cdot \mathbf{i} \tag{4.4}$$

$$q \approx \chi_{\alpha} \cdot i_{\alpha} + \chi_{\beta} \cdot i_{\beta} = \boldsymbol{\chi} \cdot \mathbf{i} \tag{4.5}$$

These equations are generally valid for three-phase balanced conditions. However, for derivation of power control strategies intended for operation under unbalanced conditions, the active and reactive powers should be expressed on basis of the positive and negative sequence Virtual Flux components.

4.2.2 Active and Reactive Power Equations under Unbalanced Conditions

Considering sinusoidal but unbalanced three-phase voltages and currents at the fundamental frequency, the active and reactive power can be expressed by the positive and negative sequence components of the voltages and currents as given by (4.6) and (4.7) respectively [108], [109] . The two last terms in these equations are oscillating power components at twice the fundamental frequency, as indicated by the annotation in the equations, originating from the interaction between positive and negative sequence currents and voltages.

$$p = \mathbf{v} \cdot \mathbf{i} = \left(\mathbf{v}^{+} + \mathbf{v}^{-}\right) \cdot \left(\mathbf{i}^{+} + \mathbf{i}^{-}\right) = \underbrace{\underbrace{\mathbf{v}^{+} \cdot \mathbf{i}^{+}}_{\bar{p}^{+}} + \underbrace{\mathbf{v}^{-} \cdot \mathbf{i}^{-}}_{\bar{p}^{-}}}_{\bar{p}} + \underbrace{\underbrace{\mathbf{v}^{+} \cdot \mathbf{i}^{-}}_{p^{+-}} + \underbrace{\mathbf{v}^{-} \cdot \mathbf{i}^{+}}_{p^{-+}}}_{\tilde{p}_{2\omega}} \tag{4.6}$$

$$q = -\left|\mathbf{v} \times \mathbf{i}\right| = \mathbf{v}_{\perp} \cdot \mathbf{i} = \left(\mathbf{v}_{\perp}^{+} + \mathbf{v}_{\perp}^{-}\right) \cdot \left(\mathbf{i}^{+} + \mathbf{i}^{-}\right) = \underbrace{\underbrace{\mathbf{v}_{\perp}^{+} \cdot \mathbf{i}^{+}}_{\bar{q}^{+}} + \underbrace{\mathbf{v}_{\perp}^{-} \cdot \mathbf{i}^{-}}_{\bar{q}^{-}}}_{\bar{q}} + \underbrace{\underbrace{\mathbf{v}_{\perp}^{+} \cdot \mathbf{i}^{-}}_{q^{+-}} + \underbrace{\mathbf{v}_{\perp}^{-} \cdot \mathbf{i}^{+}}_{q^{-+}}}_{\tilde{q}_{2\omega}} \tag{4.7}$$

Following the same approach as for balanced three-phase conditions, the voltage vector can be expressed by the positive and negative sequence components of the Virtual Flux as given by (4.8).Considering that the positive and negative sequence vector amplitudes will be constant during steady-state unbalanced conditions, the same approximation as applied in (4.3) can be introduced with similar accuracy as for balanced conditions. Thus, by assuming the derivative of the positive and negative sequence vector amplitudes to be negligible, the voltage can be expressed by the approximation shown in (4.9).

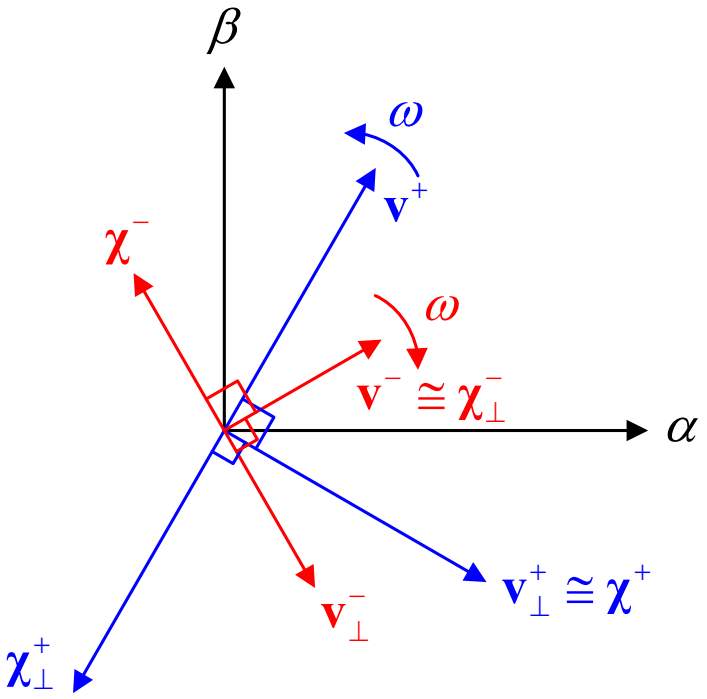

Fig. 4-1 Conventions and orientations used for power calculations based on voltage and Virtual Flux

$$\mathbf{v} = \mathbf{v}^+ + \mathbf{v}^- = \frac{d}{dt}\left(\boldsymbol{\psi}^+ + \boldsymbol{\psi}^-\right) = \frac{d}{dt}\left(\left|\boldsymbol{\psi}^+\right| \cdot e^{j\omega t} + \left|\boldsymbol{\psi}^-\right| \cdot e^{-j\omega t}\right) = \frac{d\left|\boldsymbol{\psi}^+\right|}{dt} + j\omega \cdot \boldsymbol{\psi}^+ + \frac{d\left|\boldsymbol{\psi}^-\right|}{dt} - j\omega \cdot \boldsymbol{\psi}^-$$

$$= \begin{bmatrix} \left.\frac{d\left|\boldsymbol{\psi}^+\right|}{dt}\right|_\alpha - \omega \cdot \psi_\beta^+ \\ \left.\frac{d\left|\boldsymbol{\psi}^+\right|}{dt}\right|_\beta + \omega \cdot \psi_\alpha^+ \end{bmatrix} + \begin{bmatrix} \left.\frac{d\left|\boldsymbol{\psi}^-\right|}{dt}\right|_\alpha + \omega \cdot \psi_\beta^- \\ \left.\frac{d\left|\boldsymbol{\psi}^-\right|}{dt}\right|_\beta - \omega \cdot \psi_\alpha^- \end{bmatrix} \tag{4.8}$$

$$\mathbf{v} = \mathbf{v}^+ + \mathbf{v}^- \approx \begin{bmatrix} -\omega \cdot \psi_\beta^+ \\ \omega \cdot \psi_\alpha^+ \end{bmatrix} + \begin{bmatrix} \omega \cdot \psi_\beta^- \\ -\omega \cdot \psi_\alpha^- \end{bmatrix} = \begin{bmatrix} -\chi_\beta^+ \\ \chi_\alpha^+ \end{bmatrix} + \begin{bmatrix} \chi_\beta^- \\ -\chi_\alpha^- \end{bmatrix} = -\boldsymbol{\chi}_\perp^+ + \boldsymbol{\chi}_\perp^- \tag{4.9}$$

For expressing the power equations from (4.6) and (4.7) on basis of the Virtual Flux, an expression equivalent to the in-quadrature voltage vector $\mathbf{v}_\perp$ is also needed. This can be easily identified by applying the vector operation "$\perp$" as given by (4.10).

$$\mathbf{v}_\perp = \mathbf{v}_\perp^+ + \mathbf{v}_\perp^- \approx \left(-\boldsymbol{\chi}_\perp^+ + \boldsymbol{\chi}_\perp^-\right)_\perp = \boldsymbol{\chi}^+ - \boldsymbol{\chi}^- \tag{4.10}$$

The result from these approximations is that the Virtual Flux vector components can be considered to simply be lagging the voltage by 90° in the direction of rotation. Since the vector operation "$\perp$" will be applied in the stationary, $\alpha\beta$ reference frame, it will however give the same direction of phase shift for both positive and negative sequence components. This is illustrated by the vector diagram shown in Fig. 4-1, showing the conventions and orientations applied for the voltage and Virtual Flux components.

Applying the results from (4.9) and (4.10) in the power equations from (4.6) and (4.7), the active and reactive powers can be expressed by the positive and negative sequence Virtual Flux components as given by (4.11) and (4.12).

$$p = \mathbf{v}\cdot\mathbf{i} \approx \left(-\boldsymbol{\chi}_{\perp}^{+} + \boldsymbol{\chi}_{\perp}^{-}\right)\cdot\left(\mathbf{i}^{+} + \mathbf{i}^{-}\right) = \underbrace{\underbrace{-\boldsymbol{\chi}_{\perp}^{+}\cdot\mathbf{i}^{+}}_{\bar{p}^{+}} + \underbrace{\boldsymbol{\chi}_{\perp}^{-}\cdot\mathbf{i}^{-}}_{\bar{p}^{-}}}_{\bar{p}} \underbrace{\underbrace{-\boldsymbol{\chi}_{\perp}^{+}\cdot\mathbf{i}^{-}}_{\tilde{p}^{+-}} + \underbrace{\boldsymbol{\chi}_{\perp}^{-}\cdot\mathbf{i}^{+}}_{\tilde{p}^{-+}}}_{\tilde{p}_{2\omega}} \tag{4.11}$$

$$q = \mathbf{v}_{\perp}\cdot\mathbf{i} = \left(\boldsymbol{\chi}^{+} - \boldsymbol{\chi}^{-}\right)\cdot\left(\mathbf{i}^{+} + \mathbf{i}^{-}\right) = \underbrace{\underbrace{\boldsymbol{\chi}^{+}\cdot\mathbf{i}^{+}}_{\bar{q}^{+}} \underbrace{-\boldsymbol{\chi}^{-}\cdot\mathbf{i}^{-}}_{\bar{q}^{-}}}_{\bar{q}} + \underbrace{\underbrace{\boldsymbol{\chi}^{+}\cdot\mathbf{i}^{-}}_{\tilde{q}^{+-}} \underbrace{-\boldsymbol{\chi}^{-}\cdot\mathbf{i}^{+}}_{\tilde{q}^{-+}}}_{\tilde{q}_{2\omega}} \tag{4.12}$$

The instantaneous powers of (4.11) and (4.12) can be calculated from the positive and negative sequence components of the current and the Virtual Flux, available directly from the DSOGI-VF estimation of Fig. 3-6. For the derivation of current references for power control during unbalanced conditions, it is however convenient to further factorize the currents into active and reactive components [108]-[110]. Considering positive and negative sequence components of the active and reactive current components, the total current can be expressed by four terms as given by (4.13). The positive and negative sequence active current components are then in phase with the positive and negative sequence voltage components respectively, while the positive and negative sequence reactive current components are in phase with the estimated Virtual Flux components.

$$\mathbf{i} = \mathbf{i}_p + \mathbf{i}_q \qquad \mathbf{i}_p = \mathbf{i}_p^{+} + \mathbf{i}_p^{-} \qquad \mathbf{i}_q = \mathbf{i}_q^{+} + \mathbf{i}_q^{-} \tag{4.13}$$

For expressing the active and reactive power components, it can be considered that the positive sequence reactive current component will be in quadrature to the positive sequence voltage component, and the product of these terms will therefore produce zero active power flow. Similarly, there will be zero active power flow resulting from the interaction of the negative sequence reactive current component with the negative sequence voltage component. Correspondingly, the interaction between the positive sequence Virtual Flux and the positive sequence active current component, and the interaction between the negative sequence Virtual Flux and the negative sequence active current component will cause zero reactive power flow. These relations are expressed in (4.14), on basis of the Virtual Flux components.

$$\begin{aligned} -\boldsymbol{\chi}_{\perp}^{+}\cdot\mathbf{i}_q^{+} &= 0 \qquad & \boldsymbol{\chi}_{\perp}^{-}\cdot\mathbf{i}_q^{-} &= 0 \\ \boldsymbol{\chi}^{+}\cdot\mathbf{i}_p^{+} &= 0 \qquad & \boldsymbol{\chi}^{-}\cdot\mathbf{i}_p^{-} &= 0 \end{aligned} \tag{4.14}$$

Considering the simplifications introduced by (4.14), the Virtual Flux-based active and reactive power equations can be expressed on basis of the active and reactive current components as given by (4.15) and (4.16). From these equations, it is clearly seen that only the active power components contributes to the average active power flow, while second harmonic active power oscillations are originating from both active and reactive current components due to the interaction between positive and negative sequence components. Similarly, positive sequence active current components interacting with the negative sequence Virtual Flux, and negative sequence active current components interacting with the positive sequence Virtual Flux are contributing to second harmonic oscillations in the reactive power flow.

$$p = \mathbf{v}\cdot\mathbf{i} \approx \left(-\boldsymbol{\chi}_{\perp}^{+} + \boldsymbol{\chi}_{\perp}^{-}\right)\cdot\left(\mathbf{i}^{+} + \mathbf{i}^{-}\right) = \underbrace{\underbrace{-\boldsymbol{\chi}_{\perp}^{+}\cdot\mathbf{i}_p^{+}}_{\bar{p}^{+}} + \underbrace{\boldsymbol{\chi}_{\perp}^{-}\cdot\mathbf{i}_p^{-}}_{\bar{p}^{-}}}_{\bar{p}} \underbrace{\underbrace{\underbrace{-\boldsymbol{\chi}_{\perp}^{+}\cdot\mathbf{i}_p^{-}}_{\tilde{p}_p^{+-}} \underbrace{+\boldsymbol{\chi}_{\perp}^{-}\cdot\mathbf{i}_p^{+}}_{\tilde{p}_p^{-+}}}_{\tilde{p}_{2\omega,p}} \underbrace{\underbrace{-\boldsymbol{\chi}_{\perp}^{+}\cdot\mathbf{i}_q^{-}}_{\tilde{p}_q^{+-}} \underbrace{+\boldsymbol{\chi}_{\perp}^{-}\cdot\mathbf{i}_q^{+}}_{\tilde{p}_q^{-+}}}_{\tilde{p}_{2\omega,q}}}_{\tilde{p}_{2\omega}} \tag{4.15}$$

$$q = \mathbf{v}_{\perp} \cdot \mathbf{i} = \left(\boldsymbol{\chi}^{+} - \boldsymbol{\chi}^{-}\right) \cdot \left(\mathbf{i}^{+} + \mathbf{i}^{-}\right) = \underbrace{\underbrace{\underbrace{\boldsymbol{\chi}^{+} \cdot \mathbf{i}_{q}^{+}}_{\bar{q}^{+}} \underbrace{-\boldsymbol{\chi}^{-} \cdot \mathbf{i}_{q}^{-}}_{\bar{q}^{-}}}_{\bar{q}} \underbrace{\underbrace{+\boldsymbol{\chi}^{+} \cdot \mathbf{i}_{p}^{-}}_{\tilde{q}_{p}^{+-}} \underbrace{-\boldsymbol{\chi}^{-} \cdot \mathbf{i}_{p}^{+}}_{\tilde{q}_{p}^{-+}}}_{\tilde{q}_{2\omega,p}} \underbrace{\underbrace{+\boldsymbol{\chi}^{+} \cdot \mathbf{i}_{q}^{-}}_{\tilde{q}_{q}^{+-}} \underbrace{-\boldsymbol{\chi}^{-} \cdot \mathbf{i}_{q}^{+}}_{\tilde{q}_{q}^{-+}}}_{\tilde{q}_{2\omega,q}}}_{\tilde{q}_{2\omega}} \tag{4.16}$$

4.2.3 Accuracy of Power Calculations and Current Reference Calculation based on Positive and Negative Sequence Virtual Flux Components

Considering that PNS Virtual Flux components instead of PNS voltage components will be used for power calculations and derivation of current references in the following sections, it could be expected that the approximation introduced in (4.9) and (4.10) will influence the dynamic response and accuracy. It should however be noted that there will also be a significant influence from the dynamic response of the sequence separation method, both in case of voltage-based calculations and in case of Virtual Flux-based calculations. The dynamic response of Virtual Flux-based power calculations according to (4.11) and (4.12), and the accuracy of equations derived from this starting point, will therefore depend on the applied methods for Virtual Flux estimation and sequence separation.

In section 3.3, it has however been shown that the dynamic response of the DSOGI-VF estimation is the same as the dynamic response of DSOGI-based sequence separation of voltage measurements. Power calculations based on (4.11) and (4.12) together with power control strategies implemented by using current references derived from (4.15) and (4.16), will therefore yield similar dynamic response as obtained for power control strategies based on PNS voltage components in [108]-[110], as long as the PNS Virtual Flux components are estimated by the DSOGI-VF estimation method proposed in section 3.3. In the following, it will therefore be assumed that both the PNS Virtual Flux components and the positive and negative sequence current components are originating from the DSOGI-VF estimation structure proposed in section 3.3 and shown in Fig. 3-6.

4.3 Derivation of Current References for Active and Reactive Power Control during Unbalanced Grid Conditions

In the following subsections, expressions for Virtual Flux-based calculation of current references corresponding to active and reactive power control with different objectives will be derived, in analogy to the voltage-based control strategies presented in [108], [109], [110], [113], [114]. Only control strategies based on sinusoidal current references will be considered, and therefore it will not be possible to achieve simultaneous control of non-zero active and reactive power flow with elimination of both active and reactive power oscillations. Although control strategies achieving constant active and/or reactive power flow under unbalanced conditions on the cost of harmonic distortion of the current references have been presented in, [108]-[110], [209], [211]-[213], the application of these methods will usually be limited since the distorted current references would result in violation of harmonic requirements for currents injected into the power system. Additionally, non-sinusoidal currents will also influence the voltage at the point of connection to the grid if the grid impedance is non-negligible, and such

strategies will therefore not be suitable for operation in weak grids [213]. In the specific case of voltage-sensor-less control based on the DSOGI-VF estimation, the sequence separation of the currents will also be influenced by significant distortion in the current references, and this will degrade the accuracy of the Virtual Flux estimation. Considering only control objectives resulting in sinusoidal current references is therefore a natural limitation of scope when considering power control strategies with general validity and applicability for voltage-sensor-less operation and operation in power systems with high grid impedance.

The control objectives that will be investigated can be applied independently to the control of active and reactive powers, and can be classified according to the following characteristics:

1. Operation with balanced positive sequence three-phase current references.
2. Elimination of second harmonic oscillations in active power flow
3. Elimination of second harmonic oscillations in reactive power flow

These control objectives will be expressed in the form of active and reactive current references that can be considered as Virtual Flux-based "forming equations" in analogy to voltage-based strategies where the current references are expressed by a conductance term and the PNS grid voltage components [96], [108]-[110]. The three different control objectives can be applied independently to the active and reactive power control, but the resulting active and reactive power flow characteristics will not be independent of each other. The coordinated control of active and reactive powers to achieve fulfillment of either objective 2 or 3 listed above will therefore be discussed separately, after deriving the different strategies for controlling pure active or reactive power.

In the following, it will be assumed that the PNS Virtual Flux components are estimated at the grid side of the filter inductor, following the conventional approach of using the Virtual Flux estimation to replace voltage measurements. This also allows for easy verification of the power flow characteristics in laboratory experiments by using available voltage measurements. However, the current reference expressions that will be derived can be equally valid if the Virtual Flux is estimated at any other location in the grid, as will be briefly addressed in a separate section at the end of the chapter.

4.3.1 Balanced Positive Sequence Control (BPSC)

The simplest strategy for power control under unbalanced conditions will be to maintain balanced three-phase sinusoidal currents, as labeled Balanced Positive Sequence Control (BPSC) in [108]-[110]. This approach will result in the lowest possible current amplitudes for a specified average active power transfer during unbalanced conditions, but with the consequence of second harmonic oscillations in both the active and the reactive power flow.

4.3.1.1 Current reference calculation for Active Power Control by BPSC

Starting from (4.15), the positive sequence current reference that will result in an average active power flow specified by the reference value $\bar{p}^*$, can be easily found by (4.17). The negative sequence active current component must be kept at zero to obtain the objective of balanced three-phase currents.

$$\mathbf{i}_{p,BPSC}^{*} = \mathbf{i}_{p}^{*+} = \frac{\overline{p}^{*}}{\left|\boldsymbol{\chi}^{+}\right|^{2}}\left(-\boldsymbol{\chi}_{\perp}^{+}\right) \qquad \mathbf{i}_{p}^{*-} = 0 \tag{4.17}$$

From equations (4.15) and (4.16), it can however be seen how the positive sequence active current component will interact with the negative sequence Virtual Flux, and this will result in second harmonic oscillations in both the active and reactive power flow. Assuming the converter currents to be equal to the current references, these resulting power oscillations can be derived as given by (4.18) and (4.19) respectively. The conventions for positive and negative Virtual Flux components described in Appendix D.3 are used to arrive to these equations, with the phase angle θ representing the assumed instantaneous phase angle of the positive sequence voltage component at the point where the Virtual Flux is estimated, and the angle δ representing the orientation of the elliptical Virtual Flux trajectory in the stationary reference frame. The detailed derivations can be found in Appendix D.4. It can be noticed that the amplitude of the double frequency oscillations in the active and reactive power flow is a function of the average active power reference and the ratio between the negative sequence and positive sequence components of the frequency-scaled Virtual Flux.

$$\tilde{p}_{2\omega,p,BPSC} = \tilde{p}_{p}^{-+} = \boldsymbol{\chi}_{\perp}^{-} \cdot \mathbf{i}_{p}^{+} = \boldsymbol{\chi}_{\perp}^{-} \cdot \left(-\boldsymbol{\chi}_{\perp}^{+}\right) \cdot \frac{\overline{p}^{*}}{\left|\boldsymbol{\chi}^{+}\right|^{2}} = \frac{\overline{p}^{*} \cdot \hat{\chi}^{-}}{\hat{\chi}^{+}} \cdot \cos\left(2\theta + 2\delta\right) \tag{4.18}$$

$$\tilde{q}_{2\omega,p,BPSC} = \tilde{q}_{p}^{-+} = \boldsymbol{\chi}^{-} \cdot \mathbf{i}_{p}^{+} = \boldsymbol{\chi}^{-} \cdot \left(-\boldsymbol{\chi}_{\perp}^{+}\right) \cdot \frac{\overline{p}^{*}}{\left|\boldsymbol{\chi}^{+}\right|^{2}} = -\frac{\overline{p}^{*} \cdot \hat{\chi}^{-}}{\hat{\chi}^{+}} \cdot \sin\left(2\theta + 2\delta\right) \tag{4.19}$$

It can be noted that in case of a converter control system based on the principles of Direct Power Control (DPC), active power transfer with balanced sinusoidal currents can be achieved by adding the oscillating power term given by (4.18) to the average active power reference and by using (4.19) as the reactive power references, as discussed in [220]. The same will be the case for the power control strategies and the resulting power flow characteristics derived in the following subsections, but this will not be further investigated or commented.

4.3.1.2 Current reference calculation for Reactive Power Control by BPSC

From equation (4.16), the positive sequence reactive current reference that will result in average reactive power flow equal to the reference value $\overline{q}^{*}$ can be found as given by (4.20). The negative sequence reactive current must again be kept at zero to keep balanced three-phase currents.

$$\mathbf{i}_{q,BPSC}^{*} = \mathbf{i}_{q}^{+*} = \frac{\overline{q}^{*}}{\left|\boldsymbol{\chi}^{+}\right|^{2}}\left(\boldsymbol{\chi}^{+}\right) \qquad \mathbf{i}_{q}^{*-} = 0 \tag{4.20}$$

Control of the average reactive power flow with balanced three-phase currents according to the BPSC strategy will result in double frequency oscillations in the active and reactive power flow according to (4.21) and (4.22) respectively. As for the case of active power control, it can be noticed that the amplitude of the active and reactive power oscillations is a function of the average reactive power reference, and the ratio between the negative and the positive sequence components of the Virtual Flux.

$$\tilde{p}_{2\omega,q,BPSC} = \tilde{p}_q^{-+} = \boldsymbol{\chi}_\perp^- \cdot \mathbf{i}_q^+ = \boldsymbol{\chi}_\perp^- \cdot \left(\boldsymbol{\chi}^+\right) \cdot \frac{\overline{q}^*}{\left|\boldsymbol{\chi}^+\right|^2} = \frac{\overline{q}^* \cdot \hat{\chi}^-}{\hat{\chi}^+} \cdot \sin\left(2\theta + 2\delta\right) \tag{4.21}$$

$$\tilde{q}_{2\omega,q,BPSC} = \tilde{q}_q^{-+} = -\boldsymbol{\chi}^- \cdot \mathbf{i}_q^+ = -\boldsymbol{\chi}^- \cdot \boldsymbol{\chi}^+ \cdot \frac{\overline{q}^*}{\left|\boldsymbol{\chi}^+\right|^2} = \frac{\overline{q}^* \cdot \hat{\chi}^-}{\hat{\chi}^+} \cdot \cos\left(2\theta + 2\delta\right) \tag{4.22}$$

It can also be noticed that the active power oscillations originating from the reactive power control as given by (4.21) is 90° phase shifted with respect to the active power oscillations originating from the active power control as given by (4.18). In case of simultaneous control of both average active and average reactive power control by BPSC, the amplitude of the active power oscillations will therefore be given by the square sum of the active and reactive power references. The same will be the case for the reactive power oscillations.

4.3.2 Positive-Negative-Sequence Compensation (PNSC)

Considering equation (4.15), it can be noticed that the active power oscillations, $\tilde{p}_{2\omega,p}$, originating from a specified flow of average active power can be eliminated if the negative sequence active current component is controlled in such a way that the oscillating power term $\tilde{p}_p^{+-}$ is cancelling the effect of the power oscillations from the term $\tilde{p}_p^{-+}$. The same strategy can also be used to eliminate oscillations in the reactive power flow caused by control of average reactive power. Since the negative sequence current reference is calculated to compensate for the power oscillations generated by the positive sequence current component, this approach to active and reactive power control is labeled as Positive-Negative-Sequence Compensation (PNSC) in [108]-[110].

4.3.2.1 Current reference calculation for active power control by PNSC

The characteristics of the PNSC for the active power control is achieved by imposing the condition that the active power oscillations, $\tilde{p}_{2\omega,p}$, caused by the active power flow should be zero, as expressed by (4.23). The required negative sequence active current reference can then be expressed as a function of the required positive sequence active current reference according to (4.24).

$$\tilde{p}_{2\omega,p}^* = \tilde{p}_p^{*+-} + \tilde{p}_p^{*-+} = -\boldsymbol{\chi}_\perp^+ \cdot \mathbf{i}_p^{*-} + \boldsymbol{\chi}_\perp^- \cdot \mathbf{i}_p^{*+} = 0 \tag{4.23}$$

$$\mathbf{i}_p^{*-} = \frac{\boldsymbol{\chi}_\perp^+ \cdot \boldsymbol{\chi}_\perp^-}{\left|\boldsymbol{\chi}^+\right|^2} \mathbf{i}_p^{*+} \tag{4.24}$$

Substituting (4.24) into (4.25), which expresses the average active power flow from (4.15), the positive sequence active current reference can be derived to be given by (4.26). The corresponding negative sequence active current reference can then be found by substituting (4.26) back into (4.24), resulting in (4.27).

$$\overline{p}^* = \underbrace{-\boldsymbol{\chi}_\perp^+ \cdot \mathbf{i}_p^{*+}}_{\overline{p}^+} + \underbrace{\boldsymbol{\chi}_\perp^- \cdot \mathbf{i}_p^{*-}}_{\overline{p}^-} \tag{4.25}$$

$$\mathbf{i}_p^{*+} = \frac{\overline{p}^*}{\left|\boldsymbol{\chi}^+\right|^2 - \left|\boldsymbol{\chi}^-\right|^2} \cdot \left(-\boldsymbol{\chi}_\perp^+\right) \tag{4.26}$$

$$\mathbf{i}_p^{*-} = \frac{\overline{p}^*}{\left|\boldsymbol{\chi}^+\right|^2 - \left|\boldsymbol{\chi}^-\right|^2} \cdot \left(-\boldsymbol{\chi}_\perp^-\right) \tag{4.27}$$

The total current reference for constant active power flow equal to the specified reference value will be equal to the sum of the positive and negative sequence components as given by (4.28). It should however be noticed that these expressions will approach infinity if the amplitude of the negative sequence Virtual Flux component is approaching the amplitude of the positive sequence Virtual Flux. This power control strategy, and the corresponding equations for current reference calculation, can therefore only be applied if the amplitude of the positive sequence Virtual Flux is significantly higher than the amplitude of the negative sequence components, as indicated by the condition specified in (4.28)

$$\mathbf{i}_{p,PNSC}^* = \mathbf{i}_p^{*+} + \mathbf{i}_p^{*-} = \frac{\overline{p}^*}{\left|\boldsymbol{\chi}^+\right|^2 - \left|\boldsymbol{\chi}^-\right|^2}\left(-\boldsymbol{\chi}_\perp^+ - \boldsymbol{\chi}_\perp^-\right), \qquad \left|\boldsymbol{\chi}^+\right| \gg \left|\boldsymbol{\chi}^-\right| \tag{4.28}$$

A condition where the positive and negative sequence Virtual Flux or voltage components have equal amplitude can however be considered to represent a "single-phase" condition, for instance in the case where the voltage in one phase is reduced to zero. The limited application of (4.28) is therefore as expected, since it will be impossible to achieve a constant instantaneous active power flow under a "single-phase conditions."

Assuming that the resulting converter currents will be equal to the current references specified by (4.28), the active power oscillations originating from active power control by PNSC will be zero. There will however be double line frequency oscillations in the reactive power flow, and starting from (4.16) these reactive power oscillations can be derived to be given by (4.29).

$$\tilde{q}_{2\omega,p,PNSC} = \tilde{q}_p^{+-} + \tilde{q}_p^{-+} = \boldsymbol{\chi}^+ \cdot \mathbf{i}_p^- - \boldsymbol{\chi}^- \cdot \mathbf{i}_p^+ = -\frac{2 \cdot \overline{p}^* \cdot \hat{\chi}^- \cdot \hat{\chi}^+}{\hat{\chi}^{+^2} - \hat{\chi}^{-^2}} \cdot \sin\left(2\theta + 2\delta\right) \tag{4.29}$$

Although the application of the PNSC strategy for active power control is limited with respect to the level of unbalance in the grid voltage, there is a range of conditions where the ability to control constant power during unbalanced conditions can be important. Especially, this control strategy can be applied in cases where it is important to limit or reduce voltage oscillations in the converter DC-link during low values of unbalance in the grid voltage. This can for instance be the case for converters with a small DC-link capacitance, or for active rectifiers with a sensitive load on the DC-link.

4.3.2.2 Current reference calculation for reactive power control by PNSC

The PNSC approach can also be used for the control of the reactive power flow. In this case, the objective will be to eliminate the reactive power oscillations, $\tilde{q}_{2\omega,q}$, originating from the reactive power flow, as expressed by (4.30). Following the same line as explained for the active power control, and imposing the condition that the average reactive power should be equal to its reference value as expressed by (4.31), the resulting reactive current reference can be derived to be given by (4.32).

$$\tilde{q}_{2\omega,q}^* = \tilde{q}_q^{*+-} + \tilde{q}_q^{*-+} = \boldsymbol{\chi}^+ \cdot \mathbf{i}_q^{*-} - \boldsymbol{\chi}^- \cdot \mathbf{i}_q^{*+} = 0 \tag{4.30}$$

$$\bar{q}^* = \underbrace{\boldsymbol{\chi}^+ \cdot \mathbf{i}_q^{*+}}_{\bar{q}^+} \underbrace{-\boldsymbol{\chi}^- \cdot \mathbf{i}_q^{*-}}_{\bar{q}^-} \tag{4.31}$$

$$\mathbf{i}_{q,PNSC}^* = \mathbf{i}_q^{*+} + \mathbf{i}_q^{*-} = \frac{\bar{q}^*}{\left|\boldsymbol{\chi}^+\right|^2 - \left|\boldsymbol{\chi}^-\right|^2}\left(\boldsymbol{\chi}^+ + \boldsymbol{\chi}^-\right), \qquad \left|\boldsymbol{\chi}^+\right| \gg \left|\boldsymbol{\chi}^-\right| \tag{4.32}$$

In the same way as for active power control by PNSC, the reactive power control by PNSC will only be valid as long as the positive sequence component of the Virtual Flux is significantly larger than the negative sequence. The flow of constant reactive power will however cause second harmonic oscillations in the active power flow, that can be derived to be give by (4.33).

$$\tilde{p}_{2\omega,q} = \tilde{p}_q^{+-} + \tilde{p}_q^{-+} = -\boldsymbol{\chi}_\perp^+ \cdot \mathbf{i}_q^- + \boldsymbol{\chi}_\perp^- \cdot \mathbf{i}_q^+ = \frac{2 \cdot \bar{q}^* \cdot \hat{\chi}^- \cdot \hat{\chi}^+}{\hat{\chi}^{+2} - \hat{\chi}^{-2}} \cdot \sin\left(2\theta + 2\delta\right) \tag{4.33}$$

From the derivations presented above, it should be clear that the PNSC strategy can be applied to eliminate active power oscillations caused by active power flow and reactive power oscillations caused by reactive power flow. However, in case of simultaneous control of non-zero values for both average active and average reactive powers, it will not be possible to eliminate the oscillations in the active and reactive powers by using the PNSC strategy since the active power flow will result in reactive power oscillations described by (4.29) while the reactive power flow will result active power oscillations according to (4.33). To be able to achieve simultaneous control of both average active and reactive powers with elimination of either active or reactive power oscillations, an additional control objective has to be introduced.

4.3.3 Average Active-Reactive Control (AARC)

Inspecting the different terms of (4.15) and (4.16), it can be noticed that it is possible to eliminate the reactive power oscillations, $\tilde{q}_{2\omega,p}$, caused by the average active power flow by following a similar approach as described for the PNSC strategy. Considering the voltage vector trajectory in the stationary reference frame, such an approach would imply that the active current should follow a trajectory with exactly the same shape, as this would result in zero reactive power flow. Since this will allow for control of only the average active power, such an approach is labeled as Average Active-Reactive Control (AARC) in [108]-[110]. A similar approach can also be followed to eliminate active power oscillations, $\tilde{p}_{2\omega,q}$, caused by the average reactive power as will be derived in the following subsections

4.3.3.1 Current reference calculation for active power control by AARC

Considering that the objective of active power control is to eliminate the double frequency reactive power oscillations, the condition expressed by (4.34) must be fulfilled. The required negative sequence active current component can then be expressed as a function of the positive sequence active current component as given by (4.35).

$$\tilde{q}_{2\omega,p}^* = \tilde{q}_p^{*+-} + \tilde{q}_p^{*-+} = \boldsymbol{\chi}^+ \cdot \mathbf{i}_p^{*-} - \boldsymbol{\chi}^- \cdot \mathbf{i}_p^{*+} = 0 \tag{4.34}$$

$$\mathbf{i}_p^{*-} = \frac{\boldsymbol{\chi}^+ \cdot \boldsymbol{\chi}^-}{\left|\boldsymbol{\chi}^+\right|^2} \mathbf{i}_p^{*+} \tag{4.35}$$

By substituting (4.35) into the expression for the average active power flow from (4.25), and by using the vector property of (4.36), the positive sequence current reference can be derived to be given by (4.37). By substituting this result back into (4.35) and applying (4.36), the negative sequence active current reference is found according to (4.38).

$$\boldsymbol{\chi}^{-} \cdot \boldsymbol{\chi}_{\perp}^{+} = -\boldsymbol{\chi}_{\perp}^{-} \cdot \boldsymbol{\chi}^{+} \tag{4.36}$$

$$\mathbf{i}_{p}^{*+} = \frac{\overline{p}^{*}}{\left|\boldsymbol{\chi}^{+}\right|^{2} + \left|\boldsymbol{\chi}^{-}\right|^{2}} \cdot \left(-\boldsymbol{\chi}_{\perp}^{+}\right) \tag{4.37}$$

$$\mathbf{i}_{p}^{*-} = \frac{\overline{p}^{*}}{\left|\boldsymbol{\chi}^{+}\right|^{2} + \left|\boldsymbol{\chi}^{-}\right|^{2}} \cdot \boldsymbol{\chi}_{\perp}^{-} \tag{4.38}$$

The total current reference corresponding to a specified average active power reference according to the AARC strategy is then given by (4.39). Considering the approximation in equation (4.9), it can be noticed that this current reference vector will monotonously proportional to the voltage vector in steady state conditions, as explained for voltage-based AARC in [108], [109] , and also indicated in (4.39).This strategy for current reference calculation can be considered to result in an internally "resistive" or "impedance-like" distribution of the currents between the phases, although the amplitude of the current references will be determined by the power reference and will therefore increase if the grid voltage is reduced.

$$\mathbf{i}_{p,AARC}^{*} = \mathbf{i}^{*}{}_{p}^{+} + \mathbf{i}^{*}{}_{p}^{-} = \frac{\overline{p}^{*}}{\left|\boldsymbol{\chi}^{+}\right|^{2} + \left|\boldsymbol{\chi}^{-}\right|^{2}} \left(\underbrace{-\boldsymbol{\chi}_{\perp}^{+} + \boldsymbol{\chi}_{\perp}^{-}}_{\approx v} \right) \tag{4.39}$$

Since the objective when deriving this power control strategy has been to eliminate the reactive power oscillations caused by a specified average active power flow, there will be resulting oscillations in the active power as can be derived according to (4.40).

$$\tilde{p}_{2\omega,p} = \tilde{p}_{p}^{+-} + \tilde{p}_{p}^{-+} = -\boldsymbol{\chi}_{\perp}^{+} \cdot \mathbf{i}_{p}^{-} + \boldsymbol{\chi}_{\perp}^{-} \cdot \mathbf{i}_{p}^{+} = \frac{2 \cdot \overline{p}^{*} \cdot \hat{\chi}^{-} \cdot \hat{\chi}^{+}}{\hat{\chi}^{+^{2}} + \hat{\chi}^{-^{2}}} \cdot \cos\left(2\theta + 2\delta\right) \tag{4.40}$$

It can be noticed that the AARC strategy will be able to operate with equal amplitudes of positive and negative sequence Virtual Flux components. In such a case, the amplitude of the active power oscillations will be equal to the specified active power reference, and this oscillating term will be superimposed to the average active power flow that will be equal to the specified reference value. This condition will be exactly corresponding to unity power-factor operation of a single-phase system, where the instantaneous active power will oscillate between 0 and twice the average active power transfer.

4.3.3.2 Current reference calculation for reactive power control by AARC

The same line of considerations as for the active power control can also be followed for the reactive power control. Then, the objective will be to eliminate the oscillations in active power flow caused by the average reactive power reference. This criterion can be specified by (4.41), and the derivation will follow the same line as explained for the case of active power control by the AARC strategy. The resulting reactive current reference is then given by (4.42), and in this case it can be noted that the current vector will be monotonously proportional to a 90° lagging version of the voltage vector.

$$\tilde{p}^*_{2\omega,q} = \tilde{p}^{*+-}_q + \tilde{p}^{*-+}_q = -\boldsymbol{\chi}^+_\perp \cdot \mathbf{i}^{*-}_q + \boldsymbol{\chi}^-_\perp \cdot \mathbf{i}^{*+}_q = 0 \tag{4.41}$$

$$\mathbf{i}^*_{q,AARC} = \mathbf{i}^{*+}_q + \mathbf{i}^{*-}_q = \frac{\bar{q}^*}{\left|\boldsymbol{\chi}^+\right|^2 + \left|\boldsymbol{\chi}^-\right|^2} \left(\underbrace{\boldsymbol{\chi}^+ + \left(-\boldsymbol{\chi}^-\right)}_{\approx v_\perp} \right) \tag{4.42}$$

Assuming the converter currents to be equal to the reference values, the double frequency oscillations in the reactive power resulting from this control strategy can be derived according to (4.43). As for the case of active power control, the AARC strategy will be generally valid and applicable for all possible combinations of positive and negative sequence components of the grid voltage and Virtual Flux.

$$\tilde{q}_{2\omega,q} = \tilde{q}^{+-}_q + \tilde{q}^{-+}_q = \boldsymbol{\chi}^+ \cdot \mathbf{i}^-_q - \boldsymbol{\chi}^- \cdot \mathbf{i}^+_q = \frac{2 \cdot \bar{q}^* \cdot \hat{\chi}^- \cdot \hat{\chi}^+}{\hat{\chi}^{+^2} + \hat{\chi}^{-^2}} \cdot \cos\left(2\theta + 2\delta\right) \tag{4.43}$$

Considering (4.40) and (4.43) it can again be understood that elimination of active or reactive power oscillations will not be possible in case of power control by the AARC strategy and non-zero values for both the average active and reactive power references.

4.3.4 Synthesized Expression for Current Reference Calculation and Corresponding Power Flow Characteristics

Considering the active current references of the investigated power control strategies as given in (4.17), (4.28) and (4.39), it can be found that these equations have a structure that makes it possible to develop generalized expressions that include the three presented objectives and any gradual transition between them. The same is the case for expressions of the reactive current references given in (4.20), (4.32) and (4.42). By introducing two separate gain constant, k_p and k_q, that are limited in the range between -1 and 1, as weighting factors for the negative sequence component of the Virtual Flux in the different equations, the corresponding generalized expressions for the active and reactive current references are given in (4.44) and (4.45) respectively. These expressions can be established intuitively from the equations derived in the previous sections, but they can also be derived from the Virtual Flux-based power equations in a similar way as described for voltage-based control in [111]-[114].

$$\mathbf{i}^*_p = \mathbf{i}^{*+}_p + \mathbf{i}^{*-}_p = \frac{\bar{p}^*}{\left|\boldsymbol{\chi}^+\right|^2 + k_p \left|\boldsymbol{\chi}^-\right|^2} \cdot \left(-\boldsymbol{\chi}^+_\perp + k_p \boldsymbol{\chi}^-_\perp\right), \qquad -1 \le k_p \le 1 \tag{4.44}$$

$$\mathbf{i}^*_q = \mathbf{i}^{*+}_q + \mathbf{i}^{*-}_q = \frac{\bar{q}^*}{\left|\boldsymbol{\chi}^+\right|^2 + k_q \left|\boldsymbol{\chi}^-\right|^2} \cdot \left(\boldsymbol{\chi}^+ - k_q \cdot \boldsymbol{\chi}^-\right), \qquad -1 \le k_q \le 1 \tag{4.45}$$

From these expressions, it is clearly seen that selecting a gain constant k_p equal to −1 results in active power control by the PNSC strategy of (4.28). Selecting k_p equal to 0 will result in purely positive sequence current references according to the BPSC strategy of (4.17), and selecting k_p equal to 1 will result in the AARC strategy according to (4.39). The same will be the case for the gain constant k_q used to generalize the expression for the reactive current reference. For both active and reactive power control, the case corresponding to PNSC requires the positive sequence component of the Virtual Flux to be significantly larger than the negative sequence component.

The total current reference in case of non-zero reference values for both average active and reactive power is given by (4.46). The characteristics of the current reference

calculation can be selected independently for the active and reactive components by specifying the gain factors k_p and k_q to −1, 0 or 1, or any value between −1 and 1.

$$\mathbf{i}^* = \mathbf{i}_p^* + \mathbf{i}_q^* = \frac{\overline{p}^*}{\left|\boldsymbol{\chi}^+\right|^2 + k_p\left|\boldsymbol{\chi}^-\right|^2}\cdot\left(-\boldsymbol{\chi}_\perp^+ + k_p\boldsymbol{\chi}_\perp^-\right) + \frac{\overline{q}^*}{\left|\boldsymbol{\chi}^+\right|^2 + k_q\left|\boldsymbol{\chi}^-\right|^2}\cdot\left(\boldsymbol{\chi}^+ - k_q\cdot\boldsymbol{\chi}^-\right) \tag{4.46}$$
$$-1 \le k_p \le 1, \quad -1 \le k_q \le 1, \qquad \left|\boldsymbol{\chi}^+\right| \gg \left|\boldsymbol{\chi}^-\right| \text{ for } k_p, k_q = -1$$

The expressions for the active and reactive power oscillations can also be generalized according to the same approach. Assuming the resulting currents to equal the current references, the active and reactive power flow can then be expressed by (4.47) and (4.48) respectively.

$$p = \overline{p} + \tilde{p}_{2\omega,p} + \tilde{p}_{2\omega,q} = \overline{p}^* + \frac{\overline{p}^*\cdot\left(1+k_p\right)\hat{\chi}^-\cdot\hat{\chi}^+}{\hat{\chi}^{+^2} + k_p\cdot\hat{\chi}^{-^2}}\cdot\cos\left(2\theta+2\delta\right) + \frac{\overline{q}^*\cdot\left(1-k_q\right)\hat{\chi}^-\cdot\hat{\chi}^+}{\hat{\chi}^{+^2} + k_q\cdot\hat{\chi}^{-^2}}\cdot\sin\left(2\theta+2\delta\right) \tag{4.47}$$

$$q = \overline{q} + \tilde{q}_{2\omega,q} + \tilde{q}_{2\omega,p} = \overline{q}^* + \frac{\overline{q}^*\cdot\left(1+k_q\right)\hat{\chi}^-\cdot\hat{\chi}^+}{\hat{\chi}^{+^2} + k_q\cdot\hat{\chi}^{-^2}}\cdot\cos\left(2\theta+2\delta\right) - \frac{\overline{p}^*\cdot\left(1-k_p\right)\hat{\chi}^-\cdot\hat{\chi}^+}{\hat{\chi}^{+^2} + k_p\cdot\hat{\chi}^{-^2}}\cdot\sin\left(2\theta+2\delta\right) \tag{4.48}$$

From the discussions in the previous sections, it should be clear that in case of non-zero reference values for both active and reactive powers, neither the oscillations in the active power nor the oscillations in the reactive power can be eliminated as long as the same control strategy is used for both the active and the reactive power flow. However, elimination of the active power oscillations can be achieved if PNSC is used for the active power control ($k_p = -1$) while AARC is used for the reactive power control ($k_q = 1$), as can be easily verified from (4.47). In the same way, oscillations in the reactive power flow can be eliminated if AARC is used for active power control ($k_p = 1$) while PNSC is used to for the reactive power control ($k_q = -1$), as can be verified by substituting these control objectives into (4.48).

4.4 Experimental Verification of Virtual Flux-based Active and Reactive Power Control Strategies

Laboratory experiments have been carried out to investigate the on-line operation of the derived expressions for current reference calculation corresponding to the presented power control objectives. Since the DSOGI-VF estimation method from section 3.3 was used for synchronizing the converter to the grid side of the filter inductors, the experiments also serve to verify voltage-sensor-less operation of the investigated Virtual Flux-based power control strategies. It can however be noted that the investigated power control strategies also could be applied on basis of the Virtual Flux estimated at any other location, or for operation based on voltage measurements by using the simplified DSOGI-VF estimation method presented in section 3.5.1.

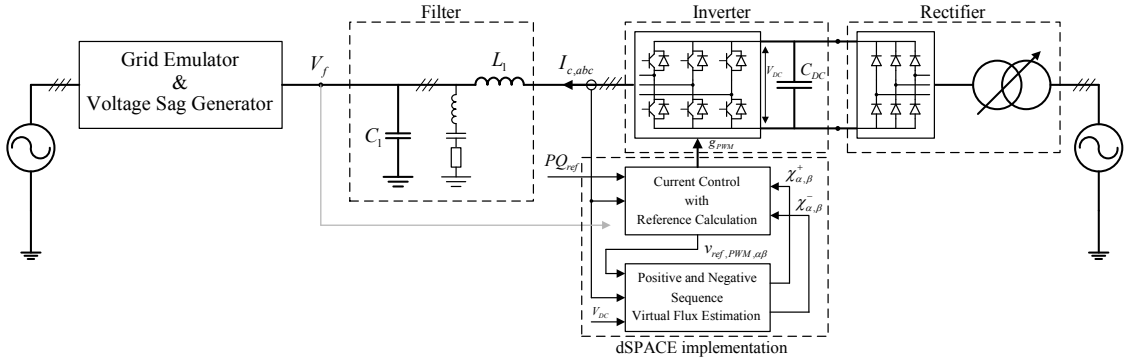

Fig. 4-2 Overview of laboratory setup

4.4.1 Experimental Configuration

The laboratory setup used for the presented experiments is outlined in Fig. 4-2, and is only slightly different from the setup described for verification of the DSOGI-VF estimation in section 3.3.3. Power to the converter DC-link was in this case supplied by a diode rectifier with an adjustable transformer, and the DC-link voltage was limited to about 300 V. An LC-filter was used on the AC-side as the interface between the converter and the grid emulator that could be configured to generate balanced and unbalanced voltage sags. The main parameters of the system are listed in Table 4-1.

A structural overview of the converter control system is outlined in Fig. 4-3. All the necessary functionality was implemented in Simulink/Matlab and operated on the dSPACE DS1103 platform used to control the converter. The block labeled "Current Reference Calculation" in the figure is basically an implementation of equation (4.46) in the stationary $\alpha\beta$ reference frame. The block labeled "Positive and Negative Sequence

Table 4-1 Details of Laboratory Setup

VSC converter module	5.5 kVA, 400 V VLT5005 Danfoss converter
Switching frequency	f_{sw} = 10 kHz
Filter inductor	L_1 = 2.46 mH ≈ 0.016 pu (Losses corresponding to R_1≈ 4Ω = 0.083 pu)
Filter capacitor	C_1 = 5 µF (Y-connected)
Trap filter	RLC-circuit tuned for 10 kHz (Y-connected)
Grid connection	Transformer-based voltage sag generator
Grid voltage (pre-fault)	V_{LL} = 110 V_{RMS} (V_b = 89.8 V)
Base power for experiments	S_b = 250 VA
Rated current for experiments	I_N = 1.3 A_{RMS} ($I_b = \hat{I}_N$ = 1.86 A)
DC-link voltage	V_{DC} = 300 V (v_{DC} ≈ 1.6 pu) - supplied by diode rectifier
Control system	Operated on the dSPACE DS1103 platform
Sampling frequency	f_{samp} = 10 kHz

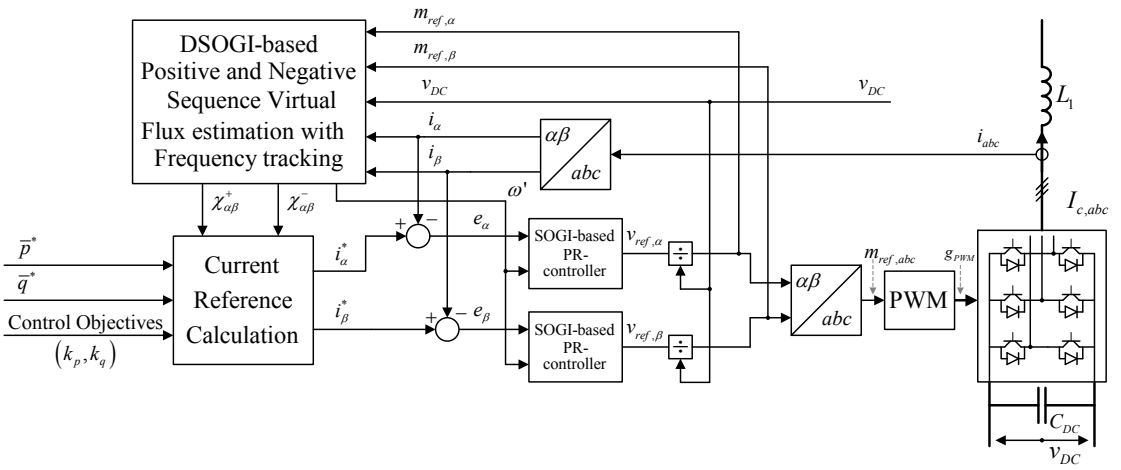

Fig. 4-3 Overview of control structure implemented in laboratory setup

Virtual Flux estimation with Frequency Tracking" is correspondingly an implementation of the DSOGI-VF estimation structure from Fig. 3-6, with the Frequency locked loop implemented as described in [195], [196]. The discrete time implementation of the PR-controllers and the SOGI-QSGs needed for the Virtual Flux estimation is described in Appendix C.

The converter operation was investigated with a voltage-sag corresponding to a single phase voltage drop of about 50 % under no-load conditions, being imposed at the grid side of the filter inductors by the voltage sag generator, and only a few of the most illustrative results will be presented and discussed in the following sections. All the data presented in the following figures was logged through the dSPACE interface for post-processing and plotting by Matlab.

4.4.2 Comments on Conditions and Limitations of Experimental Setup

The experiments were carried out in a laboratory environment with a significant background distortion in the grid voltage. As the simple Proportional-Resonant (PR-) current controllers applied in these experiments achieve a high gain only at the grid frequency, they are sensitive to the distortion in the grid voltage. Since no additional effort was made to improve the current controller performance during distorted voltage conditions, the results are therefore showing significant distortions in the current waveforms.

The influence of the grid voltage distortions on the current waveforms was also aggravated since the current controllers were operated without feed-forward of the grid voltages, as commonly applied to improve the performance in systems with grid synchronization and control based on voltage measurements. Additionally, the DC-link voltage was not available as an on-line measurement in the experimental setup, and a fixed value of 300 V was therefore used both for the Virtual Flux estimation and for calculation of the PWM signals from the voltage reference outputs of the current controllers. The margin between the AC voltage and the maximum output voltage from the converter also relatively small, since the available DC-voltage was limited to 300 V and simple sinusoidal PWM without any third harmonic injection was used. Since the maximum fundamental frequency phase voltage amplitude at the converter terminals in

this case would be about 106 V while the amplitude of the grid side phase voltages was about 90 V, only a voltage margin of about 18% was available for controlling the currents in normal operation. This was another factor reducing the performance of the current controllers, especially in case of reactive power injection from the converter resulting in voltage increase due to the inductance of the grid emulator.

The distortions in the voltages and currents are influencing the active and reactive power components calculated from measured voltages and currents, and are also challenging the performance of the applied method for Virtual Flux estimation and current reference calculation. Successful grid synchronization with accurate estimation of fundamental frequency PNS Virtual Flux components, and corresponding calculation of sinusoidal current references, can therefore be interpreted as a verification of robust performance of the proposed control approach for active and reactive power control. Therefore, the experimental results are presented with the limitations of the laboratory setup and the available equipment at the time when the experiments could be carried out. Although simulations studies of similar cases could be presented to illustrate the ideal operation, only experimental result will be discussed since they present sufficient verification the investigated power control strategies are feasible and that they can obtain the intended power flow characteristics even under non-ideal controller design and operating conditions.

4.4.3 Active Power control by the BPSC Strategy

Fig. 4-4 and Fig. 4-4 show results from a case when the active power reference is specified to be 1.0 pu and the BPSC strategy is applied to calculate the current references. The reactive power reference is set to zero. As can be seen from Fig. 4-4 (a) and (b), the three-phase currents remain balanced and in phase with the corresponding voltages when the unbalanced drop in the grid voltage occurs. The current amplitude is however increased, to maintain the average active power injected to the grid.

Fig. 4-4 (c) and (d) show that the estimated positive and negative sequence Virtual Flux components in the $\alpha\beta$-frame as expected have a fast, but well damped, response to the unbalanced voltage drop. It can however be noticed that the influence of the harmonic distortion of the currents and voltages are significantly attenuated in the Virtual Flux signals. The current references shown in Fig. 4-4 (e) are therefore sinusoidal signals, indicating that the distortions observed in the measured currents are caused by the current controllers and not by the Virtual Flux-based grid synchronization and reference current calculation.

The trajectories of the estimated Virtual Flux and the resulting currents in the stationary $\alpha\beta$ reference frame are shown in Fig. 4-5. Considering that the estimated Virtual Flux is following the same trajectory as the voltage, only delayed by 90° in time, these trajectories illustrate how the voltage and Virtual Flux trajectories becomes elliptic with the same shape and orientation during the unbalanced conditions, while the current trajectory remains circular since the control is maintaining balanced three-phase currents.

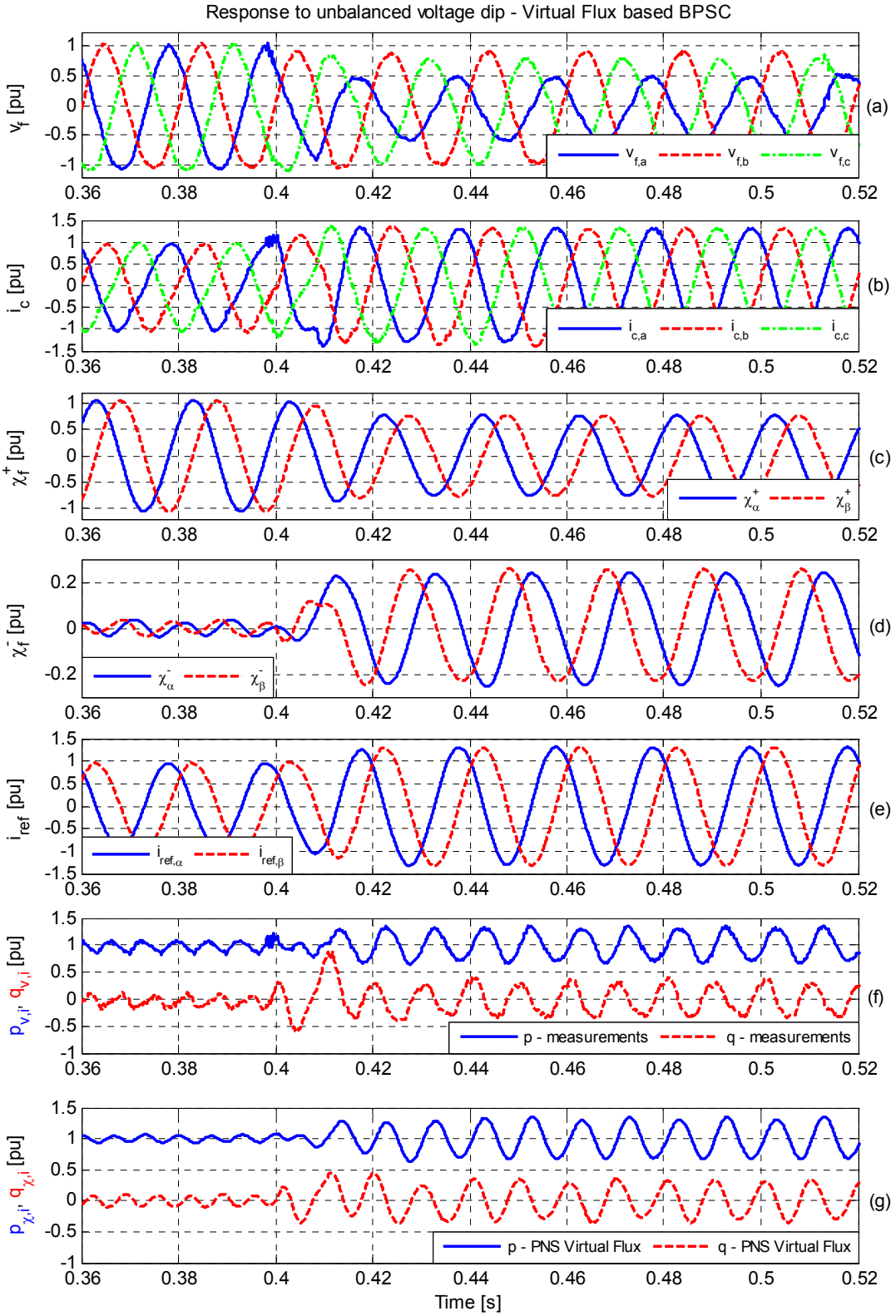

Fig. 4-4 Results from experiment with 1.0 pu active power reference and reference current calculation by BPSC (k_p = 0)

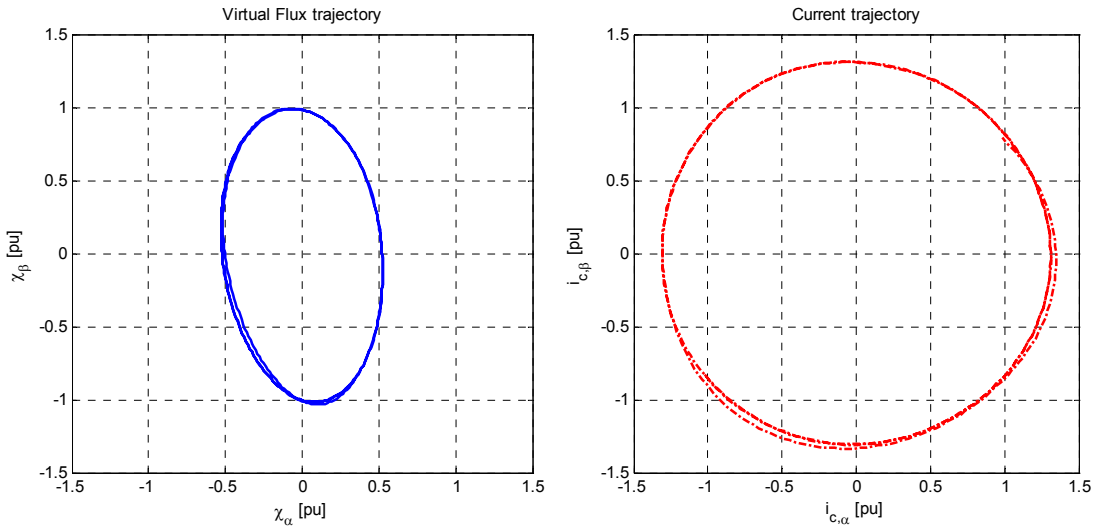

Fig. 4-5 Virtual Flux and current trajectories with active power control by BPSC

Fig. 4-4 (f) is showing the active and reactive powers calculated from measurements by using (4.1) and (4.2), and Fig. 4-4 (g) is showing the powers calculated from the sequence separated currents and Virtual Flux signals according to (4.11) and (4.12). Inspecting these power signals, it can be verified that the average power is kept constant when the unbalanced voltage dip occurs, and that second harmonic oscillations in both active and reactive power results from the unbalanced conditions.

From the plotted power signals in Fig. 4-4 (f) and (g), it can also be noticed that there is an influence from the distortion in the grid voltages and currents before the voltage dip. These distortions also influence the active and reactive power so that the second harmonic oscillations during the unbalanced conditions are not perfectly sinusoidal. The distortions have a larger influence on the active and reactive power calculated directly from the measurements than on the values calculated from sequence separated currents and the estimated positive and negative sequence Virtual Flux. This is as expected, since the sequence separation and Virtual Flux estimation have a filtering effect for frequency components above the fundamental grid frequency, as discussed in [J1] as well as in section 3.3.1.2 and 3.4.2.

The results presented in Fig. 4-4 show that the amplitude of the positive sequence Virtual Flux during the voltage sag is about 0.80 pu, and that the amplitude of the negative sequence Virtual Flux is in the range of 0.25 pu. According to (4.18) and (4.19) this should result in an amplitude of the active and reactive power oscillations around 0.31 pu, which is corresponding well with the oscillations of the powers plotted in Fig. 4-4 (f) and (g). The expected phase shift of 90° between the active and reactive power oscillations can also be easily verified from the curves in Fig. 4-4 (f) and (g).

The correspondence between the active and reactive powers calculated from measured and estimated signals, as verified by the plots in Fig. 4-4, indicate validity of the assumptions used for the presented derivations. Therefore, the active and reactive powers calculated from (4.11) and (4.12) will be shown in the following subsections to illustrate how the different specified power control objectives are achieved.

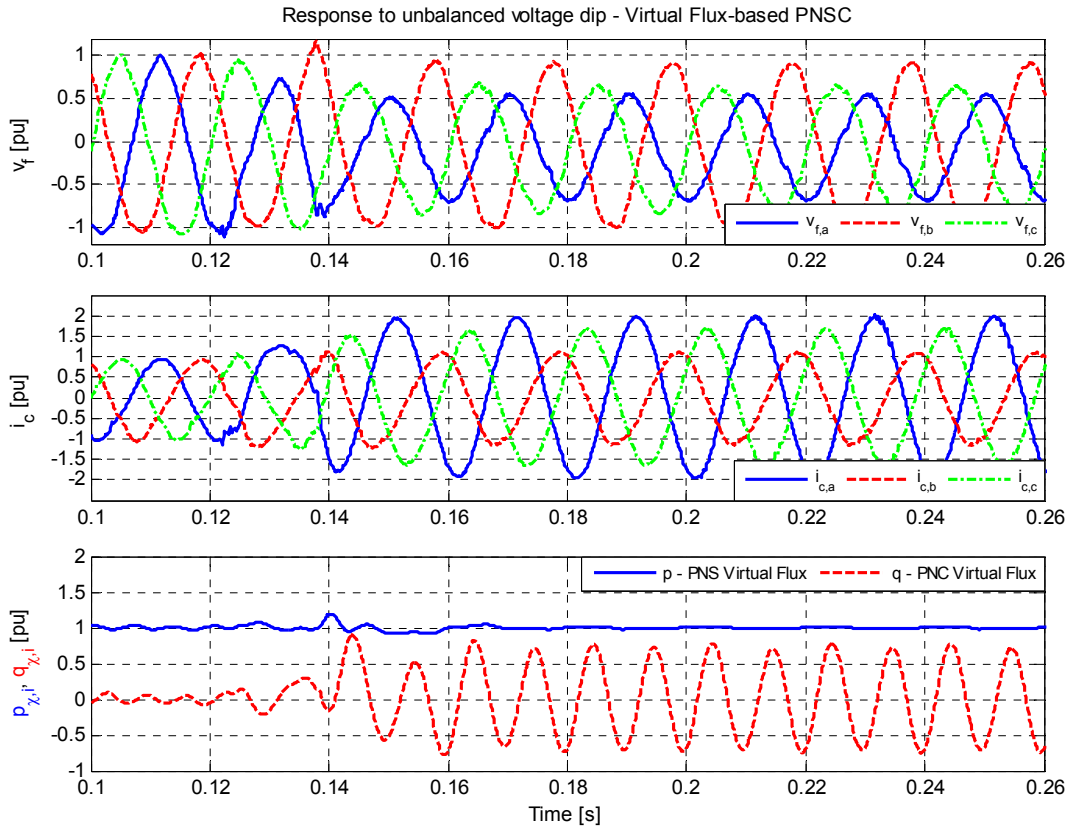

Fig. 4-6 Experimental results with $\bar{p}^*$=1.0 pu and power control by PNSC ($k_p = -1$)

4.4.4 Positive Negative Sequence Compensation (PNSC)

Fig. 4-6 shows the results from an experiment with the active power reference specified to 1.0 pu and with the current references calculated according to the PNSC strategy. The reactive power reference is set to zero .From the plots of the voltages and current in Fig. 4-6, it can be seen that the currents are increased in the phases with reduced voltage, to maintain the active power flow constant during the unbalanced conditions. The characteristics of the current with respect to the voltage or the Virtual Flux are however more clearly illustrated by the trajectories shown in Fig. 4-7 showing that the current trajectory is elliptic with an orientation that is perpendicular to the Virtual Flux trajectory.

As for the case of BPSC, the transient response to the unbalanced voltage sag is fast and well damped. Comparing the curves in Fig. 4-4 (a) with the voltages plotted in Fig. 4-6, it can however be noticed that there is an influence of the unbalanced current injection of the PNSC strategy, due to the significant grid impedance of the voltage sag generator. The same influence can be observed from the Virtual Flux trajectories in Fig. 4-7 and Fig. 4-5, showing that the PNSC results in an orientation closer to the axis of phase *b*.

The active and reactive powers calculated from the estimated Virtual Flux and the measured currents are shown at the bottom of Fig. 4-6, verifying that the active power flow is kept constant during the unbalanced conditions while there are double frequency oscillations in the reactive power flow. Although not plotted in Fig. 4-6, the amplitude

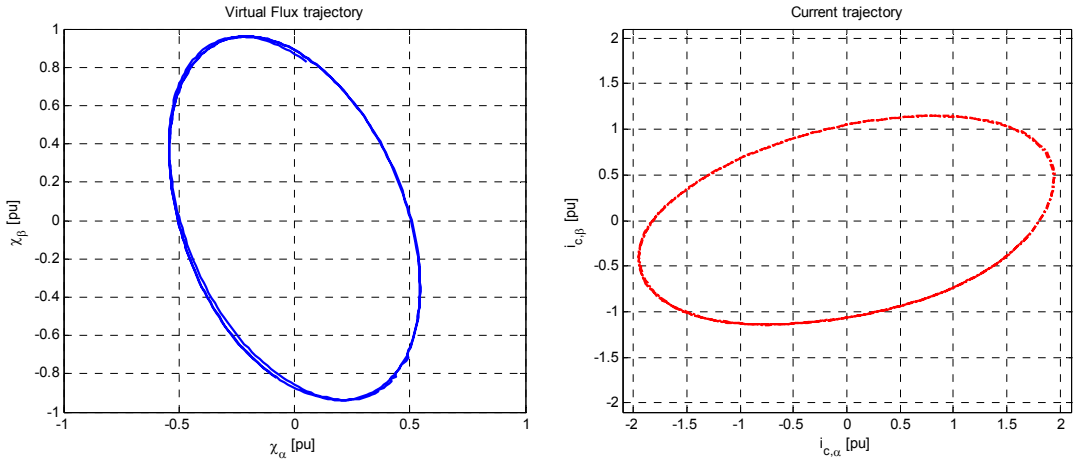

Fig. 4-7 Virtual Flux and current trajectories with active power control by PNSC

of the positive sequence Virtual Flux during the unbalanced conditions is in this case about 0.75 pu, while the amplitude of the negative sequence Virtual Flux is about 0.25 pu. According to (4.29), this should result in an amplitude of the reactive power oscillations of about 0.75 pu, corresponding well with the results plotted in Fig. 4-6.

4.4.5 Average-Active Reactive Control (AARC)

Results from experiments with active power control by the AARC strategy are shown in Fig. 4-8, with the active power reference specified to 1.0 pu, and with zero reactive power reference. Studying the measured voltages and currents, it can be seen that currents are in phase with the voltages, and that current amplitude distribution among the phases is proportional to the voltage. The trajectories of Fig. 4-9 are verifying this by showing that the current trajectory has the same orientation as the voltage and Virtual Flux trajectories. This is as expected from the control objective of eliminating reactive power oscillations and according to the explanation in section 4.3.3. From the lowest plot in Fig. 4-7, it can also be observed that the there are only negligible oscillations in the reactive power flow during the unbalanced conditions, while there are significant oscillations in the active power flow.

It can be noticed that there is a significant distortion in the currents in this case, and this is reflected in the active and reactive power flow. However, the current is equally or more distorted during the balanced conditions before the voltage sag than during the unbalanced conditions. The reactive power oscillations that can be observed during the unbalanced conditions are therefore in the same range or smaller than the reactive power oscillations that can be observed during the balanced three-phase conditions. There are also corresponding oscillations in the active power during the balanced conditions, and some influence on the waveform and amplitude of the double frequency power oscillations during the unbalanced conditions. However, considering only fundamental frequency components, it is clear that the objective of eliminating reactive power oscillations is achieved.

In this experiment, the amplitude of the positive sequence Virtual Flux during the unbalanced condition was about 0.75 pu, while the amplitude of the negative sequence component was about 0.25 pu. According to (4.40), this should result in an amplitude of the active power oscillations of 0.60 pu, which is corresponding well to the results shown in Fig. 4-7.

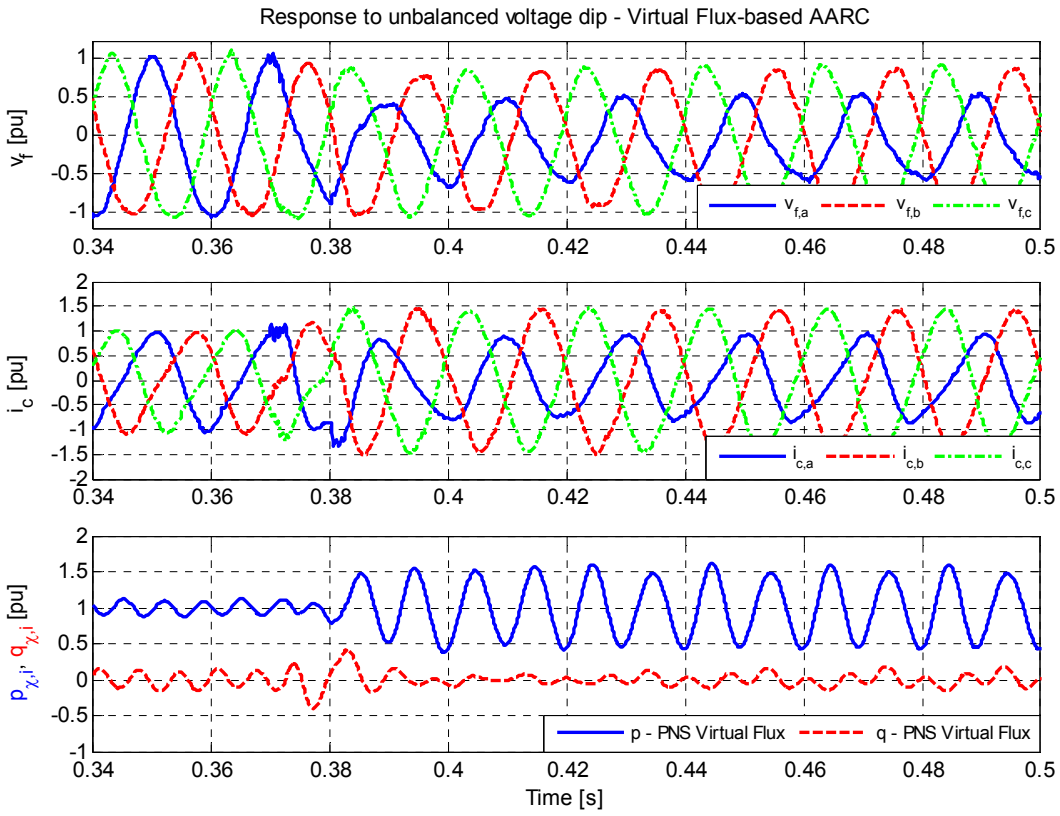

Fig. 4-8 Experimental results with $\bar{p}^* = 1.0$ pu and power control by AARC ($k_p = 1$)

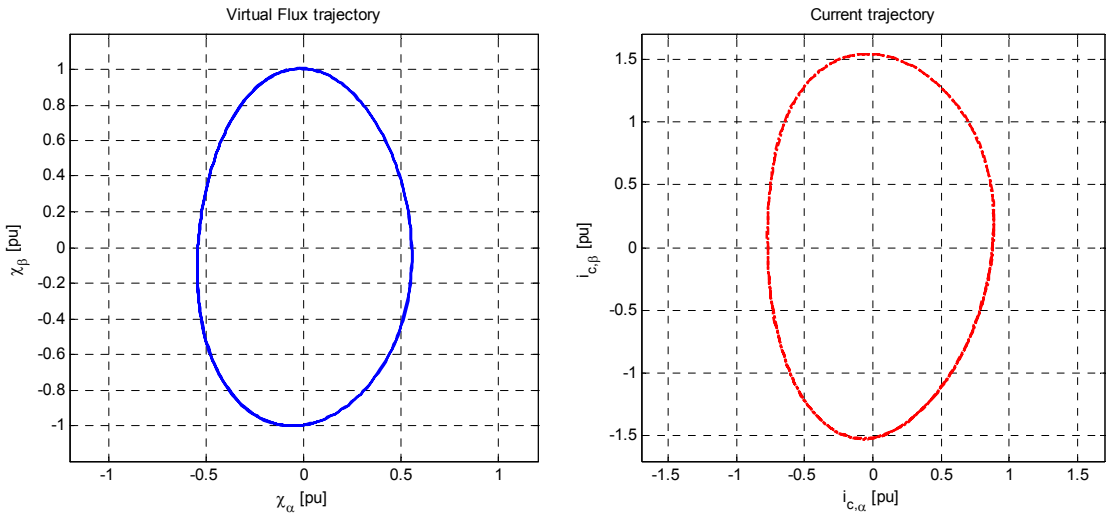

Fig. 4-9 Virtual Flux and current trajectories with active power control by AARC

4.4.6 Reactive Power Control by the Same Range of Control Objectives

The same series of experiments as presented for active power control by BPSC, PNSC and AARC in the previous subsections have also been carried out for control of pure reactive power. However, these results are only verifying that the same control

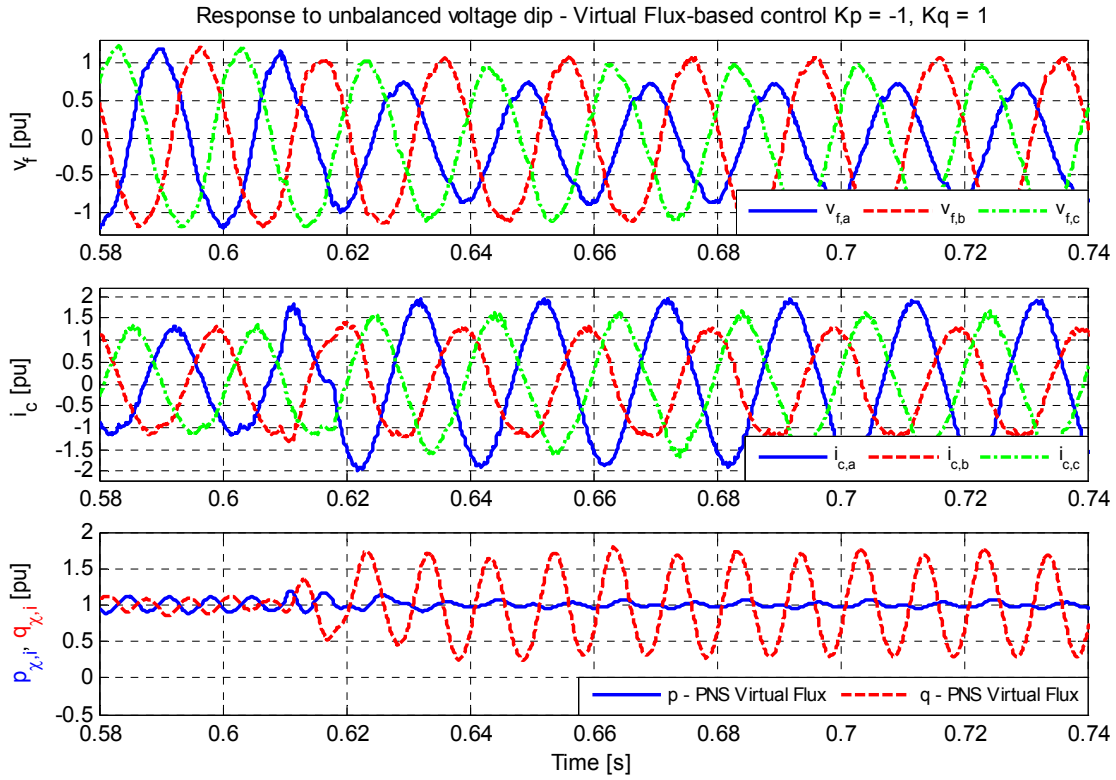

Fig. 4-10 Experimental results with $\bar{p}^* = 1.0$ pu and $\bar{q}^* = 1.0$ pu, with active current reference calculation by PNSC ($k_p = -1$) and reactive current reference calculation by AARC ($k_q = 1$) for elimination of active power oscillations

objectives as can be achieved by Virtual Flux-based voltage-sensor-less operation for both active and reactive power control and will not be presented or discussed in further details. Two examples showing the ability to achieve elimination of either active or reactive power oscillations with simultaneous control of both active and reactive power flow will however be presented in the following subsections.

4.4.7 Elimination of Active Power Oscillations with Simultaneous Control of Active and Reactive Power

Fig. 4-10 shows experimental results obtained when both the active and reactive power references specified to 1.0 pu for injection of equal amounts of active and reactive power into the grid. In this case the power control objectives have been specified to achieve elimination of active power oscillations during unbalanced conditions, by calculating the active current references according to the PNSC strategy ($k_p = -1$) while the reactive current references are calculated according to the AARC strategy ($k_q = 1$).

Studying the measured voltages and currents shown in Fig. 4-10, it can be seen how the highest current is injected in the phase with the lowest voltage, and since the reactive power reference has a non-zero value, the currents are phase-shifted with respect to the voltages. Studying the trajectories in Fig. 4-11, it can however be noticed that the orientation of the current trajectory is perpendicular to the orientation of the Virtual Flux or voltage trajectories. This is as expected, since the active current

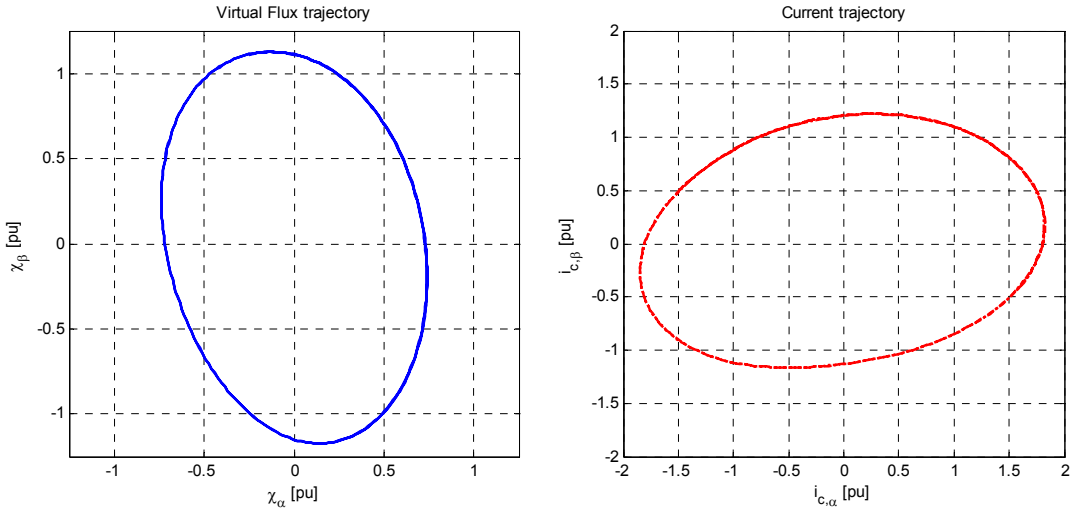

Fig. 4-11 Virtual Flux and current trajectories with active and reactive power control for elimination of active power oscillations

component controlled by the PNSC strategy should follow a trajectory perpendicularly oriented with respect to the voltage, while the reactive current component should follow a trajectory aligned with the in-quadrature voltage vector $\mathbf{v}_{\perp}$ given by (4.10). The active and reactive current components are therefore following exactly the same trajectory, although the reactive current component is 90° phase shifted in time. The total current amplitude will therefore be given by the square sum of the active and reactive components.

The active and reactive powers calculated from the estimated Virtual Flux and the positive and negative sequence currents are shown in the lower plot of Fig. 4-10, and it can be clearly seen that the objective of eliminating active power oscillations during unbalanced conditions is achieved. As expected, there are however significant reactive power.

From the voltages plotted in Fig. 4-10, it can also be noticed that the voltage is increased above 1.0 pu during the balanced pre-fault conditions, due to the reactive power injection and the inductance of the voltage sag generator. Also during the unbalanced conditions, the 1.0 pu average reactive power injection is increasing the voltage at the filter capacitors, where the converter is synchronized to the grid. The amplitude of the estimated positive sequence Virtual Flux is therefore about 1.0 pu during the fault, while the negative sequence Virtual Flux component is about 0.22 pu. According to (4.29), the amplitude of the reactive power oscillations due to the active power control should then be about 0.46 pu, while the reactive power oscillations due to the reactive power control should be about 0.42 pu according to (4.43). Since these two components are phase shifted by 90°, the total amplitude should be given by the square sum, resulting in reactive power oscillations with amplitude of about 0.62 pu. This result is corresponding well with the reactive power oscillations that can be observed in Fig. 4-10. Both the ability of simultaneous active and reactive voltage-sensor-less control and the validity of the expressions derived in the first parts of this chapter are therefore verified by the experimental results.

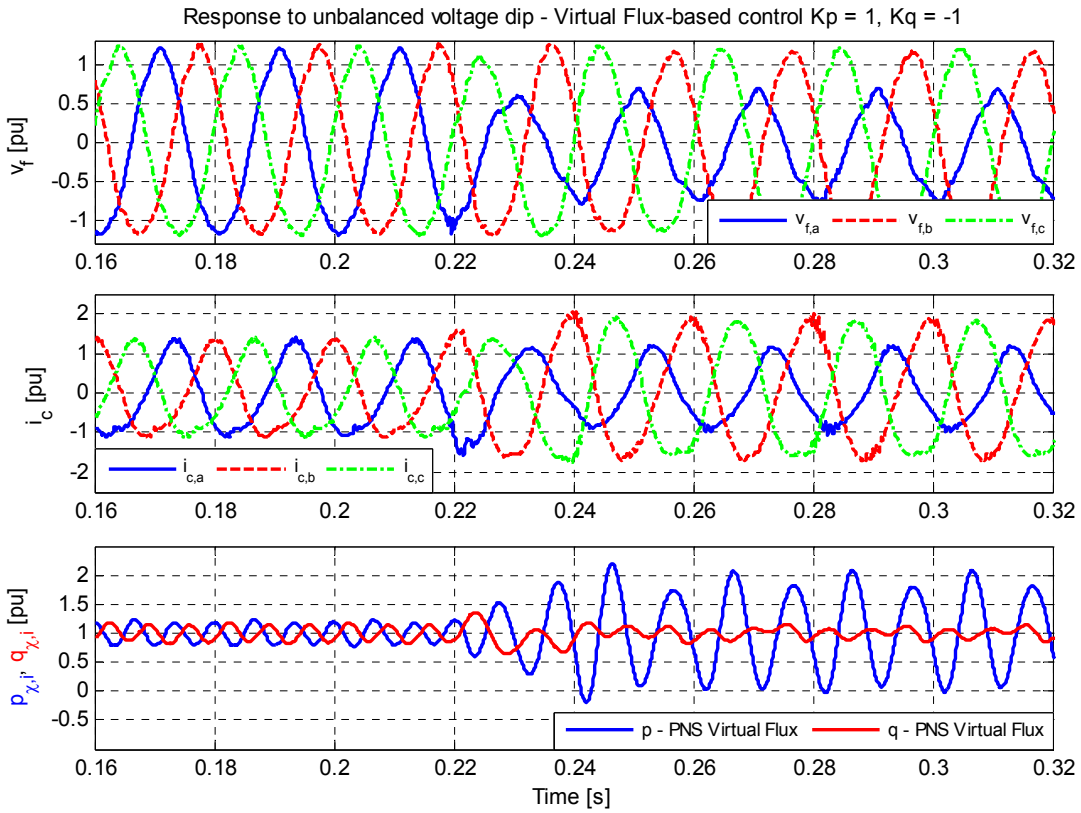

Fig. 4-12 Experimental results with $\bar{p}^* = 1.0$ pu and $\bar{q}^* = 1.0$ pu, with active current reference calculation by AARC ($k_p = 1$) and reactive current reference calculation by PNSC ($k_q = -1$) for elimination of reactive power oscillations

4.4.8 Elimination of Reactive Power Oscillations with Simultaneous Control of Active and Reactive power

A last example of different combinations of control objectives for control of active and reactive powers is shown in Fig. 4-12. In this case, the active and reactive power references are still specified kept equal to 1.0, while the current references are calculated to eliminate second harmonic oscillations in the reactive power during unbalanced condones. The results plotted in Fig. 4-12 show how the currents have the same distribution among the phases as the voltages, although they are phase shifted due to the reactive power injection to the grid. The trajectories plotted in Fig. 4-13 also verify how the current trajectory has the same orientation as the Virtual Flux or voltage trajectories. The active and reactive powers plotted in Fig. 4-12 therefore shows that the objective of eliminating reactive power oscillations is achieved during the unbalanced conditions.

It can be noted that the distortions in the current waveforms are significant in this case, and that this is influencing the active and reactive power flow both during the balanced and unbalanced conditions. The response to the occurrence of the voltage sag is however fast and well damped, and the overall control objectives are achieved as expected with respect to the fundamental frequency components and the power flow characteristics.

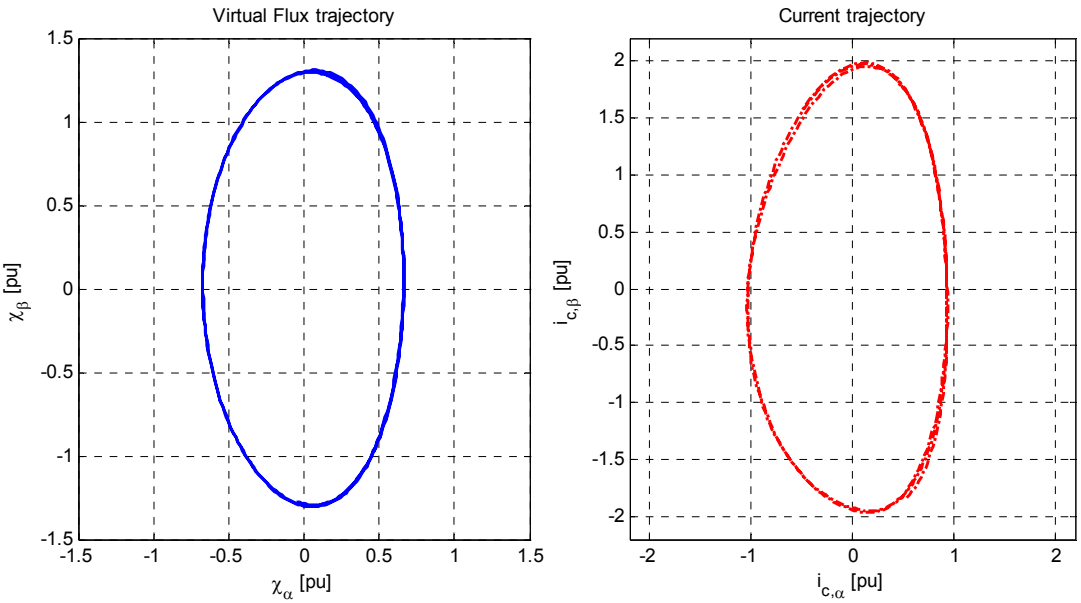

Fig. 4-13 Virtual Flux and current trajectories with active and reactive power control for elimination of reactive power oscillations

Due to the reactive power injection, the amplitude of the positive sequence Virtual Flux components in this case maintained at about 1.0 pu during the unbalanced conditions, while the negative sequence Virtual Flux component is about 0.35 pu. According to (4.40), the active power oscillations caused by the active power control by the AARC strategy should then be about 0.62 pu, while the active power oscillations due to the reactive power control by the PNSC strategy should be about 0.80 pu according to (4.33). Since these two oscillating power components are phase shifted by 90°, the total amplitude of the active power oscillations should be given by the square sum, which equals about 1.0 pu. This is corresponding well with the results plotted in Fig. 4-12, although the amplitude of the oscillations has some variations due to the distortions of the voltages and currents.

4.5 Further Application Examples of the Developed Strategies for Virtual Flux-based Active and Reactive Power Control

As shown by the experimental results presented in the previous section, the developed strategies for Virtual Flux-based current reference calculation can be successfully used to achieve voltage-sensor-less control of active and reactive power flow at the grid side of the filter inductor. Thus, voltage-sensor-less operation with the same power flow characteristics and similar performance as achieved with conventional methods for grid synchronization and power control based on voltage measurements at the grid side of the filter inductor can be achieved for any relevant application. This can for instance be used for voltage-sensor-less operation of wind turbine converters, three-phase photovoltaic systems, general purpose industrial loads and motor drives with active rectifiers, energy storage systems, and could also be applied for VSC-based HVDC transmission systems. In some of these applications, the voltage-sensor-less operation

could be most relevant as an additional option to improve reliability in case of failure of the voltage sensors, while the Virtual Flux estimation could be based on voltage measurements in normal operation.

It should also be emphasized that the investigated power control strategies in combination with the DSOGI-VF estimation could be applied in combination with any kind of current controllers. Considerations regarding current controller performance and stability as well as challenges related to low switching frequencies and digital implementation issues will then be the same as for conventional, voltage-based, control systems. Additionally, it should be noted that the derived expressions for the active and reactive power oscillations during unbalanced conditions can be used as power references in control structures based on Direct Power Control (DPC) to achieve the same range of power control objectives as discussed in this chapter.

The developed expressions for current reference calculation corresponding to the different power control objectives are also generally valid at the point in the grid where the PNS Virtual Flux components are estimated. Thus, the DSOGI-VF estimation can be used to change the point of synchronization to the grid, and by that the point where the active and reactive power flow characteristics is controlled. A few general examples of how this flexibility can be utilized will be presented in the following subsections.

4.5.1 Reduction of DC-link Voltage Oscillations during Unbalanced Conditions by Utilizing Virtual Flux Estimation at the Converter Terminals

As mentioned in section 3.5.1, it can be a relevant option to synchronize the control system to the Virtual Flux estimated at the terminals of the converter, as labelled "Converter Flux Oriented Control" in [156], [201]. This approach was also shown to have a positive influence on the performance of the particular current control strategy applied in [156]. The approach of synchronizing to the converter terminals will however have further relevant implications in the case of control under unbalanced grid voltage conditions.

One of the major objectives in many publications related to operation of VSCs during unbalanced conditions is to limit voltage oscillations in DC-link of the converter by eliminating second harmonic oscillations in the active power flow as discussed in [34], [31], [89], [98], [206], [207], [221]. For zero average reactive power reference, this corresponds to active power control by the PNSC strategy. Elimination of power oscillations at the grid side of the filter inductor, usually labelled as "Input-Power-Control" (IPC), will however reduce but not entirely eliminate the DC-link voltage oscillations, since the unbalanced currents flowing in the filter inductance will cause active power oscillations that will be reflected in the DC-link voltage of the converter. Therefore, a simple method for current reference calculation with the objective of compensating for the influence of the filter inductors by that achieving elimination of DC-link voltage oscillations during unbalanced conditions have been proposed [222]. This approach is usually labelled as "Output-Power-Control" (OPC). More advanced methods have also been proposed with the purpose of controlling the active power flow to be constant at the terminals of the converters while at the same time achieving zero or controllable average reactive power flow at the grid side of the filter inductor and by that unity displacement power factor at the point of connection to the grid [31], [99], [223]. Such methods are usually labelled as Input-Output-Power-Control (IOPC).

Iterative methods for achieving current references that causes elimination of double frequency active power oscillations at the converter terminals have also been recently proposed [224].

For Virtual Flux-based operation, the Output-Power-Control (OPC) strategy mentioned above is corresponding to the case of active power control by PNSC with zero as reference for the average reactive power and with Virtual Flux estimation at the grid side of the filter inductor as described and illustrated by experimental results in section 4.4.4.

By utilizing the possibility to estimate the Virtual Flux at the converter terminals, Virtual Flux-based Input-Power-Control (IPC) can also be easily achieved in a simpler way than for voltage-based grid synchronization and power control. The Virtual Flux at the converter terminals is as mentioned easily estimated by specifying the resistance r_1 and the inductance l_1 to be zero, and the elimination of the double frequency active power oscillations is then easily achieved by using the PNSC strategy. A set of experimental results illustrating such a case is shown in Fig. 4-14.

Among the results plotted in the figure, Fig. 4-14 (a) and (b) are showing the three-phase voltages and currents measured at the grid side of the filter inductor, while Fig. 4-14 (c) is showing the active and reactive powers calculated from these signals. The PNS Virtual Flux signals used for the current reference calculation are however estimated at the grid side of the filter inductor, and the active and reactive powers calculated from these signals and the PNS current components are shown in Fig. 4-14 (d). From the curves in Fig. 4-14 (d), it can be clearly seen that a constant value of 1.0 pu active power at the converter terminals is achieved in steady state conditions for both balanced and unbalanced operation. The average reactive power flow is also kept at the reference value of 0, although the expected double frequency oscillations are occuring under the unbalanced conditions.

Studying Fig. 4-14 (c), it can be seen that the active power flow at the grid side of the filter inductor is slightly below the 1.0 pu at the converter terminals, due to the losses in the filter inductor. Similarly, it can be seen that a negative reactive power is flowing, since the reactive power consumption of the filter inductor must be covered from the grid side when the converter is controlling zero reactive power flow. When the unbalanced voltage sag occurs, the differenced between the average active and reactive powers at the converter side and at the grid side is increased, since the current is increased to keep the average active power at its reference value. During the unbalanced conditions, a small double frequency oscillation can also be observed in the active power flow at the grid side of the filter inductor, as expected due to the unbalanced currents required to eliminate double frequency active power oscillations at the converter terminals.

The results from Fig. 4-14 verify how the objective of Output-Power-Control during unbalanced conditions can be easily achieved by DSOGI-VF-based voltage-sensor-less control. The same characteristics could also be achieved for simultaneous control of active and reactive power at the converter terminals by using the AARC strategy corresponding to $k_q = 1$ for the calculation of the reactive current reference. Input-Output-Power-Control could also be achieved by Virtual Flux-based voltage-sensor-less control by simultaneously estimating the PNS Virtual Flux signals at the converter terminals and at the grid side of the filter inductor by using the extended DSOGI-VF

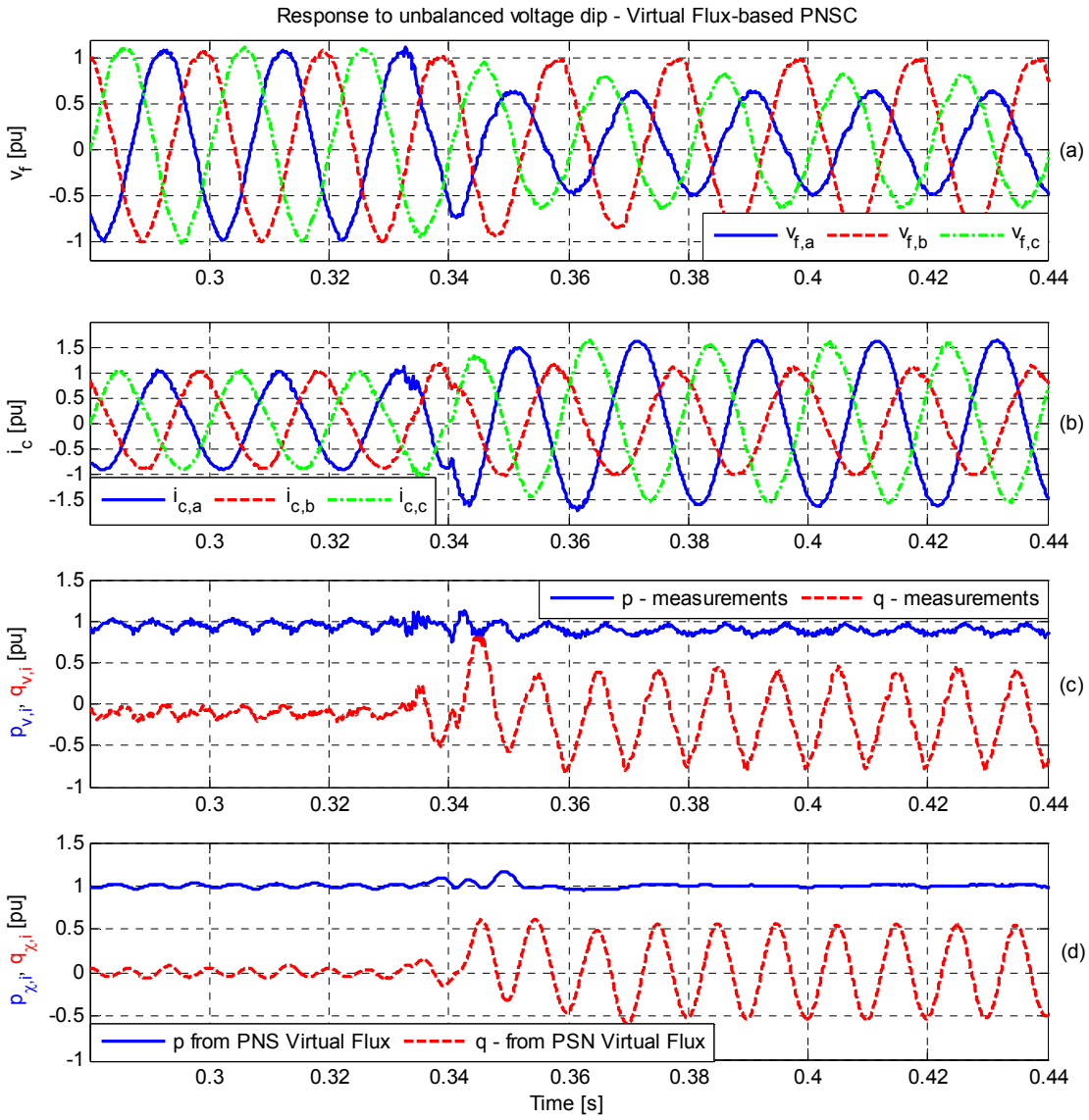

Fig. 4-14 Experimental results with $\overline{p}^* = 1.0$ pu, Virtual Flux estimation at the converter terminals and active current reference calculation by PNSC ($k_p = 1$) for elimination of active power oscillations

estimation method shown in Fig. 3-16. This approach is however not further investigated in this setting.

It is however important to note that strategies for eliminating double frequency oscillations in the active power flow can only be applied for limited degree of grid voltage unbalance. This can be seen from the equations for current reference calculation in (4.28), since an amplitude of the negative sequence Virtual Flux component that is approaching the amplitude of the positive sequence component will cause the current amplitude to increase towards infinity. Strategies for limiting the current references will therefore be necessary to protect the converter during severe unbalanced conditions, as will be discussed in the next chapter.

4.5.2 Control of Active and Reactive Power at a Remote Location

As indicated in section 3.5, the DSOGI-VF estimation approach can also be used as a basis for estimating the Virtual Flux at different points in the grid. The simplicity of such an approach will depend on the grid configuration, and on the possible presence and parameters of an LCL filter for connection to the grid. The challenges and possible approaches for Virtual Flux estimation on the grid side of a filter capacitor are discussed on a general basis in section 2.2.5, and the challenges with respect to extension of the DSOGI-VF estimation method are mentioned in section 3.5.3. However, if the current in the filter capacitor is considered negligible, the Virtual Flux can be easily estimated at any location in a radial grid structure. The Virtual Flux at a remote point can also be estimated if the grid side impedance as seen from the converter can be represented by a Thevenin equivalent, but this can make it more difficult to relate the estimated Virtual Flux to a physical point in the grid structure.

The possibility to estimate the Virtual Flux, and by that the possibility to control the active and reactive power flow, at a remote location in the grid can be useful for several different applications. This can for instance be explained by starting from the simple radial structure shown in Fig. 2-1, which can be representative for several different configurations where a converter is connected to the grid through a transformer. Such a structure will for instance be representative for low voltage wind turbine converters or industrial loads connected to a medium or high voltage distribution system. In such cases, requirements for unity power factor operation or for reactive power control is usually specified on the high voltage side of the transformer, while voltage measurements for grid synchronization and control are usually located on the low voltage side of the transformer and physically close to the converter unit. By estimating the Virtual Flux as a basis for controlling the active and reactive power at such a remote point, the operational requirements can be easily fulfilled without any secondary estimation loops.

In theory, the Virtual Flux can actually be estimated at any point in the grid, as long as the parameters needed for the estimation are known. By such an approach, it can also be considered that effect of parameter deviations is that the Virtual Flux is estimated at an inaccurate location in the grid. As analyzed in [173] the effect of such deviations from the more traditional point of view will be a deviation in the reactive power flow at the point where the converter was intended to be synchronized to the grid. If the inner control loops, usually the current controller loop, are performing satisfactorily, this will however not cause any problems for the stability or operation of the converter, except for the secondary effect that the reactive power control target is not accurately achieved. There might also be small deviations in the active power flow, but this can usually be assumed to be compensated by an outer loop DC-link voltage or power flow controller.

The detailed investigation of practical applications and possible ways of utilizing the possibility to control the active and reactive power at a remote point is left as an interesting issue of future research. However, a simple example is provided to illustrate the operation when the resistance and inductance of the Virtual Flux estimation is specified to be larger than the values of the filter inductor. In the presented case, the resistance is specified to be about 0.10 pu, while the inductance is specified to be about 0.05 pu, intended to represent an additional inductance of about 5 mH, and the results are shown in Fig. 4-15. The active and reactive power references are specified to be both 1.0 pu, and the control objective, specified by selecting $k_p = -1$ and $k_q = 1$, is to

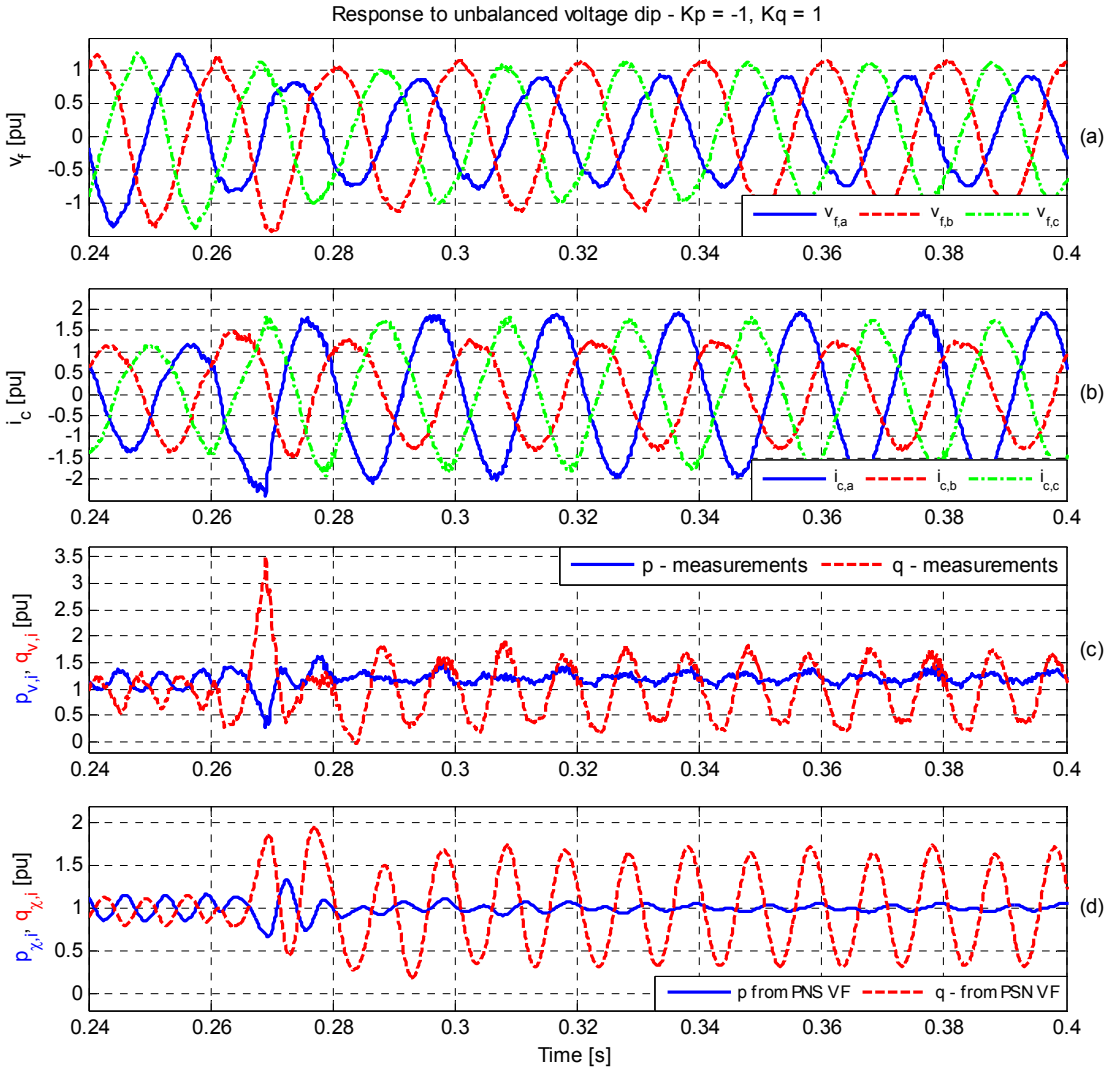

Fig. 4-15 Experimental results illustrating generic operation with Virtual Flux estimation at a remote point with $\bar{p}^* = 1.0$ pu, $\bar{q}^* = 1.0$ pu and operation for elimination of double frequency oscillations in active power flow ($k_p = -1$, $k_q = 1$)

eliminate double frequency active power oscillations at the point of synchronization to the grid. As can be seen from the results, the converter do not show any additional degradation of operation with respect to the previously presented cases, although there is a significant transient due to the operation of the voltage sag generator that results in a sudden peak of reactive power flow. The active power flow calculated from the voltage measurements at the grid side of the filter inductor show as small deviation from the reference value, since the Virtual Flux used to calculate the current references is estimated at a point that is "closer" to the equivalent voltage source of the grid. The active and reactive powers calculated from the PNS Virtual Flux and current components are however following the references, and it can be seen that the converter is able to eliminate the double frequency power oscillations at the remote point.

The results shown in Fig. 4-15 should only be considered as a generic example showing that it is possible to estimate the Virtual Flux and by that to control the active

and reactive power flow as well as the power flow characteristics at any point in a simple, radial grid structure. Since the parameters of the experimental setup were not accurately known, and at the same time more load-dependant than what can be expected from a system operating at a higher power level, the presented results will not be further analyzed. The concept of synchronization and power control oriented at a remote point can however be easily demonstrated by simulation studies.

It is also interesting to note that the possibility of synchronizing to a remote point can be utilized for influencing the operating characteristics or the loadability or stability limits of a converter. A preliminary investigation of such issues was presented in publication [C2] listed in the introduction, although the investigation was based on a different approach for PNS Virtual Flux estimation than the DSOGI-VF estimation method. The results presented in [C2] showed that the loadability of the converter in a weak grid condition with a high grid inductance could be maximized by selecting the parameters of the Virtual Flux estimation so that the converter was synchronized to the mid-point of the equivalent impedance representing the weak power line. When operated with zero reactive power reference at the point of synchronization to the grid, this condition corresponds to the case where the converter will be automatically supplying half the reactive power consumption of the line. As well known from simplified, traditional, stability considerations of electric power systems, this condition corresponds to the maximum power transfer capability of an inductive line, and this was also verified by the results presented in [C2]. It could also be noted that an approach based on utilizing the Virtual Flux estimation and the point of synchronization to the grid for making the converter to cover the reactive power consumption of an inductive line will have a fast response without any significant additional dynamics than what have been analyzed for the previously presented results. Traditional methods for reactive power control with the purpose of stability enhancement and for increasing the power transfer capability in high-impedance grids will on the other hand depend on outer loops providing reference values for the current reference calculation and/or current controllers, and will therefore have slower dynamical response. Investigation of Virtual Flux-based control with the point of synchronization to the grid selected for influencing the reactive power flow and the stability characteristics of the converter in high-impedance grids can therefore be an interesting issue for further studies related to power system integration of VSCs.

4.6 General Considerations Regarding Virtual Flux-based Power Control Strategies under Unbalanced Conditions

The experimental results presented in the main part of this chapter have been selected to illustrate only a limited range of control objectives and combinations of active and reactive power references. However, the Virtual Flux based current references derived in section 4.3 and synthesized into (4.46) will be valid for any combinations of active and reactive power references and control objectives. It can also be noted that the transient response of the current reference calculation is fast and well damped, due to the DSOGI-VF estimation that achieves voltage-sensor-less Virtual Flux estimation and sequence separation with a response time in the range of 5 ms. This time response is the same as for conventional sequence separation methods based on voltage measurements, and therefore the presented strategies for voltage-sensor-less operation do not imply any

additional delays as usually associated with control strategies based on estimation methods. The derived expressions for current reference calculation based on PNS Virtual Flux estimated by the DSOGI-VF estimation method are also generally valid in the sense that they can be easily adapted for and investigated together with other types of current controllers, to improve the performance under operation with distorted grid voltages.

It should further be noted that the presented results indicate that the presented approach for deriving Virtual Flux-based voltage sensor-less power control strategies based on the DSOGI-VF estimation is generally valid. This implies that any other strategies for power flow control during unbalanced conditions could be easily adapted to Virtual Flux-based control systems, both with or without available voltage measurements. For instance, current references for injecting pure negative sequence active or reactive power, or any combination of positive and negative sequence active and reactive power flows, as discussed in [96], can be easily derived by starting from (4.15) and (4.16). It is also worth noting that the DSOGI-VF estimation is able to estimate the PNS Virtual Flux even in case of single-phase faults with zero remaining voltage, and will therefore not impose any limitation to the operating conditions or power control objectives. Thus, control strategies designed for operation during severe single-phase faults, and strategies for limiting the converter current during such conditions as will be discussed in the next chapter, can also be easily adapted for Virtual Flux based implementation following the approach presented in this chapter.

4.7 Summary of Chapter

This chapter has presented a basis for power calculations by using positive and negative sequence Virtual Flux components during unbalanced conditions, which can be used for design of Virtual Flux-based voltage-sensor-less power control strategies. From these equations, expressions for calculating current references corresponding to different objectives of active and reactive power control have been derived. The presented investigation has been limited to three different control objectives; operation with balanced positive sequence currents, elimination of double frequency oscillations in active power flow, and elimination of double frequency oscillations in reactive power flow. The derived current references corresponding to these three control objectives for control of active and reactive power have been generalized into one simple equation where two scalar coefficients in the range between −1 and 1 can be used to select the active and reactive power flow characteristics. Expressions for the active and reactive power oscillations resulting from the different power control strategies have also been derived, and generalized to correspond to the generalized expressions for current reference calculation.

The operation of the investigated power control strategies has been verified by laboratory experiments with a small-scale converter setup, where the DSOGI-VF estimation method presented in the previous chapter was used for grid synchronization by voltage-sensor-less estimation of the positive and negative sequence components of the Virtual Flux. The results show that the derived expressions for current reference calculation, and the corresponding expressions for active and reactive power oscillations, are generally valid, and that the overall objectives of the different power

control strategies can be achieved even under the influence of significant harmonic distortions in the grid voltages and currents. The presented approach for design of Virtual Flux-based power control strategies during unbalanced conditions can therefore be a suitable basis for further investigations with respect to various power control strategies during unbalanced conditions, and for investigation in combinations with other strategies for current control and operation of a Voltage Source Converter.

It has also been shown how the different investigated power control strategies can be applied when the Virtual Flux is estimated at different points in the AC grid. This can for instance be utilized to achieve simple strategies for elimination of DC-link voltage oscillations of VSCs during unbalanced operation. The same approach can also be utilized to control the active and reactive power flow at a remote point in a radial grid. This possibility can for instance be utilized to operate with approximately unity power factor at the high voltage side of transformers where on-line voltage measurements are not easily available to the converter control system. This approach can also be used to fulfill operational requirements in for instance a wind farm, and there are indications that such an approach can be used to increase the range of stable operation of the converter. Virtual Flux-based grid synchronization and power control at different points in AC grids can therefore be a relevant issue for further studies and investigations.

Main contributions of Chapter:

- Presentation of a general approach for deriving Virtual Flux-based strategies for active and reactive power control during unbalanced conditions.
- Derivation, analysis, generalization and verification of expressions for current reference calculation corresponding to different strategies for active and reactive power control during unbalanced conditions.

5 Virtual Flux-based Power Control Strategies Operating under Current Limitation

This chapter will discuss methods for current limitation of the power control strategies presented in the previous chapter, to protect the converter from over-currents during transient and unbalanced conditions. First, the theoretical limit to utilization of the converters current capacity during severe unbalanced conditions will be discussed, and it will be shown that an approach based on limiting the phase currents can allow for better utilization of the converter than the traditional approach of limiting the peak amplitude of the current vector. Accurate expressions for calculating current references that will maintain the power control characteristics of the strategies discussed in the previous chapter while limiting the phase currents of the converter will then be derived and analyzed. The maximum current vector amplitude that can be allowed during unbalanced conditions without exceeding the phase current limitation will be shown to depend on the magnitudes and the phase angles of the positive and negative sequence components of the grid voltage or Virtual Flux. The operation of power control strategies with phase current limitation will be illustrated by simulation results for analyzing the converter operation and power flow characteristics in case of single-phase faults with zero remaining voltage.

The strategies for power control with phase current limitation developed in the first part of this chapter result in nonlinear equations where the current reference will be a function of the phase angle between the positive and negative sequence Virtual Flux components. Additionally, these strategies will not result in significant differences from the more traditional approach of limiting the current vector amplitude when the negative sequence component of the grid voltage or Virtual Flux is small. It will therefore be shown how the developed strategies for phase current limitation can be simplified to generally valid expressions for current vector amplitude limitation while still maintaining the power control objectives descried in the previous chapter. Experimental results will be presented as verification and illustration of these simple strategies for current vector amplitude limitation. This simplified approach for current limitation has also been published and documented by simulations in manuscript [J2].

Considerations regarding current limitation in case of simultaneous control of both active and reactive power will be presented at the end of the chapter.

5.1 Introduction to Current Limitation Strategies for Voltage Source Converters under Unbalanced Conditions

To operate a VSC safely in case of grid faults, while achieving the intended dynamic and steady-state performance, strategies for limiting the converter currents must be implemented as part of the control system. This current limitation can be implemented in several ways, either included as a simple limitation of the references to the current controllers, or it can be considered as a part of the power control strategies used to calculate the current references. Current limitation strategies acting directly on the instantaneous phase currents will however lead to distorted currents and voltages as shown in [225]. Therefore, current limitation is often implemented by limiting the current references in the synchronous reference frame, as applied for instance in [226].

For current limitation strategies intended for protection of the converter in case of unbalanced grid faults, it can however be important to maintain the active and/or reactive power flow characteristics according to the objectives discussed in the previous chapter, even if the average active or reactive power flow has to be limited. In [227], this issue is addressed when considering a wind turbine where the objective of the control system is to eliminate double frequency power oscillations during unbalanced conditions while keeping the current vector amplitude within the current limit of the converter. The current limitation is in this case obtained indirectly, by limiting the power injected to the DC-link from the generator side below a power limit calculated from the converter current limit and the grid voltage sequence components. A different approach is applied in [228]-[230], where the current limitation is introduced directly in the calculation of current reference values when considering the power control objective of eliminating power oscillations during unbalanced conditions. In [231] and [232], active and reactive current limitations of a wind turbine converter are instead imposed on the output of the active and reactive power control mechanisms, with the reactive current component given priority according to the depth of the voltage drop and the requirements specified in grid codes. Active and reactive power references resulting from the grid voltage and the limited current references are then calculated, before the reference values to the current controllers are re-calculated by using instantaneous power theory according to [214]-[216]. All these studies are however specifying the current references and the current limitations in the Positive and Negative Sequence (PNS) Synchronous Reference Frames (SRFs) or in a combination of PNS SRFs and the stationary reference frame.

In case of power control strategies resulting in elliptic current trajectories during unbalanced conditions, it can however be possible to further increase the utilization of the converters current capability. This requires that the individual phase currents resulting from the applied power control strategy are considered. Power control during unbalanced conditions by current reference calculation in the stationary *abc* reference frame was discussed already in [233] and [234], but in these cases limitation of the phase current amplitudes was only considered for operation with balanced three-phase currents.

The first study that presented detailed investigations of strategies for limiting the phase currents of a converter during unbalanced grid voltage conditions was presented in [115], considering the current reference calculation a STATCOM when operating with different objectives for reactive power control. In this case, the calculation of the current references were formulated in the stationary $\alpha\beta$ reference frame, and based on

reactive power control strategies discussed in [110], three objectives for reactive power injection under phase current limitation were considered; elimination of double frequency reactive power oscillations, injection of balanced positive sequence three-phase currents, and elimination of double frequency active power oscillations during unbalanced conditions. The maximum reactive power that could be injected within the phase current limitation of the STATCOM was then calculated according to the power control objective, the positive and negative sequence grid voltage components and the phase angle of the grid fault, and used as the power reference for the reactive power control strategies discussed in [108], [110].

Although the strategies for current limitation discussed in [115] resulted in maximum utilization of the phase current rating of the converter, they were only presented for three distinct cases of reactive power control. This chapter will instead attempt to derive a general approach for Virtual Flux-based active and reactive power control with current limitation by starting from the generalized current references from (4.44) and (4.45). The expressions that will be derived can however easily be reformulated to voltage-based implementation of power control strategies with current limitation.

5.2 Considerations Regarding Current Vector Amplitude Limitation versus Phase Current Limitation

The physical current limitation of a Voltage Source Converter will always be given by the current capability of the bridge-legs corresponding to each of the phases. When discussing different strategies for power control with current limitation, it is therefore useful to consider the projections of the phase current limitations in the stationary $\alpha\beta$ reference frame as shown in Fig. 5-1. As can be seen from the figure, the phase current limitations form a hexagon in the stationary $\alpha\beta$ reference frame, given by the intersections between the straight lines corresponding to the limitations of the different phases. A strategy for current limitation implemented in a synchronous reference frame or based on vector amplitude considerations in the stationary reference frame will however correspond to a circle as given by the blue dashed lines in the figure. This circle will correspond to the trajectory of balanced three-phase currents with amplitude equal to the phase current limitation.

If the current trajectory during unbalanced conditions should follow an elliptic trajectory, it can however be seen from Fig. 5-1 that the maximum current vector amplitude that can be allowed without exceeding the phase current limitations will depend on the shape and orientation of the trajectory. This is illustrated with 4 different current trajectories shown in the figure. Considering trajectory 1, which is a narrow ellipse aligned with phase *a*, it can be understood that the maximum current vector amplitude will be equal to the maximum phase current, and independent of the shape of the trajectory, if the current trajectory is aligned along the axis of any of the phases. In such cases, the result of the traditional current vector amplitude limitation will be identical to the result of any strategy for limiting the phase current amplitude. The current trajectories numbered as 2, 3 and 4 in Fig. 5-1 are however aligned in middle between the axis of phase *a* and phase *c*, and in this case, the trajectories show that a vector amplitude larger than the phase current limit can be allowed without any of the phase currents exceeding their limits It can be seen that the maximum current vector amplitude can be increased more when the current trajectory becomes narrower, and

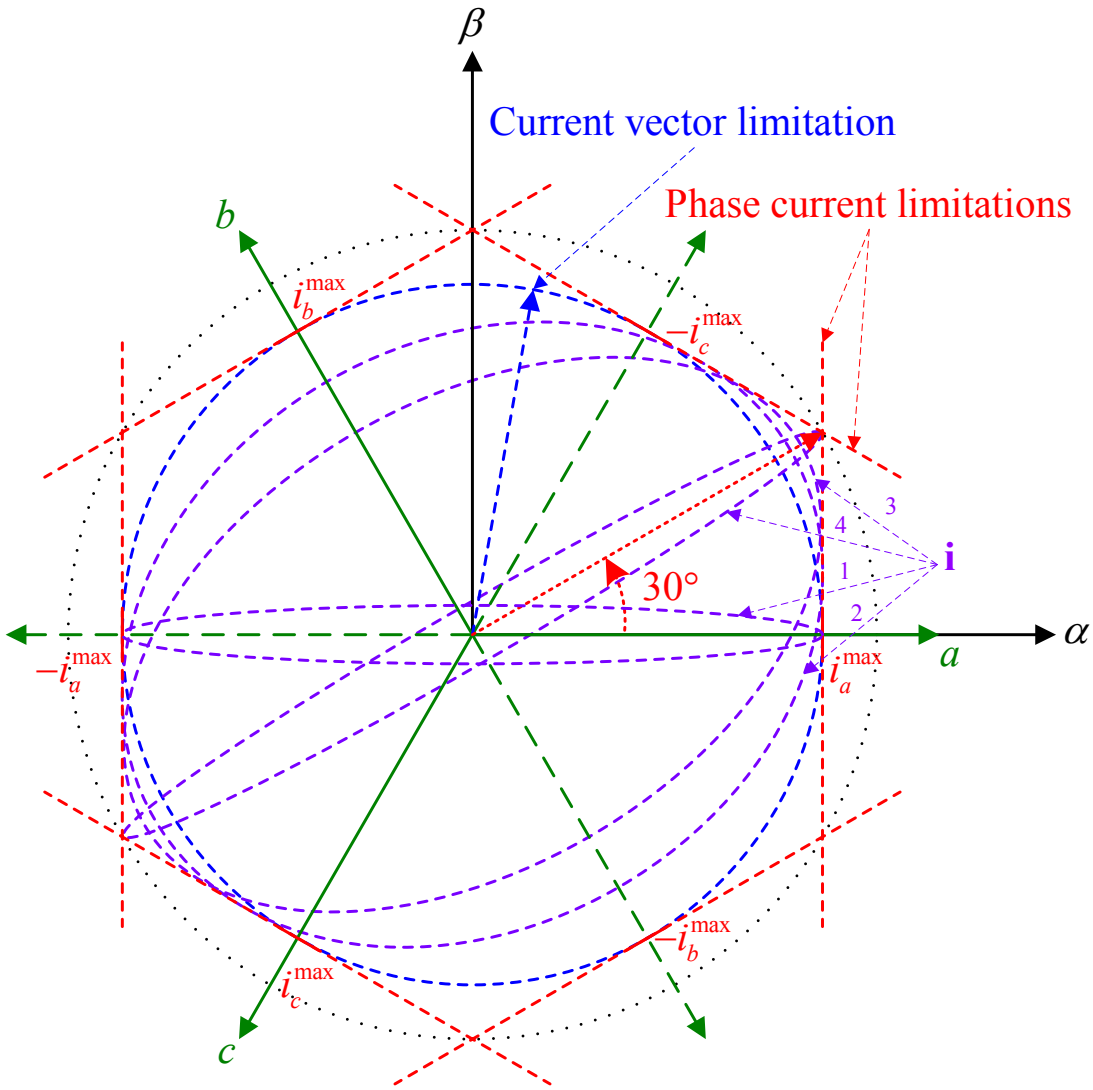

Fig. 5-1. Illustration of the difference between phase current limitation and current vector amplitude limitation

that the maximum current vector amplitude is reached when the trajectory is collapsed into a straight line. With the alignment shown in Fig. 5-1, the maximum current vector amplitude can therefore be reached if the current in the *b*-axis is zero, corresponding to "single-phase" operation with current flowing only between phase *a* and *c*.

From geometrical considerations in Fig. 5-1, the maximum current vector amplitude that can be achieved in the case of "single-phase" operation with the current trajectory aligned in the middle between any of the phases can be found according to (5.1).

$$\left|\hat{\mathbf{i}}_{\max}\right| = \frac{i_{ph,\lim}}{\cos(30°)} = i_{ph,\lim} \cdot \frac{2}{\sqrt{3}} \approx 1.155 \cdot i_{ph,\lim} \tag{5.1}$$

The consequence of equation (5.1) is that the current vector amplitude can be increased about 15 % above the phase current limitations in cases when the current trajectory is collapsed to a straight line with an orientation given by an odd multiple of 30°. Depending on the applied power control strategy, this can also potentially increase the maximum active or power transfer during single-phase fault conditions with 15 %.

The orientation and shape of the current trajectory during unbalance conditions will however depend on the amplitude of and the phase angle between the PNS components of the Virtual Flux or voltage at the point of synchronization to the grid, and on the applied power control strategy used to calculate the current references. As shown by Fig. 5-1, the advantage of applying a strategy for limiting the phase currents instead of limiting the current vector amplitude can therefore vary between 0 and 15 % depending on the fault conditions and the power control objectives.

In the following subsections, generalized strategies for phase current limitation as well as a simplified approach for current vector amplitude limitation will be derived and analyzed. Strategies for limiting the active and reactive current components will be considered separately, as they can be applied independently to the active and reactive power control strategies. Considerations regarding current limitation in case of simultaneous control of active and reactive power flow will be discussed separately at the end of the chapter, since this discussion will be common for the cases of phase current limitation as well as for vector current amplitude limitation.

5.3 Power Control Strategies under Phase Current Limitation

The investigation of strategies for phase current limitation will be based on the generalized expressions for active and reactive power control by current reference calculation according to (4.44) and (4.45). To maintain general validity, the following derivations will assume that the control parameters k_p and k_q can take any values between −1 and 1, although the integer values corresponding to the distinct power control strategies described in the previous chapter will be of main importance.

5.3.1 Active Power Control with Limitation of the Active Current Component

From the derivations and results presented in chapter 4, it is clear that the active current trajectory will have different orientation depending on the applied control objective. In case of power control with reduction of the active power oscillations, the current trajectory will be perpendicular to the Virtual Flux or voltage trajectories, while the current trajectory will have the same alignment as the Virtual Flux or voltage trajectories if the objective of the power control is to reduce or eliminate the reactive power oscillations. The different orientations of the current trajectories will imply that the maximum phase current will appear in different phases, and the active current limitation must therefore be investigated for two different cases.

5.3.1.1 Phase current limitation with reduction of active power oscillations

Considering case with unbalanced grid voltages when the objective of the active power control strategy is to reduce the second harmonic oscillations in the active power flow, the gain constant k_p in (4.44) will be specified to a value between −1 and 0. The current vector trajectory will then be oriented perpendicularly with respect to the Virtual Flux trajectory as shown in Fig. 5-2. From the figure, it can be clearly seen that the maximum phase current in this case will occur in phase b as long as the orientation angle δ of the Virtual Flux trajectory is in the range between 0° and 60°.

The active current component in phase b can then be found by first calculating the α- and β- current references resulting from (4.44), and then using the inverse Clark-

transform to express the *b*-phase current. By differentiating, solving for the phase angle when the peak value occurs, and then substituting the result back into the expression for the *b*-phase current, a general expression for the maximum *b*-phase current be found as shown in (5.2). This expression for the maximum phase current is a function of the power reference, the power control objective k_p, the amplitudes of the positive and negative sequence Virtual Flux components and the orientation of the Virtual Flux trajectory. The conventions used for expressing signals in the stationary *αβ* and *abc* are shown in Appendix D.3, while the detailed derivations of the expression in (5.2) are shown in Appendix D.5.

$$\hat{i}_{p,b}^{*} = \frac{P^{*}}{\hat{\chi}^{+^2} + k_p \cdot \hat{\chi}^{-^2}} \cdot \sqrt{\hat{\chi}^{+^2} - k_p \cdot \hat{\chi}^{+} \cdot \hat{\chi}^{-} \left(\cos(2\delta) + \sqrt{3}\sin(2\delta)\right) + \left(k_p \cdot \hat{\chi}^{-}\right)^2} \qquad (5.2)$$

$$0 \le \delta \le \frac{\pi}{3}, \qquad -1 \le k_p \le 0$$

For safe operation during unbalanced conditions, the maximum current in phase *b* should be limited below the phase current limitation, $i_{ph,lim}$, of the converter. By imposing this condition to (5.2), the maximum average active power transfer can be expressed as a function of the applied power control objective and the current grid conditions as given by (5.3).

$$\left|\overline{p}_{\max}^{*}\right| = \frac{i_{ph,\lim} \cdot \left(\hat{\chi}^{+^2} + k_p \cdot \hat{\chi}^{-^2}\right)}{\sqrt{\hat{\chi}^{+^2} - k_p \cdot \hat{\chi}^{+} \cdot \hat{\chi}^{-} \left(\cos(2\delta) + \sqrt{3}\sin(2\delta)\right) + \left(k_p \cdot \hat{\chi}^{-}\right)^2}}, \quad 0 \le \delta \le \frac{\pi}{3}, \quad -1 \le k_p \le 0 \qquad (5.3)$$

Introducing the maximum power from (5.3) into the equation for active current reference calculation, and expressing all Virtual Flux variables on vector form, results in (5.4), which can be used current reference calculation when operating under phase current limitation. It should however be noted that (5.4) will only be valid as long as the gain factor k_p used to specify the active power control objective is within the range from −1 to 0.

$$\mathbf{i}_{p,\lim}^{*} = \mathbf{i}_{p}^{*+} + \mathbf{i}_{p}^{*-} = \frac{i_{ph,\lim} \cdot \mathrm{Sign}\left(\overline{p}^{*}\right)}{\sqrt{\left|\boldsymbol{\chi}^{+}\right|^2 - k_p \cdot \left|\boldsymbol{\chi}^{+}\right| \cdot \left|\boldsymbol{\chi}^{-}\right| \cdot \left(\cos(2\delta) + \sqrt{3}\sin(2\delta)\right) + k_p^2 \cdot \left|\boldsymbol{\chi}^{-}\right|^2}} \cdot \left(-\boldsymbol{\chi}_{\perp}^{+} + k_p \boldsymbol{\chi}_{\perp}^{-}\right), \qquad (5.4)$$

$$0 \le \delta \le \frac{\pi}{3}, \qquad -1 \le k_p \le 0$$

Since the derivation of the expressions presented above was based on a case where the maximum phase current would occur in phase *b*, their direct validity for limiting the maximum phase current of the converter is limited to cases where the orientation angle δ of the Virtual Flux trajectory is within the range from 0° to 60°. For values of δ outside this range, it can be easily seen from Fig. 5-2 that the maximum phase current will occur in phase *c* if δ is in the range between 0° and −60°, and in phase *a* if δ is between 60° and 120° in the positive or negative direction. However, since the orientation of the *abc* axis are symmetrical in the stationary *αβ* reference frame, the derived expressions are easily made valid by shifting the value of δ with a multiple 60° to keep it within the specified range. Further elaboration of this issue is presented in Appendix D.5.

For on-line implementation of current reference calculation with phase current limitation according to (5.4), it will be necessary to detect the value of the fault angle δ

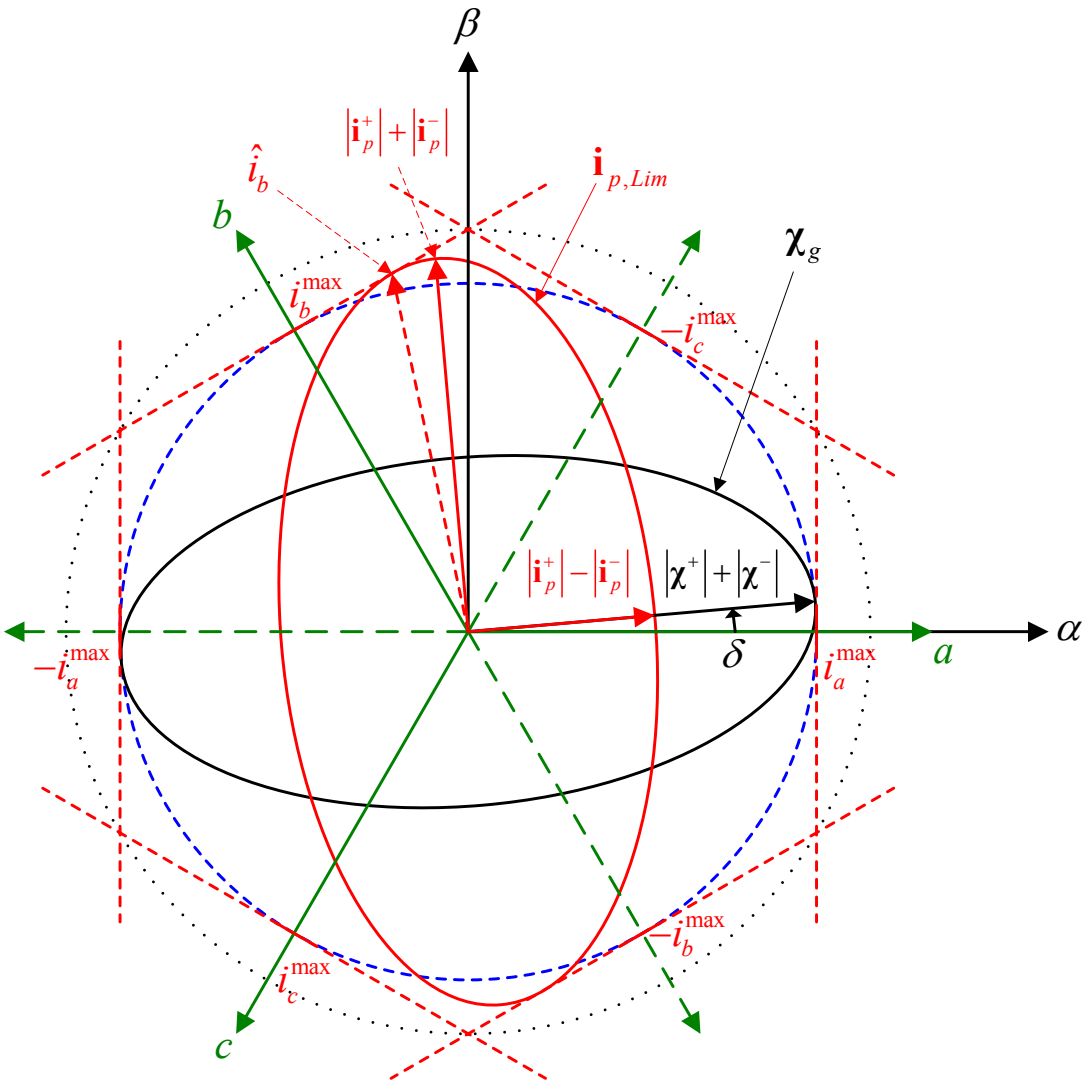

Fig. 5-2. Virtual Flux and current trajectories in the case of power control with elimination of double frequency active power oscillations

from the estimated positive and negative sequence Virtual Flux signals. A simple method to achieve this detection is however presented in Appendix D.2.3.

It should also be noted that the case of balanced three-phase currents is included in the presented equations by specifying $k_p = 0$. In such a case, the derived expressions will be simplified, since the maximum current will equal for all phases. The maximum average power that can be transferred in this case will be equal to the product of the maximum allowable phase current and the amplitude of the positive sequence Virtual Flux component. The resulting current vector reference will then have constant amplitude equal to the phase current limitation, and will be controlled to be in phase with the positive sequence voltage component at the point of synchronization to the grid.

The maximum amplitude of the active current vector that can be allowed within the phase current limitation is corresponding to the peak value of (5.4) as given by (5.5).

$$\left|\hat{\mathbf{i}}_{p,\lim}^{*}\right| = \frac{i_{ph,\lim}\cdot\left(\left|\boldsymbol{\chi}^+\right|+\left|k_p\right|\cdot\left|\boldsymbol{\chi}^-\right|\right)}{\sqrt{\left|\boldsymbol{\chi}^+\right|^2 - k_p\cdot\left|\boldsymbol{\chi}^+\right|\cdot\left|\boldsymbol{\chi}^-\right|\cdot\left(\cos(2\delta)+\sqrt{3}\sin(2\delta)\right)+k_p^2\cdot\left|\boldsymbol{\chi}^-\right|^2}}, \quad 0\le\delta\le\frac{\pi}{3}, \quad -1\le k_p\le 0 \qquad (5.5)$$

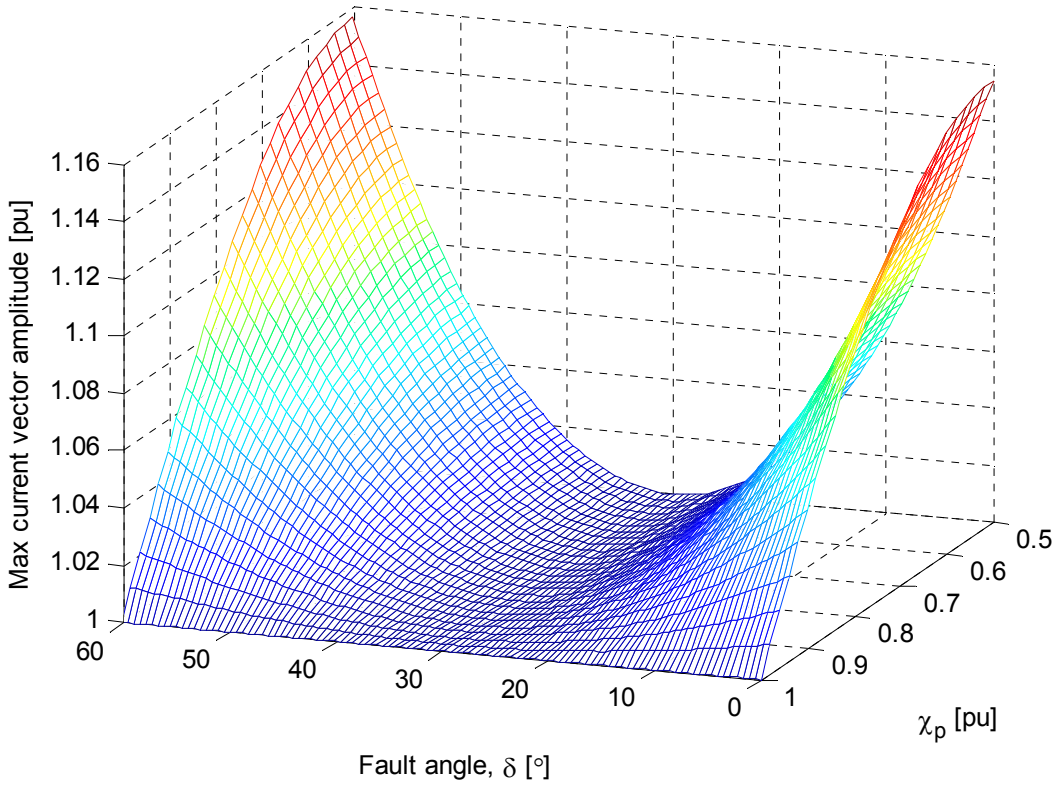

Fig. 5-3. Profile of maximum current vector amplitude as function of the fault angle and the level of unbalance

The result of this equation is plotted in Fig. 5-3 as a function of the fault angle δ and the amplitude of the positive sequence Virtual Flux component for the case when $k_p = -1$. For the plot, it is assumed that phase current limitation is equal to 1.0 pu and that the peak vector amplitude of the Virtual Flux is always equal to 1.0 pu, so that $|\boldsymbol{\chi}^-| = 1-|\boldsymbol{\chi}^+|$. The results are plotted for $|\boldsymbol{\chi}^+|$ within the range of 1 to 0.5 pu, which corresponds to the range between balanced three-phase conditions and a single phase fault to zero, where both the positive and negative sequence components of the grid voltage are equal to 0.5 pu.

As expected, it can be seen from the figure, that the maximum allowable vector amplitude is equal to the phase current limitation in case of balanced three-phase conditions. In case of increasing negative sequence components, the influence of the fault angle δ becomes stronger, but the maximum allowable current vector amplitude will always be equal to the phase current limitation for the case of δ= 30°. From Fig. 5-2, it can be seen that this is because the current vector amplitude in this case will correspond to the amplitude of the current in phase *b*. The same will therefore be the case of δ equal to any odd multiples of 30°. The maximum allowable current vector amplitude occurs for the case when δ = 0°, 60° or any multiples of 60°, and will be a function of the amplitudes of the positive and negative sequence Virtual Flux components. This is corresponding to the explanation in section 5.2, and it can be seen from Fig. 5-3 that the maximum current vector amplitude given by (5.1) will occur only in cases where $|\boldsymbol{\chi}^+| = |\boldsymbol{\chi}^-|$ and δ is equal to 0° or any multiple of 60°.

It should also be noted that it can be seen from (5.3), that the average power transfer will be zero in case of $k_p = -1$ and $|\chi^+| = |\chi^-|$. This corresponds well to the results from the previous chapter, where it was pointed out that the PNSC strategy can not be used in such cases, since it would require infinite amplitudes of the injected currents. However, operation according to the objective of the PNSC strategy, corresponding to elimination of double frequency active power oscillations, is possible when the presented current limitation strategy is applied, but on the cost of zero average active power transfer. By a simple analogy, this is as expected since it is not possible to transfer power in a single phase system without having double frequency oscillations in the instantaneous power flow. The current trajectory corresponding to operation with current limited PNSC in case of $|\chi^+| = |\chi^-|$ will be a straight line perpendicular to the voltage or Virtual Flux trajectories, and the maximum allowable current will therefore be injected in an orientation with zero remaining voltage. This can be desirable if the main control objective is to avoid active power oscillations, and at the same time allow the converter to contribute with short circuit current to the faulty phase. However, if a degree of active power transfer should be maintained during severe unbalanced conditions, another control strategy has to be applied.

5.3.1.2 Phase current limitation with reduction of reactive power oscillations

If the objective for active power control during unbalanced conditions is to reduce the reactive power oscillations caused by the active power flow, the gain constant k_p in (4.44) have to be specified within the range from 0 to 1. The current vector trajectory will then have the same orientation as the voltage or Virtual Flux trajectories, as shown by the example in Fig. 5-4 . From the figure, it can be seen that the maximum phase current will occur in phase *a* for a fault angle δ within the range from −30° to 30°. By following the same approach as described in the previous subsection, and shown in more detail in Appendix D.5.2, an expression for the maximum current in phase *a* as given by (5.6) can then be derived.

$$\hat{i}^*_{p,a} = \frac{P^*}{\hat{\chi}^{+^2} + k_p \cdot \hat{\chi}^{-^2}} \cdot \sqrt{\hat{\chi}^{+^2} + 2 + k_p \cdot \hat{\chi}^+ \cdot \hat{\chi}^- \cos(2\delta) + k_p^2 \cdot \hat{\chi}^{-^2}}, \qquad -\frac{\pi}{6} \le \delta \le \frac{\pi}{6}, \qquad 0 \le k_p \le 1 \tag{5.6}$$

By introducing the phase current limitation of the converter, an expression for the maximum transferrable power can then be established as given by (5.7). As for the case in the previous section, the maximum power flow is expressed as a function gain constant k_p and the grid conditions specified by the amplitudes of the positive and negative sequence Virtual Flux components and the fault angle δ that represents the orientation of the Virtual Flux trajectory in the *αβ* reference frame.

$$\left|\overline{p}^*_{\max}\right| = \frac{i_{ph,\lim} \cdot \left(\hat{\chi}^{+^2} + k_p \cdot \hat{\chi}^{-^2}\right)}{\sqrt{\hat{\chi}^{+^2} + 2 + k_p \cdot \hat{\chi}^+ \cdot \hat{\chi}^- \cos(2\delta) + k_p^2 \cdot \hat{\chi}^{-^2}}}, \qquad \frac{\pi}{6} \le \delta \le \frac{\pi}{6}, \qquad 0 \le k_p \le 1 \tag{5.7}$$

The current reference vector for operation under phase current limitation can then be expressed by (5.8). As can be understood from Fig. 5-4 , these expressions will only be directly valid in case of δ within the range from −30° to 30°, but they can easily be made applicable by shifting the phase angle δ so that it will always be within the specified range. It can also be noted that the case of operation with balanced three-phase

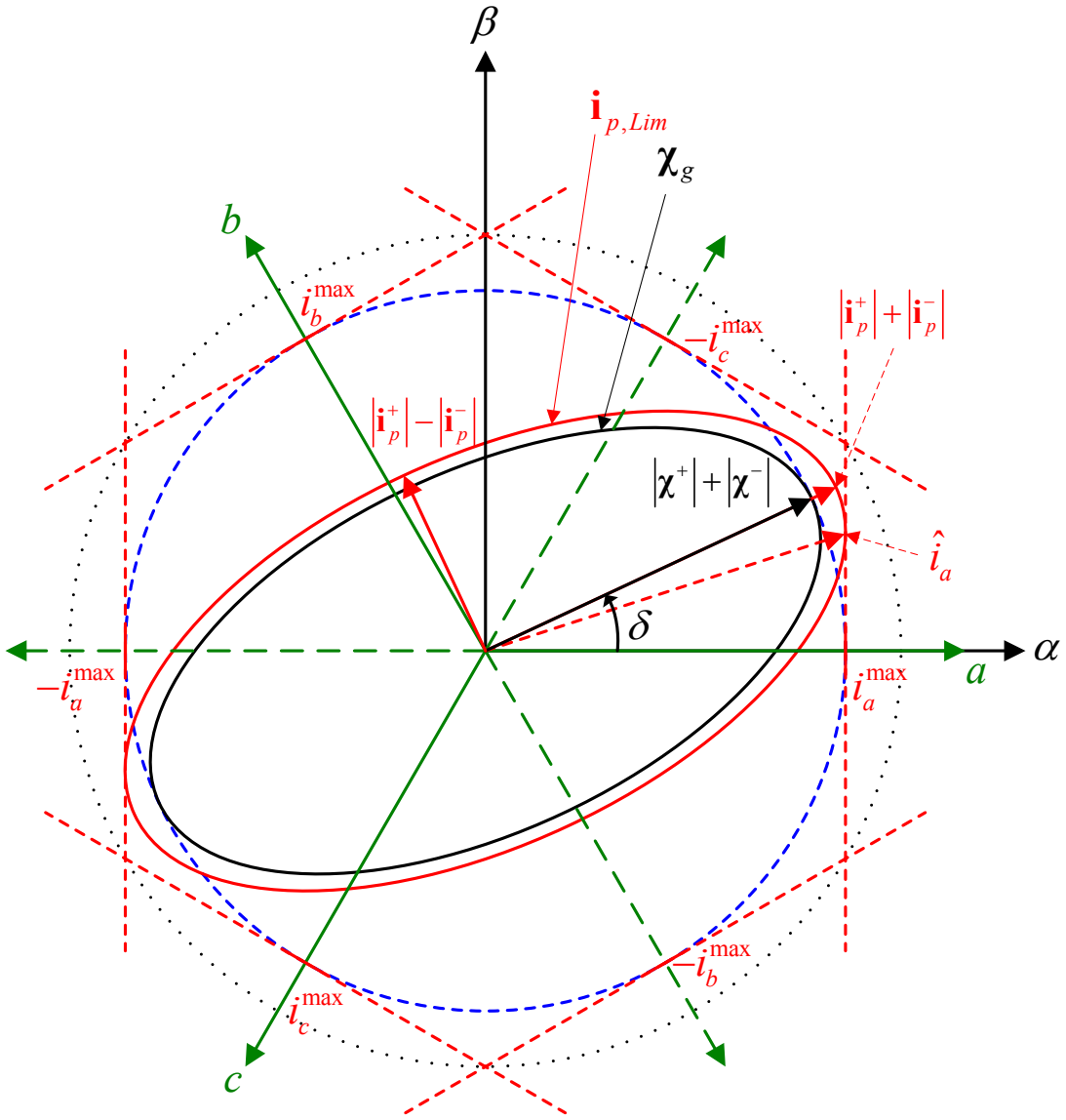

Fig. 5-4. Virtual Flux and current trajectories in case of active power control with elimination of double frequency reactive power oscillations

currents is covered by this equation, and that the result of imposing k_p is the same as for the equations derived in the previous subsection.

$$\mathbf{i}^*_{p,\lim} = \mathbf{i}^{*+}_p + \mathbf{i}^{*-}_p = \frac{i_{ph,\lim} \cdot \mathrm{Sign}\left(P^*\right)}{\sqrt{\left|\boldsymbol{\chi}^+\right|^2 + 2 \cdot k_p \cdot \left|\boldsymbol{\chi}^+\right| \cdot \left|\boldsymbol{\chi}^-\right| \cdot \cos\left(2\delta\right) + k_p^2 \cdot \left|\boldsymbol{\chi}^-\right|^2}} \cdot \left(-\boldsymbol{\chi}^+_{\perp} + k_p \boldsymbol{\chi}^-_{\perp}\right), \tag{5.8}$$

$$-\frac{\pi}{6} \le \delta \le \frac{\pi}{6}, \qquad 0 \le k_p \le 1$$

The maximum amplitude of the active current vector that can be allowed within the phase current limitation will be given by (5.9).

$$\left|\hat{\mathbf{i}}^*_{p,\lim}\right| = \frac{i_{ph,\lim} \cdot \left(\left|\boldsymbol{\chi}^+\right| + k_p \cdot \left|\boldsymbol{\chi}^-\right|\right)}{\sqrt{\left|\boldsymbol{\chi}^+\right|^2 + 2 \cdot k_p \cdot \left|\boldsymbol{\chi}^+\right| \cdot \left|\boldsymbol{\chi}^-\right| \cdot \cos\left(2\delta\right) + k_p^2 \cdot \left|\boldsymbol{\chi}^-\right|^2}}, \qquad -\frac{\pi}{6} \le \delta \le \frac{\pi}{6}, \qquad 0 \le k_p \le 1 \tag{5.9}$$

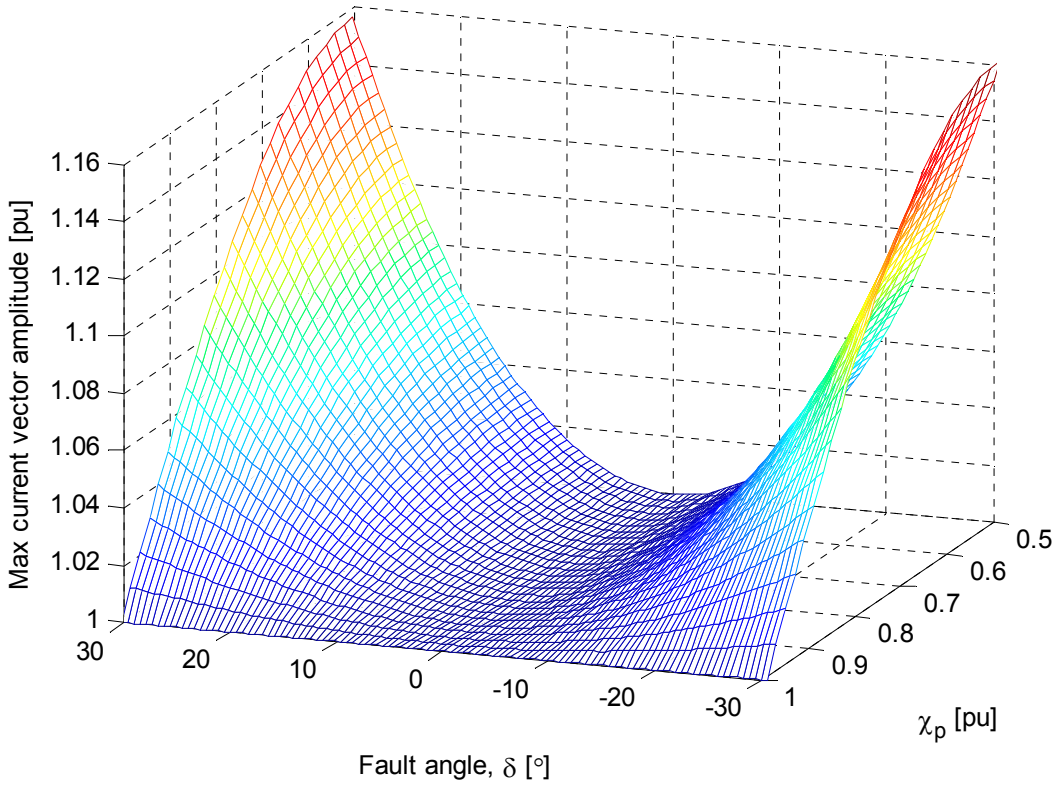

Fig. 5-5. Profile of maximum current vector amplitude as function of the fault angle and the level of unbalance

The result of (5.9) is plotted in Fig. 5-5 as a function of the fault angle δ and the remaining positive sequence Virtual Flux component for the case of $k_p = 1$. The same assumptions as in the previous subsection are made regarding the fault, so the plotted results corresponds to a case where $|\chi^-| = 1-|\chi^+|$ and the phase current limitation is specified to 1.0 pu. As expected, there are no difference between phase current limitation and vector amplitude limitation when the grid voltage is balanced or when the fault angle δ is equal to 0°. The maximum difference between traditional approach of current vector amplitude limitation and the presented approach of phase current limitation will however occur for δ = ±30° or any other odd multiple of 30°, as can be understood from studying Fig. 5-4. The maximum allowable current vector amplitude that can be allowed within the phase current limitation, corresponding to (5.1), will therefore occur only when $k_p = 1$ and $|\chi^+| = |\chi^-|$. This case will therefore correspond to maximum power transfer in a single phase converter, while the approach of vector amplitude limitation will limit the power transfer to a lower value.

5.3.2 Reactive Power Control with Limitation of the Reactive Current Component

The same approach as presented for active power control limitation of the active current component can be followed for reactive power control with phase current limitation. The reactive current trajectory resulting from reactive power control with the objective to reduce the reactive power oscillations will in this case have the same orientation as the voltage or Virtual Flux trajectories, while the current trajectory in case

of reactive power control with reduction of active power oscillations will be oriented perpendicularly to the Virtual Flux trajectory. These two cases are therefore investigated separately.

5.3.2.1 Phase current limitation with reduction of reactive power oscillations

The starting point for investigating reactive power control with phase current limitation will be the expression for current reference calculation according to (4.45). Selecting a value of k_q in this equation that is between −1 and 0 will correspond to reactive power control with the objective of reducing the second harmonic oscillations in reactive power flow during unbalanced conditions. The current reference vector will then follow the same trajectory as the grid voltage, but 90° phase shifted in time, and will therefore be in phase with the Virtual Flux for the case of reactive power injection to the grid. As explained for the case of active power control, the maximum phase current will then occur in phase *a*, as long as the fault angle δ is in the range between −30° and 30°. This situation will be similar to the case illustrated in Fig. 5-4, with the only difference that the reactive current component will be 90° delayed in time. The peak value of the current in phase *a* can then be derived, as shown in Appendix D.6.1, resulting in (5.10).

$$\hat{i}_{q,a}^{*} = \frac{-\bar{q}^{*}}{\hat{\chi}^{+^2} + k_q \hat{\chi}^{-^2}} \cdot \sqrt{\hat{\chi}^{+^2} - 2 \cdot k_q \cdot \hat{\chi}^{+} \cdot \hat{\chi}^{-} \cdot \cos(2\delta) + k_q^2 \cdot \hat{\chi}^{-^2}}, \qquad -\frac{\pi}{6} \le \delta \le \frac{\pi}{6}, \qquad -1 \le k_q \le 0 \tag{5.10}$$

The maximum average reactive power flow that can be allowed within the phase current limitation can then be expressed as a function of the control parameter k_q and the grid conditions as given by (5.11).

$$\left|\bar{q}_{\max}^{*}\right| = \frac{i_{ph,\lim} \cdot \left(\hat{\chi}^{+^2} + k_q \hat{\chi}^{-^2}\right)}{\sqrt{\hat{\chi}^{+^2} - 2 \cdot k_q \cdot \hat{\chi}^{+} \cdot \hat{\chi}^{-} \cdot \cos(2\delta) + k_q^2 \cdot \hat{\chi}^{-^2}}}, \qquad -\frac{\pi}{6} \le \delta \le \frac{\pi}{6}, \qquad -1 \le k_q \le 0 \tag{5.11}$$

Introducing the maximum transferrable average reactive power back into (4.45), is then resulting in an expression for reactive current reference calculation corresponding to reactive power control with phase current limitation given by (5.12).

$$\mathbf{i}_{q,\lim}^{*} = \mathbf{i}_{q}^{*+} + \mathbf{i}_{q}^{*-} = \frac{i_{ph,\lim} \cdot \mathrm{Sign}\left(\bar{q}^{*}\right)}{\sqrt{\left|\boldsymbol{\chi}^{+}\right|^2 - 2 \cdot k_q \cdot \left|\boldsymbol{\chi}^{+}\right| \cdot \left|\boldsymbol{\chi}^{-}\right| \cdot \cos(2\delta) + k_q^2 \cdot \left|\boldsymbol{\chi}^{-}\right|^2}} \cdot \left(\boldsymbol{\chi}^{+} - k_q \cdot \boldsymbol{\chi}^{-}\right), \qquad -\frac{\pi}{6} \le \delta \le \frac{\pi}{6}, \qquad -1 \le k_q \le 0 \tag{5.12}$$

These expressions are only directly valid as long as δ is in the range between −30° and 30°. In the same way as explained for the case of active power control with phase current limitation, the derived equations can however easily be made valid for any other orientations of the Virtual Flux trajectory by shifting δ with a multiple of 60°, so that it will always be within the specified range.

By comparing the equations above with the results presented in the previous subsections, it can be noticed that they have the same form as the equations presented for active power control with reduction of reactive power oscillations while operating under phase current limitation. The profile of the maximum allowable current vector amplitude with respect to the fault angle δ and the positive and negative sequence

components of the Virtual Flux will therefore be identical to the result shown in Fig. 5-5. The discussion of when the maximum current vector amplitude corresponding to (5.1) will occur will also be the same.

Considering (5.11) it can however be seen that the maximum average reactive power transfer will be reduced to zero if $k_q = -1$ and the grid is in a "single-phase" fault condition with equal amplitudes of the positive and negative sequence Virtual Flux components. This situation can be considered as a mirrored analogy to the case of active power control with the control objective of eliminating active power oscillations as discussed in section 5.3.1.1. The result of current reference calculation according to (5.12) will in such cases therefore be that maximum allowable current will be injected with a trajectory aligned with the Virtual Flux, causing zero average reactive power flow and only second harmonic active power oscillations.

Considering a case with $k_q = 0$, it can be easily verified that the equations presented above will be valid for the case of balanced three-phase currents. The maximum allowable current vector amplitude will then be equal to the phase current limitation and the maximum average reactive power transfer will be given by the phase current limitation and the amplitude of the remaining positive sequence Virtual Flux component.

5.3.2.2 Phase current limitation with reduction of active power oscillations

For values of k_q in the range between 0 and 1, the reactive current trajectory will be perpendicular to the voltage and Virtual Flux trajectories. Assuming the fault angle δ to be in the range between 0° and 60°, the maximum current will therefore occur in phase *b*. The derivation of maximum phase current amplitude, the maximum power transfer within the phase current limitation and the corresponding expression for current reference calculation will then follow the same line as described for the case of active power control with reduction of active power oscillations in section 5.3.1.1. The current trajectory will then be similar to the case illustrated by Fig. 5-2, but the currents in each axis will be phase shifted by 90° in time with respect to the voltages. As shown in Appendix D.6.2, the maximum current occurring in phase *b* can be derived to be given by (5.13).

$$\hat{i}^*_{q,b} = \frac{\overline{q}^*}{\hat{\chi}^{+^2} + k_q \cdot \hat{\chi}^{-^2}} \cdot \frac{1}{2}\sqrt{\hat{\chi}^{+^2} + k_q \cdot \hat{\chi}^+ \cdot \hat{\chi}^- \cdot \left(\cos(2\delta) + \sqrt{3}\sin(2\delta)\right) + k_q^2 \cdot \hat{\chi}^{-^2}}, \qquad 0 \le \delta \le \frac{\pi}{3}, \quad 0 \le k_q \le 1 \tag{5.13}$$

The maximum average reactive power that can be transferred within the phase current limitation can then be expressed by (5.14), and the corresponding expression for current reference calculation under phase current limitation is given by (5.15).

$$\left|\overline{q}^*_{\lim}\right| = \frac{i_{ph,\lim} \cdot \left(\hat{\chi}^{+^2} + k_q \cdot \hat{\chi}^{-^2}\right)}{\sqrt{\hat{\chi}^{+^2} + k_q \cdot \hat{\chi}^+ \cdot \hat{\chi}^- \cdot \left(\cos(2\delta) + \sqrt{3}\sin(2\delta)\right) + k_q^2 \cdot \hat{\chi}^{-^2}}}, \quad 0 \le \delta \le \frac{\pi}{3}, \quad 0 \le k_q \le 1 \tag{5.14}$$

$$\mathbf{i}^*_{q,\lim} = \frac{i_{ph,\lim} \cdot \mathrm{Sign}\left(\overline{q}^*\right)}{\sqrt{\left|\boldsymbol{\chi}^+\right|^2 + k_q \cdot \left|\boldsymbol{\chi}^+\right| \cdot \left|\boldsymbol{\chi}^-\right| \cdot \left(\cos(2\delta) + \sqrt{3}\sin(2\delta)\right) + k_q^2 \cdot \left|\boldsymbol{\chi}^-\right|^2}} \cdot \left(\boldsymbol{\chi}^+ - k_q \cdot \boldsymbol{\chi}^-\right), \qquad 0 \le \delta \le \frac{\pi}{3}, \quad 0 \le k_q \le 1 \tag{5.15}$$

The equations presented above have the same form as the equations presented for active power control with reduction of active power oscillations in section 5.3.1.1 The profile of the maximum allowable current vector amplitude within the phase current limitation as a function of the fault angle δ and the positive and negative sequence Virtual Flux components will therefore be the same as plotted in Fig. 5-3. The expressions can also be made valid for any orientation of the Virtual Flux trajectory during the fault by phase shifting δ by a multiple of 60° so that it will always be within the specified range. However, since the value of k_q in this case is limited between 0 and 1, average reactive power can be transferred even during single-phase faults with equal amplitudes of the positive and negative sequence Virtual Flux components.

It can also be noted that the presented equations are valid in case of $k_q = 0$, corresponding to operation with balanced three-phase currents. As for the previously described cases, the objective of balanced three-phase currents will simplify all the equations, and the maximum allowable current vector amplitude will then always be equal to the phase current limitation.

5.4 Simulation of Power Control Strategies Operated with Phase Current Limitation under Single-phase Fault Conditions

The operation of the presented strategies for power control under phase current limitation under severe unbalanced conditions corresponding to “single-phase” faults, have been investigated with simulation studies, and some illustrative results will be presented in the following subsections. The “single-phase” conditions are used as the only examples, since this can be considered as the most severe faults that can occur, and will verify the operation of power control strategies with phase current limitation under conditions that could not be allowed for the pure active and reactive power control strategies presented in chapter 4.

The presented simulations are based on a configuration with the same main parameters as listed in in Table 3-1 and described in section 3.3.2. The converter is simulated by an average model neglecting the PWM operation of the converter, and in this case the DC-link voltage is supplied by an ideal voltage source to avoid influence from any outer loop power controller or DC-link voltage controller.

For operation within the specified current limitation, the converter is operated with active and reactive power control by using the generalized expressions for current reference calculation according to (4.44) and (4.45). However, if the vector amplitude of the active current reference resulting from the average active power reference and the power control objective specified by k_p exceeds the active current vector amplitude limitation according to (5.4) or (5.9), the active current reference is limited to that value. Thus, if the phase current limitation is reached, the active current reference will be given by (5.4) or (5.9), and the power flow characteristics specified by k_p will be maintained even if the average active power transfer will be reduced. The same approach is implemented for the reactive power control, and the reactive current reference will therefore be specified by (5.12) or (5.15), if the phase current limitation is exceeded.

The active and reactive current references resulting from the active and reactive power control and the possible influence of the phase current limitation are summarized to

result in the $\alpha\beta$ current references used as input to a set of Proportional-Resonant (PR-) current controllers. The converter is operated in voltage-sensor-less mode and the amplitude of the PNS Virtual Flux components and the fault angle δ are all calculated from the PNS signals resulting from the DSOGI-VF estimation from section 3.3.

5.4.1 Converter Operation in Response to Changes in the Grid Fault Phase Angle

To verify the characteristics of the phase current limitation strategies presented in the previous subsections, the converter is simulated under a "single-phase" fault condition corresponding to $|\chi^+| = |\chi^-| = 0.5$ pu while the fault angle δ is swept from 0° to 90°. The converter is operated with 1.0 pu in average active power reference, and with a power control objective specified by $k_p = 1$, corresponding to elimination of reactive power oscillations by the AARC strategy. For simplicity, and easy illustration of the results, the phase current limitation of the active current component is also specified to 1.0 pu, and the average reactive power reference is set to 0. The main results from simulating this case are plotted in Fig. 5-6.

The three-phase voltages at the point of synchronization to the grid are shown in Fig. 5-6 (a), while the fault angle δ detected from the estimated PNS Virtual Flux components are shown in Fig. 5-6 (b). From these curves, it can clearly be seen how the full voltage remains in phase *a* when the fault angle is zero, while the voltages of phase *b* and *c* are in phase and reduced to 0.5 in amplitude. When the fault angle is equal to 30°, it can be seen that the remaining voltage in phase *b* is zero, since the voltage or Virtual Flux trajectory will be perpendicular to the *b*-axis. At $\delta = 60°$ the same situation as for $\delta = 0°$ occurs, with the only difference that the full voltage of 1.0 pu is now remaining in phase *c*. Similarly, when the fault angle is equal to 90°, the remaining voltage in phase *a* is zero. The trajectory of the estimated Virtual Flux, that will be equal to the trajectory resulting from plotting the curves from Fig. 5-6 (a) in the stationary $\alpha\beta$ reference frame, is shown in to the left in Fig. 5-7 to further illustrate the evolvement of the voltages and Virtual Flux signals when the fault angle is swept from 0 to 90°.

The three-phase currents resulting from the operation with phase current limitation and $k_p = 1$, are shown in Fig. 5-6 (c). From these curves, it can be seen that the currents are always in phase with the voltages, since the control objective is to eliminate double frequency oscillation in the reactive power flow. It can also be clearly seen that the amplitude of the three-phase currents is always limited to 1.0 pu as expected. The $\alpha\beta$-components of the converter currents are however plotted in Fig. 5-6 (d), and the resulting trajectory is plotted in the right side of in Fig. 5-7, where also the phase current limitation of the converter is indicated. From these curves, it can be seen that the maximum current capability of the converter is always utilized and that the maximum current vector amplitude that occurs in case of $\delta = 30°$ or 90° is about 15 % higher than the phase current limitation, as predicted by (5.1) and the previous discussions.

The active power flow resulting at the point of synchronization to the grid is also plotted in is also plotted in Fig. 5-6 (e). The instantaneous active power flow, plotted by blue lines in the figure is in this case calculated from the measured voltages and currents according to (4.1), while the average active power flow plotted by a black dashed line is calculated from the PNS Virtual Flux and current components from the DSOGI-VF estimation according to (5.16).

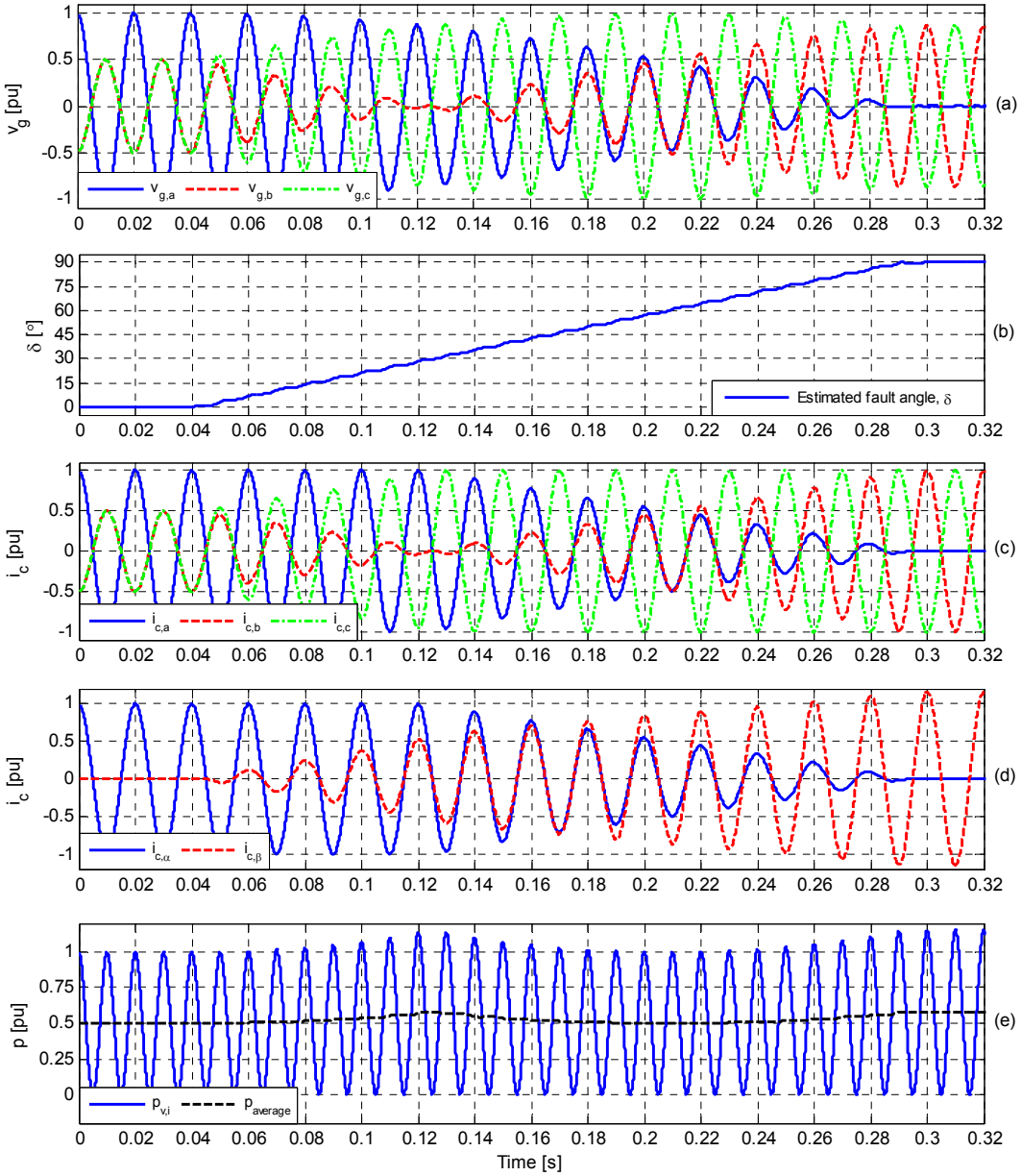

Fig. 5-6 Simulation results for control by AARC with phase current limitation under unbalanced conditions with $|\chi^+| = |\chi^-| = 0.5$ pu when the phase angle δ between positive and negative sequence components is swept from 0 to 90°

$$\overline{p} = -\boldsymbol{\chi}_{\perp}^{+} \cdot \mathbf{i}^{+} + \boldsymbol{\chi}_{\perp}^{-} \cdot \mathbf{i}^{-} \tag{5.16}$$

From the plotted powers, it can be seen that when the fault angle δ is equal to 0° and 60°, the average active power transfer is equal to 0.5 pu, while the total power is oscillating between 0 and 1.0 pu. This is similar to what would have resulted from operation with balanced three-phase currents, since the amplitude of the positive sequence voltage component is equal to 0.5 pu and the phase current limitation is specified to 1.0 pu. However, it can also be seen that the average power transfer is increased when $\delta \neq 0°$ or 60°. As expected, the maximum power is transferred when $\delta =$ 30° or 90°, as given by (5.17). Thus, for the particular case of a single phase fault with

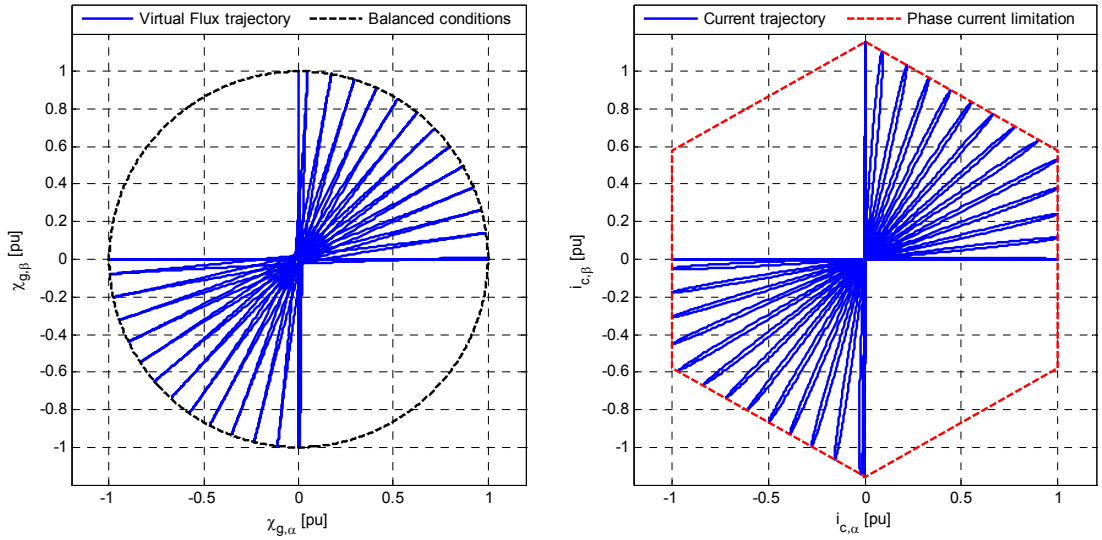

Fig. 5-7 Simulated trajectories of Virtual Flux and current for control by AARC with phase current limitation under unbalanced conditions with $|\chi^+| = |\chi^-| = 0.5$ pu when the phase angle δ between positive and negative sequence components is swept from 0 to 90°

zero remaining voltage, the power transfer capability can be increased by about 15 % when limiting the phase currents instead of the active current vector amplitude. This implies that maximum power transfer in such cases can only be achieved by the AARC strategy corresponding to $k_p = 1$, and not by controlling balanced three-phase currents.

$$\overline{p}_{\max} = -\boldsymbol{\chi}_{\perp}^{+} \cdot \mathbf{i}^{+} + \boldsymbol{\chi}_{\perp}^{-} \cdot \mathbf{i}^{-} = 0.5 \cdot \frac{1}{\sqrt{3}} + 0.5 \cdot \frac{1}{\sqrt{3}} = \frac{1}{\sqrt{3}} \approx 0.577 \tag{5.17}$$

A similar case as presented above can also be investigated for reactive power control. The result will however be similar in the sense that maximum current vector amplitude and maximum reactive power transfer will occur only with $k_q = 1$, and with the current trajectory alignment in the $\alpha\beta$ reference frame given by an odd multiple of 30°

5.4.2 Converter Operation in Response to Changes in the Active Power Control Objective

The general validity of the phase current limitation with respect to the applied objective for active power control can be illustrated with a simulated case where the value of the control parameter k_p is swept from 1 to −1. The simulated case is still a single phase fault condition with $|\chi^+| = |\chi^-| = 0.5$ pu, and with a constant fault angle δ equal to 30°. The average active power reference is specified to 1.0 pu, and the phase current limitation is also set to 1.0 pu, while the reactive power reference is set to zero.

The main results from the simulated case are shown in Fig. 5-8, and it can be clearly seen from the voltages plotted in Fig. 5-8 (a) that this fault condition corresponds to zero remaining voltage in phase *b*. The curve plotted in Fig. 5-8 (b) shows the control parameter k_p that is swept from 1 to −1 during the simulation.

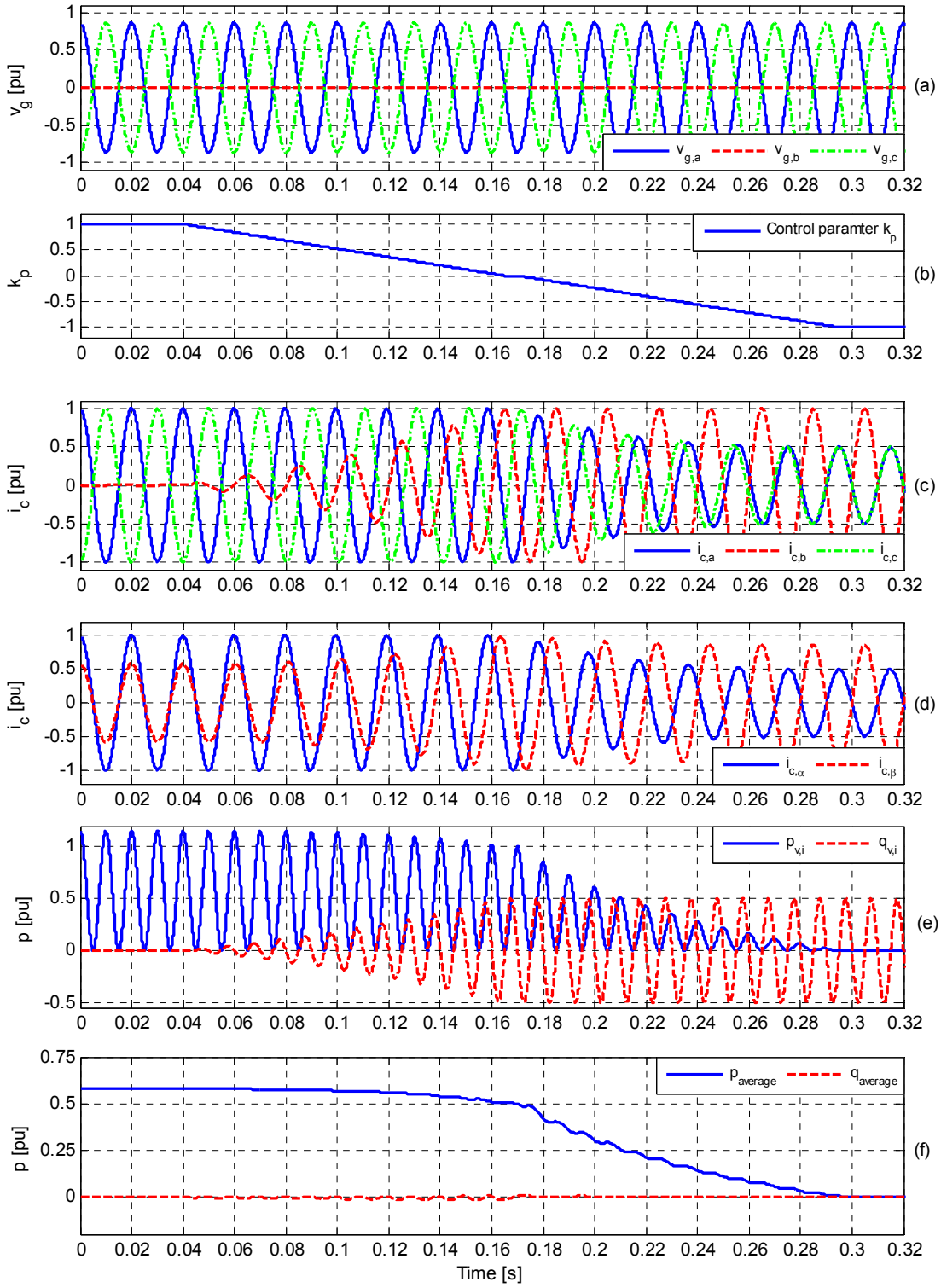

Fig. 5-8 Simulation results for active power control with phase current limitation under unbalanced conditions with $|\chi^+|=|\chi^-|=0.5$ pu when the control parameter k_p is swept from 1 (AARC) to −1 (PNSC)

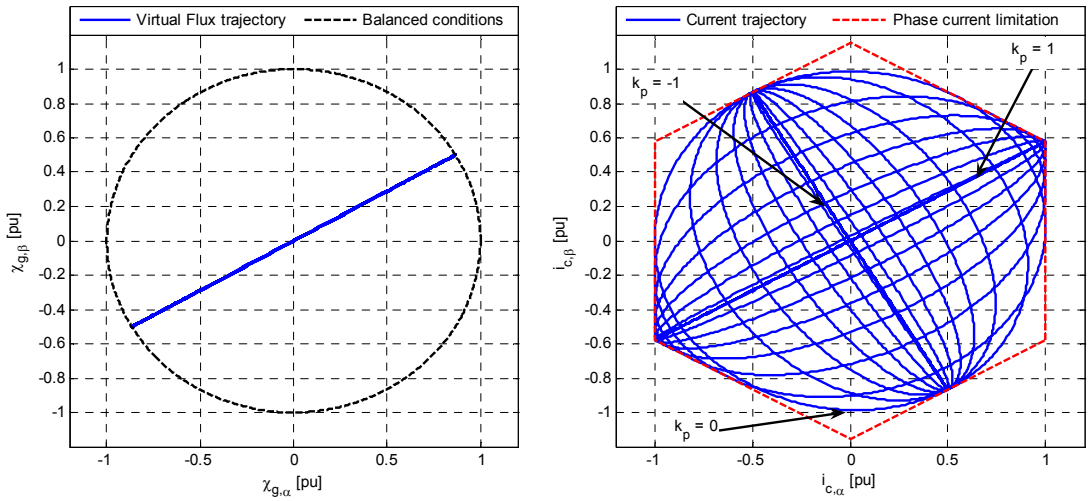

Fig. 5-9 Simulated trajectories of Virtual Flux and current for active power control with $|\chi^+| = |\chi^-| = 0.5$ pu when k_p is swept from 1 (AARC) to −1 (PNSC)

At the beginning of the plotted time series, the converter is operated according to the AARC strategy with $k_p = 1$ and, as described in the previous subsection, this results in the maximum current vector amplitude and the maximum power transfer that is about 15 % higher than what can be achieved with balanced three-phase currents in the same condition. The current trajectory is then a straight line with the same alignment as the voltage and Virtual Flux trajectories, as shown in Fig. 5-9. This can also be interpreted from the three-phase currents plotted in Fig. 5-8 (c), the $\alpha\beta$ current components plotted in Fig. 5-8 (d) and the active and reactive powers plotted in Fig. 5-8 (e) and (f). It can be noted that the instantaneous active and reactive powers plotted in Fig. 5-8 (e) are calculated from measured voltages and currents according to (4.1) and (4.2). The average active and reactive powers plotted in Fig. 5-8 (f) are however calculated from the PNS Virtual Flux and current components resulting from the DSOGI-VF estimation according to(5.16) and (5.18) respectively. As expected, the reactive power oscillations are kept at 0 as long as $k_p = 1$.

$$\overline{q} = \boldsymbol{\chi}^+ \cdot \mathbf{i}^+ - \boldsymbol{\chi}^- \cdot \mathbf{i}^- \tag{5.18}$$

When the value of k_p is reduced towards zero, currents start flowing also in phase b as can be seen from Fig. 5-8 (c), resulting in increasing oscillations in the reactive power flow as can be seen from Fig. 5-8 (e). It can be seen in Fig. 5-9 that this results in a wider and wider elliptic trajectory of the current, until a circular trajectory is achieved when balanced three-phase currents are injected into the grid when $k_p = 0$. At this condition, the average active power transfer is, as expected, reduced to 0.5 pu and the active and reactive power oscillations have equal amplitudes equal to 0.5 pu.

When k_p is further reduced and takes negative values, Fig. 5-9 shows how the current will follow an elliptic trajectory that is perpendicular to the Virtual Flux trajectory and that becomes narrower as k_p is approaching −1. As the current is controlled into a trajectory that is perpendicular to the voltage trajectory, the average active power flow and the amplitude of the active power oscillations is reduced. The amplitude of the reactive power oscillations is maintained at 0.5 pu. When k_p reaches −1, a current of 1.0 pu is flowing in the faulted phase b with zero remaining voltage, and the current trajectory is collapsed to a straight line aligned with the b-axis. This situation is corresponding to current limited control by the PNSC strategy. The average active

power flow is therefore reduced to zero. The objective of eliminating active power oscillations during unbalanced conditions is therefore achieved on the cost of reducing the average active power flow to zero.

The presented simulations show how the developed expressions for phase current limitation are valid for any values of the control parameter k_p used to specify the objective of the active power control. Similar results can also be presented for reactive power control, showing that the strategies for phase current limitation will be valid and will give the maximum utilization of the converters current capability for any specified reactive power control objective.

5.4.3 General Comment Regarding Strategies for Phase Current Limitation

The simulation results presented above where selected to illustrate the general validity of the derived expressions current reference calculation of power control strategies operating under phase current limitation. Although only results for active power control have been presented in detail, similar results can also be presented for reactive power control under the same conditions. As the investigated strategies for phase current limitation has shown to perform as expected during single-phase fault conditions, that can be considered the most severe level of unbalance in a three-phase system, they will also be valid for any other fault conditions and any combination of control objectives and reference values for active and reactive power flow. In case of non-zero values for both the average active and reactive power references, additional considerations are however necessary to limit the total amplitude of the phase currents. This will be discussed later in a separate section.

The presented strategies for phase current limitation are however resulting in complicated, nonlinear expressions that have to be solved on-line for practical implementation in a converter control system. It is also necessary to detect the fault angle δ from the estimated PNS Virtual Flux or voltage components, as discussed in Appendix D.2 to be able to take advantage of the potential to increase the current vector amplitude beyond the phase current limitation of the converter. Therefore, the simpler approach of current vector amplitude limitation, without considering the orientation of the current vector trajectory during unbalanced conditions, can be useful for practical implementation. This approach will therefore be investigated in the following subsections.

5.5 Simplified Current Reference Calculation for Operation under Current Vector Amplitude Limitation

A simple, but still generally valid, approach for current vector amplitude limitation can easily be derived from the equations for current reference calculation for active and reactive power control given by (4.44) and (4.45). The operation of such an approach will be similar to the methods previously presented in the literature for implementation in synchronous reference frames as discussed for specific control objectives in [228], [229], [230], [231], [232]. Strategies for vector amplitude limitation of the active and reactive current references derived directly from by (4.44) and (4.45) will however be generally valid for any specified control objective.

5.5.1 Active Power Control with Current Vector Amplitude Limitation

According to the expression for active current reference calculation in (4.44), the maximum amplitude of the current reference vector will be given by (5.19). By introducing a fixed limit for vector amplitude of the active current reference, given by $i_{p,lim}$, the maximum power that can be controlled by the converter within this limitation will be given by (5.20).

$$\left|\hat{\mathbf{i}}_p^*\right| = \frac{\left|\overline{p}^*\right|}{\left|\boldsymbol{\chi}^+\right|^2 + k_p \cdot \left|\boldsymbol{\chi}^-\right|^2} \cdot \left(\left|\boldsymbol{\chi}^+\right| + \left|k_p\right| \cdot \left|\boldsymbol{\chi}^-\right|\right) \tag{5.19}$$

$$\overline{p}_{\lim} = \frac{i_{p,\lim} \cdot \mathrm{Sign}(\overline{p}^*)}{\left|\boldsymbol{\chi}^+\right| + \left|k_p\right| \cdot \left|\boldsymbol{\chi}^-\right|} \cdot \left(\left|\boldsymbol{\chi}^+\right|^2 + k_p \cdot \left|\boldsymbol{\chi}^-\right|^2\right) \tag{5.20}$$

Substituting the maximum power from (5.20) back into the equation for the active current reference in (4.44) results in (5.21), that will keep the active current vector trajectory within $i_{p,Lim}$ for any combination of grid voltages and control objectives.

$$\mathbf{i}_{p,\lim}^* = \frac{i_{p,\lim} \cdot \mathrm{Sign}\left(\overline{p}^*\right)}{\left|\boldsymbol{\chi}^+\right| + \left|k_p\right| \cdot \left|\boldsymbol{\chi}^-\right|} \cdot \left(-\boldsymbol{\chi}_\perp^+ + k_p \boldsymbol{\chi}_\perp^-\right), \qquad -1 \le k_p \le 1 \tag{5.21}$$

It can also be noted that the expression for the current reference calculation with vector amplitude limitation will result as a simplification of (5.4) by specifying the fault angle δ to be constantly equal to 30° when $k_p < 0$, and similarly from (5.8) by specifying δ to be equal to 0° when $k_p > 0$.

By considering different value of k_p in (5.21), it can be easily verified that a value of k_p equal to −1 will result in a current trajectory with the same shape as for power control by the PNSC strategy, but with vector amplitude limited to $i_{p,Lim}$. Similarly, operation with k_p equal to 0 will correspond to BPSC and k_p equal to 1 will correspond to current limited operation with the AARC strategy. The power control objective specified by k_p will therefore be maintained, while the average value of the transferred power will be limited to keep the maximum amplitude of the current reference vector below the specified limit.

As for the approach based on phase current limitation, current reference calculation by (5.21) will allow for operation with the $k_p = -1$ according to the PNSC strategy even in the case of $|\chi^+|=|\chi^-|$. The only difference from the case of phase current limitation will be that the current vector amplitude will always be limited to the maximum phase current of the converter, and that the additional 15 % of current capability that was discussed in the previous sections can not be utilized. The difference between the two approaches will however be smaller in case of less severe fault conditions where the positive sequence component of the remaining grid voltage is significantly larger than the negative sequence component. Equation (5.21) is also simpler to implement than the expressions presented for phase current limitation and is generally valid for all values of k_p.

5.5.2 Reactive Power Control with Current Vector Amplitude Limitation

The same simple derivations as for the active current reference can be applied to the reactive current reference calculation in (4.45). The resulting maximum value of the reactive current reference vector amplitude is given by (5.22). The maximum reactive power that can be controlled within the reactive current limit $i_{q,Lim}$ is then given by (5.23).

$$\left|\hat{\mathbf{i}}_q^*\right| = \frac{\left|\overline{q}^*\right|}{\left|\boldsymbol{\chi}^+\right|^2 + k_q\left|\boldsymbol{\chi}^-\right|^2} \cdot \left(\left|\boldsymbol{\chi}^+\right| + \left|k_q\right| \cdot \left|\boldsymbol{\chi}^-\right|\right) \tag{5.22}$$

$$\overline{q}_{\lim} = \frac{i_{q,\lim} \cdot \mathrm{Sign}(\overline{q}^*)}{\left|\boldsymbol{\chi}^+\right| + \left|k_q\right| \cdot \left|\boldsymbol{\chi}^-\right|} \cdot \left(\left|\boldsymbol{\chi}^+\right|^2 + k_q \cdot \left|\boldsymbol{\chi}^-\right|^2\right) \tag{5.23}$$

By substituting the expression for maximum average reactive power transfer back into the current references from (4.45), the general expression for current reference calculation when operating under current vector amplitude limitation can be found as given by (5.24).

$$\mathbf{i}_{q,\lim}^* = \frac{i_{q,\lim} \cdot \mathrm{Sign}\left(\overline{q}^*\right)}{\left|\boldsymbol{\chi}^+\right| + \left|k_q\right| \cdot \left|\boldsymbol{\chi}^-\right|} \cdot \left(\boldsymbol{\chi}^+ - k_q \cdot \boldsymbol{\chi}^-\right), \qquad -1 \le k_q \le 1 \tag{5.24}$$

It can also be noticed that this equation will result as a simplification of (5.12) by specifying the fault angle δ to be constant and equal to 0° when $k_q < 0$, and from (5.15) by specifying $\delta = 30°$ when $k_q > 0$. Again, it is easily verified that a value k_q equal to −1 will result in reactive power control by the PNSC strategy with the average reactive power flow limited by the current vector amplitude limitation. Similarly, operation with k_q equal to 0 will correspond to BPSC and k_q equal to 1 will correspond to operation according to the AARC strategy.

5.6 Experimental Results of Active and Reactive Power Control Strategies with Current Vector Amplitude Limitation

The operation of power control strategies with current vector amplitude limitation as described in the previous section have been verified by laboratory experiments. Results from operation with current limited control of active and reactive power will be presented separately, complimenting the simulation results presented with phase current limitation. A general discussion regarding current limitation in case of simultaneous active and reactive power control will be presented separately in section 5.7.

5.6.1 Description of Laboratory Setup and Control System Implementation

The same laboratory setup as already described in section 4.4.1 was used for the experiments, and the main parameters were the same as listed in Table 4-1. The only additional parameter introduced in this case is the current vector limitation, which is specified to be 1.08 pu (2.0 A). However, the control structure implemented in the dSPACE platform had to be extended to include the strategy for current vector

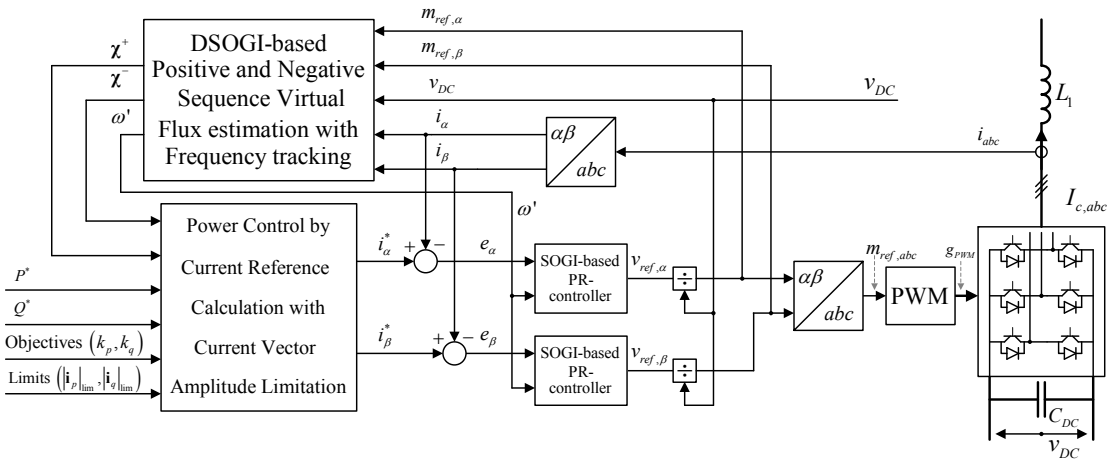

Fig. 5-10 Overview of control configuration operated on the dSPACE platform

amplitude limitation as described in section 5.5. The resulting structure of the control system is outlined in Fig. 5-10, and a more detailed illustration of the current reference calculation including the mechanism for current limitation is shown in Fig. 5-11.

From this figure it can be seen that the implementation is simplified by first calculating the scalar part of the active and reactive current references resulting from the specified power control objectives and the average active and reactive power references. The scalar coefficient corresponding to the active power control can be considered as a Virtual Flux-based conductance and is therefore labeled as g_p in analogy to the notation used in [108], [109]. Similarly, the scalar coefficient resulting corresponding to the reactive power control can be considered as a suseptance, and is labeled as b_q in analogy to the notation used in [108], [110]. The scalar parts of (5.21) and of (5.24), can then be interpreted as a conductances, g_{lim}, and a suseptance, b_{lim}, respectively, when operating under current vector amplitude limitation. In normal operation, the conductance value g_p and the suseptance value b_q, corresponding to the specified average active and reactive power references are used to calculate the active and reactive current references. However, as soon as the amplitude of the resulting active and/or reactive current vector exceeds the specified limitations, the conductance g_{lim} and/or the suseptance b_{lim} are selected as starting point for calculating the active and reactive current references. The resulting active and reactive current references are summed, to result in the total current references in the stationary $\alpha\beta$ reference frame, that are used as inputs to the current controllers indicated in Fig. 5-10.

5.6.2 Active Power Control with Current Vector Amplitude Limitation

The operation of Virtual Flux-based active power control with current vector amplitude limitation has been tested for the three following cases; 1) elimination of active power oscillations according to the PNSC strategy ($k_p = -1$), 2) operation with balanced positive sequence currents according to the BPSC strategy ($k_p = 0$), and 3) elimination of reactive power oscillations according to the AARC strategy ($k_p = 1$). The presented results have been obtained when the grid emulator was set to generate a sag corresponding a voltage drop of about 50% in phase *a* under no-load conditions. A detailed set of results will be presented for the case of operation with PNSC, while

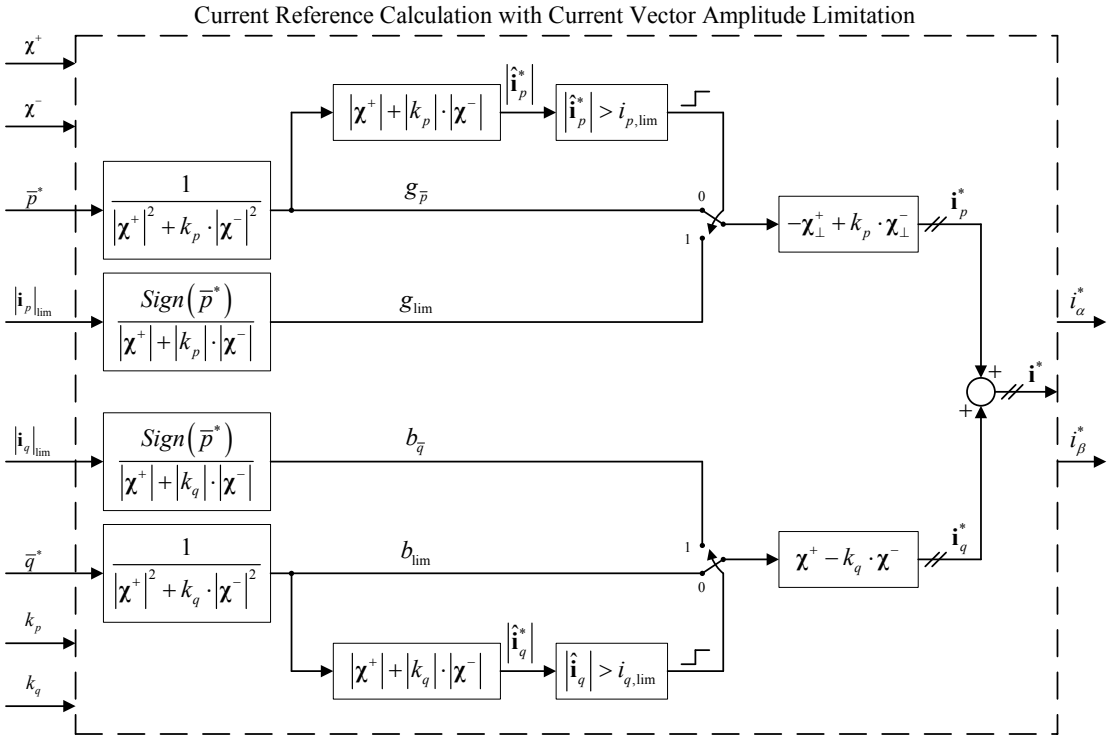

Fig. 5-11 Current Reference Calculation with Vector Amplitude Limitation

results showing only the voltages, currents and resulting active and reactive power flows will be presented for the other two cases.

5.6.2.1 Elimination of second harmonic active power oscillations during unbalanced conditions by current limited PNSC

Fig. 5-12 shows the results for the case of current limited active power control by the PNSC strategy, with the pre-fault power reference set to 1.0 pu. The measured three-phase voltages are plotted in Fig. 5-12 (a), while Fig. 5-12 (b) shows the measured three-phase currents. Since the PNSC strategy aims to eliminate second harmonic oscillations in the active power flow, the highest current occurs in phase a, that has the lowest voltage during the fault. Except for a small overshoot around the time when the voltage dip occurs, the current in phase a is limited below the specified current limitation of 1.08 pu. The currents in phase b and c are lower than before the fault due to the objective of eliminating the active power oscillations.

The plots in Fig. 5-12 (c) and (d) show the positive and negative sequence components of the estimated Virtual Flux, and Fig. 5-12 (e) shows the calculated current references in the stationary *αβ* reference frame. The *αβ* trajectories of the total Virtual Flux ($\boldsymbol{\chi} = \boldsymbol{\chi}^+ + \boldsymbol{\chi}^-$) and of the current references are shown in Fig. 5-13, and it can be clearly seen how the PNSC strategy makes the trajectory of the active current reference to be perpendicular to the Virtual Flux trajectory. As expected, the peak value of the current reference vector is restrained by the imposed active current limitation of 1.08 pu. However, it can be noticed that since the elliptic current reference trajectory in this case is aligned between the axis of phase *a* and phase *c*, the resulting current in phase *a* will be slightly below the phase current limitation that could have been reached with the strategies discussed in section 5.3.1.

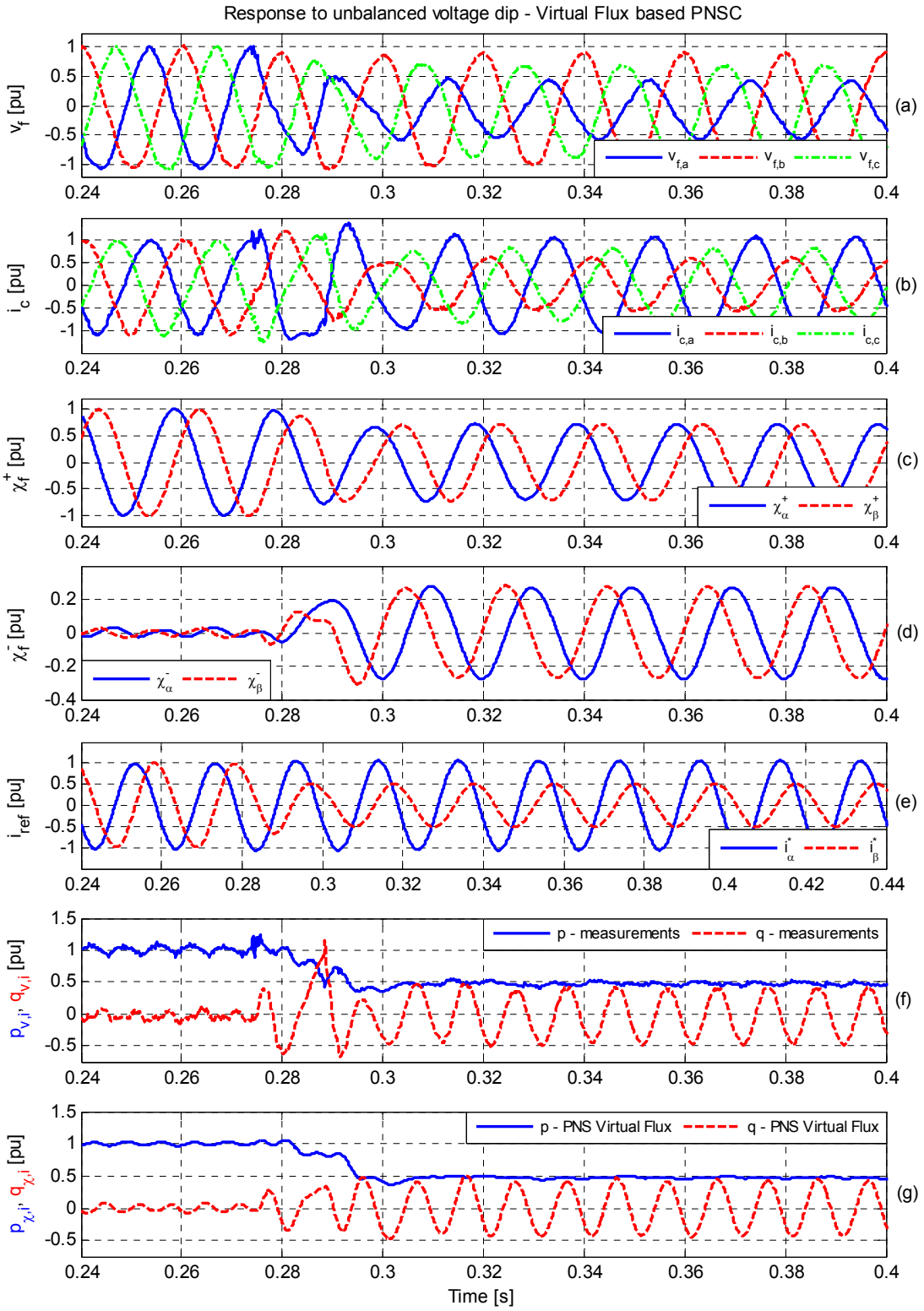

Fig. 5-12 Active power control by PNSC with the amplitude of the active current vector reference i_p^* limited to 1.08 pu

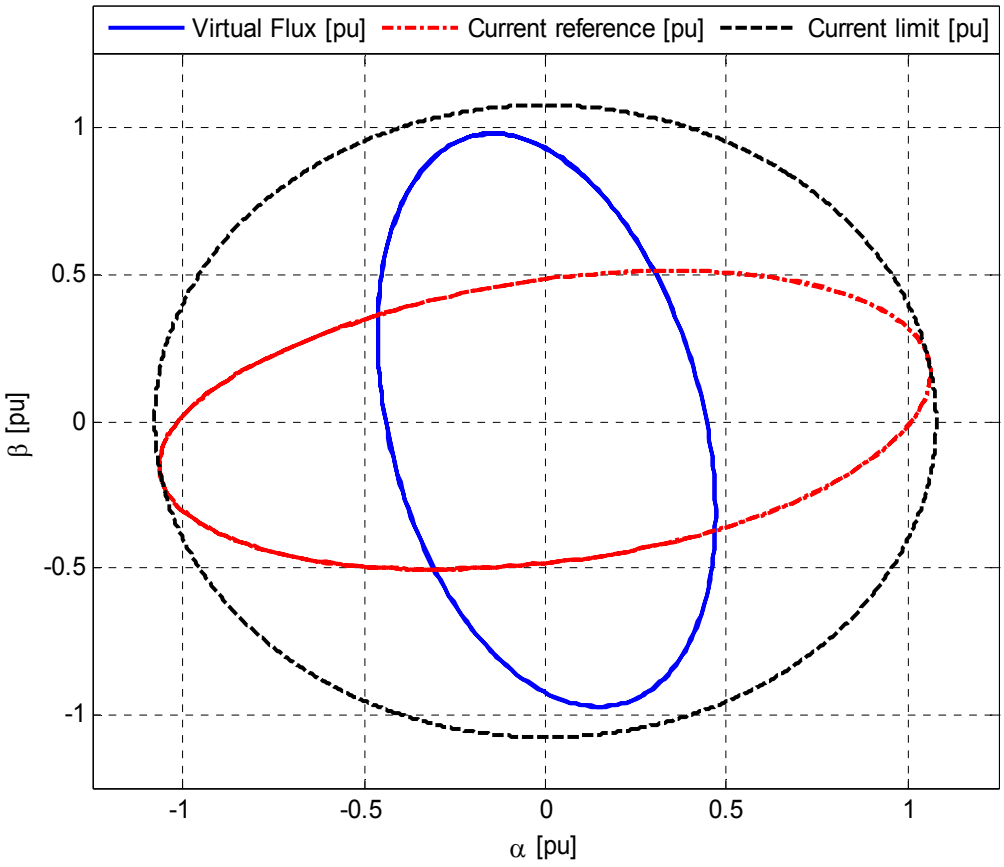

Fig. 5-13 Trajectory of estimated Virtual Flux and calculated current reference for power control by PNSC with current vector amplitude limitation

The curves in Fig. 5-12 (f) are showing the active and reactive power calculated from the measured voltages and currents according to (4.1) and (4.2), while the curves in Fig. 5-12 (g) are showing the active and reactive powers calculated from the positive and negative sequence components of the currents and the Virtual Flux resulting from the DSOGI-VF estimation by using (4.11) and (4.12). As expected, the active power is reduced when the voltage dip occurs, to keep the current within its limitation. In this case, the average active power transfer is reduced to about 0.5 pu, and the active power flow is constant in steady state since the double frequency power oscillations are successfully eliminated by the PNSC strategy. It can be noted that the curves in Fig. 5-12 (f) and (g) are corresponding well in the same way as discussed in chapter 4, verifying the performance of the Virtual Flux estimation and the validity of the applied method for power control and current reference calculation under current limitation.

5.6.2.2 Operation with balanced three-phase currents by current limited BPSC

Results for current limited operation with power control by the BPSC strategy is shown in Fig. 5-14, with the pre-fault power reference set to 1.0 pu. From the results, it is clearly seen that the converter is injecting balanced three-phase currents during the unbalanced conditions, and that the amplitude of these currents is kept within the specified limit of 1.08 pu. As a result, the average active power is slightly reduced during the unbalanced conditions, and double frequency oscillations occur in both the

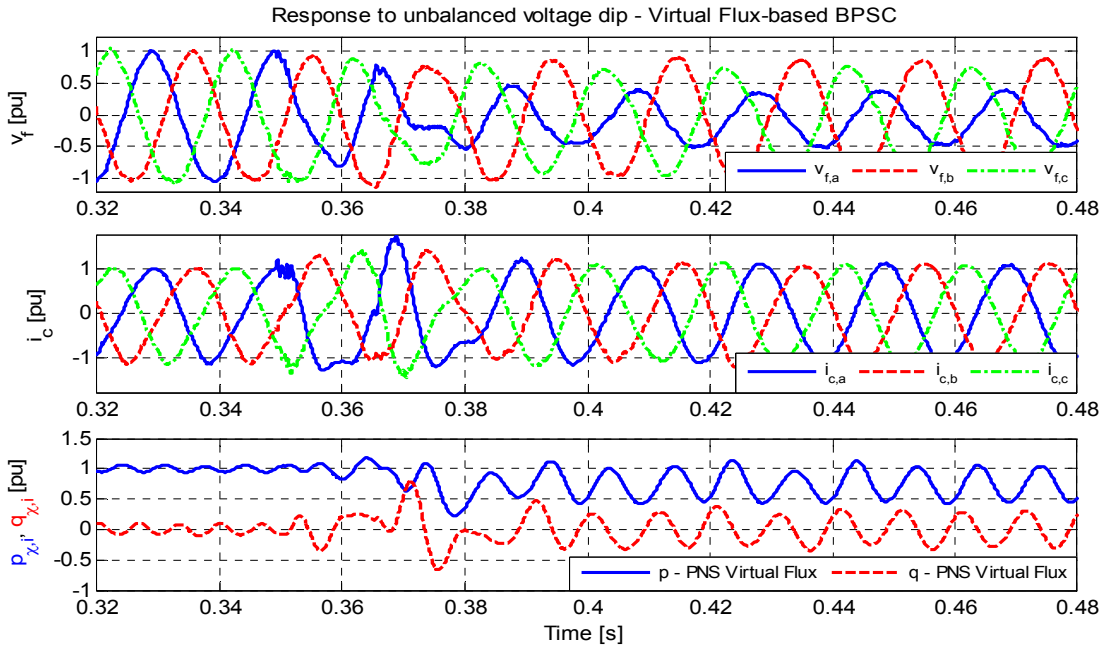

Fig. 5-14 Active power control by BPSC with the active current reference i_p^* limited to 1.08 pu

active and reactive powers. It can be noticed that the average active power transfer during the unbalanced conditions is kept at about 0.75 pu in this case, compared to the 0.5 pu constant active power delivered by the current limited PNSC strategy under the same conditions.

It can be noticed that the transient when the unbalanced voltage sag occurs is more severe in this case than for the previously presented results. This is however mainly caused by the operation of the electromechanical contactors of the voltage sag generator.

5.6.2.3 Elimination of second harmonic reactive power oscillations during unbalanced conditions by AARC with current vector amplitude limitation

Results from operation with active power control by the AARC strategy with a vector current limitation of 1.08 pu are shown in Fig. 5-15. In this case, the current vector will be proportional to the voltage and Virtual Flux vector trajectories, and the largest current is therefore injected into the phase with the highest voltage. Disregarding some transient response around the occurrence of the voltage sag, the results verify that the current limitation strategy is operating as expected, and the reactive power oscillations are therefore eliminated during the unbalanced conditions. Because of the elimination of reactive power oscillations, the double frequency oscillations in active power are larger in this case than for the BPSC. The average active power transfer is also slightly reduced compared to the case of current limited BPSC, but is still larger than for the case of PNSC.

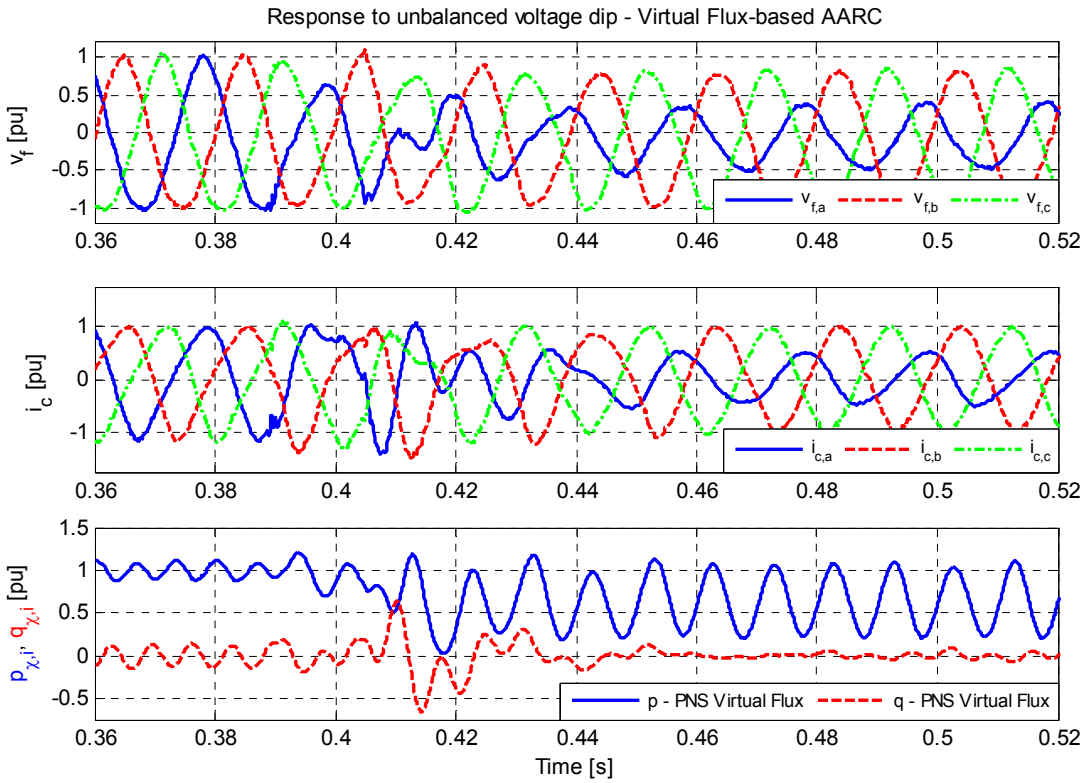

Fig. 5-15 Active power control by AARC with the amplitude of the active current vector reference i_p^* limited to 1.08 pu

5.6.3 Reactive Power Control with Current Vector Amplitude Limitation

The operation of Virtual Flux-based reactive power control with current limitation has been tested for the same range of cases as presented for active power control with current limitation. In this case, the different control strategies corresponds to; 1) elimination of reactive power oscillations by the PNSC strategy ($k_q = -1$), 2) operation with balanced positive sequence currents according to the BPSC strategy ($k_q = 0$), and 3) elimination of active power oscillations by the AARC strategy ($k_q = 1$). To illustrate the operation with a different unbalanced grid fault, the cases with current limited reactive power control are presented for the case of a two-phase fault condition, with the voltage sage generator set to generate a voltage drop of about 50 % in both phase *a* and *b* under no-load conditions.

5.6.3.1 Elimination of reactive power oscillations by current limited PNSC

The results from a case with a pre-fault reactive power reference of 1.0 pu and power control by current limited PNSC is shown in Fig. 5-16. In this case, the reactive power injection is causing the voltage to increase significantly above 1.0 in the pre-fault condition. As mentioned regarding the limitations of the experimental setup discussed in section 4.4.2, this is causing additional degradation of the current controller performance. This can be observed as a significant low-frequency distortion, with a predominant second harmonic component, of the current waveforms. Thus, there is a

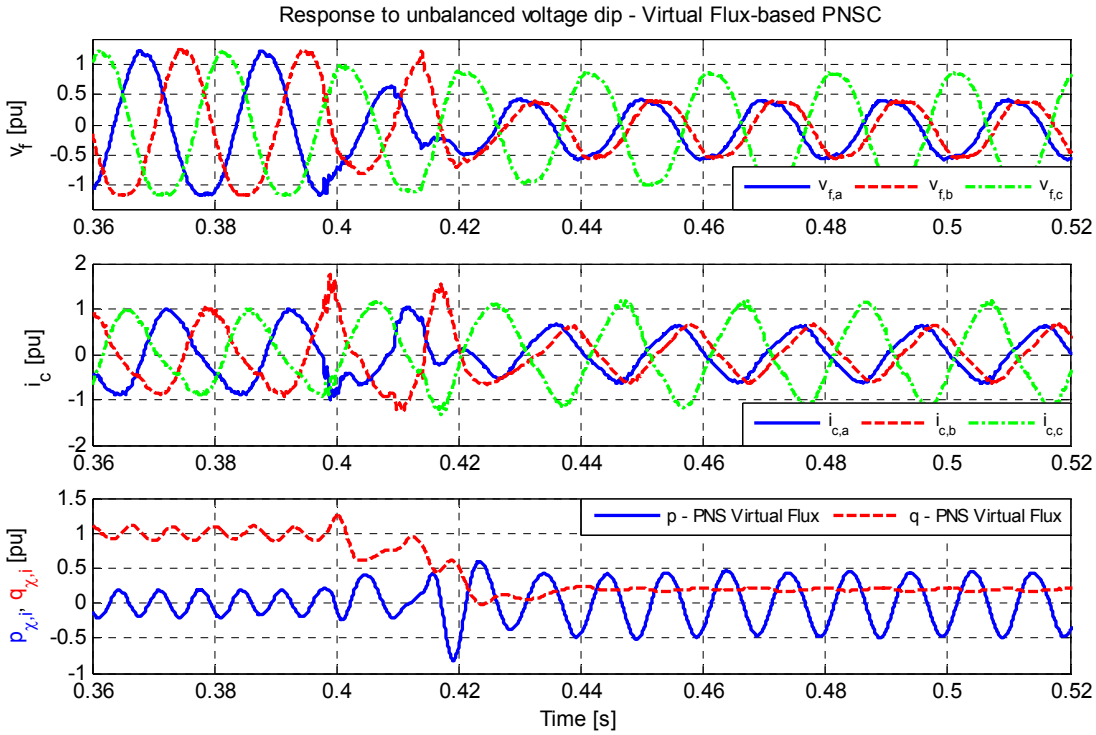

Fig. 5-16 Reactive power control by PNSC with the amplitude of the reactive current vector reference i_q^* limited to 1.08 pu

significant third harmonic oscillation in the active and reactive power flow during the pre-fault conditions.

When the fault occurs, there is a significant transient due to the electromechanical operation of the voltage sag generator, but the dynamic response of the system is fast and well damped as soon as the voltage drop is stabilized. It can be noted that the transient is more severe than for the previously presented cases where only one of the phase-voltages is influenced by the fault, since the two-phase fault condition requires that two of the phases are reconfigured by the electromechanical contactors of the voltage sag generator. From the figure, it can also be seen that is less low frequency distortion of the currents during the unbalanced conditions, although significant higher frequency distortion remain both in the voltages and currents. This is partly because the voltage drop makes a larger margin between the peak phase voltages and the DC-link voltage of the converter.

During the fault, it can be seen that the highest current is injected in the phase with the highest remaining voltage, but phase shifted by 90° in time since it is a purely reactive current. The current in phase *c* is however kept within the specified limit during steady-state unbalanced conditions.

The trajectories of the estimated Virtual Flux and the calculated current reference are shown in Fig. 5-17, where it can be seen how the Virtual Flux trajectory is a relatively narrow ellipse aligned with the *c*-axis, since the voltage is reduced in both phase *a* and *b*. The figure also shows how the reactive current reference is kept proportional to the Virtual Flux trajectory by the PNSC strategy. The orientation of the elliptic current trajectory will therefore be perpendicular to the orientation of the trajectories for $\boldsymbol{v}_\perp$ and $(\boldsymbol{\chi}^+ - \boldsymbol{\chi}^-)$ that are determining the reactive power injection according to (4.2) and (4.12).

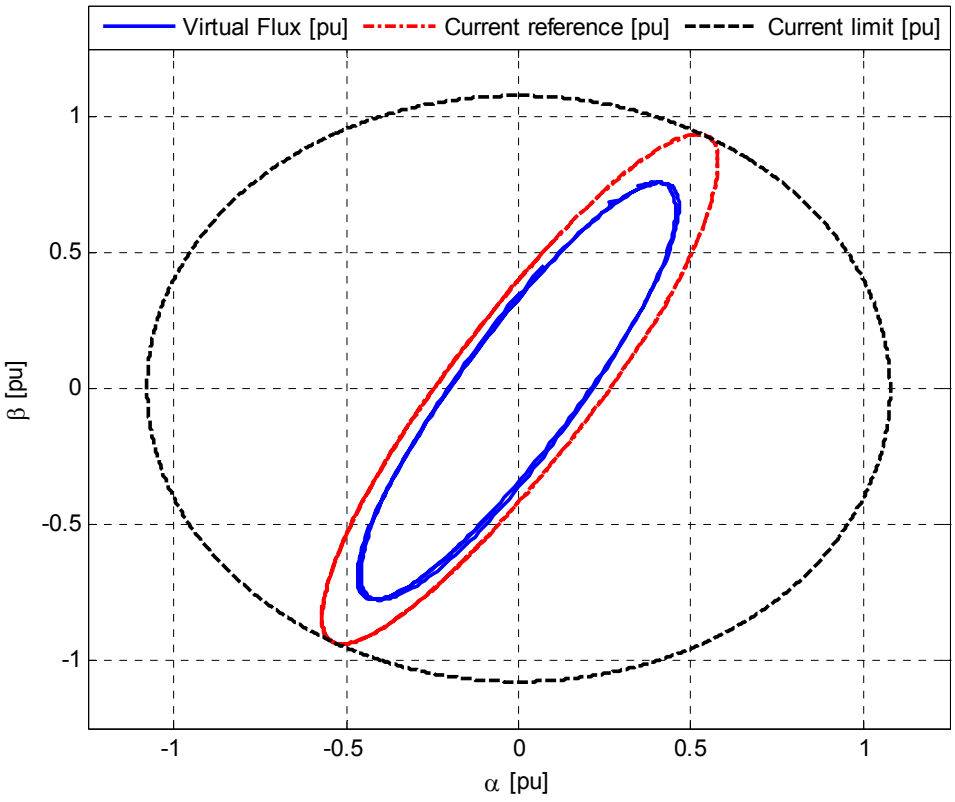

Fig. 5-17 Trajectory of estimated Virtual Flux and calculated current reference for current limited reactive power control by PNSC

The trajectories in Fig. 5-17 also show how the current reference is kept within the specified current limit. Since the elliptic current trajectory in this case is aligned along the axis of the c phase, the maximum phase current amplitude observed in Fig. 5-16 corresponds to the specified reactive current limit of 1.08 pu.

Since the fault conditions investigated in this case is more severe than the single-phase voltage sags shown for the previously presented experimental results, it should be expected that the average reactive power transfer is significantly reduced. The active and reactive powers plotted in the lower part of Fig. 5-16 therefore show how the reactive power in this case is reduced from the specified 1.0 pu before the fault to about 0.25 pu during the fault. The curves are however showing that the control objective of eliminating double frequency reactive power oscillations is however maintained, and second harmonic oscillations are therefore appearing only in the active power flow.

5.6.3.2 Operation with current limited BPSC

Results for current limited operation with balanced three-phase currents are shown in Fig. 5-18. A significant transient in voltages and currents can again be observed when the voltage sag occurs, but this is mainly due to the operation of the electromechanical contactors of the voltage sag generator. As for the case of PNSC, it can be observed that there is low frequency distortion in the currents before the fault, and less distortions during the fault.

From the plotted curves, it can be seen that the currents are controlled to be balanced and with amplitudes equal to the specified limit within short time after the occurrence of

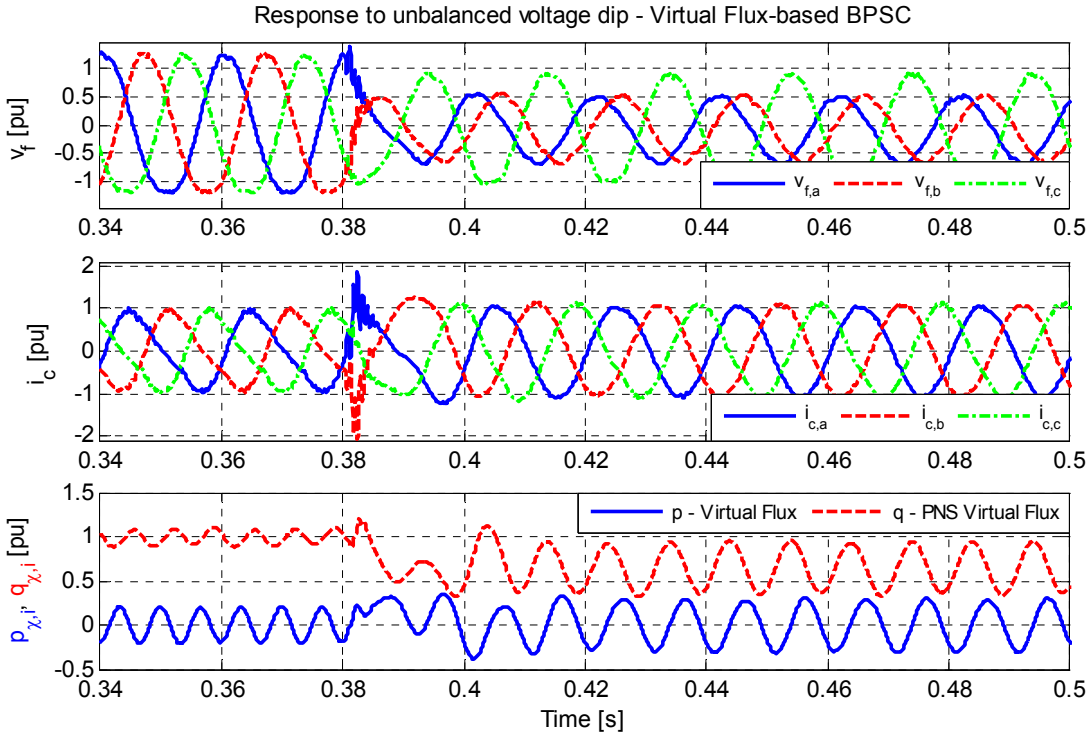

Fig. 5-18 Reactive power control by BPSC with the vector amplitude of the reactive current reference i_q^* limited to 1.08 pu

the voltage sag. Due to the current limitation, the average reactive power is reduced from the pre-fault value of 1.0 pu to about 0.7 pu, and the characteristic double frequency oscillations are observed in both the active and reactive powers.

5.6.3.3 Elimination of active power oscillations by current limited AARC

In Fig. 5-19 results are shown for the case of reactive power control by AARC with current vector amplitude limitation. The behavior before the fault and the transient at the occurrence of the voltage sag are however similar to what has been described for the previous cases.

For this case, the current trajectory should be monotonously proportional to the trajectory given by the in-quadrature voltage vector $\boldsymbol{v}_\perp$ or by $\boldsymbol{\chi}^+ - \boldsymbol{\chi}^-$, as can be seen from (4.42). The orientation of the current trajectory should therefore be perpendicular to the trajectories of the voltage and the Virtual Flux. Accordingly, the largest current should be injected in the phase with the lowest remaining voltage, while the smallest current should be injected in the phase with the highest remaining voltage. This characteristics can be clearly recognized in Fig. 5-19 where a reactive current close to the vector amplitude limitation is flowing in phase *a* and *b*, while a lower current is injected in phase *c*. It can also be seen from the figure how the currents are phase shifted with respect to the voltages since only reactive power should be injected from the VSC into the grid.

From the plots of the active and reactive powers, it is clearly seen that the objective of eliminating double frequency active power oscillations during the unbalanced conditions is achieved. The average reactive power flow is however reduced from the

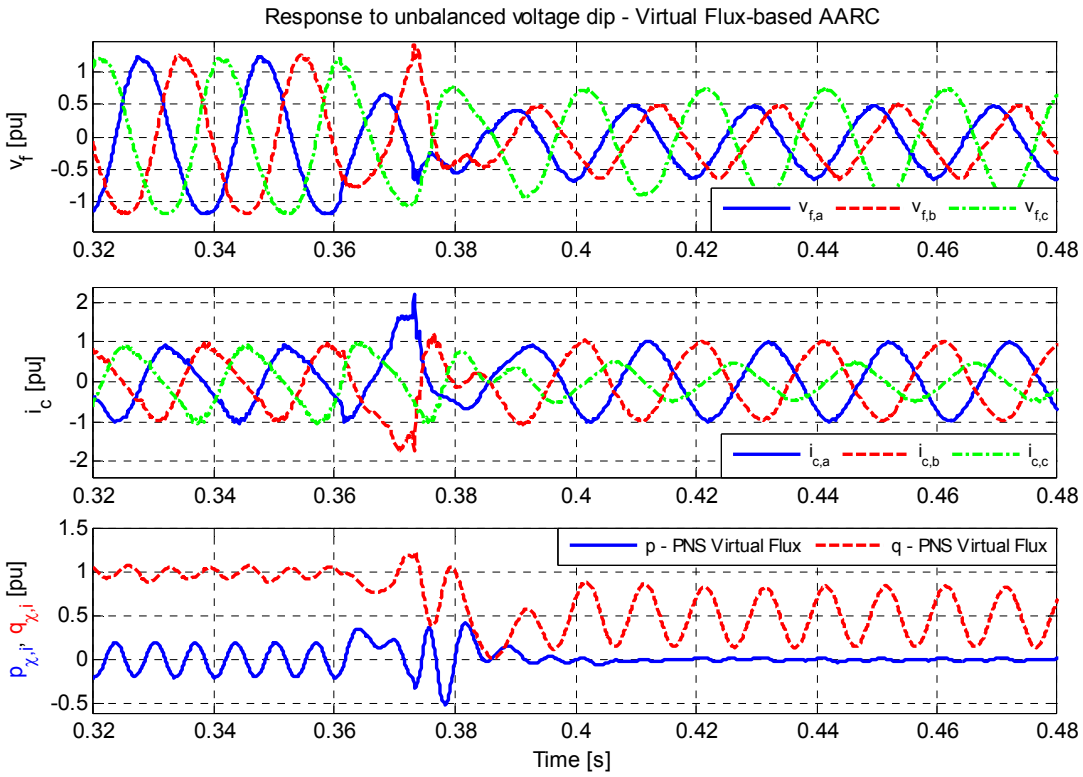

Fig. 5-19 Reactive power control by AARC with the vector amplitude of the reactive current reference i_q^* limited to 1.08 pu

pre-fault value of 1.0 pu to about 0.5 pu due to the current limitation. By comparing to the case previous cases, it can be noticed that the average reactive power flow is limited to a value slightly below what was achieved by the BPSC, but significantly higher than for the case of PNSC.

5.7 Maximum Current and Current Limitation Strategies with Simultaneous Control of Active and Reactive Power

The results from simulation and experiments presented in the previous subsections have all been limited to cases with only active or reactive power control. In many cases, simultaneous control of both active and reactive power will however be required, and the total current should then be limited below the maximum current limit of the VSC. This will require a mechanism for prioritizing the active and reactive current components. Such priorities will depend on the application, but was for instance discussed in [231] for the case of a wind turbine. Implementation of the current component priority might require a separate control loop for adapting to the actual operating conditions and will therefore not be further discussed. The basic relations for calculating the maximum current resulting from the active and reactive power control will however be discussed on basis of the previously presented results, and the conditions under which the priority of active and reactive current components within the available current limitation can be easily implemented should be clarified.

5.7.1 Calculation of Total Current Amplitude in Case of Simultaneous Control of Active and Reactive Power Flow

Considering that the constants k_p and k_q which are used to specify the power control objectives can be allowed to have any value between -1 and l, there could be an infinitely range of combinations that should be investigated when considering limitation of the total current vector. However, in most cases, only the three following distinct combinations of control objectives for the active and reactive power flow during unbalanced conditions will be of main importance.

5.7.1.1 Maximum current with active and reactive power control for elimination of double frequency active power oscillations

In case the overall power control objective is to eliminate second harmonic oscillations in the active power flow during unbalanced conditions, the active power flow must be controlled according to the PNSC strategy by specifying $k_p = -1$, while the reactive power flow must be controlled according to the AARC strategy by selecting $k_q = 1$. Thus, both the active and the reactive current references will have trajectories that are oriented perpendicularly to the voltage or Virtual Flux trajectories. The reactive current reference will however always be phase shifted by ±90° in time with respect to the voltage. Therefore the peak vector amplitude of the total current trajectory can be easily calculated by the traditional square sum as given by (5.25).

$$\left|\hat{\mathbf{i}}^*\right| = \sqrt{\left|\hat{\mathbf{i}}_p^*\right|^2 + \left|\hat{\mathbf{i}}_q^*\right|^2} \tag{5.25}$$

5.7.1.2 Maximum current for operation with balanced three-phase currents

When the control objective is to achieve balanced three-phase currents in the converter, the BPSC strategy should be used for both active and reactive power control by specifying $k_p = 0$ and $k_q = 0$. The total current vector amplitude will then be constant and can be found by traditional calculations for balanced conditions, corresponding to (5.25).

5.7.1.3 Maximum current with active and reactive power control for elimination of double frequency reactive power oscillations

If the main control objective is to eliminate double frequency reactive power oscillations, the active power flow should be controlled according to the AARC strategy by selecting $k_p = 1$, while the reactive power flow should be controlled according to the PNSC strategy by selecting $k_q = -1$. In this case, the elliptic current trajectory under unbalanced conditions will have the same orientation as the voltage or Virtual Flux trajectory, with the reactive current reference phase-shifted by ±90° in time with respect to the active current reference. Therefore the peak vector amplitude can also in this case be calculated by (5.25).

5.7.1.4 Maximum current in case of different active and reactive power control objectives

In case of any other combinations of control objectives for the active and reactive power flow than the three cases discussed above, it will be more complicated to calculate the maximum current vector amplitude resulting from a set of active and

reactive power references. Since the simple equation given in (5.25) will not be generally valid if the active and reactive currents follow trajectories with different shapes or orientations in the stationary $\alpha\beta$ reference frame, a more detailed analysis will be required. Such an investigation can be intended to find the maximum current vector amplitude, or to identify the maximum phase current that will result. An outline of an approach that can be followed for such detailed investigations based on voltage measurements is presented in [96], and similar considerations can be made for investigations based on estimated Virtual Flux signals. The results of such derivations will however be more case-specific and less general than the considerations presented in this chapter, and are therefore considered outside the intended scope of investigation.

5.7.2 Current Limitation with Priority of either Active or Reactive Current

For the three cases with clearly defined power control objectives that were listed above, the maximum value of the current vector amplitude can be easily limited within the current capability of the converter by starting from (5.25). In case the active current control should have priority under unbalanced conditions, the reactive current reference will then be zero if the current needed to reach the active power reference is larger than the current limitation. However, if the active power reference can be fulfilled within the current limit of the converter, the maximum reactive current that can be injected by the converter will be given by (5.26). The value resulting from this equation can then be used as the reactive current limitation, labeled as $i_{q,Lim}$ in the equation, as it could be used directly in (5.24). The same approach could however also be used in the case of phase current limitation.

$$\left|\hat{\mathbf{i}}_{q,\lim}^{*}\right| = \sqrt{\left|\hat{\mathbf{i}}_{\lim}^{*}\right|^2 - \left|\hat{\mathbf{i}}_{p}^{*}\right|^2} \tag{5.26}$$

In case reactive power injection should be prioritized during the unbalanced conditions, the situation will be the opposite of what is implied by (5.26). However, the available active current limitation $i_{p,Lim}$ can be calculated according to the same considerations.

5.8 Summary of chapter

This chapter has presented derivations and analysis of methods for Virtual Flux-based power control strategies with current limitation for operation during unbalanced voltage sag. As a starting point for the derivations, the differences between methods for current vector amplitude limitation and for phase current limitation have been discussed. This has shown that techniques for phase current limitation can allow for current vector amplitudes to be about 15 % higher than the phase current limitation in particular cases of faults with zero remaining voltage in at least one of the phases.

Detailed expressions for current reference calculation and for calculating the maximum average active and reactive power transfer within a specified phase current limitation have then been developed and analyzed. On this basis, it has been shown how the maximum allowable current vector amplitude will be a function of the grid condition during the fault and the control objective determining the orientation of the current

trajectory with respect to the trajectory of the voltage or Virtual Flux. The developed strategies for phase current limitation during unbalanced conditions will protect the converter from over-currents by limiting the current references, and maintaining the specified control objective during unbalanced conditions by reducing the average active or reactive power flow. Simulation studies have been presented to verify and illustrate the operation of the developed strategies during severe single-phase faults with different control objectives.

Although phase current limitation allows for maximum utilization of a converters current capability while still maintaining the specified power control objectives, the resulting expressions for current reference calculation are complicated nonlinear equations. These equations depend on detection of the phase angle characterizing the positive and negative sequence components of the Virtual Flux. Simplified strategies for current vector amplitude limitation can therefore still be relevant for practical implementation. The expressions for current reference calculation under current vector amplitude limitation have been developed and have been shown to result in simple equations with general validity for maintaining the power control objectives. Strategies for current vector amplitude limitation have been verified by laboratory experiments and a wide range of results for operation with active and reactive power control have been presented and discussed.

In case of simultaneous control of active and reactive power, the current limitation must be prioritized between the active and reactive current components. The conditions when the total maximum current vector amplitude can be easily calculated have been identified and can be used for prioritizing the active and reactive current components. For other combinations of control objectives, detailed case-specific investigations will however be necessary.

Main contributions of Chapter:

- Analysis and discussion of phase current limitation versus conventional strategies for current vector amplitude limitation.
- Derivation and analysis of detailed expressions for maximum active and reactive power transfer capability and corresponding equations for current reference calculation during unbalanced conditions.
- Presentation of results illustrating current limited operation of a VSC in case of unbalanced voltage sags. Thus, grid synchronization based on the method proposed in Chapter 3 combined with active and reactive power control according to Chapter 4 and the current limitation strategies proposed in this Chapter can be considered a general approach for Virtual Flux-based voltage-sensor-less operation of VSCs

6 Conclusion and Suggestions for Further Research

A short summary of the main results from the previous chapters is presented here. On the basis of these results, possible applications of the developed methods and suggestions for further research on similar topics will be outlined.

6.1 Summary of Main Results and Contributions

The research question identified in section 1.2 has been addressed in three steps, as documented by the analysis and the results presented in Chapter 3, 4 and 5.

In chapter 3, a method for on-line frequency-adaptive Virtual Flux estimation based on utilization of a Second Order Generalized Integrator configured as a Quadrature Signal Generator (SOGI-QSG) has been proposed and analyzed. The SOGI-QSG was shown to be a suitable building block for Virtual Flux estimation, which can be used to implement simple and on-line frequency-adaptive, filter-based strategies for Virtual Flux estimation. Two SOGI-QSGs can also be operated in a proposed structure for Virtual Flux estimation which achieves inherent sequence separation. Since this structure is based on two SOGI-QSGs operating in parallel on the α- and β-axes, it can be labeled as a method for Dual SOGI-based Virtual Flux (DSOGI-VF) estimation. The operation and performance of this proposed estimation method has been verified by simulations and experiments, verifying that the transient response of the DSOGI-VF estimation method is similar to the response of DSOGI-based sequence separation of measured voltages. The DSOGI-VF estimation is therefore able to achieve Virtual Flux estimation under unbalanced grid voltage conditions with a faster and more damped transient response compared to other possible configurations. It has further been indicated how the DSOGI-VF estimation structure can be simplified or extended depending on the requirements of a particular application, and that it can be used to estimate the positive and negative sequence Virtual Flux components at different points in the AC system. The presented approach for Virtual Flux estimation can therefore be considered a suitable basis for frequency-adaptive grid synchronization with the inherent capability to operate during unbalanced conditions.

A general approach for deriving Virtual Flux-based equations for current reference calculation corresponding to different objectives for active and reactive power control has been presented in Chapter 4. This approach has been used to derive Virtual Flux-based equivalents to voltage-based strategies for active and reactive power flow control during unbalanced conditions. The resulting equations have been synthesized into a

generalized expression for current reference calculation where the power flow characteristics can be specified by two parameters. The active and reactive power flow characteristics, and the amplitudes of the double frequency oscillations corresponding to different objectives for active and reactive power control, have also been analyzed in a generalized way. Experimental results have been presented as verification of voltage-sensor-less operation based on the proposed approach. These results illustrate how the intended power flow characteristics could be achieved with reasonable accuracy even under non-ideal conditions with harmonic distortions in the grid voltage and degraded performance of the inner current control loops. Thus, the presented results and analysis indicate general validity of the assumption used to derive the Virtual Flux-based expressions for current reference calculation. The same approach can therefore be followed in case of other objectives for active and reactive power control, and can potentially be adapted to a wide range of applications and control system configurations.

Strategies for current limitation under unbalanced grid faults are investigated in Chapter 5. This chapter presents a general and simple evaluation and illustration of the differences between approaches for limiting the phase currents of the converter compared to strategies for limiting the current vector amplitude. For balanced conditions, and when operating with balanced three-phase currents during unbalanced conditions, there is no difference between limiting the amplitude of the phase currents and the conventional approach of current vector amplitude limitation that corresponds to imposing current limits in the synchronous reference frames. For operation with unbalanced currents during unbalanced grid faults, the maximum allowable current vector amplitude within the phase current limitation of the converter will, however, depend on the actual fault. General expressions for the maximum average active and reactive power flow that can be allowed while at the same time maintaining the desired power flow characteristics, with corresponding equations for current reference calculation have therefore been derived. The maximum current vector amplitude that can be allowed within the phase current limitation occurs for unbalanced faults with equal amplitudes of the remaining positive and negative sequence voltage components. Depending on the control objective, the current vector amplitude, and the corresponding active or reactive power flow under such conditions can be increased by about 15 % compared to the case when the current vector amplitude is limited. Simulation results have been presented to illustrate how the presented approach for active and reactive power control with selectable power flow characteristics is generally valid for unbalanced conditions when the phase current limitation is imposed. Strategies for current vector amplitude limitation have also been derived as a simplification of the presented approach for phase current limitation, and the operation of a VSC with current vector amplitude limitation has been verified by laboratory experiments.

6.2 Outline of Relevant Topics for Further Research

There are several topics that can be relevant for further studies and research by starting from the results presented in the previous chapters. Some of these issues can be of general interest with respect to power system stability studies involving grid integration of VSCs, while other issues are more related to the local control of individual converter units.

6.2.1 General Topics Related to Power System Integration and Stability of VSCs with Virtual Flux-based Grid Synchronization and Control

The discussion in section 3.5, indicated how the basis structure of the DSOGI-VF estimation can be utilized to estimate the Virtual Flux at different points in the AC system. Such considerations, based on simulation of another method for Virtual Flux estimation, have been further presented in [C2], [C3]. In these manuscripts, it was shown that the stability and loadability of a VSC injecting power into a high-impedance grid could be improved by increasing the impedance included in the Virtual Flux estimation and by that changing the point of synchronization to the grid. This stability improvement was attributed partly to the effect of increased reactive power support from the converter when changing the point of synchronization, and partly to the consideration that the control system was synchronized to a more stable point in the grid that would be less influenced by the operation of the converter itself. These considerations were based on trial-and-error simulations and were not supported by thorough analytical studies. Further studies based on the DSOGI-VF estimation method would therefore be relevant. It should also be noted that the outer loop controllers and the influence of the different active and reactive power control objectives under unbalanced conditions on the stability of the converter operation have not been investigated in this Thesis.

In the authors' opinion, the following topics could therefore be relevant for further studies based on the DSOGI-VF estimation method and the presented strategies for active and reactive power control:

- The stability of the converter control system, including the outer loop controllers and the impact of the different objectives for active and reactive power control, should be investigated under unbalanced grid voltage conditions. In particular, the stability in a weak grid with high impedance and significant variations in the grid frequency should be studied systematically.
- The influence of the point of synchronization selected for the DSOGI-VF estimation on the stability of the converter control system, and on the stability of the local power system should be systematically investigated.
- Further elaborations and studies could be relevant with respect to the ability of the converter to control the active power flow as well as the reactive power or the AC voltage in a remote point that is not available for real time voltage measurements. This could for instance be relevant for operation in wind turbines or industrial loads where the power factor or the grid voltage should be controlled at the grid side of a transformer or at a distant Point of Common Coupling (PCC).
- The selection of the parameters used for the Virtual Flux estimation could also be utilized to indirectly influence the active or reactive power flow of the converter. This could be considered a similar approach to the concept of Virtual Impedance known from UPS systems and control systems designed for parallel connection of VSCs. It could also be expected that influencing the active and/or reactive power control through the parameters of the Virtual Flux estimation can

be used to achieve a faster dynamic response than when acting through the outer loop controllers of a cascaded control system.

- The stability of the converter control system and the influence on the local power system should also be investigated when several VSCs with Virtual Flux-based grid control systems are operated in parallel and with synchronization to different points in the grid.
- The stability of closed loop active and reactive power control based on the DSOGI-VF estimation could be systematically studied with respect to the influence of harmonic distortions in the power system.

6.2.2 Relevant Topics for Further Investigation of Control Systems for VSCs based on the Proposed Approach for Virtual Flux Estimation and Power Control

As mentioned in Chapter 3, 4 and 5, there are several possibilities for extending the investigations presented in this Thesis. Some relevant issues related to control system implementation for individual converter units are listed in the following:

- The presented strategies for DSOGI-VF estimation and Virtual Flux-based power control can be further studied and analyzed for combination with various types of inner loop current controllers.
- The presented approach for active and reactive power control with selectable power flow characteristics could be applied to control systems based on Direct Power Control (DPC). The generalized equations describing the active and reactive power flow characteristics in section 4.3.4 could then constitute the basis for calculating the active and reactive power references.
- The implementation of the DSOGI-VF estimation could be further studied with respect to particular practical applications and in combination with various types of control strategies. There can for instance be relevant challenges with respect to discrete time implementation of the DSOGI-VF estimation in applications with low switching frequency, and when combined with inner loop controllers resulting in variable switching frequency.
- Possible enhancements and extensions of the DSOGI-VF estimation could be further investigated with respect to converter over-modulation or the presence of significant low frequency harmonics in the grid voltage.
- The DSOGI-VF estimation should be investigated and analyzed with respect to combination with methods for active damping of LCL filters.
- DC-link voltage oscillations under unbalanced grid voltages can be controlled by using the DSOGI-VF estimation to synchronize the control system to the terminals of the converter. It can further be relevant to investigate the particular case when the active power oscillations should be eliminated at the converter terminals, while the power factor or the average reactive power flow should be controlled at the grid side of the filter. This can be especially relevant for VSCs with minimized DC-link capacitance, where significant double frequency active power oscillations can cause unacceptable DC-link oscillations.

- The SOGI-QSG, considered as a basic building block for on-line frequency-adaptive Virtual Flux estimation, can also be utilized in single-phase systems. Thus, the SOGI-QSG-based Virtual Flux estimation could be investigated with respect to voltage-sensor-less control of single-phase VSCs.
- Voltage-sensor-less control of three-phase four-wire VSCs could be investigated based on the DSOGI-VF estimation method combined with a strategy for single-phase Virtual Flux estimation applied to the zero-sequence component.

6.3 Closing Remarks

Grid synchronization based on the proposed method for DSOGI-VF estimation from Chapter 3 combined with Virtual Flux-based power control and strategies for current limitation according to Chapter 4 and 5 can be considered as a general basis for voltage-sensor-less control of VSCs under unbalanced conditions and grid frequency variations. As outlined above, the results presented here can also serve as a starting point for a wide range of further investigations related to aspects of control and operation of grid connected VSCs. Thus, the identified research question from section 1.2 has been addressed, as the presented approach can be potentially adapted for implementation together with various types of inner loop control techniques and can be utilized in a wide range of applications.

7 References

[1] J. R. Rodríguez, J. W. Dixon, J. R. Espinoza, J. Pontt, P. Lezana, "PWM Regenerative Rectifiers: State of the Art," in *IEEE Transactions on Industrial Electronics*, Vol. 52, No. 1, February 2005, pp. 5-22

[2] M. Liserre, F. Blaabjerg, S. Hansen, "Design and Control of an LCL-Filter-Based Three-Phase Active Rectifier," in *IEEE Transactions on Industry Applications*, Vol. 41, No. 5, September 2005, pp. 1281-1291

[3] W. Gullvik, "*Modeling, Analysis and Control of Active Front End (AFE) Converter*," PhD Thesis, Norwegian University of Science and Technology, Trondheim, Norway, 2007

[4] S. Chakraborty, B. Kramer, B. Kroposki, "A review of power electronics interfaces for distributed energy systems toward achieving low-cost modular design," in *Renewable and Sustainable Energy Reviews*, Vol. 13, No. 9, December 2009, pp. 2323-2335

[5] M. Liserre, R. Cárdenas, M. Molinas, J. Rodríguez, "Overview of Multi-MW Wind Turbines and Wind Parks," in *IEEE Transactions on Industrial Electronics*, Vol. 58, No. 4, April 2011, pp. 1081-1095

[6] M. Molinas, "The Role of Power Electronics in Distributed Energy Systems," in *Proceedings of the 5th AIST Symposium on Distributed Energy Systems*, Tokyo, Japan, 9th of December 2008, 7 pp

[7] J. M. Carrasco, L. G. Franquelo, J. T. Bialasiewicz, E. Galván, R. C. P. Guisado, Ma. Á. M. Prats, J. I. León, N. Moreno-Alfonso, "Power-Electronic Systems for the Grid Integration of Renewable Energy Sources: A Survey," in *IEEE Transactions on Industrial Electronics*, Vol. 53, No. 4, August 2006, pp. 1002-1016

[8] T. Kerekes, R. Teodorescu, M. Liserre, C. Klumpner, M. Sumner, "Evaluation of Three-Phase Transformerless Photovoltaic Inverter Topologies," in *IEEE Transactions on Power Electronics*, Vol. 24, No. 9, September 2009, pp. 2202-2211

[9] C. Schauder, H. Mehta, "Vector analysis and control of advanced static VAR compensators," in *IEE Proceedings-C*, Vol. 140, No. 4, July 1993, pp. 299-306

[10] S. N. Kalachnikov, H. Berger, "AC-Drive with Three-Phase PWM-Rectifier as a Reactive Power Compensator," in *Proceedings of the Stockholm PowerTech International Symposium on Electric Power Engineering*, 18-22 June 1995, Stockholm, Sweeden, Vol. 3, pp. 426-431

[11] M. H. J. Bollen, A. Sannino, ”Voltage Control With Inverter-Based Distributed Generation,” in *IEEE Transactions on Power Delivery*, Vol. 20, No. 1, January 2005, pp. 519-520

[12] H. Akagi, “Trends in Active Power Line Conditioners,” in *IEEE Transactions on Power Electronics*, Vol. 9, No. 3, May 1994, pp. 263-268

[13] L. A. Morán, J. W. Dixon, R. R. Wallace, “A Three-Phase Active Power Filter Operating with Fixed Switching Frequency for Reactive Power and Current Harmonic Compensation,” in *IEEE Transactions on Industrial Electronics*, Vol. 42, No. 4, August 1995, pp. 402-408

[14] Information about ABB medium voltage frequency converters, available from http://www.abb.com/ProductGuide/, accessed January 2012

[15] Information about SIEMENS Medium Voltage Converters, available from http://www.automation.siemens.com/mcms/drives/en/frequency-converter/Pages/Default.aspx, accessed January 2012

[16] J. Böcker, J.Janning, H. Jebenstreit, ”High Dynamic Control of a Three-Level Voltage-Source-Converter Drive for a Main Strip Mill,” in *IEEE Transactions on Industrial Electronics*, Vol. 49, No. 5, October 2002, pp. 1081-1092

[17] H. Abu-Rub, J. Holtz, J. Rodriguez, G. Baoming, “Medium-Voltage Multilevel Converters – State of the Art, Challenges, and Requirements in Industrial Applications,” in *IEEE Transactions on Industrial Electronics*, Vol. 57, No. 8, August 2010, pp. 2581-2596

[18] B. R. Andersen, L. Xu, P. J. Horton, P. Cartwright, “Topologies for VSC transmission,” in *Power Engineering Journal*, June 2002, pp.142-150

[19] S. Cole, R. Belmans, “Transmission of Bulk Power – The History and Applications of Voltage-Source Converter High-Voltage Direct Current Systems,” in *IEEE Industrial Electronics Magazine*, September 20009, pp. 19-24

[20] N. Flourentzou, V. G. Agedelis, G. D. Demetriades, “VSC-Based HVDC Power Transmission Systems: an Overview,” in *IEEE Transactions on Power Electronics*, Vol. 24, No. 3, March 2009, pp. 592-602

[21] N. G. Hingoriani, L. Gyugyi, “*Understanding FACTS, Concepts and Technology of Flexible AC Transmission Systems*,” IEEE Press, New York, 2000

[22] A. Sannino, J. Svensson, T. Larsson, “Power-electronic solutions to power quality problems,” in *Electric Power System Research*, Vol. 66, No. 1 July 2003, pp. 71-82

[23] G. Olguin, M. H. J. Bollen, “Stochastic Assessment of Unbalanced Voltage Dips in Large Transmission Systems,” in *Proceedings of the 2003 IEEE Bologna PowerTech*, Bologna, Italy, 23-26 June 2003, Vol. 4, 8. pp.

[24] G. Olguin, “*Voltage Dip (Sag) Estimation in Power Systems based on Stochastic Assessment and Optimal Monitordin*,” PhD Thesis, Chalmers University of Technology, Göteborg, Sweeden, 2005

[25] M. H. J. Bollen, J. R. Gordon, S. Z. Djokic, K. Stockman, J. V. Milanovic, R. Neumann, G. Ethier, “Voltage-dip immunity: statistics and need for further work,” in *Proceedings of the International Conference on Renewable Energies and Power Quality*, IQREPQ’10, Granada, Spain, 23-25 March 2010, 6 pp.

[26] G. Saccomando, J. Svensson, "Transient Operation of Grid-connected Voltage Source Converter Under Unbalanced Voltage Conditions," in *Conference Record of the 2001 IEEE Industry Applications Conference and the 36th IAS Annual Meeting*, Chicago, Illinois, USA, 30 September – 4 October 2001, Vol. 4, pp. 2419-2424

[27] G. Saccomando, J. Svensson, A. Sannino, "Improving Voltage Disturbance Rejection for Variable-Speed Wind Turbines," in *IEEE Transactions on Energy Conversion*, Vol. 17, No.3, September 2002, pp. 422-428

[28] F. A. Maguees, J. Svensson, A. Sannino, "Transient Performance of Voltage Source Converter under Unbalanced Voltage Dips," in *Proceedings of the 2004 IEEE 34th Annual Power Electronics Specialists Conference*, Aachen, Germany, 20-25 June 2004, Vol. 2, pp. 1163-1168

[29] F. A. Magueed, J. Svensson, A. Sannino, "Transient Performance of Voltage Source Converter Connected to Grid through LCL Filter under Unbalanced Voltage Conditions," in *Proceedings of the 2005 IEEE Russia PowerTech*, St. Petersburg, Russia, 27-30 June 2005, pp. 1697-1703

[30] F. A. Magueed, J. Svensson, A. Sannino, "Design of Robust Converter Interface for Wind Power Applications," in *Wind Energy*, Vol. 8, No. 3, July-September 2005, pp. 319-332

[31] A. V. Stankovic, T. A. Lipo, "A Novel Control Method for Input Output Harmonic Elimination of the PWM Boost Type Rectifier Under Unbalanced Operating Conditions," in *IEEE Transactions on Power Electronics*, Vol. 16, No. 5, September 2001, pp. 603-611

[32] L. Xu, B. R. Andersen, P. Cartwright, "VSC Transmission Operating Under Unbalanced AC Conditions – Analysis and Control Design," in *IEEE Transactions on Power Delivery*, Vol. 20, No. 1, January 2005, pp. 427-434

[33] M. Tsili, S. Papathanassiou, "A review of grid code technical requirements for wind farms," in *IET Renewable Power Generation*, Vol. 3, No. 3, September 2009, pp. 308-332

[34] Y. Suh, Y. Go, D. Rho, "A Comparative Study on Control Algorithms for Active Front-End Rectifier of Large Motor Drives Under Unbalanced Input," in *IEEE Transactions on Industry Applications*, Vol. 47, No. 3, May/June 2011, pp. 1419-1431

[35] L. Morán, P. D. Ziogas, G. Joos, "Design Aspects of Synchronous PWM Rectifier-Inverter Systems under Unbalanced Input Voltage Conditions," in *IEEE Transactions on Industry Applications*, Vol. 28, No. 6, November/December 1992, pp. 1286-1293

[36] Y. Jiang, Å. Ekström, "General Analysis of Harmonic Transfer Through Converters," in *IEEE Transactions on Power Electronics*, Vol. 12, No. 2, March 1997, pp. 287-293

[37] A. Sannino, M. H. J. Bollen, J. Svensson, "Voltage Tolerance Testing of Three-Phase Voltage Source Converters," in *IEEE Transactions on Power Delivery*, Vol. 20, No. 2, April 2005, pp. 1633-1639

[38] C. Du, A. Sannino, M. H. J. Bollen, "Analysis of response of VSC-based HVDC to unbalanced faults with different control systems," in *Proceedings of the 2005*

IEEE/PES Transmission and Distribution Conference & Exhibition: Asia and Pacific, Dalian, China, 15-18 Augus, 2005, 6 pp.

[39] F. Blaabjerg, R. Teodorescu, M. Liserre, A. V. Timbus, "Overview of Control and Grid Synchronization for Distributed Power Generation Systems," in *IEEE Transactions on Industrial Electronics*, Vol. 53, No. 5, Oct. 2006, pp. 1398-1409

[40] V. Kaura, V. Blasko, "Operation of a Phase Locked Loop System Under Distorted Utility Conditions," in *IEEE Transactions on Industry Applications*, Vol. 33, No. 1, January/February 1997, pp. 58-63

[41] S.–K. Chung, "Phase-locked loop for grid-connected three-phase power conversion systems," in *IEE Proceedings on Electric Power Applications*, Vol. 147, No. 3, May 2000, pp. 213-219

[42] S.-K. Chung, "A Phase Tracking System for Three Phase Utility Interface Inverters," in *IEEE Transactions on Power Electronics*, Vol. 15, No. 3, May 2000, pp. 431-438

[43] L. N. Arruda, S. M. Silva, B. J. C. Filho, "PLL Structures for Utility Connected Systems," in *Conference Record of the 2001 IEEE Industry Applications Conference and the 36th IAS Annual Meeting*, Chicago, Illinois, USA, 30 September – 4 October 2001, Vol. 4, pp. 2655-2660

[44] A. V. Timbus, R. Teodorescu, F. Blaabjerg, M. Liserre, "Synchronization Methods for Three Phase Distributed Power Generation Systems, An Overview and Evaluation," in *Proceedings of the 36th IEEE Power Electronics Specialists Conference*, PESC'05, Recife, Brazil, 12-18 June 2005, pp. 2474-2481

[45] P. Rodríguez, J. Pou, J. Bergas, J. I. Candela, R. P. Burgos, D. Boroyevich, "Decoupled Double Synchronous Reference Frame PLL for Power Converters Control," in *IEEE Transactions on Power Electronics*, Vol. 22, No. 2, March 2007, pp. 584-592

[46] A. Ghoshal, J, V. John, "A Method to Improve PLL Performance Under Abnormal Grid Conditions," in *Proceedings of the National Power Electronics Conference*, Bangalore, India, 17-19 December 2007, 7 pp.

[47] F. D. Freijedo, J. Doval-Gandoy, O. Lopez, J. Cabaleiro, "Robust Phase Locked Loops Optimized for DSP Implementation in Power Quality Applications," in *Proceedings of the 34th Annual Conference of the IEEE Industrial Electronics Society*, IECON 2008, Orlando, Florida, USA, 10-13 November 2008, pp. 3052-3057

[48] E. Robles, S. Ceballos, J. Pou, J. J. Martín, J. Zaragoza, P. Ibañez, "Variable-Frequency Grid-Sequence Detector Based on a Quasi-Ideal Low-Pass Filter Stage and A Phase Locked Loop," in *IEEE Transactions on Power Electronics*, Vol. 25, No. 10, October 2010, pp. 2552-2563

[49] S.-J. Lee, J.-K. Kang, S.-K. Sul, "A New Phase Detecting Method for Power Conversion Systems Considering Distorted Conditions in Power Systems," in *Conference Record of the 1999 IEEE Industry Applications Conference and Thirty-Fourth IAS Annual Meeting*, Phoenix, Arizona, USA, 3-7 October 1999, Vol. 4, pp. 2167-2172

[50] R. F. de Camargo, H. Pinheiro, "Synchronization method for three-phase PWM converters under unbalanced and distorted grid," in *IEE Proceedings on Electric Power Applications*, Vol. 153, No. 5, September 2006, pp. 763-772

[51] P. Rodríguez, R. Teodorescu, I. Candela, A. V. Timbus, M. Liserre, F. Blaabjerg, "New Positive-Sequence Voltage Detector for Grid Synchronization of Power Converters Under Faulty Grid Conditions," in *Proceedings of the 37th Annual IEEE Power Electronics Specialists Conference*, PESC'06, Jeju, Korea, 18-22 June 2006, 7 pp.

[52] P. Rodríguez, A. Luna, M. Chiobotaru, R. Teodorescu, F. Blaabjerg, "Advanced Grid Synchronization System for Power Converters under Unbalanced and Distorted Operating Conditions," in *Proceedings of the 32nd Annual Conference of the IEEE Industrial Electronics Society*, IECON 2006, Paris, France, 6-10 November 2006, pp. 5173-5178

[53] J. Svensson, M. Bongiorno, A. Sannino, "Practical Implementation of Delayed Signal Cancellation Method for Phase-Sequence Separation," in *IEEE Transactions on Power Delivery*, Vol. 22, No. 1, January 2007, pp. 18-26

[54] L. R. Limongi, R. Bojoi, C. Pica, F. Profumo, A. Tenconi, "Analysis and Comparison of Phase Locked Loop Techniques for Grid Utility Applications," *in Proceedings of the Power Conversion Conference*, PCC'07, Nagoya, Japan, 2-5 April 2007, pp. 674-681

[55] F. Wang, M. C. Benhabib, J. L. Duarte, M. A. Hendrix, "High Performance Stationary Frame Filters for Symmetrical Sequences or Harmonics Separation Under a Variety of Grid Conditions," in *Proceedings of the 24th Annual IEEE Applied Power Electronics Conference and Exposition*, APEC 2009, Washington DC, USA, 15-19 February 2009, pp. 1570-1576

[56] X. Guo, W. Wu, Z. Chen, "Multiple-Complex Coefficient-Filter-Based Phase-Locked Loop and Synchronization Technique for Three-Phase Grid-Interfaced Converters in Distributed Utility Networks," in *IEEE Transactions on Industrial Electronics*, Vol. 58, No. 4, April 2011, pp. 1194-1204

[57] M. Boyra, J.-L. Thomas, "A review on synchronization methods for grid-connected three-phase VSC under unbalanced and distorted conditions," in *Proceedings of the 14th European Conference on Power Electronics and Applications*, EPE 2011, Birmigham, UK, 30 August – 1 September 2011, 8 pp.

[58] Y. Ito, Y. Kanno, S. Kawauchi, "Source Voltage Sensor-less Digital Control Using Observer for PWM Converter," in *Proceedings of the 25th Annual Power Electronics Specialists Conference*, PESC'94, Taipei, Taiwan, 20-25 June 1994, Vol. 1, pp. 160-165

[59] T. Noguchi, H. Tomiki, S. Kondo, I. Takahashi, "Direct Power Control of PWM Converter Without Power-Source Voltage Sensors," in *Conference Record of the 1996 IEEE Industry Applications Conference and the Thirty-First IAS Annual Meeting,* IAS'96, San Diego, California, USA, 6-10 October 1996, Vol. 2, pp. 941-946

[60] T. Noguchi, H. Tomiki, S. Kondo, I. Takahashi, "Direct Power Control of PWM Converter Without Power-Source Voltage Sensors," in *IEEE Transactions on Industry Applications*, Vol. 34, No. 3, May/June 1998, pp. 473-479

[61] I. Agirman, V. Blasko, “A Novel Control Method of a VSC Without AC Line Voltage Sensors,” in *IEEE Transactions on Industry Applications*, Vol. 39, No. 2, March/April 2003, pp. 519-524

[62] S. Hansen, M. Malinowski, F. Blaabjerg, M. P. Kazmierkowski, ”Sensorless Control strategies for PWM Rectifier,” in *Proceedings of the fifteenth Annual IEEE Applied Power Electronics Conference and Exposition*, APEC 2000, New Orleans, Louisiana, USA, 6-10 February 2000, Vol. 2, pp. 832-838

[63] P. Barrass, M. Cade, “PWM rectifier using indirect voltage sensing,” in *IEE Proceedings – Electric Power Applications*, Vol. 146, No. 5, September 1999, pp. 539-544

[64] B.-H. Kwon, J.-H. Youm, J.-W. Lim, K.-W Seok, G.-Y. Jeong, “Three-phase PWM synchronous rectifiers without line voltage sensors,” in *IEE Proceedings – Electric Power Applications,* Vol. 146, No. 6, November 1999, pp. 632-636

[65] B.-H. Kwon, J.-H. Youm, J.-W. Lim, “A Line-Voltage-Sensorless Synchronous Rectifier,” in *IEE Transactions on Power Electronics*, Vol. 14, No. 5, September 1999, pp. 966-972

[66] M. Malinowski, M. P. Kazmierkowski, S. Hansen, F. Blaabjerg, G. Marques, “Virtual-Flux –Based Direct Power Control of Three-Phase PWM Rectifiers,” in *Conference Record of the 2000 IEEE Industry Applications Conference and Thirty-Fifth IAS Annual Meeting and World Conference on Industrial Applications of Electrical Energy*, Rome, Italy, 8-12 October 2000, Vol. 4, pp. 2369-2375

[67] M. Malinowski, M. P. Kazmierkowski, S. Hansen, F. Blaabjerg, G. D. Marques, “Virtual-Flux-Based Direct Power Control of Three-Phase PWM Rectifiers,” in *IEEE Transactions on Industry Applications*, Vol. 37, No. 4, July/August 2001, pp. 1019-1027

[68] M. Malinowski, “*Sensorless Control Strategies for Three-Phase PWM Rectifiers*,” PhD Thesis, Warsaw University of Technology, Warsaw, Poland, 2001

[69] M. P. Kazmierkowski, L. Malesani, “Current Control Techniques for Three-Phase Voltage Source PWM Converters: A Survey,” in *IEEE Transactions on Industrial Electronics*, Vol. 45, No. 5, October 1998, pp. 691-703

[70] D. M. Brod, D. W. Novotny, “Current Control of VSI-PWM Inverters,” in *IEEE Transactions on Industry Applications*, Vol. IA-21, No. 4, May/June 1985, pp. 562-570

[71] J. W. Dixon, B.-T. Ooi, “Indirect Current Control of a Unity Power Factor Sinusoidal Current Boost Type Three-Phase Rectifier,” in *IEEE Transactions on Industrial Electronics*, Vol. 35, No. 4, November 1988, pp. 508-515

[72] N. R. Zargari, G. Joós, “Performance Investigation of a Current-Controlled Voltage-Regulated PWM Rectifier in Rotating and Stationary Frames,” in *IEEE Transactions on Industrial Electronics*, Vol. 42, No. 4, August, 1995, pp. 369-401

[73] M. P. Kazmierkowski, M. A. Dzieniakowski, “Review of Current Regulation Methods for VS-PWM Inverters,” in *Proceedings of the Budapest IEEE*

International Symposium on Industrial Electronics, ISIE'93, Budapest, Hungary, 1-3 June 1993, pp. 448-456

[74] R. F. de Camargo, H. Pinheiro, "Comparison of Six Digital Current Control Techniques for Three-Phase Voltage-Fed PWM Converters Connected to the Utility Grid," in *Proceedings of the IEEE 36th Power Electronics Specialists Conference*, PESC'2005, Recife, Brazil, 12-16 June 2005, pp. 1422-1428

[75] D. N. Zmood, D. G. Holmes, "Stationary Frame Current Regulation of PWM Inverters With Zero Steady-State Error," in *IEEE Transactions on Power Electronics*, Vol. 18, No. 3, May 2003, pp. 814-822

[76] S. Fukada, R. Imamura, "Application of a Sinusoidal Internal Model to Current Control of Three-Phase Utility-Interface Converters," in *IEEE Transactions on Industrial Electronics*, Vol. 52, No. 2, April 2005, pp. 420-426

[77] R. Teodorescu, F. Blaabjerg, M. Liserre, P. C. Loh, "Proportional-resonant controllers and filters for grid-connected voltage-source converters," in *IET Proceedings – Electric Power Applications*, Vol. 153, No. 5, September 2006, pp. 750-762

[78] P. Cortés, M. P. Kazmierkowski, R. M. Kennel, D. E. Quevedo, J. Rodríguez, "Predictive Control in Power Electronics and Drives," in *IEEE Transactions on Industrial Electronics*, Vol. 55, No. 12, December 2008, pp 4312-4324

[79] J. Rodríguez, J. Pontt, C. A. Silva, P. Correa, P. Lezana, P. Cortés, U. Ammann, "Predictive Current Control of a Voltage Source Inverter," in *IEEE Transactions on Industrial Electronics*, Vol. 54, No. 1, February 2007, pp. 495-503

[80] M. Malinowski, M. Jasiński, M. P. Kazmierkowski, "Simple Direct Power Control of Three-Phase PWM Rectifier Using Space Vector Modulation (DPC-SVM)," in *IEEE Transactions on Industrial Electronics*, Vol. 51, No. 2, April 2004, pp. 447-454

[81] S. Buso, P. Mattavelli, "*Digital Control in Power Electronics*," Morgan & Claypool, 2006, ISBN: 9781598291124

[82] J. A. Houldsworth, D. A. Grant, "The Use of Harmonic Distortion to Increase the Output Voltage of a Three-Phase PWM Inverter," in *IEEE Transactions on Industry Applications*, Vol. IA-20, No. 5, September/October 1984, pp. 1224-1228

[83] M. A. Boost, P. D. Ziogas, "State-of-the-Art Carrier PWM Techniques: A Critical Evaluation," in *IEEE Transactions on Industry Applications*, Vol. 24, No. 2, March/April 1988, pp. 271-280

[84] K. Zhou, D. Wang, "Relationship Between Space-Vector Modulation and Three-Phase Carrier-Based PWM: A Comprehensive Analysis," in *IEEE Transactions on Industrial Electronics*, Vol. 49, No. 1, February 2002, pp. 186-196

[85] D. N. Zmood, D. G. Holmes, G. H. Bode, "Frequency-Domain Analysis of Three-Phase Linear Current Regulators," in *IEEE Transactions on Industry Applications*, Vol. 37, No. 2, March/April 2001, pp. 601-610

[86] P. N. Lan, V. Mueller, L. H. Viet, "High Dynamic Control of a PWM Rectifier under Unbalanced Voltage Supply with Deadbeat Current Controllers" in *Proceedings of the 11th European Conference on Power Electronics and Applications*, EPE 2005, Dresden, Germany, 11-14 September 2005, 11 pp.

[87] M. Liserre, R. Teodorescu, F. Blaabjerg, "Multiple Harmonics Control for Three-Phase Grid Converter Systems With the Use of PI-RES Current Controller in a Rotating Frame," in *IEEE Transactions on Power Electronics*, Vol. 21, No. 3, May 2006, pp. 836-841

[88] S. Alepuz, S. Busquets-Monge, J. Bordonau, J. A. Martínez-Velasco, C. A. Silva, J. Pontt, J. Rodríguez, "Control Strategies Based on Symmetrical Components for Grid-Connected Converters Under Voltage Dips," in *IEEE Transactions on Industrial Electronics*, Vol. 56, No. 6, June 2009, pp. 2162-2172

[89] H.-S. Song, K. Nam, "Dual Current Control Scheme for PWM Converters Under Unbalanced Input Voltage Conditions," in *IEEE Transactions on Industrial Electronics*, Vol. 46, No. 5, October 1999, pp. 953-959

[90] A. Timbus, M. Liserre, R. Teodorescu, P. Rodriguez, F. Blaabjerg, "Evaluation of Current Controllers for Distributed Power Generation Systems," in *IEEE Transactions on Power Electronics*, Vol. 24, No. 3, March 2009, pp. 654-664

[91] P. Verdelho, G. D. Marques, "DC Voltage Control and Stability Analysis of PWM-Voltage-Type Reversible Rectifier," in *IEEE Transactions on Industrial Electronics*, Vol. 45, No. 2, April 1998, pp. 263-273

[92] D. Salomonsson, A. Sannino, "Comparative Design and Analysis of dc-Link-Voltage Controllers for Grid-Connected Voltage-Source Converter," in *Conference Record of the 2007 IEEE Industry Applications Conference and 42nd Annual Meeting*, New Orleans, Lousiana, USA, 23-27 September 2007, pp. 1593-1600

[93] M. K. Mishra, K. Karthikeyan, "A Fast-Acting DC-Link Voltage Controller for Three-Phase DSTATCOM to Compensate AC and DC Loads," in *IEEE Transactions on Power Delivery*, Vol. 24, No. 4, October 2009, pp. 2291-2299

[94] W. Freitas, A. Morelato, W. Xu, F. Sato, "Impacts of AC Generators and DSTATCOM Devices on the Dynamic Performance of Distributed Systems" in *IEEE Transactions on Power Delivery*, Vol. 20, No. 2, April 2005, pp. 1493-1501

[95] S. M. Muyeen, R. Takahashi, M. H. Ali, T. Murata, J. Tamura, "Transient Stability Augmentation of Power System Including Wind Farms by using ECS," in *IEEE Transactions on Power Systems*, Vol. 23, No. 3, August 2008, pp. 1179-1187

[96] R. Teodorescu, M. Liserre, P. Rodríguez, "*Grid Converters for Photovoltaic and Wind Power Systems*," Wiley / IEEE-press 2011

[97] H. Gaztañaga, I. Etxeberria-Otadui, D. Ocnasu, S. Bacha, "Real-Time Analysis of the Transient Response Improvement of Fixed-Speed Wind Farms by Using a Reduced-Scale STATCOM Prototype," in *IEEE Transactions on Power Systems*, Vol. 22, No. 2, May 2007, pp. 658-666

[98] P. Rioual, H. Pouliquen, J.-P. Louis, "Regulation of a PWM Rectifier in the Unbalanced Network State Using a Generalized Model," in *IEEE Transactions on Power Electronics*, Vol. 11, No. 3, May 1996, pp. 495-502

[99] Y. Suh, T. A. Lipo, "Control Scheme in Hybrid Synchronous Stationary Frame for PWM AC/DC Converter Under Generalized Unbalanced Operating

Conditions," in *IEEE Transactions on Industry Applications*, Vol. 42, No.3, May/June 2006, pp. 825-835

[100] M. Weinhold, "A new control for optimal operation of a three-phase voltage dc link PWM converter," in *Official Proceedings of the Nineteenth International Intelligent Motion (PCIM) Conference*, PCIM'91, Nürnberg, Germany, 25-27 June 1991, pp. 371-383

[101] M. C. Chandorkar, D. M. Divan, R. Adapa, "Control of Parallel Connected Inverters in Stand-Alone AC Supply Systems," in *Conference Records of the 1991 IEEE Industrial Applications Society Annual Meeting*, Dearborn, Michigan, USA, 28. September – 4. October 1991, pp. 1003-1009

[102] S. Bhattacharaya, A. Veltman, D. M. Divan, R. D. Lorentz, "Flux-Based Active Filter Controller," in *Conference Record of the 1995 IEEE Industry Applications Conference and the Thirtieth IAS Annual Meeting,* Orlando, Florida, USA, 8-12 October 1995, Vol. 3, pp. 2483-2491

[103] J. L. Duarte, A. van Zwam, C. Wijnands, A. Vandenput, "Reference Frames Fit for Controlling PWM Rectifiers," in *IEEE Transactions on Industrial Electronics*, Vol. 46, No. 3, June 1999, pp. 628-630

[104] V. Manninen, "Application of Direct Torque Control Modulation Technology to a Line Converter," in *Proceedings of the 6th European Conference on Power Electronics and Applications*, Sevilla, Spain, 19-21 Sept 1995, Vol. 1, pp. 292-296

[105] M. Malinowski, G. Marques, M. Cichowlas, M. P. Kazmierkowski, "New Direct Power Control of Three-Phase PWM Boost Rectifiers under Distorted and Imbalanced Line Voltage Conditions," in *Proceedings of the 2003 IEEE International Symposium on Industrial Electronics*, ISIE 2003, Rio de Janeiro, Brazil, 9-11 June 2003, Vol. 1, pp. 438-443

[106] M. Cichowlas, M. Malinowski, M. P. Kazmierkowski, D. L. Sobczuk, P. Rodriguez, J. Pou, "Active Filtering Function of Three-Phase PWM Boost Rectifier Under Different Line Voltage Conditions," in *IEEE Transactions on Industrial Electronics*, Vol. 52, No. 2, April 2005, pp. 410-419

[107] A. Kulka, "*Sensorless Digital Control of Grid Connected Three Phase Converters for Renewable Sources*," PhD Thesis, Norwegian University of Science and Technology, Trondheim, Norway, 2009

[108] P. Rodríguez, A. V. Timbus, R. Teodorescu, M. Liserre, F. Blaabjerg, "Independent PQ Control for Distributed Power Generation Systems under Grid Faults," in *Proceedings of the 32nd Annual Conference of the IEEE Industrial Electronics Society*, IECON 2006, Paris, France, 6-10 November 2006, pp. 5185-5190

[109] P. Rodriguez, A. V. Timbus, R. Teodorescu, M. Liserre, F. Blaabjerg, "Flexible Active Power Control of Distributed Power Generation Systems During Grid Faults, " in *IEEE Transactions on Industrial Electronics*, Vol. 54, No. 5, October 2007, pp. 2583-2592

[110] P. Rodríguez, A. Timbus, R. Teodorescu, M. Liserre, F. Blaabjerg, "Reactive Power Control for Improving Wind Turbine System Behavior Under Grid Faults," in *IEEE Transactions on Power Electronics*, Vol. 24, No. 7, July 2009, pp. 1798-1801

[111] F. Wang, J. L. Duarte, M. A. M. Hendrix, "Active Power Control Strategies for Inverter-Based Distributed Power Generation Adapted to Grid-Fault Ride-Through Requirements," in *Proceedings of the 13th European Conference on Power Electronics and Applications*, EPE'09, Barcelona, Spain, 8-10 September 2009, 10 pp.

[112] F. Wang, J. L. Duarte, M. A. M. Hendrix, "Active and Reactive Power Control Schemes for Distributed Generation Systems Under Voltage Dips," in *Proceedings of the 2009 IEEE Energy Conversion Congress and Exposition*, ECCE 2009, San Jose, California, USA, 20-24 September 2009, pp. 3564-3571

[113] F. Wang, J. L. Duarte, M. A. M. Hendrix, "Design and analysis of active power control strategies for distributed generation inverters under unbalanced grid faults," in *IET Generation, Transmission & Distribution*, Vol. 4, No. 8, August 2010, pp. 905-916

[114] F. Wang, J. L. Duarte, M. A. M. Hendrix, "Pliant Active and Reactive Power Control for Grid-Interactive Converters Under Unbalanced Voltage Dips," in *IEEE Transactions on Power Electronics*, Vol. 26, No. 5, May 2011, pp. 1511-1521

[115] P. Rodriguez, G. Medeiros, A. Luna, M. C. Cavalcanti, R. Teodorescu, "Safe Current Injection Strategies for a STATCOM under Asymmetrical Grid Faults," in *Proceedings of the 2010 IEEE Energy Conversion Congress and Exposition*, ECCE 2010, Atlanta, Georgia, USA, 12-16 September 2010, pp. 3929-3935

[116] V. Blasko, V. Kaura, "A New Mathematical Model and Control of a Three-Phase AC-DC Voltage Source Converter," in *IEEE Transactions on Power Electronics*, Vol. 12, No. 1, January 1997, pp. 116-123

[117] Y. A.-R. I. Mohamed, E. F. El-Saadany, M. M. A. Salama, "Adaptive Grid-Voltage Sensorless Control Scheme for Inverter-Based Distributed Generation," in *IEEE Transactions on Energy Conversion*, Vol. 24, No. 3, September 2009, pp. 683-694

[118] P. J. M. Smidt, J. L. Duarte, "An Unity Power Factor Convertor Without Current Measurement," in *Proceedings of the 6th European Conference on Power Electronics and Applications*, EPE'95, Sevilla, Spain, 19-21 Sept 1995, Vol. 3, pp. 275-280

[119] S. Bhowmik, A. van Zyl, R. Spée, J. H. R. Enslin, "Sensorless Current Control for Active Rectifiers," in *IEEE Transactions on Industry Applications*, Vol. 33, No. 3, May/June 1997, pp. 765-773

[120] W.-C. Lee, D.-S. Hyun, T.-K. Lee, "A Novel Control Method for Three-Phase PWM Rectifiers Using a Single Current Sensor," in *IEEE Transactions on Power Electronics*, Vol. 15, No. 5, September 2000, pp. 861-870

[121] D.-C. Lee, D.-S. Lim, "AC Voltage and Current Sensorless Control of Three-Phase PWM Rectifiers," in *IEEE Transactions on Power Electronics,*" Vol. 17, No. 6, November 2002, pp. 883-890

[122] T. Ohnuki, O. Miyashita, P. Lataire, G. Maggetto, "Control of a Three-Phase PWM Rectifier Using Estimated AC-Side and DC-Side Voltages," in *IEEE Transactions on Power Electronics*, Vol. 14, No. 2, March 1999, pp. 222-226

[123] Y. A.-R. I. Mohamed, E. F. El-Saadany, "Adaptive Discrete-Time Grid-Voltage Sensorless Interfacing Scheme for Grid-Connected DG-Inverters Based on Neural-Network Identification and Deadbeat Current Regulation," in *IEEE Transactions on Power Electronics*, Vol. 23, No. 1, January 2008, pp. 308-321

[124] T. Ohnishi, K. Fujii, "Line Voltage Sensorless Three Phase PWM Converter by Tracking Control of Operating Frequency," in *Proceedings of the Power Conversion Conference*, PCC'97, Nagaoka, Japan, 3-6 August 1997, Vol. 1, pp. 247-252

[125] G.-Y. Jeong, T.-J. Park, B.-H. Kwon, "Line-voltage-sensorless active power filter for reactive power compensation," in *IEE Proceedings – Electric Power Applications*, Vol. 147, No. 5, September 2000, pp. 385-390

[126] H. Zhu, B. Arnet, L. Haines, E. Shaffer, J.-S. Lai, "Grid Synchronization Control without AC Voltage Sensors," in *Proceedings of the Eighteenth Annual IEEE Applied Power Electronics Conference and Exposition*, APEC 2003, Miami Beach, Florida, USA, 9-13 February 2003, Vol. 1, pp. 172-178

[127] F. Hao. Y. Fang, R. Wang, Y. Xing, Y. Ma, "Digital Control Without Line Voltage Sensing for a Three Phase Bidirectional Inverter," in *Proceedings of the 11th International Conference on Electrical Machines and Systems*, ICEMS 2008, Wuhan, China, 17-20 October 2008, pp. 1506-1510

[128] R. M. Kennel, M. Linke. P. Szczupak, ""Sensorless" Control of 4-Quadrant-Rectifiers for Voltage Source Inverters (VSI)," in *Proceedings of the 34th Annual Power Electronics Specialists Conference*, PESC 2003, Acapulco, Mexico, 15-19 June 2003, Vol. 3, pp. 1057-1062

[129] P. Szczupak, R. Kennel, "Sensorless Control of PWM Rectifier by Distorted Supply Voltage," in *Proceedings of the 35th Annual Power Electronics Specialists Conference*, PESC '04, Aachen, Germany, 20-25 June 2004, pp 203-206

[130] S. Chattopadhyay, V. Ramanarayanan, "Digital Implementation of a Line Current Shaping Algorithm for Three Phase High Power Factor Boost Rectifier without input Voltage Sensing," in *Proceedings of the Sixteenth Annual IEEE Applied Power Electronics Conference and Exposition*, APEC 2001, Anaheim, California, USA, 4-8 March 2001, Vol. 1, pp. 592-598

[131] S. Chattopadhyay, V. Ramanarayanan, "Digital Implementation of a Line Current Shaping Algorithm for Three Phase High Power Factor Boost Rectifier without input Voltage Sensing," in *IEEE Transactions on Power Electronics*, Vol. 19, No. 3, May 2004, pp. 709-721

[132] M. Knapczyk, K. Pieńkowski, "Robust Current Control Technique for Boost-Type AC-DC Line Side Converter with Sliding-Mode Voltage Observer," in *Prace Naukowe Instytutu Maszyn, Napędów i Pomiarów, Politechniki Wrocławskiej (Scientific Work of the Institute of Machines, Drives and Electrical Measurements, Wroclaw University of Technology)* No. 58 / *Studia i Materiały (Studies and Materials)*, No. 25, 12 pp.

[133] B. Bolsens, K. De Brabandere, J. Van den Keybus, J. Driesen, R. Belmans, "Three-Phase Observer-based Low Distortion Grid Current Controller Using LCL Output Filter," in *Proceedings of the 36th Annual Power Electronics*

Specialists Conference, PESC 2005, Recife, Brazil, 12-16 June 2005, pp. 1705-1711

[134] K. H. Ahmed, A. M. Massoud, S. J. Finney, B. W. Williams, "Sensorless Modified Adaptive Kalman Filter for Current Control of a Three-Phase Inverter Based Distributed Generation," in *Proceedings of the 2008 IEEE International Symposium on Industrial Electronics*, ISIS 2008, Cambridge, United Kingdom, 30 June – 2 July, 2008, pp. 1592-1597

[135] K. H. Ahmed, A. M. Massoud, S. J. Finney, B. W. Williams, "Sensorless Current Control of Three-Phase Inverter-Based Distributed Generation," in *IEEE Transactions on Power Delivery*, Vol. 24, No. 2, April 2009, pp. 919-929

[136] Y. A.-R. I. Mohamed, E. F. El-Saadany, R. A. El-Shatshat, "Natural Adaptive Observers-Based Estimation Unit for Robust Grid-Voltage Sensorless Control Characteristics in Inverter-Based DG Units," in *Proceedings of the 2007 IEEE Power Engineering Society General Meeting*, Tampa, Florida, USA, 24-28 June 2007, 8 pp.

[137] Y. A.-R. I. Mohamed, E. F. El-Saadany, "Adaptive Discrete-Time Grid-Voltage Sensorless Interfacing Scheme for Grid-Connected DG-Inverters Based on Neural Network Identification and Deadbeat Current Regulation," in *IEEE Transactions on Power Electronics*, Vol. 23, No. 1, January 2008, pp. 308-321

[138] Y. A.-R. I. Mohamed, E. F. El-Saadany, "A Robust Natural-Frame-Based Interfacing Scheme for Grid-Connected Distributed Generation Inverters," in *IEEE Transactions on Energy Conversion*, Vol. 26, No. 3, September 2011, pp. 728-736

[139] I.-W. Joo, H.-S. Song, K. Nam, "Source-Voltage Sensorless Scheme for PWM Rectifier under Voltage Unbalance Condition," in *Proceedings of the 4th International Conference on Power Electronics and Drive Systems*, PEDS 2001, Denpasar, Indonesia, 22-25 October 2001, Vol. 1, pp. 33-38

[140] H.-S. Song, I.-W. Joo, K. Nam, "Source Voltage Sensorless Estimation Scheme for PWM Rectifiers Under Unbalanced Conditions," in *IEEE Transactions on Industrial Electronics*, Vol. 50, No. 6, December 2003, pp. 1238-1245

[141] A. E. Leon, J. M. Mauricio, J. A. Solsona, A. Gomez-Exposito, "Software Sensor-Based STATCOM Control under Unbalanced Conditions," in *IEEE Transactions on Power Delivery*, Vol. 24, No. 3, July 2009, pp. 1623-1632

[142] K. Lee, T. M. Jahns, T. A. Lipo, V. Blasko, "New Observer-based Source Voltage Unbalance Control Methods in PWM Voltage-Source Converters," in *Proceedings of the 39th IEEE Power Electronics Specialists Conference*, PESC'08, Rhodes, Greece, 15-19 June 2008, pp. 1509-1514

[143] K. Lee, T. M. Jahns, T. A. Lipo, V. Blasko, R. D. Lorenz, "New Parameter-Insensitive Observer-based Control Methods for Combined Source Voltage Harmonics and Unbalance Disturbances in PWM Voltage-Source Converters," in *Proceedings of the 24th Annual IEEE Applied Power Electronics Conference and Exposition*, APEC 2009, Washington DC, USA, 15-19 February 2009, pp. 1323-1330

[144] K. Lee, T. M. Jahns, T. A. Lipo, V. Blasko, R. D. Lorenz, "Observer-Based Control Methods for Combined Source-Voltage Harmonics and Unbalance Disturbances in PWM Voltage-Source Converters," in *IEEE Transactions on*

Industry Applications, Vol. 45, No. 6, November/December 2009, pp. 2010-2021

[145] E. Jung, M. Kim, S.-K. Sul, "Control Scheme for Source Voltage Sensorless PWM Converters under Source Voltage Unbalance, " in *Proceedings of the 14th European Conference on Power Electronics and Applications*, EPE 2011, Birmingham, UK, 30 August – 1 September 2011, 10 pp.

[146] Y. A.-R. I. Mohamed, M.A.-Rahman, R. Seethapathy, "Robust Line-Voltage Sensorless Control and Synchronization of LCL-Filtered Distributed Generation Inverters for High Power Quality Grid Connection" in *IEEE Transactions on Power Electronics*, In press

[147] S. Chattopadhyay, V. Ramanarayanan, "A Voltage Sensorless Control Method to Balance the Input Current of the Boost Rectifier Under Unbalanced Input Voltage Conditions," in *Proceedings of the 33rd Annual IEEE Power Electronics Specialists Conference*, PESC 2002, Cairns, Queensland, Australia, 23-27 June 2002, Vol. 4, pp. 1941-1946

[148] S. Chattopadhyay, V. Ramanarayanan, "A Voltage Sensorless Control Method to Balance the Input Current of the Boost Rectifier Under Unbalanced Input Voltage Conditions," in *IEEE Transactions on Industrial Electronics*, Vol. 52, No. 2, April 2005, pp 386-398

[149] V. G. Török, "Near-optimum on-line modulation of PWM inverters," in *Proceedings of the Third IFAC Symposium on Control in Power Electronics and Electrical Drives*, Lausanne, Switzerland, 12-14 September 1983, pp. 247-254

[150] T. Svensson, "*On Modulation and Control of Electronic Power Convertors*," PhD Thesis, Chalmers University of Technology, Göteborg, Sweden, 1988

[151] I. Takahashi, T. Noguchi, "A New Quick-Response and High-Efficiency Control Strategy of an Induction Motor," in *IEEE Transactions on Industry Applications*, Vo. IA-22, No. 5, September/October 1986, pp. 820-827

[152] M. Depenbrock, "Direct Self-Control (DSC) of Inverter-Fed Induction Machine," in *IEEE Transactions on Power Electronics*, Vol. 3, No. 4, October 1988, pp. 420-429

[153] H. Xie, L. Ängquist, H.-P. Nee, "Comparison of Voltage And Flux Modulation Schemes of StatComs Regarding Transformer Saturation During Fault Recovery," in *IEEE Transactions on Power Systems*, Vol. 23, No. 4, November 2008, pp. 1653-1661

[154] M. Malinowski, M. P. Kazmierkowski, A. Trzynadlowski, "Review and comparative study of control techniques for three-phase PWM rectifiers," in *Mathematics and Computers in Simulation*, Vol. 63, No. 3-5, November 2003, pp. 349-361

[155] M. Malinowski, M. P. Kazmierkowski, A. M. Trzynadlowski, "A Comparative Study of Control Techniques for PWM Rectifiers in AC Adjustable Speed Drives," in *IEEE Transactions on Power Electronics*, Vol. 18, No. 6, November 2003, pp. 1390-1396

[156] R. Pöllänen, "*Converter-Flux-Based Current Control of Voltage Source PWM Rectifiers – Analysis and Implementation*," PhD-Thesis, Lappeenranta University of Technology, Lappeenranta, Finland, 2003

[157] H. Li, G. Tan, J. Fang, X. Wu, "Study of Multi-level Rectifier in High Power System Based on a Novel Virtual Flux Observer," in *Proceedings of the 6th IEEE International Power Electronics and Motion Control Conference,* IPEMC'09, Wuhan, China, 17-20 May 2009, pp. 1618-1621

[158] G. Tan, X. Wu, H. Li, M. Liu, "Novel Control Strategy for Multi-Level Active Power Filter without Phase-Locked-Loop," in *Energy and Power Engineering*, Vol. 2, No. 4, November 2010, pp. 262-270

[159] N. R. N. Idris, A. H. M. Yatim, "An Improved Stator Flux Estimation in Steady-State Operation for Direct Torque Control of Induction Machine," in *IEEE Transactions on Industry Applications*, Vol. 38, No. 1, January/February 2002, pp. 110-116

[160] L. A. Serpa, S. Ponnaluri, P. M. Barbosa, J. W. Kolar, "A Modified Direct Power Control Strategy Allowing the Connection of Three-Phase Inverters to the Grid Through LCL Filters," in *IEEE Transactions on Industry Applications*, Vol. 43, No. 5 September/October 2007, pp. 1388-1400

[161] L. A. Serpa, S. D. Round, J. W. Kolar, "A Virtual Flux Decoupling Hysteresis Current Controller for Mains Connected Inverter Systems," in *IEEE Transactions on Power Electronics*, Vol. 22, No. 5, September 2007, pp. 1766-1777

[162] P. Dai, S. Dong, X. Fu, Y. Li, "Vector Control of PWM Rectifier Based on A Novel Virtual Flux Observer," in *Proceedings of the 2011 IEEE International Conference on Mechatronics and Automation*, ICMA 2011, Beijing, China, 7-10 August 2011, pp. 1641-1645

[163] J. Hu, B. Wu, "New Integration Algorithms for Estimating Motor Flux over a Wide Speed Range," in IEEE Transactions on Power Electronics, Vol. 13, No. 5, September 1998, pp. 969-977

[164] C. Bian, C. Shi, C. Song, A. Wang, "Study of the Control System of Three-level PWM Rectifier Based on Virtual Flux Oriented," in *Proceedings of the Third International Conference on Intelligent Human-Machine Systems and Cybernetics,* IHMSC 2011, Hangzhou, China, 26-27 August 2011, Vol. 2, pp. 53-56

[165] M. Niemelä, "*Position Sensorless Electrically Excited Synchronous Motor Drive for Industrial use based on Direct Flux Linkage and Torque Control*," PhD-Thesis, Lappeenranta University of Technology, Lappeenranta, Finland, 1999

[166] J. Luukko, M. Niemelä, J. Pyrhönen, "Estimation of the Flux Linkage in a Direct-Torque-Controlled Drive," in *IEEE Transactions on Industrial Electronics*, Vol. 50, No.2, April 2003, pp. 283-287

[167] M. Knapczyk, K. Pieńkowski, "Sensorless Control of AC/DC/AC Converter-Fed Induction Motor with Sliding-Mode Observers," in *Prace Naukowe Instytutu Maszyn, Napędów i Pomiarów, Politechniki Wrocławskiej (Scientific Work of the Institute of Machines, Drives and Electrical Measurements, Wroclaw University of Technology)* No. 62 / *Studia i Materiały (Studies and Materials)*, No. 28, 6 pp.

[168] M. Knapczyk, K. Pieńkowski, "Simulation Studies of Sensorless Current Control of AC/DC/AC Converter-Fed Induction Motor Based on Sliding-Mode Observers," in *Prace Naukowe Instytutu Maszyn, Napędów i Pomiarów,*

Politechniki Wrocławskiej (Scientific Work of the Institute of Machines, Drives and Electrical Measurements, Wroclaw University of Technology) No. 62 / *Studia i Materiały (Studies and Materials)*, No. 28, 6 pp.

[169] V. Blasko, V, Kaura, "A Novel Control to Actively Damp Resonance in Input LC Filter of a Three-Phase Voltage Source Converter," in *IEEE Transactions on Industry Applications*, Vol. 33, No. 2, March/April 1997, pp. 542-550

[170] M. Malinowski, M. P. Kazmierkowski, S. Bernet, "New Simple Active Damping of Resonance in Three-Phase PWM Converter with LCL Filter," in *Proceedings of the IEEE International Conference on Industrial Technology*, ICIT 2005, Hong Kong, 14-17 December 2005, pp. 861-865

[171] M. Malinowski, S. Stynski, W. Kolomyjski, M. P. Kazmierkowski, "Control of Three-Level PWM Converter Applied to Variable-Speed Type Turbines," in *IEEE Transactions on Industrial Electronics*, Vol. 56, No. 1, January 2009, pp. 69-77

[172] W. Gullvik, L. Norum, R. Nilsen, "Active Damping of Resonance Oscillations in LCL-Filters Based on Virtual Flux and Virtual Resistor," in *Proceedings of the 12th European Conference on Power Electronics and Applications*, EPE'07, Aalborg, Denmark, 2-5 September 2007, 10 pp.

[173] R. Pöllänen, A. Tarkiainen, M. Niemelä, J. Pyrhönen, "Supply Voltage Sensorless Reactive Power Control of DTC Modulation Based Line Converter with L- and LCL-Filters," in *Proceedings of the 10th European Conference on Power Electronics and Applications*, Toulouse, France, 2-4 September 2003, 10 pp.

[174] M. Liserre, R. Teodorescu, F. Blaabjerg, "Stability of Photovoltaic and Wind Turbine Grid-Connected Inverters for a Large Set of Grid Impedance Values," in *IEEE Transactions on Power Electronics*, Vol. 21, No. 1, January 2006, pp. 263-272

[175] J. Dannehl, F. W. Fuchs, S. Hansen, "PWM Rectifier with LCL-Filter using different Current Control Structures," in *Proceedings of the 12th European Conference on Power Electronics and Applications*, EPE'07, Aalborg, Denmark, 2-5 September 2007, 10 pp.

[176] J. Dannehl, C. Wessels, F. W. Fuchs, "Limitations of Voltage-Oriented PI Current Control of Grid-Connected PWM Rectifiers With LCL Filters," in *IEEE Transactions on Industrial Electronics*, Vol. 56, No. 2, February 2009, pp. 380-388

[177] L. A. Serpa, J. W. Kolar, "Virtual-Flux Direct Power Control for Mains Connected Three-Level NPC Inverter Systems" in *Proceedings of the Fourth Power Conversion Conference*, PCC-NAGOYA 2007, Nagoya, Japan, 2-5 April 2007, pp. 130-136

[178] J. Dannehl, F. W. Fuchs, S. Hansen, P. B. Thøgersen, "Investigation of Active Damping Approaches for PI-Based Current Control of Grid-Connected Pulse Width Modulation Converters With LCL Filters," in *IEEE Transactions on Industry Applications*, Vol. 46, No. 4, July/August 2010, pp. 1509-1517

[179] M. Malinowski, S. Bernet, "A Simple Voltage Sensorless Active Damping Scheme for Three-Phase PWM Converters With an LCL Filter," in *IEEE*

Transactions on Industrial Electronics, Vol. 55, No. 4, April 2008, pp. 1876-1880

[180] D. Zhi, L. Xu, B. W. Williams, "Improved Direct Power Control of Grid-Connected DA/AC Converters," in *IEEE Transactions on Power Electronics*, Vol. 24, No. 5, May 2009, pp. 1280-1292

[181] P. Antoniewicz, M. P. Kazmierkowski, "Virtual-Flux-Based Predictive Direct Power Control of AC/DC Converters With Online Inductance Estimation," in *IEEE Transactions on Industrial Electronics*, Vol. 55, No. 12, December 2008, pp. 4381-4390

[182] P. Antoniewicz, "*Predictive Control of Three Phase AC/DC Converters*," Warsaw University of Technology, Warsaw, Poland, 2009

[183] A. Rahmati, A. Abrishamifar, E. Abiri, "Direct Power Control of an HVDC system based on VSCs," in *Proceedings of the IEEE International Conference on Information Technology*, Mumbai, India, 15-17 December 2006, pp. 2984-2989

[184] E. Abiri, A. Rahmati, A. Abrishamifar, "A sensorless and simple controller for VSC based HVDC system," in *Journal of Zhejiang University: Science A*, Vol. 10, No. 12, December 2009, pp. 1824-1834

[185] M. Jasinski, P. Okon, M. P. Kazmierkowski, "Control of Grid-Interfacing AC-DC-AC Converter for Variable Speed Energy Generation under Unbalanced and Distorted Voltage Conditions," in *Proceedings of the International Conference and Exhibition on Ecological Vehicles and Renewable Energies*, EVER 2009, Monaco, 26-29 March 2009, 7 pp.

[186] M. Jasinski, M. P. Kazmierkowski, M. Bobrowska, P. Okon, "Control of AC-DC-AC Converter under Unbalanced and Distorted Input Conditions," in *Proceedings of the 6th International Conference-Workshop - 2009 Compatibility and Power Electronics*, CPE2009, Badajoz, Spain, 20-22 May 2009, pp. 139-145

[187] M. P. Kazmierkowski, M. Jasinski, M. Bobrowska-Rafal, "AC-DC-AC Converter with Grid Voltage Dips Mitigation," in *Proceedings of the 14th International Power Electronics and Motion Control Conference*, EPE-PEMC 2010, Ohrid, Macedonia, 6-8 September 2010, pp. T11-69 – T11-74

[188] S. Piasecki, M. Jasiński, A. Milicua, "Brief view on control of grid-interfacing AC-DC-AC converter and active filter under unbalanced and distorted voltage conditions," in *COMEPL: The International Journal for Computation and Mathematics in Electrical and Electronic Engineering*, Vol. 30, No. 1, January/February 2011, pp. 351-373

[189] W. V. Lyon, "*Transient Analysis of Alternating-Current Machinery*," The Technology Press of Massachusetts Institute of Technology / John Wiley & Sons, New York, 1954

[190] G. C. Paap, "Symmetrical Components in the Time Domain and Their Application to Power Network Calculations," in *IEEE Transactions on Power Systems*, Vol. 15, No. 2, May 2000, pp. 522-528

[191] M. Chiobotaru, R. Teodorescu, F. Blaabjerg, "A New Single-Phase PLL Structure Based on Second Order Generalized Integrator," in *Proceedings of the*

37th Annual IEEE Power Electronics Specialists Conference, PESC'06, Jeju, Korea, 18-22 June 2006

[192] P. Rodríguez, A. Luna, I. Candela, R. Teodorescu, F. Blaabjerg, "Grid Synchronization of Power Converters using Multiple Second Order Generalized Integrators," in *Proceedings of the 34th Annual Conference of the IEEE Industrial Electronics Society*, Orlando, Florida, USA, 10-13 November 2008, pp. 755-760

[193] M. Karimi-Ghartemani, S. A. Khajehoddin, P. Jain, A. Bakhshai, M. Mojiri, "Addressing DC Component in PLL and Notch Filter Algorithms," in *IEEE Transactions on Power Electronics*, In press,

[194] P. Rodriguez, A. Luna, I. Etxeberría, J. R. Hermoso, R. Teodorescu, "Multiple Second Order Generalized Integrators for Harmonic Synchronization of Power Converters," in *Proceedings of the 2009 IEEE Energy Conversion Congress and Exposition*, ECCE 2009, San Jose, California, USA, 20-24 September 2009, pp. 2239-2246

[195] P. Rodríguez, A. Luna, I. Candela. R. Mujal, R. Teodorescu, F. Blaabjerg, "Multiresonant Frequency-Locked Loop for Grid Synchronization of Power Converters Under Distorted Grid Conditions," in *IEEE Transactions on Industrial Electronics*, Vol. 58, No. 1, January 2011, pp. 127-138

[196] P. Rodriguez, A. Luna, I. Etxeberria, R. Teodorescu, F. Blaabjerg, "A Stationary Reference Frame Grid Synchronization System for Three-Phase Grid-Connected Power Converters under Adverse Grid Conditions," in *IEEE Transactions on Power Electronics*, Vol. 27, No. 1, January 2012, pp. 99-112

[197] G. F. Franklin, J. D. Powell, M. Workman, "*Digital Control of Dynamic Systems*," Pearson Education Inc., Upper Saddle River, New Jersey, USA, 2002, Third Edition

[198] F. J. Rodríguez, E. Bueno, M. Aredes, L. G. B. Rolim, F. A. S. Neves, M. C. Cavalcanti, "Discrete-time implementation of second order generalized integrators for grid converters," in *Proceedings of the 34th Annual Conference of the IEEE Industrial Electronics Society*, IECON 2008, Orlando, Florida, USA, 10-13 November 2008, pp.176-181

[199] A. Luna, J. Rocabert, G. Vazquez, P. Rodríguez, R. Teodorescu, F. Corcoles, "Grid Synchronization for Advanced Power Processing and FACTS in Wind Power Systems," in *Proceedings of the 2010 IEEE Symposium on Industrial Electronics*, ISIE 2010, Bari, Italy, 4-7 July 2010, pp. 2915-2920

[200] S. Alepuz, S. Busquets, J. Bordonau, J. Ponnt, C. Silva, J. Rodriguez, "Fast on-line symmetrical components separation method for synchronization and control purposes in three-phase distributed power generation systems," in *Proceedings of the 12th European Conference on Power Electronics and Applications*, EPE'07, Aalborg, Denmark, 2-5 September 2007, 10 pp.

[201] A. Tarkiainen, R. Pöllänen, M. Niemelä, J. Pyrhönen, "Converter Flux Linkage Oriented Current Vector Control Using Synchronous Co-ordinate Vector Modulation," in *Proceedings of the 10th European Conference on Power Electronics and Applications*, Toulouse, France, 2-4 September 2003, 10 pp.

[202] A. Tarkiainen, R. Pöllänen, M. Niemelä, J. Pyrhönen, "Current Controlled Line Converter Using Direct Torque Control Method," in *European Transactions on Electrical Power*, Vol. 14, No. 5, September/October 2004, pp. 277-291

[203] A. V. Stankovic, T. A. Lipo, "A Generalized Control Method for Input-Output Harmonic Elimination for the PWM Boost Rectifier Under Simultaneous Unbalanced Input Voltage and Input Impedances," in *Proceedings of the 32nd Annual Power Electronics Specialists Conference*, PESC 2001, Vancouver, British Colombia, Canada, 17-21 June 2001, Vol. 3, pp. 1309-1314

[204] J. Hu, Y. He, "Modeling and Control of Grid-Connected Voltage-Sourced Converters Under Generalized Unbalanced Operation Conditions," in *IEEE Transactions on Energy Conversion*, Vol. 23, No. 3, September 2008, pp. 903-913

[205] A. V. Stankovic, K. Chen, "A New Control Method for Input-Output Harmonic Elimination of the PWM Boost-Type Rectifier Under Extreme Unbalanced Operating Conditions," in *IEEE Transactions on Industrial Electronics*, Vol. 56, No. 7, July 2009, pp. 2420-2430

[206] P. N. Enjeti, P. D. Ziogas, M. Ehsani, "Unbalanced PWM Converter Analysis and Corrective Measures," in *Conference Record of the 1989 IEEE Industry Applications Society Annual Meeting*, 1-5 October 1989, San Diego, California, USA, Vol. 1, pp. 861-870

[207] E. P. Wiechmann, J. R. Espinoza, J. L. Rodriguez, "Compensated Carrier PWM Synchronization: A Novel Method to Achieve Self-Regulation and AC Unbalance Compensation in AC Fed Converters," in *IEEE Transactions on Power Electronics*, Vol. 7, No. 2, April 1992, pp. 342-348

[208] H. S. Kim, H. S. Mok, G. H. Choe, D. S. Hyun, S. Y. Choe, "Design of Current Controller for 3-Phase PWM Converter with Unbalanced Input Voltage," in *Proceedings of the 29th Annual IEEE Power Electronics Specialists Conference*, PESC'98, 17-22 May 1998, Fukuoka, Japan, Vol. 1, pp. 503-509

[209] A. V. Timbus, P. Rodríguez, R. Teodorescu, M. Liserre, F. Blaabjerg, "Control Strategies for Distributed Power Generation Systems Operating on Faulty Grid," in *Proceedings of the International Symposium on Industrial Electronics*, ISIE 2006, Montreal, Quebec, Canada, 9-13 July 2006, pp. 1601-1607

[210] I. Etxeberria-Otadui, U. Viscarret, M. Cabellero, A. Rufer, S. Bacha, "New Optimized PWM VSC Control Structures and Strategies Under Unbalanced Voltage Transients," in *IEEE Transactions on Industrial Electronics*, Vol. 54, No. 5, October 2007, pp. 2902-2914

[211] A. Notholt, D. Coll-Mayor, "Performance Limitations of B6 Inverters during Unsymmetrical Voltage Sag Conditions," in *Proceedings of the International Conference on Renewable Energies and Power Quality*, ICREPQ'08, Santander, Spain, 12-14 March 2008, 6 pp.

[212] M. Castilla, J. Miret, J. L. Sosa, J. Matas, L. G. de Vicuña, "Grid-Fault Control Scheme for Three-Phase Photovoltaic Inverters With Adjustable Power Quality Measurements," in *IEEE Transactions on Power Electronics*, Vol. 25, No. 12, December 2010, pp. 2930-2940

[213] A. J. Roscoe, S. J. Finney, G. M. Burt, "Tradeoffs Between AC Power Quality and DC Bus Ripple for 3-Phase 3-Wire Inverter-Connected Devices Within

Microgrids," in *IEEE Transactions on Power Electronics*, Vol. 26, No. 3, March 2011, pp. 674-688

[214] H. Akagi, Y. Kanazawa, A. Nabae, "Generalized Theory of the Instantaneous Reactive Power in Three-Phase Circuits," in *Conference Record of the International Power Electronics Conference 1983*, IPEC-Tokyo, Tokyo, Japan, 27-21 March 1983, Vol. 2, pp. 1275-1386

[215] H. Akagi, Y. Kanazawa, A. Nabae, "Instantaneous Reactive Power Compensators Comprising Switching Devices without Energy Storage Components," in *IEEE Transactions on Industry Applications*, Vol. IA-20, No. 3, May/June 1984, pp. 625-630

[216] H. Akagi, E. Watanabe, M. Aredes, "*Instantaneous Power Theory and Applications to Power Conditioning*," Wiley/IEEE Press, 2007

[217] F. Z. Peng, J.-S. Lai, "Generalized Instantaneous Reactive Power Theory for Three-phase Power System," in *IEEE Transactions on Instrumentation and Measurement*, Vol. 45, No. 1, February 1996, pp. 293-297

[218] F. Z. Peng, G. W. Ott Jr., D. J. Adams, "Harmonic and Reactive Power Compensation Based on the Generalized Instantaneous Reactive Power Theory for Three-Phase Four-Wire Systems," in *IEEE Transactions on Power* Electronics, Vol. 13, No. 6, November 1998, pp. 1174-1181

[219] M. Depenbrock, V. Staudt, H. Wrede, "A Theoretical Investigation of Original and Modified Instantaneous Power Theory Applied to Four-Wire Systems," in *IEEE Transactions on Industry Applications*, Vol. 39, No. 4, July/August 2003, pp. 1160-1167

[220] J. Eloy-García, S. Arnaltes, J. L. Rodríguez-Amenedo, "Direct power control of voltage source inverters with unbalanced grid voltages," in *IET Power Electronics*, Vol. 1, No. 3, August/September 2008, pp. 395-407

[221] S.-C. Ahn, D.-S. Hyun, "New Control Scheme of Three-Phase PWM AC/DC Converter Without Phase Angle Detection Under the Unbalanced Input Voltage Conditions," in *IEEE Transactions on Power Electronics*, Vol. 17, No.5, September 2002, pp. 616-622

[222] B. Yin, R. Oruganti, S. K. Panda, A. K. S. Bhat, "An Output-Power-Control Strategy for a Three-Phase PWM Rectifier Under Unbalanced Supply Conditions," in *IEEE Transactions on Industrial Electronics*, Vol. 55, No. 5, May 2008, pp. 2140-2151

[223] Z. Li, Y. Li, P. Wang, C. Liu, W. Xu, "Control of Three-Phase Boost-Type PWM Rectifier in Stationary Frame Under Unbalanced Input Voltage," in *IEEE Transactions on Power Electronics*, Vol. 25, No. 10, Octover 2010, pp. 2521-2530

[224] A. Junyent-Ferré, O. Gomis-Bellmunt, T. C. Green, D. E. Soto-Sanches, "Current control reference calculation issues for the operation of renewable source grid interface VSCs under unbalanced voltage sags," in *IEEE Transactions on Power Electronics*, Vol. 26, No. 12, December 2011, pp. 3744-3753

[225] M. Brucoli, T. C. Green, “Fault Response of Inverter Dominated Microgrids.” in *International Journal of Distributed Energy Resources*, Vol. 3, No. 2, April/June 2007, pp. 157-175

[226] C. Du, M. H. J. Bollen, E. Agneholm, A. Sannino, “A New Control Strategy of a VSC-HVDC System for High-Quality Supply of Industrial Plants,” in *IEEE Transactions on Power Delivery*, Vol. 22, No. 3, October 2007, pp. 2386-2394

[227] C. H. Ng, L. Ran, J. Bumby, “Unbalanced-Grid-Fault Ride-Through Control for a Wind Turbine Inverter,” in *IEEE Transactions on Industry Applications*, Vol. 44, No. 3, May/June 2008, pp. 845-856

[228] M. Vekić, Z. Ivanović, S. Grabić, V. Katić, “Control of Variable Speed Wind Turbine under Grid Disturbances,” in *Electronics*, Vol. 9, No. 2, December 2005, pp. 66-69

[229] Z. Ivanović, M. Vekić, S. Grabić, V. Katić, “Control of Multilevel Converter Driving Variable Speed Wind Turbine in Case of Grid Disturbances,” in *Proceedings of the 12th International Power Electronics and Motion Control Conference*, EPE-PEMC 2006, Portoroz, Slovenia, 30 August – 1 September 2006, pp. 1569-1573

[230] Z. Ivanovic, M. Vekic, S. Grabic, E. Adzic, V. Katic, “Wide Bandwidth Power Flow Control Algorithm of the Grid Connected VSI under Unbalanced Grid Voltages,” in *Proceedings of the 13th International Power Electronics and Motion Control Conference*, EPE-PEMC 2008, Poznan, Poland, 1-3 September 2008, pp. 1957-1962

[231] A. E. Leon, J. M. Mauricio, A. Gómez-Expósito, J. A. Solsona, “An Improved Control Strategy for Hybrid Wind Farms,” in *IEEE Transactions on Sustainable Energy*, Vol. 1, No. 3, October 2010, pp. 131-141

[232] A. E. Leon, J. M. Mauricio, J. A . Solsona, A. Gómez-Expósito, “Adaptive Control Strategy for VSC-Based Systems Under Unbalanced Network Conditions,” in *IEEE Transactions on Smart Grid*, Vol. 1, No. 3, December 2010, pp. 311-319

[233] S.-J. Jeon, F. C. Lee, “Three control strategies for a three-leg AC-DC converter under unbalanced AC voltage conditions,” in *Proceedings of the 29th Annual Conference of the IEEE Industrial Electronics Society*, IECON’03, Roanoke, Virginia, USA, 2-6 November 2003, Vol. 1, pp. 186-191

[234] O. Ojo, Z. Wu, “A New Controller for Three-phase Boost Rectifiers Lacking Balance in Source Voltage and Impedances,” in *Proceedings of the Twentieth Annual IEEE Applied Power Electronics Conference and Exposition*, APEC 2005, Austin, Texas, USA, 6-10 March 2005, pp. 508-514

[235] S. Rivera, S. Kouro, P. Cortés, S. Alepuz, M. Malinowski, B. Wu, J. Rodríguez, “Generalized Direct Power Control for Grid Connected Multilevel Converters,” in *Proceedings of the 2010 IEEE International Conference on Industrial Technology*, Via del Mar, Chile, 14-17 March 2010, pp. 1351-1358

[236] M. R. Harris, P. J. Lawrenson, J. M. Stephenson, “*Per-unit systems with special reference to electrical machines*,” Cambridge University Press / The Institution of Electrical Engineers, London, UK, 1970.

[237] P. Kundur, "*Power System Stability and Control*", McGraw-Hill / Tata McGraw-Hill, New York, USA / New Dehli, India, 2006

[238] E. Clarke, "*Circuit Analysis of A-C Power Systems, Volume I, Symmetrical and Related Components*," Johan Wiley & Sons, New York, USA, 1943, Fourth Printing, September1950

[239] R. H. Park, "Two-Reaction Theory of Synchronous Machines, Generalized Method of Analysis – Part I," in *Transactions of the American Institute of Electrical Engineers*, Vol. 48, No. 3, July 1929, pp. 716-727

[240] K. P. Kovács, I. Rácz, "*Transiente Vorgänge in Wechselstrommaschinen*" (*Transient Events in Alternating Current Machines*, in German), Verlag der Ungarischen Akademie der Wissenschaften (The Publishing House of the Hungarian Academy of Science), Budapest, Hungary, 1959

[241] C. L. Fortescue, "Method of Symmetrical Co-Ordinates Applied to the Solution of Polyphase Networks," in *Transactions o the American Institute of Electrical Engineers*, Vol. XXXVII, No. 2, July-December 1918, pp. 1027-1140

[242] T.-N Lé, "Kompensation schnell veränderlicher Blindströme eines Drehstromverbrauchers, (Compensation of quickly changing reactive currents of an AC load," ETZ-Archiv, Vol. 11, No. 8, 1989, pp. 249-253

[243] A. G. Yepes, F. D. Freijedo, J. Doval-Gandoy, "On the Discrete-Time Implementation of Resonant Controllers for Active Power Filters", in *Proceedings of the 35th Annual Conference of the IEEE Industrial Electronics Society*, IECON 2009, Porto, Portugal, 3-5 November 2009, pp. 3686-3691

[244] A. G. Yepes, F. D. Freijedo, J. Doval-Gandoy, O. López, J. Malvar, P. Fernandez-Comesaña, "Effects of Discretication Methods on the Performance of Resonant Controllers," in *IEEE Transactions on Power Electronics*, Vol. 25, No. 7, July 2010, pp.1692-1712

[245] Web page of Manitoba HVDC Research Centre for the PSCAD®/EMTDC™ simulation environment, https://pscad.com/, accessed in January 2012

[246] Web page of Mathworks Inc., http://www.mathworks.se/index.html, accessed in January 2012

[247] Web page of dSPACE GmbH, http://www.dspace.com/en/pub/start.cfm, accessed in January 2012

Appendix A Conventions for Reference Frame Transformations and Per Unit Scaling

This Appendix is defining the per unit system used for derivations and results presented in this Thesis. The conventions that are applied for representation of three-phase signals in different reference frames are also presented.

A.1 Base Values for Per Unit Systems

In this Thesis, mathematical derivations, as well as the results from simulations and experiments, are presented in per unit quantities. The applied per unit system is based on the rated voltages and currents of the converter or system investigated in the actual cases. Thus, the nominal values for the total kVA rating and the angular frequency can be expressed by (A.1)

$$S_N = \sqrt{3} \cdot V_{LL,RMS,N} \cdot I_{RMS.N} = 3 \cdot V_{phase,RMS,N} \cdot I_{RMS.N} = \frac{3}{2} \cdot \hat{V}_{phase,N} \cdot \hat{I}_N$$
$$\omega_N = 2 \cdot \pi \cdot f_N \tag{A.1}$$

The base values for defining the per unit system are then specified to correspond to the peak values of the nominal phase voltage, and the peak value of the nominal phase currents when operating at rated frequency [236], [237]. The base values for the total kVA rating, the impedance, inductance and capacitance are then derived from the voltage, current and frequency base values. The resulting definitions of base values for defining the per unit system on the AC side of the converter are listed in (A.2).

$$S_b = S_N = \frac{3}{2} \cdot V_b \cdot I_b$$
$$V_b = \hat{V}_{phase,N} \qquad \Psi_b = \frac{V_b}{\omega_b}$$
$$I_b = \hat{I}_N$$
$$f_b = f_N \qquad \omega_b = 2 \cdot \pi \cdot f_b \tag{A.2}$$
$$Z_b = R_b = \frac{V_b}{I_b} = \frac{V_{LL,RMS,N}^2}{S_N}$$
$$L_b = \frac{Z_b}{\omega_b}$$
$$C_b = \frac{1}{\omega_b \cdot Z_b}$$

The main considerations behind this selection of base values for defining the per unit ([pu]) system is similar to what is explained for electrical machines in [236]. Thus the phase voltages and currents should take the values of 1.0 pu when operating at the rated conditions. This is also convenient for implementation of digital control systems as well

as for plotting of results, since the interpretation is simplified by always having 1.0 pu as the reference.

A per unit system for the DC-link of the converter can also be defined, although it is not extensively used in this Thesis. The basic consideration is then to keep the same base value for the kVA rating at both the AC and DC side. At the same time, the base value for the DC-link voltage should be twice the base value for the AC side phase voltages, since this will correspond to the output ratio of the converter when operated with sinusoidal carrier-based PWM. The resulting base values for kVA rating, DC link voltage and current are then given by (A.3).

$$\begin{aligned} S_{b,DC} &= S_b \\ V_{b,DC} &= 2 \cdot V_b \\ I_{b,DC} &= \frac{S_b}{2 \cdot V_b} = \frac{3}{4} \cdot I_b \end{aligned} \tag{A.3}$$

A.2 Two-phase Representation of Three-phase Variables in the Stationary Reference Frame

To simplify the derivations and the presentation of the results, three-phase variables are in this Thesis preferably expressed in the stationary *αβ* reference frame. The approach of representing three-phase signals by an equivalent set of two-phase signals with the purpose of simplification has been considered for soon hundred years, but was first thoroughly treated in [238]. Thus, the shift of reference frame from three-phase *abc* signals to two phase *αβ* signals has later become well known as Clarke's transformation. This transformation is now widely used in analysis and control of electric machines and drive systems as well as in grid synchronization and control of grid connected converters.

In all results presented in this Thesis, the amplitude-invariant version of the Clarke transformation is used, as given for a generic set of signals *x* by (A.4) [236]-[238]. Thus, under balanced three-phase conditions, the amplitude of the *αβ* signals will be equal to the amplitude of the *abc* signals. This is also convenient with respect the per unit system defined in A.1, ensuring that rated current or voltage will appear as 1.0 pu when represented as both *abc* or *αβ* signals.

$$\begin{bmatrix} x_\alpha \\ x_\beta \\ x_0 \end{bmatrix} = \underbrace{\frac{2}{3}\begin{bmatrix} 1 & -\frac{1}{2} & -\frac{1}{2} \\ 0 & \frac{\sqrt{3}}{2} & -\frac{\sqrt{3}}{2} \\ \frac{1}{2} & \frac{1}{2} & \frac{1}{2} \end{bmatrix}}_{\mathbf{T}_{\alpha\beta 0}} \begin{bmatrix} x_a \\ x_b \\ x_c \end{bmatrix} \tag{A.4}$$

The transformation given by (A.4) includes a separation of the three-phase *abc* variables into the α- β- and 0- components. In three-phase three-wire systems, there will however not be any possible path for zero sequence currents, and three-phase VSCs are often protected from zero sequence voltages by star-delta-connected transformers. Thus, the condition given by (A.5) will usually be fulfilled, and the zero sequence component can be omitted from (A.4).

$$x_a + x_b + x_c = 0 \tag{A.5}$$

In most industrial applications, the grid synchronization of a VSC converter is based on measuring two line-to-line voltages instead of the phase-to-ground voltages. Possible zero sequence components of the grid voltage can then not be observed even if they are presented. The *αβ* voltage components can however be calculated directly from the measured line-to-line voltages as given by (A.6).

$$\begin{bmatrix} v_\alpha \\ v_\beta \end{bmatrix} = \frac{2}{3}\begin{bmatrix} 1 & \frac{1}{2} \\ 0 & \frac{\sqrt{3}}{2} \end{bmatrix}\begin{bmatrix} v_{ab} \\ v_{bc} \end{bmatrix} \tag{A.6}$$

With the amplitude-invariant Clarke transformation from (A.4), the reverse transformation from *αβ0* signals to three-phase *abc* signals is given by (A.7).

$$\begin{bmatrix} x_a \\ x_b \\ x_c \end{bmatrix} = \underbrace{\begin{bmatrix} 1 & 0 & 1 \\ -\frac{1}{2} & \frac{\sqrt{3}}{2} & 1 \\ -\frac{1}{2} & -\frac{\sqrt{3}}{2} & 1 \end{bmatrix}}_{\mathbf{T}_{\alpha\beta 0}^{-1}}\begin{bmatrix} x_\alpha \\ x_\beta \\ x_0 \end{bmatrix} \tag{A.7}$$

A.3 Transformation to the Synchronous Reference Frame

Three phase signals can also be represented in the *dq*- Synchronous Reference Frame (SRF), as first introduced by Park for analysis of synchronous machines in [239]. The SRF Park transformation is not extensively used in this Thesis, but is implicitly considered in several of the presented discussions. Representation in the *dq* SRF has also been applied as part of SRF PLLs used for verification and auxiliary functions in some of the simulation models used to generate some of the presented results. The applied transformations are therefore presented here.

The transformation from three-phase *abc* signals to dq0 variables is given by (A.8), where θ is the phase angle defining the *dq* SRF. In this equation, the q-axis is defined to be leading the d-axis by 90°, and the scaling factor or 2/3 is the same as for the Clarke transformation to maintain an amplitude-invariant transformation [236], [237] The inverse transformation from *dq0* signals back to three-phase *abc* signals is then given by (A.9). The zero sequence components given in these equations is the same as discussed for representation in the stationary *αβ* reference frame, and the corresponding elements can be omitted from the equations when considering three-phase three-wire systems.

$$\begin{bmatrix} x_d \\ x_q \\ x_0 \end{bmatrix} = \underbrace{\frac{2}{3}\begin{bmatrix} \cos\theta & \cos\left(\theta-\frac{2\pi}{3}\right) & \cos\left(\theta+\frac{2\pi}{3}\right) \\ -\sin\theta & -\sin\left(\theta-\frac{2\pi}{3}\right) & -\sin\left(\theta+\frac{2\pi}{3}\right) \\ \frac{1}{2} & \frac{1}{2} & \frac{1}{2} \end{bmatrix}}_{\mathbf{T}_{dq0}} \begin{bmatrix} x_a \\ x_b \\ x_c \end{bmatrix} \tag{A.8}$$

$$\begin{bmatrix} x_a \\ x_b \\ x_c \end{bmatrix} = \underbrace{\begin{bmatrix} \cos\theta & -\sin\theta & 1 \\ \cos\left(\theta-\frac{2\pi}{3}\right) & -\sin\left(\theta-\frac{2\pi}{3}\right) & 1 \\ \cos\left(\theta+\frac{2\pi}{3}\right) & -\sin\left(\theta+\frac{2\pi}{3}\right) & 1 \end{bmatrix}}_{\mathbf{T}_{dq0}^{-1}} \begin{bmatrix} x_d \\ x_q \\ x_0 \end{bmatrix} \tag{A.9}$$

In most cases, the transformation of *abc* signals for representation in the *dq*- SRF is calculated in two steps, where the first step is the representation as *αβ* signals in the stationary reference frame. The transformation from *αβ* signals to the SRF *dq*-signals is then given by (A.10), while the transformation from *dq* SRF back to the stationary *αβ* reference frame is given by (A.11)

$$\begin{bmatrix} x_d \\ x_q \end{bmatrix} = \underbrace{\begin{bmatrix} \cos\theta & \sin\theta \\ -\sin\theta & \cos\theta \end{bmatrix}}_{\mathbf{T}_{dq}} \begin{bmatrix} x_\alpha \\ x_\beta \end{bmatrix} \tag{A.10}$$

$$\begin{bmatrix} x_\alpha \\ x_\beta \end{bmatrix} = \underbrace{\begin{bmatrix} \cos\theta & -\sin\theta \\ \sin\theta & \cos\theta \end{bmatrix}}_{\mathbf{T}_{dq}^{-1}} \begin{bmatrix} x_d \\ x_q \end{bmatrix} \tag{A.11}$$

A.4 Space Vector Representation of Three-phase Variables

Assuming no zero sequence components in currents and voltages, three-phase signals can be represented on complex space vector form as introduced by [240]. Considering a generic three-phase signal x_{abc} represented in per unit quantities, the corresponding space vector is given by (A.12). Calculating the real and imaginary components of the phase shifting operator *a*, it can be easily verified that the real part corresponds to the first row of the transformation matrix from (A.4) while the imaginary part corresponds to the second row from (A.4).

$$\mathbf{x} = \frac{2}{3}\left(x_a + a \cdot x_b + a^2 \cdot x_c\right), \qquad a = e^{j\frac{2\pi}{3}} \tag{A.12}$$

Signals represented in the stationary *αβ* can also be easily expressed by complex space vector notation, as given by (A.13). Similarly, complex space vector notation can also be used in the *dq* SRF, as given by (A.14), but must then be referred to the rotating *dq* frame instead of the stationary reference frame.

$$\mathbf{x} = x_\alpha + jx_\beta \tag{A.13}$$

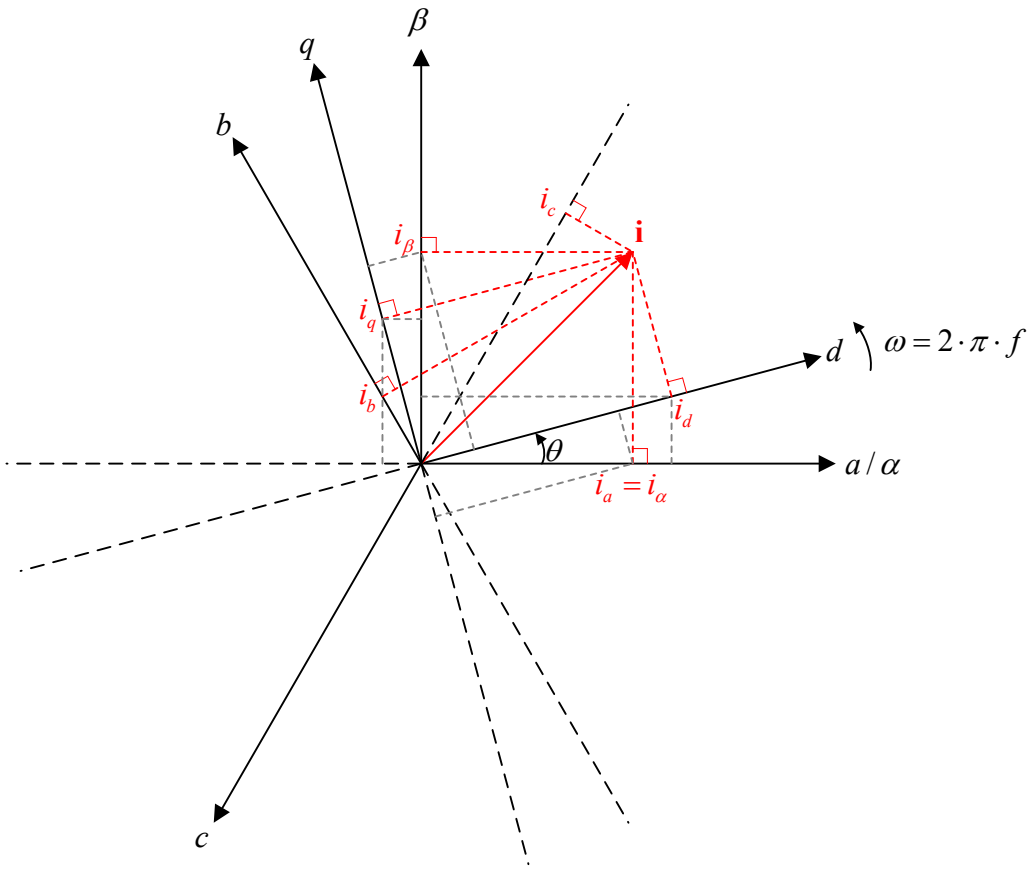

Fig. A-1 Space vector diagram showing the projection of the current space vector into the different reference frames

$$\mathbf{x} = x_d + jx_q \tag{A.14}$$

A vector diagram showing how a generic current vector **i** can be represented in the various reference frames is shown in Fig. A-1. From this figure, the transformations between the stationary *αβ* reference frame and the *dq* SRF can also be easily verified, by considering the grey dashed lines. Similarly, the transformations between three-phase *abc* representation and the two-phase *αβ* representation, as well as the transformation directly between three-phase signals and *dq* signals as given by (A.8) and (A.9), can be verified by graphically considering the projection of the current vector, or the individual current components onto the appropriate axis. Complex space vector notation is therefore a general and flexible approach that enables simple calculations and easy illustration as long as there are no zero sequence components that have to be considered.

Complex space vector notation is however not extensively used in this Thesis, since the vector notation from [108]-[114] is applied. However, for some of the derivations that will be presented in the following appendixes, the complex space vector-based approach is most convenient, and will therefore be applied.

Appendix B Analysis of Methods for Symmetrical Component Sequence Separation and Virtual Flux Estimation

This appendix is first presenting the general approach for symmetrical component sequence separation in the stationary reference frame. Then, the frequency response of the delay- or filter-based methods for sequence separation discussed in section 2.3.2, 3.2 and 3.3 will be presented, followed by the frequency response of the various methods for positive and negative sequence Virtual Flux estimation. This analysis serves as a basis for the comparisons and discussions presented in 3.4.

B.1 Sequence Separation in the Stationary Reference Frame

The concept of Symmetrical Components, as presented by Fortescue, is well known in quasi-stationary phasor analysis of power systems under unbalanced conditions [241], [237], and was later applied by Lyon for transient analysis in the time domain [189]. The expressions for calculating the positive and negative sequence components can then be simplified by expressing all variables in *αβ0* components as discussed in section A.2 [189], [190], [238]. Following the conventions applied in [51], [192], [194]-[196], the expression for calculating the positive and negative sequence components of a generic variable x can then be found from (B.1), where q is defined as a phase-shifting operator corresponding to 90° delay of fundamental frequency sinusoidal components.

$$\begin{bmatrix} x_\alpha^+ \\ x_\beta^+ \end{bmatrix} = \frac{1}{2}\begin{bmatrix} 1 & -q \\ q & 1 \end{bmatrix} \cdot \begin{bmatrix} x_\alpha \\ x_\beta \end{bmatrix}$$
$$\begin{bmatrix} x_\alpha^- \\ x_\beta^- \end{bmatrix} = \frac{1}{2}\begin{bmatrix} 1 & q \\ -q & 1 \end{bmatrix} \cdot \begin{bmatrix} x_\alpha \\ x_\beta \end{bmatrix} \tag{B.1}$$

Several different approaches for practical implementation of the required phase shift have been presented in the literature. An explicit time delay corresponding to a quarter of a fundamental frequency period was for instance proposed in [242], establishing the sequence separation method usually labeled as Delayed Signal Cancellation [53]. Implementation of the −90° phase shift by using all-pass filters was later proposed by [49], while [50] proposed a configuration of low-pass filters to identify two phase-shifted signals that could be used for sequence separation. Implementation of q by using two cascaded low-pass filters with crossover frequency equal to the grid angular frequency was later proposed by [107]. The method proposed in [51] was however made explicitly on-line frequency adaptive by using the SOGI-QSG presented for Virtual Flux estimation in 3.1.1. In the following, only the approaches from [51] and [107] will be considered and analyzed.

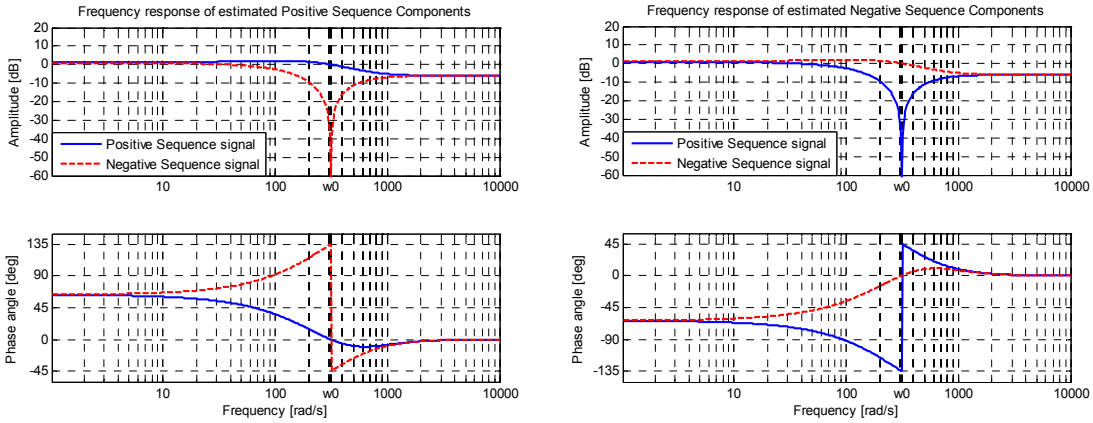

(a) Positive Sequence estimation (b) Negative Sequence estimation

Fig. B-1 Frequency response of sequence separation based on 2nd order low-pass filters

B.2 Analysis of Filter-based Methods for Sequence Separation

In section 2.3 and 3.2, it is implicitly shown how methods for sequence separation in the stationary reference frame can be applied to voltage, current and Virtual Flux signals. The characteristics of the sequence separation methods could therefore be analyzed in a general way, without limiting the discussion to the context of the various methods for Virtual Flux estimation. Although only the methods from [51] and [107] will be briefly analyzed here, the same approach could be followed for any other approach for filter- or delay-based methods for sequence separation.

B.2.1 Sequence Separation by using Second-order Low-pass Filters

The sequence separation methods applied in [107] is based on using a second order low pass filter to generate the 90° phase shift needed for implementation of (B.1), as given by (B.2). The characteristics of this low-pass filter, resulting in unity gain and −90° phase shift for fundamental frequency signals has already been discussed with respect to Virtual Flux estimation in section 2.2.3.

$$q_{LP2} = \frac{2 \cdot \omega_0^2}{\left(s + \omega_o\right)^2} \tag{B.2}$$

By using the same approach as described in section 3.3.1, and considering only the steady state frequency characteristics, the positive sequence α-axis component of a generic three-phase signal will be given by (B.3). The same expression can also be found for the β-axis component.

$$x_\alpha^+\left(j\omega\right) = \frac{1}{2}\left[1 + j \cdot \frac{2 \cdot \omega_0^2}{\left(j\omega + \omega_o\right)^2}\right] \cdot x_\alpha\left(j\omega\right) \tag{B.3}$$

By expressing (B.3) on a common denominator, the steady state transfer function from an unbalanced set of $\alpha\beta$-signals to the corresponding positive sequence components is given by (B.4). Similarly, the transfer function for estimation of the negative sequence components can be found as given by (B.5).

$$h_{LP2}^{+}(j\omega)=\frac{x_{\alpha\beta}^{+}(j\omega)}{x_{\alpha\beta}(j\omega)}=\frac{1}{2}\cdot\frac{\omega_0^2-\omega^2+j\cdot 2\omega_0(\omega+\omega_0)}{\omega_0^2-\omega^2+j\cdot 2\omega_0\cdot\omega} \tag{B.4}$$

$$h_{LP2}^{-}(j\omega)=\frac{x_{\alpha\beta}^{-}(j\omega)}{x_{\alpha\beta}(j\omega)}=\frac{1}{2}\cdot\frac{\omega_0^2-\omega^2+j\cdot 2\omega_0(\omega-\omega_0)}{\omega_0^2-\omega^2+j\cdot 2\omega_0\cdot\omega} \tag{B.5}$$

The frequency characteristics of (B.4) and (B.5) are plotted in Fig. B-1 (a) and (b) respectively. The curves are plotted for both positive and negative values of the angular frequency, corresponding to positive and negative sequence components. Fig. B-1 a) clearly shows how unity gain and zero phase shift is achieved for estimation of fundamental frequency positive sequence signals. The influence of negative sequence components on the estimated positive sequence components is effectively eliminated, since the frequency characteristics show zero gain for fundamental frequency negative sequence components. Similarly, Fig. B-1 (b) shows how fundamental frequency negative sequence components are estimated with unity gain and zero phase shift, while the influence from the positive sequence components is filtered out.

From the frequency characteristics in Fig. B-1, it is worth noting that the response for both positive and negative sequence components is approaching 0.5 at high frequencies. This can be easily understood from (B.3), where the first term is a pure gain, while the second term is the second order low-pass filter. The possible implications of this characteristic with respect to sequence separation of current measurements and the bandwidth of current control loops in case of implementation in the PNS SRFs are briefly addresses in publication [C2].

B.2.2 Sequence Separation by using SOGI-QSGs

The SOGI-QSG described in section 3.1.1 according to [51] was initially proposed for achieving on-line frequency-adaptive sequence separation of measured grid voltages for the purpose of grid synchronization. The phase shifting operator q will in this case be given by the transfer function corresponding to the in-quadrature output signal from the SOGI-QSG according to (B.6).

$$q_{SOGI-QSG}=\frac{qv'(s)}{v(s)}=Q(s)=\frac{k\cdot\omega'^2}{s^2+k\cdot\omega'\cdot s+\omega'^2} \tag{B.6}$$

The sequence separation method presented in [51] was intended for grid synchronization, and was utilized by using both output signals from the SOGI-QSG. Although not commonly applied, it is however also possible to configure a structure for sequence separation based on SOGI-QSGs in way which is more similar to the method presented in the previous subsection.

B.2.2.1 Sequence separation by using both outputs from the SOGI-QSGs

When using both outputs from the SOGI-QSG for sequence separation, the filtered in-phase output signal is used in place of the actual input signal. The transfer function defining the in-phase output signal is given by (B.7)

$$\frac{v'(s)}{v(s)}=D(s)=\frac{k\cdot\omega'\cdot s}{s^2+k\cdot\omega'\cdot s+\omega'^2} \tag{B.7}$$

By using (B.7) and (B.6), the equation for sequence separation according to (B.1) can be expressed by (B.8).

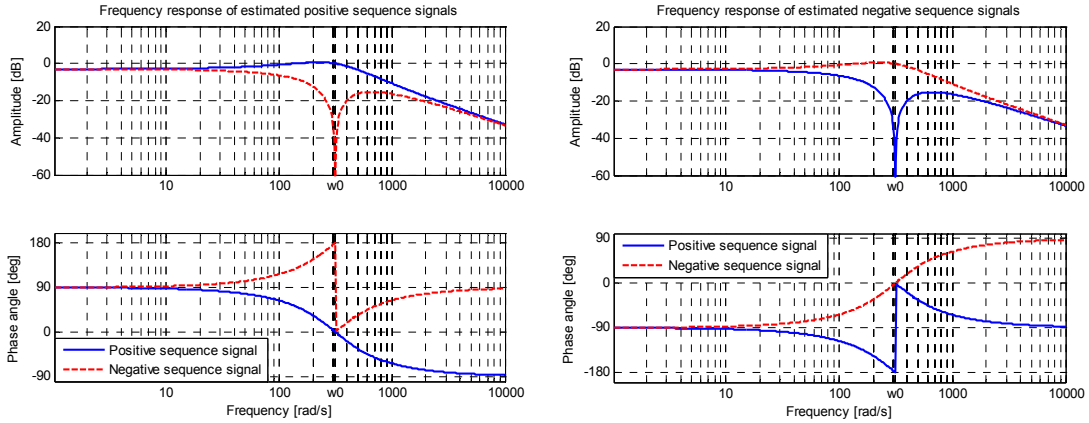

a) Positive Sequence estimation b) Negative Sequence estimation

Fig. B-2 Frequency response of Sequence Separation based on SOGI-QSGs

$$\begin{bmatrix} x_\alpha^+ \\ x_\beta^+ \end{bmatrix} = \frac{1}{2}\begin{bmatrix} D(s) & -Q(s) \\ Q(s) & D(s) \end{bmatrix} \cdot \begin{bmatrix} x_\alpha \\ x_\beta \end{bmatrix}$$
$$\begin{bmatrix} x_\alpha^- \\ x_\beta^- \end{bmatrix} = \frac{1}{2}\begin{bmatrix} D(s) & Q(s) \\ -Q(s) & D(s) \end{bmatrix} \cdot \begin{bmatrix} x_\alpha \\ x_\beta \end{bmatrix} \quad \text{(B.8)}$$

Substituting into (B.8) according to the previously describe approach, the steady-state transfer functions defining the frequency characteristics of the estimated positive and negative sequence components can be found as (B.9) and (B.10).

$$h_{DSOGI,D\&Q}^{+}(j\omega) = \frac{x_{\alpha\beta}^{+}(j\omega)}{x_{\alpha\beta}(j\omega)} = \frac{1}{2}\cdot\frac{k\omega'(\omega+\omega')}{k\omega'\cdot\omega + j\left(\omega^2-\omega'^2\right)} \quad \text{(B.9)}$$

$$h_{DSOGI,D\&Q}^{-}(j\omega) = \frac{x_{\alpha\beta}^{-}(j\omega)}{x_{\alpha\beta}(j\omega)} = \frac{1}{2}\cdot\frac{k\omega'(\omega-\omega')}{k\omega'\cdot\omega + j\left(\omega^2-\omega'^2\right)} \quad \text{(B.10)}$$

It can be noticed that these equations are similar to the equations describing the frequency characteristics of the proposed DSOGI-VF estimation as discussed in section 3.3 with the only difference being a phase shift of ±90 due to the Virtual Flux estimation. This can be easily verified by comparing the frequency responses plotted in Fig. B-2 with the results from Fig. 3-7, or by simply evaluating the transfer functions at the nominal grid angular frequency. The transfer functions in (B.9) and (B.10) can also be expressed in the same way as the equations in section 3.3, as further analyzed and discussed in [96], [196].

B.2.2.2 Sequence separation by using only in-quadrature outputs from the SOGI-QSGs

Although not explicitly discussed in the available literature on grid synchronization and sequence separation of three-phase variables, the sequence separation can be based only on the in-quadrature output signals from the SOGI-QSGs. The expressions for estimation of positive will then be given by (B.11)

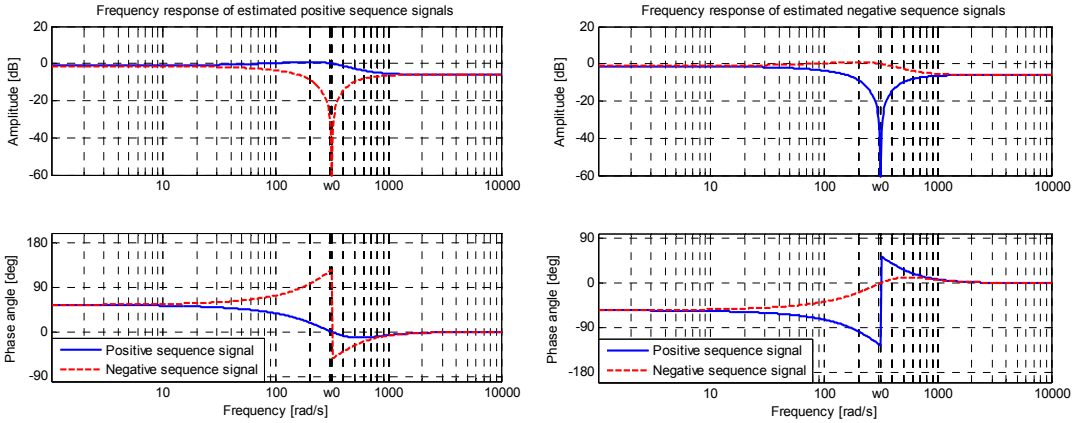

a) Positive Sequence estimation b) Negative Sequence estimation

Fig. B-3 Frequency response of Sequence Separation based on unfiltered input signals and in-quadrature signals from SOGI-QSGs

$$\begin{bmatrix} x_\alpha^+ \\ x_\beta^+ \end{bmatrix} = \frac{1}{2}\begin{bmatrix} 1 & -Q(s) \\ Q(s) & 1 \end{bmatrix} \cdot \begin{bmatrix} x_\alpha \\ x_\beta \end{bmatrix}$$
$$\begin{bmatrix} x_\alpha^- \\ x_\beta^- \end{bmatrix} = \frac{1}{2}\begin{bmatrix} 1 & Q(s) \\ -Q(s) & 1 \end{bmatrix} \cdot \begin{bmatrix} x_\alpha \\ x_\beta \end{bmatrix} \quad \text{(B.11)}$$

The steady-state transfer functions characterizing the estimation of the positive and negative sequence components can then be found as given by (B.12) and (B.13), and the corresponding frequency responses are plotted in Fig. B-3. The implications with respect to the bandwidth of the sequence separation will be the same as for the method from B.2.1, and this configuration can thus be relevant for sequence separation in the feedback loop of PNS current controllers.

$$h_{DSOGI,Q}^{+}(j\omega) = \frac{x_{\alpha\beta}^{+}(j\omega)}{x_{\alpha\beta}(j\omega)} = \frac{1}{2}\cdot\frac{\omega_0^2 - \omega^2 + j\cdot k\omega'(\omega+\omega')}{\omega'^2 - \omega^2 + j\cdot k\omega'\cdot\omega} \quad \text{(B.12)}$$

$$h_{DSOGI,Q}^{-}(j\omega) = \frac{x_{\alpha\beta}^{-}(j\omega)}{x_{\alpha\beta}(j\omega)} = \frac{1}{2}\cdot\frac{\omega_0^2 - \omega^2 + j\cdot k\omega'(\omega-\omega')}{\omega'^2 - \omega^2 + j\cdot k\omega'\cdot\omega} \quad \text{(B.13)}$$

B.3 Analysis of Methods for Estimation of Positive and Negative Sequence Virtual Flux Components

As discussed in section 2.3 and 3.2, Virtual Flux-based strategies designed for grid synchronization in unbalanced conditions are usually implemented by cascading methods for sequence separation with filter-based techniques for Virtual Flux estimation. The frequency characteristics of such methods will therefore be determined by the combination of the transfer function of the Virtual Flux estimation and the transfer function of the sequence separation method as discussed in the previous subsections.

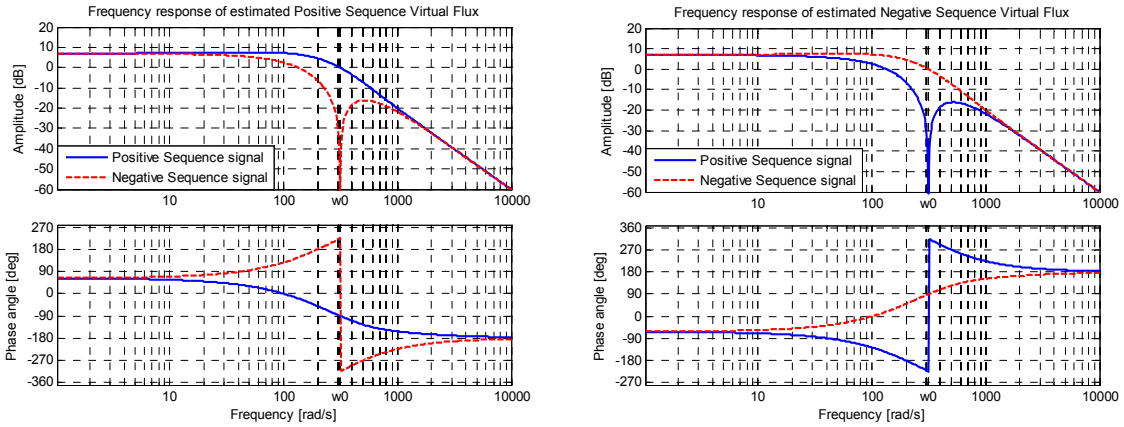

a) Estimation of Positive Sequence Virtual Flux

b) Estimation of Negative Sequence Virtual Flux

Fig. B-4 Frequency response of Sequence Separation cascaded with PNS VF estimation based on Second Order Low-pass Filters

B.3.1 Frequency Response of Sequence Separation and Virtual Flux Estimation based on Second-order Low-pass Filters

The frequency response of the PNS VF estimation method from [107] and Fig. 2-7 in section 2.3 can be investigated by combining the transfer functions of the sequence separation from section B.2.1 with the transfer function for Virtual Flux estimation according to (2.11). The resulting transfer functions for estimation of the PNS VF components are given by (B.14) and (B.15), and the corresponding frequency responses are plotted in Fig. B-4 (a) and (b).

From Fig. B-4 a), it is clearly seen that the positive sequence Virtual Flux is correctly estimated, since unity gain and −90° phase shift is achieved at the fundamental angular grid frequency ω_0. This figure also shows how the influence of negative sequence components is eliminated from the estimated positive sequence Virtual Flux. For frequencies significantly above ω_0 it can be noticed the frequency response is asymptotically approaching a straight line corresponding to −40 dB/decade. Fig. B-4 b) shows the equivalent characteristics for the estimation of negative sequence Virtual Flux components.

$$\frac{\psi_\alpha^+(j\omega)}{v_\alpha(j\omega)} = \underbrace{\left[\frac{\omega_0^2-\omega^2+j\cdot 2\omega_0(\omega+\omega_0)}{2\left(\omega_0^2-\omega^2+j\cdot 2\omega_0\cdot\omega\right)}\right]}_{h_{LP2}^+(j\omega)} \cdot \underbrace{\frac{2\cdot\omega_0^2}{(j\omega+\omega_o)^2}}_{h_{LP2}^{\int}(j\omega)} \tag{B.14}$$

$$\frac{\psi_\alpha^-(j\omega)}{v_\alpha(j\omega)} = \underbrace{\left[\frac{\omega_0^2-\omega^2+j\cdot 2\omega_0(\omega-\omega_0)}{2\left(\omega_0^2-\omega^2+j\cdot 2\omega_0\cdot\omega\right)}\right]}_{h_{LP2}^-(j\omega)} \cdot \underbrace{\frac{2\cdot\omega_0^2}{(j\omega+\omega_o)^2}}_{h_{LP2}^{\int}(j\omega)} \tag{B.15}$$

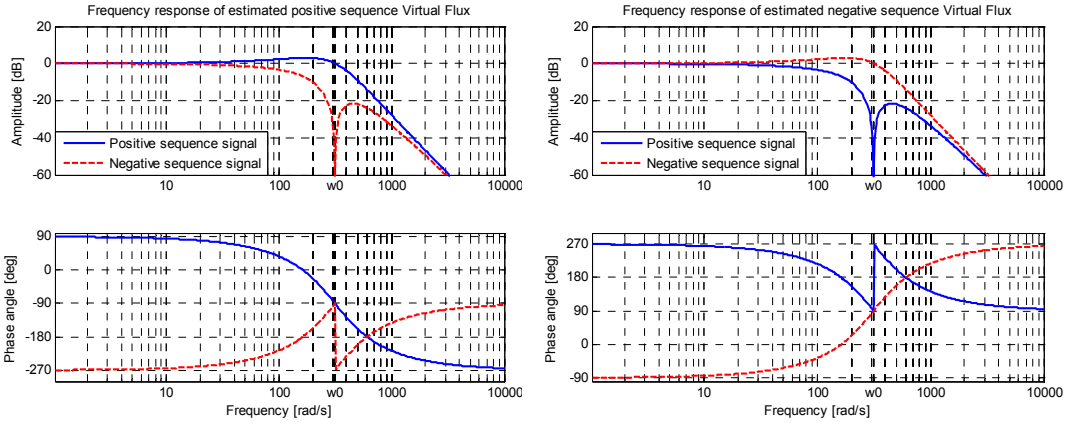

a) Estimation of Positive Sequence Virtual Flux

b) Estimation of Negative Sequence Virtual Flux

Fig. B-5 Frequency response of Sequence Separation cascaded with PNS VF estimation based on SOGI-QSGs

B.3.2 Cascaded Methods for Sequence Separation and Virtual Flux Estimation based on SOGI-QSGs

The methods for PNS VF estimation discussed in section 3.2, can be investigated by starting from the transfer function of sequence separation based on SOGI-QSGs in section B.2.2 and the transfer function from (3.7) in section 3.1 for Virtual Flux estimation by using SOGI-QSGs. The resulting steady state transfer functions are given in (B.16) and (B.17), and are plotted in Fig. B-5 (a) and (b) respectively. It can be noticed that the frequency characteristics will be the same if the sequence separation is based on estimated Virtual Flux signals or if the Virtual Flux estimation is based on positive and negative sequence components. Equations (B.16) and (B.17) can therefore be considered to represent both structures presented in section 3.2.1 and 3.2.2.

$$\frac{\chi_\alpha^+(j\omega)}{v_\alpha(j\omega)} = \underbrace{\left[\frac{1}{2}\cdot\frac{k\omega'(\omega+\omega')}{k\omega'\cdot\omega + j\left(\omega^2-\omega'^2\right)}\right]}_{h^+_{DSOGI,D\&Q}(j\omega)} \cdot \underbrace{\frac{k\cdot\omega'^2}{\omega'^2-\omega^2+j\cdot k\cdot\omega'\cdot\omega}}_{h^j_{SOGI-QSG}(j\omega)} \tag{B.16}$$

$$\frac{\chi_\alpha^-(j\omega)}{v_\alpha(j\omega)} = \underbrace{\left[\frac{1}{2}\cdot\frac{k\omega'(\omega-\omega')}{k\omega'\cdot\omega + j\left(\omega^2-\omega'^2\right)}\right]}_{h^-_{DSOGI,D\&Q}(j\omega)} \cdot \underbrace{\frac{k\cdot\omega'^2}{\omega'^2-\omega^2+j\cdot k\cdot\omega'\cdot\omega}}_{h^j_{SOGI-QSG}(j\omega)} \tag{B.17}$$

Due to the SOGI-QSG-based implementation, both the Virtual Flux estimation and the sequence separation will be explicitly frequency-adaptive as long as an appropriate estimate ω' of the grid angular frequency is available. This is indicated by using the notation ω' instead of ω_0 in the equations.

From Fig. B-5 (a), it can be verified that the positive sequence Virtual Flux will be correctly estimated in steady state by achieving unity gain and −90° phase shift for fundamental frequency signals. The influence of possible negative sequence components are again eliminated from the estimated positive sequence components, since (B.16) results in zero gain for frequencies equal to $-\omega_0 = -\omega'$. The equivalent characteristics can be seen in Fig. B-5 (b), ensuring that the negative sequence

components are correctly estimated without influence from the positive sequence components. It can also be noticed that the amplitude response is asymptotically approaching a line corresponding to −60 dB/decade for high frequencies

As indicated by the discussion in section 3.4, frequency-adaptive PNS VF estimation based on SOGI-QSGs can be implemented by using the sequence separation strategy from section B.2.2.2 to improve the dynamic response. The resulting transfer functions for estimation of PNS VF components will then be given by the product of (B.12) and (B.13) with the transfer function for Virtual Flux estimation according to (3.7). The asymptotic amplitude characteristics for high frequency signals will then result in −40 dB/decade, as for the Virtual Flux estimation method from [107] and B.3.1.

Appendix C Discrete Time Implementation of SOGI and SOGI-QSG Structures

This Appendix presents the discrete time implementation of SOGIs and SOGI-QSGs applied in this Thesis.

C.1 General Comment on Discrete Time Implementation of SOGI-based Structures

It is well known that the performance of resonant structures like the Second Order Generalized Integrator (SOGI) is sensitive to the discretization methods applied for discrete time digital implementation. This issue has recently received significant attention regarding accuracy of implementation for resonant current controllers as discussed in [243], [244], but is equally important with respect to applications in grid synchronization strategies as discussed in [51], [52], [191], [198], [199].

The basic structure of the SOGI is shown in Fig. C-1, and can be used as a general building block for implementing Proportional-Resonant (PR) controllers as well as band-pass filters or Quadrature Signal Generators (QSGs) as discussed in section 3.1.1. If only one of the output signals from the SOGI should be utilized, and if the resonant frequency ω' can be considered constant, the corresponding transfer function can be identified and discretized using an appropriate numerical integration technique. This approach can be used to assure accurate placement of the poles of the transfer function, but can also complicate the possibilities for frequency-adaptive operation based on on-line updates of the resonant frequency ω'. Implementations based on explicit discretization of the individual integrators in Fig. C-1 are therefore attractive since they are simple and can be easily combined with frequency-adaptive operation. However, the poles of the resulting transfer function will not exactly match the intended resonance frequency, and the desired infinite gain will therefore appear at a frequency that is slightly different from the intended value. The inaccuracies of such two-integrator implementation schemes will however depend on the sampling frequency of the discrete time implementation, and this approach can therefore in some cases be an acceptable compromise between accuracy and simplicity.

A detailed discussion on discrete time implementation issues regarding SOGIs and SOGI-QSGs is beyond the scope of this Thesis. The main purpose of this Appendix is therefore to explicitly document the approaches followed to obtain the various results presented in the previous chapters. The numerical methods applied in simulation studies with the PSCAD/EMTDC simulation environment, [245], and for discrete time implementation in Matlab/Simulink, [246], for operation of the dSPACE platform, [247], in the experimental setup can be summarized as follows:

- For simulation of PR current controllers without possibility for explicitly frequency-adaptive operation, the appropriate transfer function of the SOGI has been specified. The simulation will then be based on trapezoidal integration, as this is the numerical integration method applied by PSCAD/EMTDC.

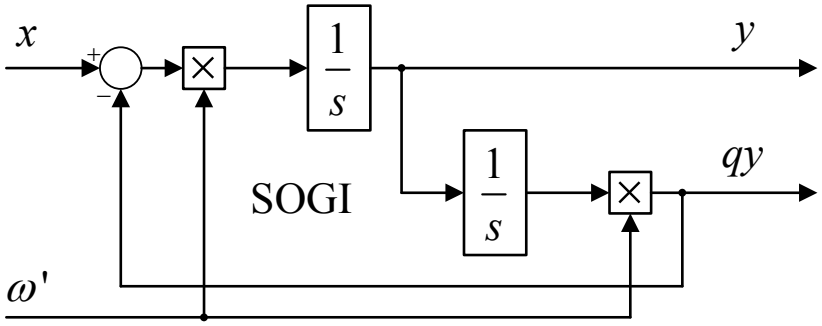

Fig. C-1 Structure of Second Order Generalized Integrator in the continuous time domain

- For simulation of SOGI-QSGs, where both frequency-adaptive operation and explicit access to all the variables of the structures is required, the structure from Fig. C-1 has been implemented directly. Thus, each integrator is simulated by using the trapezoidal integration method applied by PSCAD/EMTDC. This has been considered to provide sufficient accuracy as long as the simulation time-step is very small with respect to the resonant frequency corresponding to the fundamental grid frequency.
- For frequency-adaptive implementation of PR current controllers, a two-integrator scheme that will be explained in the following subsection has been applied. The implementation is similar to the approach recommended by [198]. This approach has been used in the experimental setup, as it was already in use for other applications in the laboratory where the presented experiments were conducted. The same approach has also been verified by simulations, although this does not have significant influence on any of the presented simulation results.
- For implementation of SOGI-QSGs in the laboratory setup, a state-space approach presented in [194], [199] was applied, since this approach was already implemented in the laboratory where the experiments were conducted. The same implementation has also been verified by simulation studies, although this does not have significant influence on any of the presented simulation results. The derivation of the difference equations for discrete time implementation resulting from this state-space approach is documented in a separate subsection.

C.2 Two-Integrator-based Scheme for Implementation of PR current controllers

The two-integrator-based scheme applied for implementation of PR current controllers is based on the discretization approach documented in [198]. Thus, a computational delay of one sample is considered, and the two integrators are discretized by using the Euler backward approximation given by (C.1) [198] [197]. The resulting block diagram corresponding to discrete time implementation is then given by Fig. C-2.

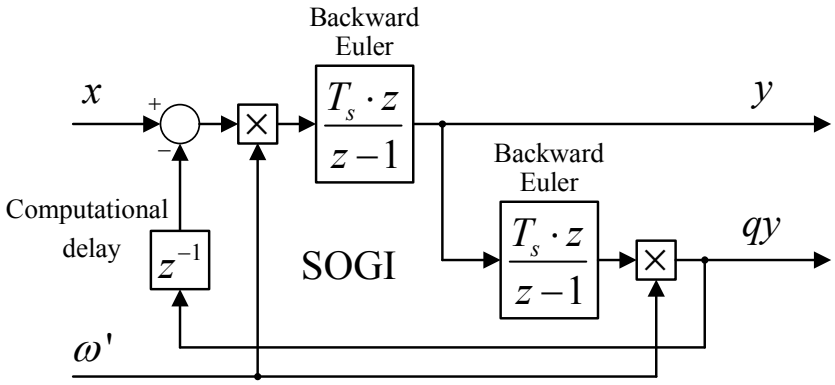

Fig. C-2 Structure of Second Order Generalized Integrator implemented by a two-integrator scheme in the discrete time domain

$$s = \frac{1 - z^{-1}}{T_s \cdot z} \tag{C.1}$$

The z-domain transfer function of this discrete time implementation of the PR controller is given by (C.2).

$$G(z) = \frac{y(z)}{x(z)} = \frac{\omega' \cdot T_s \cdot (z-1) \cdot z}{\left(1 + \omega'^2 \cdot T_s^2\right) \cdot z^2 - 2 \cdot z + 1} = \frac{\frac{\omega' \cdot T_s}{\left(1 + \omega'^2 \cdot T_s^2\right)} \cdot (z-1) \cdot z}{z^2 - \frac{2}{\left(1 + \omega'^2 \cdot T_s^2\right)} \cdot z + \frac{1}{\left(1 + \omega'^2 \cdot T_s^2\right)}} \tag{C.2}$$

From this transfer function, it can be fond that the poles will not be located exactly on the unit circle unless the sampling period T_s is equal to zero. For low sampling frequencies, the influence on the resonance frequency of the PR controller can also be significant. This implies that a PR controller implemented by this approach will experience the peak gain at a different frequency than the grid frequency. Thus the gain at the fundamental grid frequency can be significantly reduced, resulting in steady state errors when intending to track a sinusoidal reference signal. Compared to the continuous time characteristics, there can also be significant phase errors for frequencies above the resonant frequency.

C.3 State-space Model and Difference Equations for Implementation of SOGI-QSGs

To achieve a generally valid representation and discrete time implementation with improved accuracy, a state-space approach for discretization of the SOGI-QSG has been applied [194], [199]. This approach is based on a starting from a continuous time state space representation of the SOGI-QSG as will be presented in the following.

C.3.1 Continuous Time State-Space Model of SOGI-QSG

The structure of the SOGI-QSG is shown in Fig. C-3, with indication of the appropriate state-variables. The state-space variables, the inputs and the outputs of the model can then be defined by (C.3), and the corresponding equations for the state-variables and the outputs are given by (C.4).

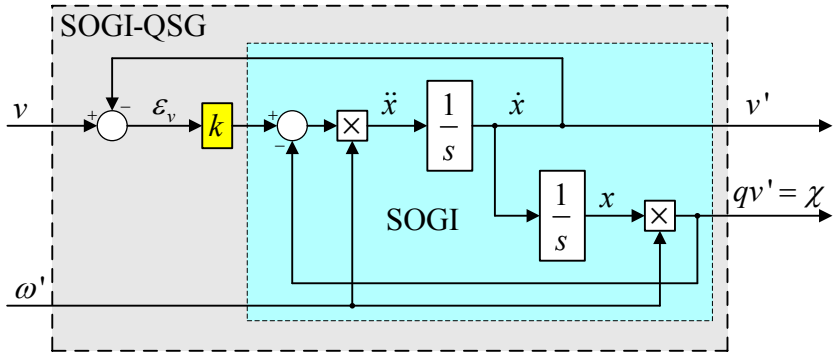

Fig. C-3 Structure of SOGI-QSG for establishing state space model

$$\begin{aligned} x_1 &= x \\ x_2 &= \dot{x} \\ u_1 &= v \\ y_1 &= v' \\ y_2 &= qv' \end{aligned} \tag{C.3}$$

$$\begin{aligned} \dot{x}_1 &= x_2 \\ \dot{x}_2 &= -\omega'^2 \cdot x_1 - k \cdot \omega' \cdot x_2 + k \cdot \omega' \cdot v \\ y_1 &= x_2 \\ y_2 &= \omega' \cdot x_1 \end{aligned} \tag{C.4}$$

Considering that the SOGI-QSG structure should be represented on the general state-space form given by (C.5), the resulting state-space model can be expressed by (C.6) [199].

$$\begin{aligned} \dot{\mathbf{x}}(t) &= \mathbf{A} \cdot \mathbf{x}(t) + \mathbf{B} \cdot \mathbf{u}(t) \\ \mathbf{y}(t) &= \mathbf{C} \cdot \mathbf{x}(t) + \mathbf{D} \cdot \mathbf{u}(t) \end{aligned} \tag{C.5}$$

$$\begin{aligned} \underbrace{\begin{bmatrix} \dot{x}_1 \\ \dot{x}_2 \end{bmatrix}}_{\dot{\mathbf{x}}} &= \underbrace{\begin{bmatrix} 0 & 1 \\ -\omega'^2 & -k \cdot \omega' \end{bmatrix}}_{\mathbf{A}} \cdot \underbrace{\begin{bmatrix} x_1 \\ x_2 \end{bmatrix}}_{\mathbf{x}} + \underbrace{\begin{bmatrix} 0 \\ k \cdot \omega' \end{bmatrix}}_{\mathbf{B}} \cdot \underbrace{u_1}_{\mathbf{u}} \\ \begin{bmatrix} y_1 \\ y_2 \end{bmatrix} &= \underbrace{\begin{bmatrix} 0 & 1 \\ \omega' & 0 \end{bmatrix}}_{\mathbf{C}} \cdot \begin{bmatrix} x_1 \\ x_2 \end{bmatrix} \end{aligned} \tag{C.6}$$

C.3.2 Discrete Time State-Space Model of SOGI-QSG

For digital implementation of the continuous time state space model of (C.5), the discrete time equivalent model is given by the difference equation of (C.7). When applying trapezoidal integration by using the Tustin approximation given by (C.8), the characteristic matrices are defined by (C.9) [197], [194].

$$\begin{aligned} \mathbf{x}[\mathrm{k}+1] &= \boldsymbol{\Phi} \cdot \mathbf{x}[\mathrm{k}] + \boldsymbol{\Gamma} \cdot \mathbf{u}[\mathrm{k}] \\ \mathbf{y}[\mathrm{k}+1] &= \mathbf{H} \cdot \mathbf{x}[\mathrm{k}] + \mathbf{J} \cdot \mathbf{u}[\mathrm{k}] \end{aligned} \tag{C.7}$$

$$s = \frac{2}{T_s} \cdot \frac{1 - z^{-1}}{1 + z^{-1}} \tag{C.8}$$

$$\begin{aligned}
\mathbf{\Phi} &= \left(\mathbf{I} + \frac{T_s}{2} \mathbf{A} \right) \cdot \left(\mathbf{I} - \frac{T_s}{2} \mathbf{A} \right)^{-1} \\
\mathbf{\Gamma} &= \left(\mathbf{I} - \frac{T_s}{2} \mathbf{A} \right)^{-1} \cdot \mathbf{B} \\
\mathbf{H} &= T_s \cdot \mathbf{C} \cdot \left(\mathbf{I} - \frac{T_s}{2} \mathbf{A} \right)^{-1} \\
\mathbf{J} &= \mathbf{D} + \mathbf{C} \cdot \left(\mathbf{I} - \frac{T_s}{2} \mathbf{A} \right)^{-1} \cdot \mathbf{B} \cdot \frac{T_s}{2}
\end{aligned} \tag{C.9}$$

The matrix operations which define the characteristic matrices of this state-space model can be calculated as given by (C.10).

$$\begin{aligned}
\left(\mathbf{I} + \frac{T_s}{2} \mathbf{A} \right) &= \begin{bmatrix} 1 & \frac{T_s}{2} \\ -\frac{T_s}{2} \cdot \omega'^2 & 1 - \frac{T_s}{2} \cdot k \cdot \omega' \end{bmatrix} \\
\left(\mathbf{I} - \frac{T_s}{2} \mathbf{A} \right)^{-1} &= \frac{1}{1 + \frac{T_s}{2} \cdot k \cdot \omega' + \frac{T_s^2}{4} \cdot \omega'^2} \cdot \begin{bmatrix} 1 + \frac{T_s}{2} \cdot k \cdot \omega' & -\frac{T_s}{2} \\ \frac{T_s}{2} \cdot \omega'^2 & 1 \end{bmatrix}
\end{aligned} \tag{C.10}$$

Thus, the matrices **Φ**, **Γ H** and **J** of (C.7) can be calculated as given by (C.11), (C.12), (C.13) and (C.14) respectively.

$$\begin{aligned}
\mathbf{\Phi} &= \left(\mathbf{I} + \frac{T_s}{2} \mathbf{A} \right) \cdot \left(\mathbf{I} - \frac{T_s}{2} \mathbf{A} \right)^{-1} \\
&= \frac{1}{4 + 2 \cdot T_s \cdot k \cdot \omega' + T_s^2 \cdot \omega'^2} \cdot \begin{bmatrix} 4 + 2 \cdot T_s \cdot k \cdot \omega' - T_s^2 \cdot \omega'^2 & 4 \cdot T_s \\ -4 \cdot T_s \cdot \omega' & 4 - 2 \cdot T_s \cdot k \cdot \omega' - T_s^2 \cdot \omega'^2 \end{bmatrix}
\end{aligned} \tag{C.11}$$

$$\mathbf{\Gamma} = \left(\mathbf{I} - \frac{T_s}{2} \mathbf{A} \right)^{-1} \cdot \mathbf{B} = \frac{1}{4 + 2 \cdot T_s \cdot k \cdot \omega' + T_s^2 \cdot \omega'^2} \cdot \begin{bmatrix} 2 \cdot T_s \cdot k \cdot \omega' \\ 4 \cdot k \cdot \omega' \end{bmatrix} \tag{C.12}$$

$$\begin{aligned}
\mathbf{H} &= T_s \cdot \mathbf{C} \cdot \left(\mathbf{I} - \frac{T_s}{2} \mathbf{A} \right)^{-1} \\
&= \frac{1}{4 + 2 \cdot T_s \cdot k \cdot \omega' + T_s^2 \cdot \omega'^2} \cdot \begin{bmatrix} -2 \cdot T_s^2 \cdot \omega'^2 & 4 \cdot T_s \\ \left(2 + T_s \cdot k \cdot \omega' \right) \cdot 2 \cdot T_s \cdot \omega' & 2 \cdot T_s^2 \cdot \omega'^2 \end{bmatrix}
\end{aligned} \tag{C.13}$$

$$\mathbf{J} = \mathbf{D} + \mathbf{C} \cdot \left(\mathbf{I} - \frac{T_s}{2} \mathbf{A} \right)^{-1} \cdot \mathbf{B} \cdot \frac{T_s}{2} = \frac{1}{4 + 2 \cdot T_s \cdot k \cdot \omega' + T_s^2 \cdot \omega'^2} \cdot \begin{bmatrix} 2 \cdot T_s \cdot k \cdot \omega' \\ k \cdot T_s^2 \cdot \omega'^2 \end{bmatrix} \tag{C.14}$$

It can be noticed that all the elements in these matrices have the same denominator. At the same time, it should be remembered that the grid angular frequency ω' must be continuously updated to keep the SOGI-QSG frequency-adaptive. Thus, the resulting state-space equations are nonlinear, and the matrix elements must be calculated for every time-step. Illustrating that ω' is also a variable, the state space equations are given on the same form as (C.15).

$$\begin{aligned}\mathbf{x}[\mathrm{k}+1] &= f\left(\mathbf{x}[\mathrm{k}], \omega'[\mathrm{k}], v[\mathrm{k}]\right) \\ \mathbf{y}[\mathrm{k}+1] &= g\left(\mathbf{x}[\mathrm{k}], \omega'[\mathrm{k}], v[\mathrm{k}]\right)\end{aligned} \tag{C.15}$$

Defining the common denominator by (C.16), the resulting difference equations for the state variables and the outputs are given by (C.17) and (C.18) respectively. These equations are therefore implemented for achieving for achieving explicitly frequency-adaptive discrete time implementation of the SOGI-QSG.

$$\Lambda = \frac{1}{4 + 2 \cdot T_s \cdot k \cdot \omega'[\mathrm{k}] + T_s^2 \cdot \omega'[\mathrm{k}]^2} \tag{C.16}$$

$$\begin{aligned}&\begin{bmatrix} x_1[\mathrm{k}+1] \\ x_2[\mathrm{k}+1] \end{bmatrix} \\ &= \underbrace{\frac{1}{\Lambda} \cdot \begin{bmatrix} 4 + 2 \cdot T_s \cdot k \cdot \omega'[\mathrm{k}] - T_s^2 \cdot \omega'[\mathrm{k}]^2 & 4 \cdot T_s \\ -4 \cdot T \cdot \omega'[\mathrm{k}]^2 & 4 - 2 \cdot T_s \cdot k \cdot \omega'[\mathrm{k}] - T_s^2 \cdot \omega'[\mathrm{k}]^2 \end{bmatrix}}_{\boldsymbol{\Phi}(\omega[k])} \cdot \begin{bmatrix} x_1[\mathrm{k}] \\ x_2[\mathrm{k}] \end{bmatrix} \\ &\quad + \underbrace{\frac{1}{\Lambda} \cdot \begin{bmatrix} 2 \cdot T_s \cdot k \cdot \omega'[\mathrm{k}] \\ 4 \cdot k \cdot \omega'[\mathrm{k}] \end{bmatrix}}_{\boldsymbol{\Gamma}(\omega[k])} \cdot v[\mathrm{k}]\end{aligned} \tag{C.17}$$

$$\begin{aligned}\begin{bmatrix} v'[\mathrm{k}+1] \\ qv'[\mathrm{k}+1] \end{bmatrix} &= \underbrace{\frac{1}{\Lambda} \cdot \begin{bmatrix} -2 \cdot T_s^2 \cdot \omega'[\mathrm{k}]^2 & 4 \cdot T_s \\ \left(2 + T_s \cdot k \cdot \omega'[\mathrm{k}]\right) \cdot 2 \cdot T_s \cdot \omega'[\mathrm{k}] & 2 \cdot T_s^2 \cdot \omega'[\mathrm{k}] \end{bmatrix}}_{\mathbf{H}(\omega[k])} \cdot \begin{bmatrix} x_1[\mathrm{k}] \\ x_2[\mathrm{k}] \end{bmatrix} \\ &\quad + \underbrace{\frac{1}{\Lambda} \cdot \begin{bmatrix} 2 \cdot T_s \cdot k \cdot \omega'[\mathrm{k}] \\ T_s^2 \cdot k \cdot \omega'[\mathrm{k}]^2 \end{bmatrix}}_{\mathbf{J}(\omega[k])} \cdot v[\mathrm{k}]\end{aligned} \tag{C.18}$$

Appendix D Definitions and Derivations Related to Virtual Flux-based Power Control and Current Limitation

This Appendix presents the definitions and conventions applied for voltage and Virtual Flux signals in the derivations and considerations behind the results presented in Chapter 4 and 5. The Appendix also includes the derivations of the expressions for active and reactive power oscillations corresponding to the control objectives discussed in Chapter 4, as well as the derivations of the equations presented in Chapter 5 related to current reference calculation under phase current limitation.

D.1 Basic Definition of Positive and Negative Sequence Voltage and Virtual Flux Signals

As a starting point for the following derivations, the assumed conventions for voltage and Virtual Flux signals will be defined.

D.1.1 Positive and Negative Sequence Voltage Signals

The positive and negative sequence components of the grid voltage are assumed to be given on a general form corresponding to (D.1) and (D.2) respectively. Under steady state conditions, the amplitudes of the positive and negative sequence voltage components will be constant, while the phase angles ϕ^+ and ϕ^- are representing a phase shift with respect to a global phase angle $\theta = \omega \cdot t$.

$$\mathbf{v}^+ = \begin{bmatrix} v_\alpha^+ \\ v_\beta^+ \end{bmatrix} = \begin{bmatrix} \hat{v}^+ \cdot \cos\left(\theta + \phi^+\right) \\ \hat{v}^+ \cdot \sin\left(\theta + \phi^+\right) \end{bmatrix} \tag{D.1}$$

$$\mathbf{v}^- = \begin{bmatrix} v_\alpha^- \\ v_\beta^- \end{bmatrix} = \begin{bmatrix} \hat{v}^- \cdot \cos\left(-\theta + \phi^-\right) \\ \hat{v}^- \cdot \sin\left(-\theta + \phi^-\right) \end{bmatrix} \tag{D.2}$$

The total voltage in the α- and β- axes will then be given by (D.3)

$$\mathbf{v} = \begin{bmatrix} v_\alpha \\ v_\beta \end{bmatrix} = \begin{bmatrix} \hat{v}^+ \cdot \cos\left(\theta + \phi^+\right) + \hat{v}^- \cdot \cos\left(-\theta + \phi^-\right) \\ \hat{v}^+ \cdot \sin\left(\theta + \phi^+\right) + \hat{v}^- \cdot \sin\left(-\theta + \phi^-\right) \end{bmatrix} \tag{D.3}$$

D.1.2 Positive and Negative Sequence Virtual Flux Signals

The Virtual Flux signals should correspond to the integral of the corresponding voltage signals. Thus, the positive and negative sequence Virtual Flux signals are assumed to be expressed by (D.4) and (D.5).

$$\boldsymbol{\chi}^{+} = \begin{bmatrix} \chi_{\alpha}^{+} \\ \chi_{\beta}^{+} \end{bmatrix} = \begin{bmatrix} \hat{\chi}^{+} \cdot \sin\left(\theta + \phi^{+}\right) \\ -\hat{\chi}^{+} \cdot \cos\left(\theta + \phi^{+}\right) \end{bmatrix} \tag{D.4}$$

$$\boldsymbol{\chi}^{-} = \begin{bmatrix} \chi_{\alpha}^{-} \\ \chi_{\beta}^{-} \end{bmatrix} = \begin{bmatrix} -\hat{\chi}^{-} \cdot \sin\left(-\theta + \phi^{-}\right) \\ \hat{\chi}^{-} \cdot \cos\left(-\theta + \phi^{-}\right) \end{bmatrix} \tag{D.5}$$

From these equations, it can easily be verified that there will be a 90° phase shift between the corresponding voltage and Virtual Flux signals, and that this can be interpreted as a phase delay in the direction of rotation. The expression for the total, unbalanced, Virtual Flux vector is given by (D.6)

$$\boldsymbol{\chi} = \boldsymbol{\chi}^{+} + \boldsymbol{\chi}^{-} = \begin{bmatrix} \chi_{\alpha} \\ \chi_{\beta} \end{bmatrix} = \begin{bmatrix} \hat{\chi}^{+} \cdot \sin\left(\theta + \phi^{+}\right) - \hat{\chi}^{-} \cdot \sin\left(-\theta + \phi^{-}\right) \\ -\hat{\chi}^{+} \cdot \cos\left(\theta + \phi^{+}\right) + \hat{\chi}^{-} \cdot \cos\left(-\theta + \phi^{-}\right) \end{bmatrix} \tag{D.6}$$

D.2 Maximum Vector Amplitudes and Graphical Orientation of Elliptic Trajectories under Unbalanced Conditions

Under unbalanced conditions, the voltage and Virtual Flux signals defined in the previous subsections will describe an elliptic trajectory in the stationary reference frame. This section will show how the shape and orientation of such elliptic trajectory are defined in this Thesis.

D.2.1 Phase Angle Corresponding to Peak Amplitude of the Voltage Vector

The amplitude of a voltage vector in the stationary reference frame is generally given by (D.7). Substituting the functions defined for the $\alpha\beta$ components by (D.3), the voltage vector amplitude under unbalanced conditions can be expressed by (D.8). By using trigonometric identities, (D.8) can be simplified to (D.9) where r is defined as the vector amplitude.

$$|\mathbf{v}| = \sqrt{v_{\alpha}^{2} + v_{\beta}^{2}} \tag{D.7}$$

$$|\mathbf{v}| = \sqrt{\left(\hat{v}^{+} \cdot \cos\left(\theta + \phi^{+}\right) + \hat{v}^{-} \cdot \cos\left(\theta - \phi^{-}\right)\right)^{2} + \left(\hat{v}^{+} \cdot \sin\left(\theta + \phi^{+}\right) - \hat{v}^{-} \cdot \sin\left(\theta - \phi^{-}\right)\right)^{2}} \tag{D.8}$$

$$|\mathbf{v}| = \sqrt{\underbrace{\hat{v}^{+^{2}} + \hat{v}^{-^{2}} + 2 \cdot \hat{v}^{+} \cdot \hat{v}^{-} \cdot \left(\cos\left(\theta + \phi^{+}\right) \cdot \cos\left(\theta - \phi^{-}\right) - \sin\left(\theta + \phi^{+}\right) \cdot \sin\left(\theta - \phi^{-}\right)\right)}_{r^{2}}} \tag{D.9}$$

The phase angle θ corresponding to the maximum vector amplitude can be found by differentiation of the expression under the square root in (D.9) as given by (D.10).

$$\begin{aligned} \frac{d \cdot r^{2}}{d\theta} = {} & 2 \cdot \hat{v}^{+} \cdot \hat{v}^{-} \cdot \left(-\sin\left(\theta + \phi^{+}\right) \cdot \cos\left(\theta - \phi^{-}\right) + \cos\left(\theta + \phi^{+}\right) \cdot -\sin\left(\theta - \phi^{-}\right)\right) \\ & - 2 \cdot \hat{v}^{+} \cdot \hat{v}^{-} \cdot \left(\cos\left(\theta + \phi^{+}\right) \cdot \sin\left(\theta - \phi^{-}\right) + \sin\left(\theta + \phi^{+}\right) \cdot \cos\left(\theta - \phi^{-}\right)\right) \end{aligned} \tag{D.10}$$

The peak amplitude of the voltage vector will occur when the expression from (D.10) equals zero, as given by (D.11) and resulting in (D.12).

$$2 \cdot \sin\left(\theta + \phi^{+}\right) \cdot \cos\left(\theta - \phi^{-}\right) + 2 \cdot \cos\left(\theta + \phi^{+}\right) \cdot \sin\left(\theta - \phi^{-}\right) = 0 \tag{D.11}$$

$$-\frac{\sin\left(\theta+\phi^{+}\right)}{\cos\left(\theta+\phi^{+}\right)}=\frac{\sin\left(\theta-\phi^{-}\right)}{\cos\left(\theta-\phi^{-}\right)}=-\tan\left(\theta+\phi^{+}\right)=\tan\left(\theta-\phi^{-}\right) \tag{D.12}$$

Thus, the phase angle corresponding to the maximum amplitude of the voltage vector will occur when the condition given by (D.13) is fulfilled, resulting in (D.14).

$$-\left(\theta_{|v|_{\max}}+\phi^{+}\right)=\theta_{|v|_{\max}}-\phi^{-} \tag{D.13}$$

$$\theta_{|v|_{\max}}=\frac{-\phi^{+}+\phi^{-}}{2} \tag{D.14}$$

D.2.2 Graphical Orientation of Elliptic Trajectories in the Stationary αβ Reference Frame under Unbalanced Conditions

The graphical orientation of the elliptic trajectory described by (D.3) will be defined by an axis aligned along the voltage vector with the maximum amplitude. Thus, the voltage space vector with the maximum amplitude will define the orientation and the maximum amplitude of the elliptic trajectory. The voltage space vector in case of unbalanced conditions can be can be expressed on complex form as given by (D.15).

$$\begin{aligned}\vec{v}&=v_{\alpha}+j\cdot v_{\beta}\\&=\hat{v}^{+}\cdot\cos\left(\theta+\phi^{+}\right)+\hat{v}^{-}\cdot\cos\left(\theta-\phi^{-}\right)+j\cdot\left(\hat{v}^{+}\cdot\sin\left(\theta+\phi^{+}\right)-\hat{v}^{-}\cdot\sin\left(\theta-\phi^{-}\right)\right)\end{aligned} \tag{D.15}$$

The space vector with the maximum amplitude can then be found by substituting (D.14) into (D.15), resulting in (D.16) that can be reorganized into (D.17).

$$\begin{aligned}\vec{v}\left(\theta_{|v|_{\max}}\right)&=\hat{v}^{+}\cdot\cos\left(\frac{\phi^{+}+\phi^{-}}{2}\right)+\hat{v}^{-}\cdot\cos\left(\frac{\phi^{+}+\phi^{-}}{2}\right)\\&\quad+j\cdot\left(\hat{v}^{+}\cdot\sin\left(\frac{\phi^{+}+\phi^{-}}{2}\right)-\hat{v}^{-}\cdot\sin\left(\frac{\phi^{+}+\phi^{-}}{2}\right)\right)\end{aligned} \tag{D.16}$$

$$\vec{v}\left(\theta_{|v|_{\max}}\right)=\left(\hat{v}^{+}+\hat{v}^{-}\right)\cdot\cos\left(\frac{\phi^{+}+\phi^{-}}{2}\right)+j\cdot\left(\hat{v}^{+}+\hat{v}^{-}\right)\cdot\sin\left(\frac{\phi^{+}+\phi^{-}}{2}\right) \tag{D.17}$$

The maximum voltage vector amplitude and the corresponding graphical orientation in the stationary $\alpha\beta$ reference frame are then given by (D.18) and (D.19) respectively.

$$\begin{aligned}\left|\vec{v}\right|_{\max}&=\sqrt{\left(\left(\hat{v}^{+}+\hat{v}^{-}\right)\cdot\sin\left(\frac{\phi^{+}+\phi^{-}}{2}\right)\right)^{2}+\left(\left(\hat{v}^{+}+\hat{v}^{-}\right)\cdot\cos\left(\frac{\phi^{+}+\phi^{-}}{2}\right)\right)^{2}}\\&=\sqrt{\left(\hat{v}^{+}+\hat{v}^{-}\right)^{2}\underbrace{\left(\sin^{2}\left(\frac{\phi^{+}+\phi^{-}}{2}\right)+\cos^{2}\left(\frac{\phi^{+}+\phi^{-}}{2}\right)\right)}_{=1}}=\hat{v}^{+}+\hat{v}^{-}=\left|\mathbf{v}^{+}\right|+\left|\mathbf{v}^{-}\right|\end{aligned} \tag{D.18}$$

$$\angle\vec{v}_{\max}=\tan^{-1}\left(\frac{\left(\hat{v}^{+}+\hat{v}^{-}\right)\cdot\sin\left(\frac{\phi^{+}+\phi^{-}}{2}\right)}{\left(\hat{v}^{+}+\hat{v}^{-}\right)\cdot\cos\left(\frac{\phi^{+}+\phi^{-}}{2}\right)}\right)=\tan^{-1}\left(\tan\left(\frac{\phi^{+}+\phi^{-}}{2}\right)\right)=\frac{\phi^{+}+\phi^{-}}{2}=\delta \tag{D.19}$$

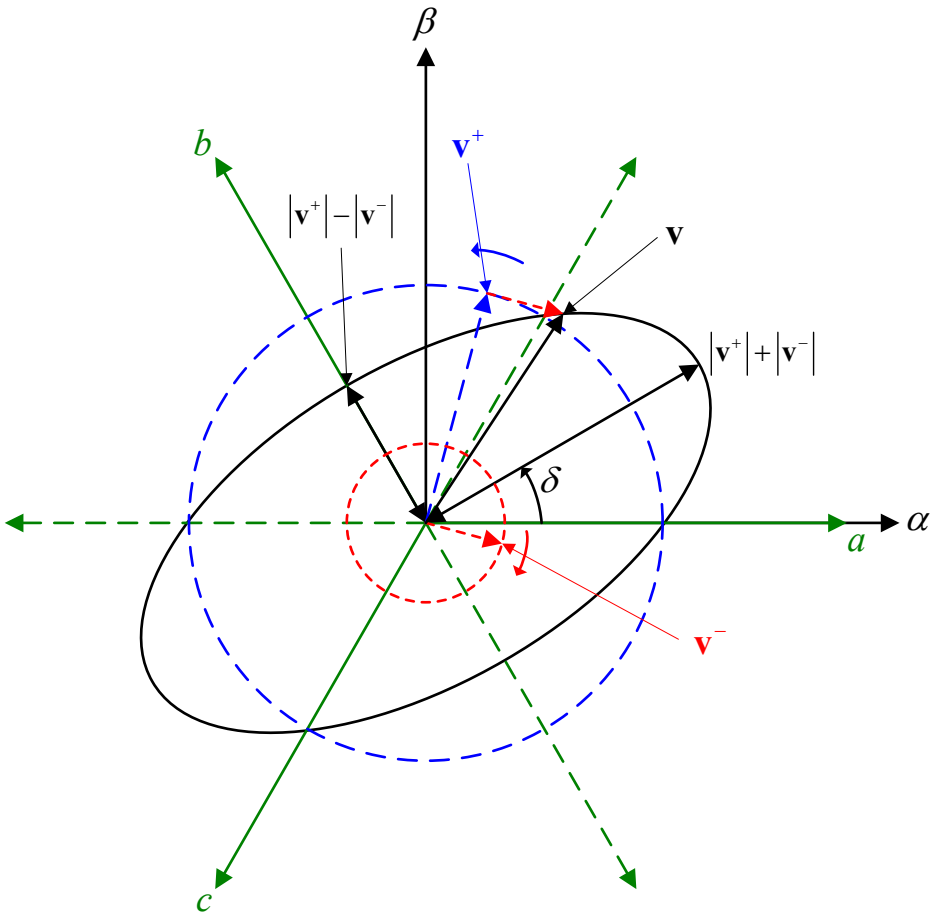

Fig. D-1 Graphical orientation of elliptic voltage trajectory under unbalanced conditions

In (D.19), the angle δ is introduced to represent the graphical orientation of the elliptic trajectory, as shown by the generic example presented in Fig. D-1. This figure also shows how the maximum vector amplitude, corresponding to the major axis of the elliptic trajectory is given by (D.18). The figure further indicates how the minimum vector amplitude is given by $|\mathbf{v}^+|-|\mathbf{v}^-|$, and that the graphical orientation of the minor axis of the elliptic trajectory will be perpendicular to the major axis defined by δ.

The positive and negative sequence voltage components are also indicated in Fig. D-1. It can be seen from the figure how the positive sequence voltage component is represented by a space vector with constant amplitude, rotating in the counterclockwise direction, while the negative sequence voltage component is also represented by a space vector with constant amplitude, rotating in the clockwise direction. Thus, the figure also demonstrates how the voltage vector trajectory will be elliptic under unbalanced, and how the orientation of this elliptic trajectory is determined by the phase angles of the positive and negative sequence voltage components.

Comparing the equation in section D.1.1 with the equations in section D.1.2, it can also be found that the Virtual Flux trajectory under unbalanced conditions will be identical to the voltage trajectory. However, the Virtual Flux space vector will be 90° delayed in time with respect to the voltage vector.

D.2.3 Detection of Phase Angles of Positive and Negative Sequence Components

For detecting the orientation of the elliptic trajectories of voltage and Virtual Flux during unbalanced conditions, the phase angle δ from (D.19) should be detected from the positive and negative sequence voltage or Virtual Flux components.

Considering the difference between the product of the positive and negative sequence α- and β- voltage components as given by (D.20) and applying the general trigonometric identity of (D.21) results in (D.22). Thus, the sum of the phase angles of the positive and negative sequence voltage components can be expressed by (D.23).

$$v_\alpha^+ \cdot v_\alpha^- - v_\beta^+ \cdot v_\beta^- = \hat{v}^+ \cdot \hat{v}^- \cdot \left(\cos\left(\theta + \phi^+\right) \cdot \cos\left(\theta - \phi^-\right) + \sin\left(\theta + \phi^+\right) \cdot \sin\left(\theta - \phi^-\right)\right) \quad \text{(D.20)}$$

$$\cos\left(x \pm y\right) = \cos\left(x\right) \cdot \cos\left(y\right) \mp \sin\left(x\right) \cdot \sin\left(y\right) \quad \text{(D.21)}$$

$$v_\alpha^+ \cdot v_\alpha^- - v_\beta^+ \cdot v_\beta^- = \hat{v}^+ \cdot \hat{v}^- \cdot \cos\left(\theta + \phi^+ - \left(\theta - \phi^-\right)\right) = \hat{v}^+ \cdot \hat{v}^- \cdot \cos\left(\phi^+ + \phi^-\right) \quad \text{(D.22)}$$

$$\cos\left(\phi^+ + \phi^-\right) = \frac{v_\alpha^+ \cdot v_\alpha^- - v_\beta^+ \cdot v_\beta^-}{\hat{v}^+ \cdot \hat{v}^-} \quad \text{(D.23)}$$

The graphical orientation of the elliptic trajectory can then be identified by (D.24), as also applied in [115].

$$\delta = \frac{\phi^+ + \phi^-}{2} = \frac{1}{2} \cdot \cos^{-1}\left(\frac{v_\alpha^+ \cdot v_\alpha^- - v_\beta^+ \cdot v_\beta^-}{\hat{v}^+ \cdot \hat{v}^-}\right) \quad \text{(D.24)}$$

The same approach can also be followed for detecting the graphical orientation of the Virtual Flux trajectory. Using the definitions from (D.4) and (D.5), result in (D.25), which can be simplified by the trigonometric identity from (D.21), to arrive at (D.26).

$$\begin{aligned} &\chi_\alpha^+ \cdot \chi_\alpha^- - \chi_\beta^+ \cdot \chi_\beta^- \\ &\quad = \hat{\chi}^+ \cdot \hat{\chi}^- \cdot \left(\sin\left(\theta + \phi^+\right) \cdot -\sin\left(-\theta + \phi^-\right) + \cos\left(\theta + \phi^+\right) \cdot \cos\left(-\theta + \phi^-\right)\right) \end{aligned} \quad \text{(D.25)}$$

$$\chi_\alpha^+ \cdot \chi_\alpha^- - \chi_\beta^+ \cdot \chi_\beta^- = \hat{\chi}^+ \cdot \hat{\chi}^- \cdot \cos\left(\theta + \phi^+ + \left(-\theta + \phi^-\right)\right) = \hat{\chi}^+ \cdot \hat{\chi}^- \cdot \cos\left(\phi^+ + \phi^-\right) \quad \text{(D.26)}$$

Equation (D.26) can be reconfigured into (D.27), and thus the graphical orientation of the voltage or Virtual Flux trajectory can be identified by (D.28).

$$\cos\left(\phi^+ + \phi^-\right) = \frac{\chi_\alpha^+ \cdot \chi_\alpha^- - \chi_\beta^+ \cdot \chi_\beta^-}{\hat{\chi}^+ \cdot \hat{\chi}^-} \quad \text{(D.27)}$$

$$\delta = \frac{\phi^+ + \phi^-}{2} = \frac{1}{2} \cdot \cos^{-1}\left(\frac{\chi_\alpha^+ \cdot \chi_\alpha^- - \chi_\beta^+ \cdot \chi_\beta^-}{\hat{\chi}^+ \cdot \hat{\chi}^-}\right) \quad \text{(D.28)}$$

D.3 Simplified Expressions for Positive and Negative Sequence Voltage and Virtual Flux Signals

The orientation of the voltage or Virtual Flux trajectories are independent of the individual phase angles ϕ^+ and ϕ^- of the positive and negative sequence components, and will only depend on the average of these phase angles as defined by the orientation angle δ from (D.19). For simplifying the further derivations and analysis of positive and negative sequence components, the reference of the phase angle θ can therefore be shifted so that it is aligned with either the positive or the negative sequence component.

The convention applied for the following derivation is to keep ϕ^- equal to zero. Thus, the individual phase angles with a shifted point of reference can be defined by (D.29). The resulting expressions for the positive and negative sequence voltage and Virtual Flux components will be defined in the following.

$$\phi'^{+} = 2 \cdot \delta \qquad \phi'^{-} = 0 \tag{D.29}$$

D.3.1 Voltage Vectors and Corresponding Orthogonal Signals

Applying the phase shift implied by (D.29), the positive and negative sequence voltage components from (D.1) and (D.2) can be rewritten as given by (D.30) and (D.31). The total voltage vector can then be expressed by (D.32).

$$\mathbf{v}^+ = \begin{bmatrix} v_\alpha^+ \\ v_\beta^+ \end{bmatrix} = \begin{bmatrix} \hat{v}^+ \cdot \cos(\theta + 2\delta) \\ \hat{v}^+ \cdot \sin(\theta + 2\delta) \end{bmatrix} \tag{D.30}$$

$$\mathbf{v}^- = \begin{bmatrix} v_\alpha^- \\ v_\beta^- \end{bmatrix} = \begin{bmatrix} \hat{v}^- \cdot \cos(\theta) \\ -\hat{v}^- \cdot \sin(\theta) \end{bmatrix} \tag{D.31}$$

$$\mathbf{v} = \mathbf{v}^+ + \mathbf{v}^- = \begin{bmatrix} v_\alpha \\ v_\beta \end{bmatrix} = \begin{bmatrix} \hat{v}^+ \cdot \cos(\theta + 2\delta) + \hat{v}^- \cdot \cos(\theta) \\ \hat{v}^+ \cdot \sin(\theta + 2\delta) - \hat{v}^- \cdot \sin(\theta) \end{bmatrix} \tag{D.32}$$

The orthogonal voltage vectors defined by the vector operation "$\perp$" introduced in Chapter 4 will then be defined by (D.33), (D.34) and (D.35).

$$\mathbf{v}_\perp^+ = \begin{bmatrix} \hat{v}^+ \cdot \sin(\theta + 2\delta) \\ -\hat{v}^+ \cdot \cos(\theta + 2\delta) \end{bmatrix} \tag{D.33}$$

$$\mathbf{v}_\perp^- = \begin{bmatrix} -\hat{v}^- \cdot \sin(\theta) \\ -\hat{v}^- \cdot \cos(\theta) \end{bmatrix} \tag{D.34}$$

$$\mathbf{v}_\perp = \mathbf{v}_\perp^+ + \mathbf{v}_\perp^- = \begin{bmatrix} \hat{v}^+ \cdot \sin(\theta + 2\delta) - \hat{v}^- \cdot \sin(\theta) \\ -\hat{v}^+ \cdot \cos(\theta + 2\delta) - \hat{v}^- \cdot \cos(\theta) \end{bmatrix} \tag{D.35}$$

D.3.2 Virtual Flux Vectors and Corresponding Orthogonal Signals

By applying the convention introduced by (D.29), the Virtual Flux vectors can be defined as given by (D.36), (D.37) and (D.38).

$$\boldsymbol{\chi}^+ = \begin{bmatrix} \chi_\alpha^+ \\ \chi_\beta^+ \end{bmatrix} = \begin{bmatrix} \hat{\chi}^+ \cdot \sin(\theta + 2\delta) \\ -\hat{\chi}^+ \cdot \cos(\theta + 2\delta) \end{bmatrix} \tag{D.36}$$

$$\boldsymbol{\chi}^- = \begin{bmatrix} \chi_\alpha^- \\ \chi_\beta^- \end{bmatrix} = \begin{bmatrix} \hat{\chi}^- \cdot \sin(\theta) \\ \hat{\chi}^- \cdot \cos(\theta) \end{bmatrix} \tag{D.37}$$

$$\boldsymbol{\chi} = \boldsymbol{\chi}^+ + \boldsymbol{\chi}^- = \begin{bmatrix} \chi_\alpha \\ \chi_\beta \end{bmatrix} = \begin{bmatrix} \hat{\chi}^+ \cdot \sin(\theta + 2\delta) + \hat{\chi}^- \cdot \sin(\theta) \\ -\hat{\chi}^+ \cdot \cos(\theta + 2\delta) + \hat{\chi}^- \cdot \cos(\theta) \end{bmatrix} \tag{D.38}$$

By corresponding orthogonal components of the positive and negative sequence Virtual Flux vectors are then defined by (D.39), (D.40) and (D.41).

$$\boldsymbol{\chi}_{\perp}^{+} = \begin{bmatrix} -\hat{\chi}^{+} \cdot \cos\left(\theta + 2\delta\right) \\ -\hat{\chi}^{+} \cdot \sin\left(\theta + 2\delta\right) \end{bmatrix} \tag{D.39}$$

$$\boldsymbol{\chi}_{\perp}^{-} = \begin{bmatrix} \hat{\chi}^{-} \cdot \cos\left(\theta\right) \\ -\hat{\chi}^{-} \cdot \sin\left(\theta\right) \end{bmatrix} \tag{D.40}$$

$$\boldsymbol{\chi}_{\perp} = \boldsymbol{\chi}_{\perp}^{+} + \boldsymbol{\chi}_{\perp}^{-} = \begin{bmatrix} -\hat{\chi}^{+} \cdot \cos\left(\theta + 2\delta\right) + \hat{\chi}^{-} \cdot \cos\left(\theta\right) \\ -\hat{\chi}^{+} \cdot \sin\left(\theta + 2\delta\right) - \hat{\chi}^{-} \cdot \sin\left(\theta\right) \end{bmatrix} \tag{D.41}$$

D.4 Active and Reactive Power Oscillations Resulting from the Different Power Control Strategies

The following subsections will present the detailed steps of the derivations needed to arrive at the expressions for double frequency active and reactive power oscillations corresponding to the different active and reactive power control strategies discussed in section 4.3.1, 4.3.2 and 4.3.3.

D.4.1 Active and Reactive Power Control by BPSC

By the BPSC strategy, the active and reactive current references are given by (4.17) and (4.20). Assuming the resulting currents to be equal to the current references, the corresponding double frequency active and reactive power oscillations can be found by substituting the current reference equations back into the proper terms of (4.15) and (4.16).

D.4.1.1 Double frequency active and reactive power oscillations resulting from active power control by BPSC

The double frequency active power oscillations originating from active power control by the BPSC strategy can be expressed by (D.42). Applying the trigonometric identities given in (D.43), this equation can be simplified as shown by (D.44).

$$\begin{aligned} \tilde{p}_{2\omega,p} = \tilde{p}_{p}^{-+} &= \underbrace{-\boldsymbol{\chi}_{\perp}^{+} \cdot \mathbf{i}_{p}^{-}}_{0} + \boldsymbol{\chi}_{\perp}^{-} \cdot \mathbf{i}_{p}^{+} = \boldsymbol{\chi}_{\perp}^{-} \cdot \left(-\boldsymbol{\chi}_{\perp}^{+}\right) \cdot \frac{\overline{p}^{*}}{\left|\boldsymbol{\chi}^{+}\right|^{2}} \\ &= \frac{\overline{p}^{*}}{\hat{\chi}^{+^{2}}} \cdot \begin{bmatrix} \hat{\chi}^{-} \cdot \cos\left(\theta\right) \\ -\hat{\chi}^{-} \cdot \sin\left(\theta\right) \end{bmatrix} \bullet \begin{bmatrix} \hat{\chi}^{+} \cdot \cos\left(\theta + 2\delta\right) \\ \hat{\chi}^{+} \cdot \sin\left(\theta + 2\delta\right) \end{bmatrix} \\ &= \frac{\overline{p}^{*} \cdot \hat{\chi}^{-} \cdot \hat{\chi}^{+}}{\hat{\chi}^{+^{2}}} \cdot \left(\cos\left(\theta\right) \cdot \cos\left(\theta + 2\delta\right) - \sin\left(\theta\right) \cdot \sin\left(\theta + 2\delta\right)\right) \end{aligned} \tag{D.42}$$

$$\begin{aligned} \cos\left(\theta + 2\delta\right) &= \cos\left(\theta\right) \cdot \cos\left(2\delta\right) - \sin\left(\theta\right) \cdot \sin\left(2\delta\right) \\ \sin\left(\theta + 2\delta\right) &= \sin\left(\theta\right) \cdot \cos\left(2\delta\right) + \cos\left(\theta\right) \cdot \sin\left(2\delta\right) \end{aligned} \tag{D.43}$$

$$\begin{aligned} \tilde{p}_{2\omega,p} &= \frac{\overline{p}^{*} \cdot \hat{\chi}^{-}}{\hat{\chi}^{+}} \cdot \left(\underbrace{\left(\cos^{2}\left(\theta\right) - \sin^{2}\left(\theta\right)\right)}_{\cos(2\theta)} \cdot \cos\left(2\delta\right) - \underbrace{2 \cdot \cos\left(\theta\right) \cdot \sin\left(\theta\right)}_{\sin(2\theta)} \cdot \sin\left(2\delta\right) \right) \\ &= \frac{\overline{p}^{*} \cdot \hat{\chi}^{-}}{\hat{\chi}^{+}} \cdot \left(\cos\left(2\theta\right) \cdot \cos\left(2\delta\right) - \sin\left(2\theta\right) \cdot \sin\left(2\delta\right)\right) = \frac{\overline{p}^{*} \cdot \hat{\chi}^{-}}{\hat{\chi}^{+}} \cdot \cos\left(2\theta + 2\delta\right) \end{aligned} \tag{D.44}$$

The same approach can be followed to derive the reactive power oscillations resulting from active power control by the BPSC strategy, as shown by (D.45). By applying the trigonometric identities from (D.43), this equation can be simplified as shown in (D.46).

$$\begin{aligned}\tilde{q}_{2\omega,p} = \tilde{q}_p^{-+} &= \underbrace{\boldsymbol{\chi}^+ \cdot \mathbf{i}_p^-}_{0} - \boldsymbol{\chi}^- \cdot \mathbf{i}_p^+ = -\boldsymbol{\chi}^- \cdot \left(-\boldsymbol{\chi}_\perp^+\right) \cdot \frac{\overline{p}^*}{\left|\boldsymbol{\chi}^+\right|^2} \\ &= \frac{\overline{p}^*}{\hat{\chi}^{+^2}} \cdot \begin{bmatrix} -\hat{\chi}^- \cdot \cos(\theta) \\ -\hat{\chi}^- \cdot \sin(\theta) \end{bmatrix} \bullet \begin{bmatrix} \hat{\chi}^+ \cdot \cos(\theta + 2\delta) \\ \hat{\chi}^+ \cdot \sin(\theta + 2\delta) \end{bmatrix} \\ &= \frac{\overline{p}^* \cdot \hat{\chi}^- \cdot \hat{\chi}^+}{\hat{\chi}^{+^2}} \cdot \left(-\sin(\theta) \cdot \cos(\theta + 2\delta) - \cos(\theta) \cdot \sin(\theta + 2\delta)\right)\end{aligned} \tag{D.45}$$

$$\begin{aligned}\tilde{q}_{2\omega,p} &= \frac{P^* \cdot \hat{\chi}^-}{\hat{\chi}^+} \cdot \left(-\sin(2\delta) \cdot \underbrace{\left(\cos^2(\theta) - \sin^2(\theta)\right)}_{\cos(2\theta)} - \underbrace{2 \cdot \cos(\theta) \cdot \sin(\theta)}_{\sin(2\theta)} \cdot \cos(2\delta) \right) \\ &= -\frac{P^* \cdot \hat{\chi}^-}{\hat{\chi}^+} \cdot \left(\cos(2\theta) \cdot \sin(2\delta) + \sin(2\theta) \cdot \cos(2\delta)\right) = -\frac{\overline{p}^* \cdot \hat{\chi}^-}{\hat{\chi}^+} \cdot \sin(2\theta + 2\delta)\end{aligned} \tag{D.46}$$

D.4.1.2 Double frequency active and reactive power oscillations resulting from reactive power control by BPSC

The double frequency active power oscillations originating from reactive power control by the BPSC strategy can be expressed by (D.47). Again, the trigonometric identities from (D.43), can be applied to simplify the equations as shown in (D.48).

$$\begin{aligned}\tilde{p}_{2\omega,q} = \tilde{p}_q^{-+} &= \underbrace{-\boldsymbol{\chi}_\perp^+ \cdot \mathbf{i}_q^-}_{0} + \boldsymbol{\chi}_\perp^- \cdot \mathbf{i}_q^+ = \boldsymbol{\chi}_\perp^- \cdot \boldsymbol{\chi}^+ \cdot \frac{\overline{q}^*}{\left|\boldsymbol{\chi}^+\right|^2} \\ &= \frac{\overline{q}^*}{\hat{\chi}^{+^2}} \cdot \begin{bmatrix} \hat{\chi}^- \cdot \cos(\theta) \\ -\hat{\chi}^- \cdot \sin(\theta) \end{bmatrix} \bullet \begin{bmatrix} \hat{\chi}^+ \cdot \sin(\theta + 2\delta) \\ -\hat{\chi}^+ \cdot \cos(\theta + 2\delta) \end{bmatrix} \\ &= \frac{\overline{q}^* \cdot \hat{\chi}^- \cdot \hat{\chi}^+}{\hat{\chi}^{+^2}} \cdot \left(\cos(\theta) \cdot \sin(\theta + 2\delta) + \sin(\theta) \cdot \cos(\theta + 2\delta)\right)\end{aligned} \tag{D.47}$$

$$\begin{aligned}\tilde{p}_{2\omega,q} &= \frac{\overline{q}^* \cdot \hat{\chi}^-}{\hat{\chi}^+} \cdot \left(\underbrace{\left(\cos^2(\theta) - \sin^2(\theta)\right)}_{\cos(2\theta)} \cdot \sin(2\delta) + \underbrace{2 \cdot \cos(\theta) \cdot \sin(\theta)}_{\sin(2\theta)} \cdot \cos(2\delta) \right) \\ &= \frac{\overline{q}^* \cdot \hat{\chi}^-}{\hat{\chi}^+} \cdot \left(\cos(2\theta) \cdot \sin(2\delta) + \sin(2\theta) \cdot \cos(2\delta)\right) = \frac{\overline{q}^* \cdot \hat{\chi}^-}{\hat{\chi}^+} \cdot \sin(2\theta + 2\delta)\end{aligned} \tag{D.48}$$

The corresponding double frequency reactive power oscillations originating from reactive power control by the BPSC strategy can be expressed by (D.49). By the trigonometric identities from (D.43), this equation can be simplified as shown in (D.50).

$$\begin{aligned}\tilde{q}_{2\omega,q} &= \tilde{q}_q^{-+} = \underbrace{\boldsymbol{\chi}^+ \cdot \mathbf{i}_q^-}_{0} - \boldsymbol{\chi}^- \cdot \mathbf{i}_q^+ = -\boldsymbol{\chi}^- \cdot \left(-\boldsymbol{\chi}_\perp^+\right) \cdot \frac{\overline{q}^*}{\left|\boldsymbol{\chi}^+\right|^2} \\ &= \frac{\overline{q}^*}{\hat{\chi}^{+^2}} \cdot \begin{bmatrix} -\hat{\chi}^- \cdot \cos(\theta) \\ -\hat{\chi}^- \cdot \sin(\theta) \end{bmatrix} \bullet \begin{bmatrix} \hat{\chi}^+ \cdot \cos(\theta + 2\delta) \\ -\hat{\chi}^+ \cdot \sin(\theta + 2\delta) \end{bmatrix} \\ &= \frac{\overline{q}^* \cdot \hat{\chi}^- \cdot \hat{\chi}^+}{\hat{\chi}^{+^2}} \cdot \left(-\sin(\theta) \cdot \sin(\theta + 2\delta) + \cos(\theta) \cdot \cos(\theta + 2\delta)\right)\end{aligned} \tag{D.49}$$

$$\begin{aligned}\tilde{q}_{2\omega,q} &= \frac{\overline{q}^* \cdot \hat{\chi}^-}{\hat{\chi}^+} \cdot \left(\underbrace{\left(\cos^2(\theta) - \sin^2(\theta)\right)}_{\cos(2\theta)} \cdot \cos(2\delta) - \underbrace{2 \cdot \cos(\theta) \cdot \sin(\theta)}_{\sin(2\theta)} \cdot \sin(2\delta) \right) \\ &= \frac{\overline{q}^* \cdot \hat{\chi}^-}{\hat{\chi}^+} \cdot \left(\cos(2\theta) \cdot \cos(2\delta) - \sin(2\theta) \cdot \sin(2\delta)\right) = \frac{\overline{q}^* \cdot \hat{\chi}^-}{\hat{\chi}^+} \cdot \sin(2\theta + 2\delta)\end{aligned} \tag{D.50}$$

D.4.2 Active and Reactive Power Control by PNSC

The active and reactive current references corresponding to active and reactive power control by the PNSC strategy are given by (4.28) and (4.32), and the corresponding double frequency active and reactive power oscillations can be found by the same approach as shown for the case of BPSC.

D.4.2.1 Double frequency reactive power oscillations resulting from active power control by PNSC

For active power control by the PNSC strategy, the condition given by (D.51) will be inherently fulfilled.

$$\tilde{p}_{2\omega,p} = \tilde{p}_p^{+-} + \tilde{p}_p^{-+} = -\boldsymbol{\chi}_\perp^+ \cdot \mathbf{i}_p^- + \boldsymbol{\chi}_\perp^- \cdot \mathbf{i}_p^+ = 0 \tag{D.51}$$

The double frequency reactive power oscillations can however be expressed by (D.52) . Again, the trigonometric identities from (D.43) can be applied to simplify the equation, as shown by (D.53).

$$\begin{aligned}\tilde{q}_{2\omega,p} &= \tilde{q}_p^{+-} + \tilde{q}_p^{-+} = \boldsymbol{\chi}^+ \cdot \mathbf{i}_p^- - \boldsymbol{\chi}^- \cdot \mathbf{i}_p^+ = \boldsymbol{\chi}^+ \cdot \left(-\boldsymbol{\chi}_\perp^-\right) \cdot \frac{\overline{p}^*}{\left|\boldsymbol{\chi}^+\right|^2 - \left|\boldsymbol{\chi}^-\right|^2} - \boldsymbol{\chi}^- \cdot \left(-\boldsymbol{\chi}_\perp^+\right) \cdot \frac{\overline{p}^*}{\left|\boldsymbol{\chi}^+\right|^2 - \left|\boldsymbol{\chi}^-\right|^2} \\ &= \frac{\overline{p}^*}{\hat{\chi}^{+^2} - \hat{\chi}^{-^2}} \cdot \left(\begin{bmatrix} \hat{\chi}^+ \cdot \sin(\theta + 2\delta) \\ -\hat{\chi}^+ \cdot \cos(\theta + 2\delta) \end{bmatrix} \bullet \begin{bmatrix} -\hat{\chi}^- \cdot \cos(\theta) \\ \hat{\chi}^- \cdot \sin(\theta) \end{bmatrix} + \begin{bmatrix} \hat{\chi}^- \cdot \sin(\theta) \\ \hat{\chi}^- \cdot \cos(\theta) \end{bmatrix} \bullet \begin{bmatrix} -\hat{\chi}^+ \cdot \cos(\theta + 2\delta) \\ -\hat{\chi}^+ \cdot \sin(\theta + 2\delta) \end{bmatrix} \right) \\ &= -\frac{\overline{p}^* \cdot \hat{\chi}^- \cdot \hat{\chi}^+}{\hat{\chi}^{+^2} - \hat{\chi}^{-^2}} \cdot \left(2 \cdot \cos(\theta) \cdot \sin(\theta + 2\delta) + 2 \cdot \sin(\theta) \cdot \cos(\theta + 2\delta)\right)\end{aligned} \tag{D.52}$$

$$\begin{aligned}\tilde{q}_{2\omega,q} &= -\frac{2 \cdot \overline{p}^* \cdot \hat{\chi}^- \cdot \hat{\chi}^+}{\hat{\chi}^{+^2} - \hat{\chi}^{-^2}} \cdot \left(\underbrace{\left(\cos^2(\theta) - \sin^2(\theta)\right)}_{\cos(2\theta)} \cdot \sin(2\delta) + \underbrace{2 \cdot \cos(\theta) \cdot \sin(\theta)}_{\sin(2\theta)} \cdot \cos(2\delta) \right) \\ &= -\frac{2 \cdot \overline{p}^* \cdot \hat{\chi}^- \cdot \hat{\chi}^+}{\hat{\chi}^{+^2} - \hat{\chi}^{-^2}} \cdot \left(\cos(2\theta) \cdot \sin(2\delta) - \sin(2\theta) \cdot \cos(2\delta)\right) \\ &= -\frac{2 \cdot \overline{p}^* \cdot \hat{\chi}^- \cdot \hat{\chi}^+}{\hat{\chi}^{+^2} - \hat{\chi}^{-^2}} \cdot \sin(2\theta + 2\delta)\end{aligned} \tag{D.53}$$

D.4.2.2 Double frequency active power oscillations resulting from reactive power control by PNSC

For reactive power control by the PNSC strategy, the condition given by (D.54) will be inherently fulfilled.

$$\tilde{q}_{2\omega,q} = \tilde{q}_p^{+-} + \tilde{q}_p^{-+} = \boldsymbol{\chi}^+ \cdot \mathbf{i}_p^- - \boldsymbol{\chi}^- \cdot \mathbf{i}_p^+ = 0 \tag{D.54}$$

The double frequency active power oscillations can however be expressed by (D.55) and simplified as shown by (D.56).

$$\begin{aligned}
\tilde{p}_{2\omega,q} &= \tilde{p}_q^{+-} + \tilde{p}_q^{-+} = -\boldsymbol{\chi}_\perp^+ \cdot \mathbf{i}_q^- + \boldsymbol{\chi}_\perp^- \cdot \mathbf{i}_q^+ = -\boldsymbol{\chi}_\perp^+ \cdot \boldsymbol{\chi}^- \cdot \frac{\overline{q}^*}{\left|\boldsymbol{\chi}^+\right|^2 - \left|\boldsymbol{\chi}^-\right|^2} + \boldsymbol{\chi}_\perp^- \cdot \boldsymbol{\chi}^+ \cdot \frac{\overline{q}^*}{\left|\boldsymbol{\chi}^+\right|^2 - \left|\boldsymbol{\chi}^-\right|^2} \\
&= \frac{\overline{q}^*}{\hat{\chi}^{+^2} - \hat{\chi}^{-^2}} \cdot \left(\begin{bmatrix} \hat{\chi}^+ \cdot \cos(\theta + 2\delta) \\ \hat{\chi}^+ \cdot \sin(\theta + 2\delta) \end{bmatrix} \bullet \begin{bmatrix} \hat{\chi}^- \cdot \sin(\theta) \\ \hat{\chi}^- \cdot \cos(\theta) \end{bmatrix} + \begin{bmatrix} \hat{\chi}^- \cdot \cos(\theta) \\ -\hat{\chi}^- \cdot \sin(\theta) \end{bmatrix} \bullet \begin{bmatrix} \hat{\chi}^+ \cdot \sin(\theta + 2\delta) \\ -\hat{\chi}^+ \cdot \cos(\theta + 2\delta) \end{bmatrix} \right) \\
&= \frac{\overline{q}^* \cdot \hat{\chi}^- \cdot \hat{\chi}^+}{\hat{\chi}^{+^2} - \hat{\chi}^{-^2}} \cdot \left(2 \cdot \cos(\theta) \cdot \sin(\theta + 2\delta) + 2 \cdot \sin(\theta) \cdot \cos(\theta + 2\delta) \right)
\end{aligned} \tag{D.55}$$

$$\begin{aligned}
\tilde{p}_{2\omega,q} &= \frac{2 \cdot \overline{q}^* \cdot \hat{\chi}^- \cdot \hat{\chi}^+}{\hat{\chi}^{+^2} - \hat{\chi}^{-^2}} \cdot \left(\underbrace{\left(\cos^2(\theta) - \sin^2(\theta) \right)}_{\cos(2\theta)} \cdot \sin(2\delta) + \underbrace{2 \cdot \cos(\theta) \cdot \sin(\theta)}_{\sin(2\theta)} \cdot \cos(2\delta) \right) \\
&= \frac{2 \cdot \overline{q}^* \cdot \hat{\chi}^- \cdot \hat{\chi}^+}{\hat{\chi}^{+^2} - \hat{\chi}^{-^2}} \cdot \left(\cos(2\theta) \cdot \sin(2\delta) + \sin(2\theta) \cdot \cos(2\delta) \right) \\
&= \frac{2 \cdot \overline{q}^* \cdot \hat{\chi}^- \cdot \hat{\chi}^+}{\hat{\chi}^{+^2} - \hat{\chi}^{-^2}} \cdot \sin(2\theta + 2\delta)
\end{aligned} \tag{D.56}$$

D.4.3 Active and Reactive Power Control by AARC

The active and reactive current references corresponding to active and reactive power control by the AARC strategy are given by (4.40) and (4.42), and the corresponding double frequency active and reactive power oscillations can be found by the same approach as shown for the cases of BPSC PSNC.

D.4.3.1 Double frequency active power oscillations resulting from active power control by AARC

For active power control by the AARC strategy, double frequency reactive power oscillations will be inherently eliminated as long as the resulting currents are equal to the current references. The resulting double frequency active power oscillations can however be expressed by (D.57) and simplified as given by (D.58).

$$\begin{aligned}
\tilde{p}_{2\omega,p} &= \tilde{p}_p^{+-} + \tilde{p}_p^{-+} = -\boldsymbol{\chi}_\perp^+ \cdot \mathbf{i}_p^- + \boldsymbol{\chi}_\perp^- \cdot \mathbf{i}_p^+ = -\boldsymbol{\chi}_\perp^+ \cdot \boldsymbol{\chi}_\perp^- \cdot \frac{\overline{p}^*}{\left|\boldsymbol{\chi}^+\right| + \left|\boldsymbol{\chi}^-\right|^2} + \boldsymbol{\chi}_\perp^- \cdot \left(-\boldsymbol{\chi}_\perp^+\right) \cdot \frac{\overline{p}^*}{\left|\boldsymbol{\chi}^+\right|^2 + \left|\boldsymbol{\chi}^-\right|^2} \\
&= -\frac{2 \cdot \overline{p}^*}{\left|\boldsymbol{\chi}^+\right|^2 + \left|\boldsymbol{\chi}^-\right|^2} \cdot \boldsymbol{\chi}_\perp^+ \cdot \boldsymbol{\chi}_\perp^- = -\frac{2 \cdot \overline{p}^*}{\left|\boldsymbol{\chi}^+\right|^2 + \left|\boldsymbol{\chi}^-\right|^2} \cdot \left(\begin{bmatrix} -\hat{\chi}^+ \cdot \cos(\theta + 2\delta) \\ -\hat{\chi}^+ \cdot \sin(\theta + 2\delta) \end{bmatrix} \bullet \begin{bmatrix} \hat{\chi}^- \cdot \cos(\theta) \\ -\hat{\chi}^- \cdot \sin(\theta) \end{bmatrix} \right) \\
&= -\frac{2 \cdot \overline{p}^* \cdot \hat{\chi}^- \cdot \hat{\chi}^+}{\hat{\chi}^{+^2} + \hat{\chi}^{-^2}} \cdot \left(-\cos(\theta + 2\delta) \cdot \cos(\theta) + \sin(\theta + 2\delta) \cdot \cos(\theta) \right)
\end{aligned} \tag{D.57}$$

$$\tilde{p}_{2\omega,p} = -\frac{2\cdot\overline{p}^{*}\cdot\hat{\chi}^{-}\cdot\hat{\chi}^{+}}{\hat{\chi}^{+^2}+\hat{\chi}^{-^2}}\cdot\left(-\underbrace{\left(\cos^2(\theta)-\sin^2(\theta)\right)}_{\cos(2\theta)}\cdot\cos(2\delta)+\underbrace{2\cdot\cos(\theta)\cdot\sin(\theta)}_{\sin(2\theta)}\cdot\sin(2\delta)\right)$$

$$= \frac{2\cdot\overline{p}^{*}\cdot\hat{\chi}^{-}\cdot\hat{\chi}^{+}}{\hat{\chi}^{+^2}+\hat{\chi}^{-^2}}\cdot\left(\cos(2\theta)\cdot\cos(2\delta)-\sin(2\theta)\cdot\sin(2\delta)\right) \tag{D.58}$$

$$= \frac{2\cdot\overline{p}^{*}\cdot\hat{\chi}^{-}\cdot\hat{\chi}^{+}}{\hat{\chi}^{+^2}+\hat{\chi}^{-^2}}\cdot\cos(2\theta+2\delta)$$

D.4.3.2 Double frequency reactive power oscillations resulting from reactive power control by AARC

For reactive power control by the AARC strategy, double frequency active power oscillations will be inherently eliminated. The resulting double frequency reactive power oscillations can however be expressed by (D.59) and simplified as given by (D.60).

$$\tilde{q}_{2\omega,q} = \tilde{q}_{q}^{+-}+\tilde{q}_{q}^{-+} = \boldsymbol{\chi}^{+}\cdot\mathbf{i}_{q}^{-}+\boldsymbol{\chi}^{-}\cdot\mathbf{i}_{p}^{+} = \boldsymbol{\chi}^{+}\cdot\left(-\boldsymbol{\chi}^{+}\right)\cdot\frac{\overline{q}^{*}}{\left|\boldsymbol{\chi}^{+}\right|^2+\left|\boldsymbol{\chi}^{-}\right|^2}-\boldsymbol{\chi}^{-}\cdot\boldsymbol{\chi}^{+}\cdot\frac{\overline{q}^{*}}{\left|\boldsymbol{\chi}^{+}\right|^2+\left|\boldsymbol{\chi}^{-}\right|^2}$$

$$= -\frac{2\cdot\overline{q}^{*}}{\left|\boldsymbol{\chi}^{+}\right|^2+\left|\boldsymbol{\chi}^{-}\right|^2}\cdot\boldsymbol{\chi}^{+}\cdot\boldsymbol{\chi}^{-} = -\frac{2\cdot\overline{q}^{*}}{\left|\boldsymbol{\chi}^{+}\right|^2+\left|\boldsymbol{\chi}^{-}\right|^2}\cdot\left(\begin{bmatrix}\hat{\chi}^{+}\cdot\sin(\theta+2\delta)\\-\hat{\chi}^{+}\cdot\cos(\theta+2\delta)\end{bmatrix}\bullet\begin{bmatrix}\hat{\chi}^{-}\cdot\sin(\theta)\\\hat{\chi}^{-}\cdot\cos(\theta)\end{bmatrix}\right) \tag{D.59}$$

$$= -\frac{2\cdot\overline{q}^{*}\cdot\hat{\chi}^{-}\cdot\hat{\chi}^{+}}{\hat{\chi}^{+^2}+\hat{\chi}^{-^2}}\cdot\left(\sin(\theta+2\delta)\cdot\sin(\theta)-\cos(\theta+2\delta)\cdot\cos(\theta)\right)$$

$$\tilde{q}_{2\omega,q} = -\frac{2\cdot\overline{q}^{*}\cdot\hat{\chi}^{-}\cdot\hat{\chi}^{+}}{\hat{\chi}^{+^2}+\hat{\chi}^{-^2}}\cdot\left(-\underbrace{\left(\cos^2(\theta)-\sin^2(\theta)\right)}_{\cos(2\theta)}\cdot\cos(2\delta)+\underbrace{2\cdot\cos(\theta)\cdot\sin(\theta)}_{\sin(2\theta)}\cdot\sin(2\delta)\right)$$

$$= \frac{2\cdot\overline{q}^{*}\cdot\hat{\chi}^{-}\cdot\hat{\chi}^{+}}{\hat{\chi}^{+^2}+\hat{\chi}^{-^2}}\cdot\left(\cos(2\theta)\cdot\cos(2\delta)-\sin(2\theta)\cdot\sin(2\delta)\right) \tag{D.60}$$

$$= \frac{2\cdot\overline{q}^{*}\cdot\hat{\chi}^{-}\cdot\hat{\chi}^{+}}{\hat{\chi}^{+^2}+\hat{\chi}^{-^2}}\cdot\cos(2\theta+2\delta)$$

D.5 Derivation of Active Power Transfer Limitations and Current Reference Equations for Operation of Active Power Control Strategies under Phase Current Limitation

The starting point for the following derivations is the general active current reference equation from (4.44). By the definitions from the previous subsections, this current reference equation can be expressed by (D.61).

$$\mathbf{i}_p^* = \begin{bmatrix} i_{p,\alpha}^* \\ i_{p,\beta}^* \end{bmatrix} = \frac{\overline{p}^*}{\hat{\chi}^{+2} + k_p \cdot \hat{\chi}^{-2}} \cdot \begin{bmatrix} \hat{\chi}^+ \cdot \cos(\theta + 2\delta) + k_p \cdot \hat{\chi}^- \cdot \cos(\theta) \\ \hat{\chi}^+ \cdot \sin(\theta + 2\delta) - k_p \cdot \hat{\chi}^- \cdot \sin(\theta) \end{bmatrix}, \qquad -1 \le k_p \le 1 \tag{D.61}$$

The derivations will be kept general by allowing the control parameter k_p to take any value between −1 and 1. The orientation of the current reference vector trajectory will however be perpendicular to the Virtual Flux trajectory when $k_p < 0$, while it will be aligned with the Virtual Flux trajectory when $k_p > 1$. The derivations must therefore be carried out separately for these two cases.

D.5.1 Operation with Reduction of Active Power Oscillations ($-1 \le k_p \le 0$)

For operation with the purpose of reducing double frequency active power oscillations, the current reference trajectory will be oriented perpendicularly with respect to the voltage or Virtual Flux trajectories. If the orientation of the voltage or Virtual Flux trajectories under unbalanced conditions is within the range of $0 \le \delta \le 60°$, the maximum phase current will then occur in phase *b*. According to the Clarke transformation from (A.7), the current in phase *b* can be expressed by the *α*- and *β*-current components as given by (D.62). By applying (D.61), the equivalent *b*-phase current reference is then given by (D.63).

$$i_b = -\frac{1}{2} i_\alpha + \frac{\sqrt{3}}{2} i_\beta \tag{D.62}$$

$$i_{p,b}^* = \frac{\overline{p}^*}{\hat{\chi}^{+2} + k_p \cdot \hat{\chi}^{-2}} \cdot \left(-\frac{1}{2} \cdot \left(\hat{\chi}^+ \cdot \cos(\theta + 2\delta) + k_p \cdot \hat{\chi}^- \cdot \cos(\theta) \right) + \frac{\sqrt{3}}{2} \cdot \left(\hat{\chi}^+ \cdot \sin(\theta + 2\delta) - k_p \cdot \hat{\chi}^- \cdot \sin(\theta) \right) \right) \tag{D.63}$$

By expressing (D.63) in terms of only sine functions, the *b*-phase current reference is then given by (D.64).

$$i_{p,b}^* = \frac{\overline{p}^*}{\hat{\chi}^{+2} + k_p \cdot \hat{\chi}^{-2}} \cdot \left(\hat{\chi}^+ \cdot \sin\left(\theta + 2\delta - \frac{\pi}{6} \right) - k_p \cdot \hat{\chi}^- \cdot \sin\left(\theta + \frac{\pi}{6} \right) \right) \tag{D.64}$$

The peak value of the equivalent *b*-phase current reference is then found by differentiation of (D.64), as given by (D.65).

$$\frac{d \cdot i_{p,b}^*}{d\theta} = \frac{\overline{p}^*}{\hat{\chi}^{+2} + k_p \cdot \hat{\chi}^{-2}} \cdot \left(\hat{\chi}^+ \cdot \cos\left(\theta + 2\delta - \frac{\pi}{6} \right) - k_p \cdot \hat{\chi}^- \cdot \cos\left(\theta + \frac{\pi}{6} \right) \right) = 0 \tag{D.65}$$

The cosine functions of this equation can be expanded as given by (D.66), and then further expressed by (D.67).

$$\cos\left(\theta+2\delta-\frac{\pi}{6}\right)=\frac{\sqrt{3}}{2}\cos\left(\theta+2\delta\right)+\frac{1}{2}\sin\left(\theta+2\delta\right)$$
$$\cos\left(\theta+\frac{\pi}{6}\right)=\frac{\sqrt{3}}{2}\cos\left(\theta\right)-\frac{1}{2}\sin\left(\theta\right) \tag{D.66}$$

$$\hat{\chi}^{+}\cdot\left(\frac{\sqrt{3}}{2}\left[\cos\left(\theta\right)\cdot\cos\left(2\delta\right)-\sin\left(\theta\right)\cdot\sin\left(2\delta\right)\right]+\frac{1}{2}\left[\sin\left(\theta\right)\cdot\cos\left(2\delta\right)+\cos\left(\theta\right)\cdot\sin\left(2\delta\right)\right]\right) \tag{D.67}$$
$$-k_p\cdot\hat{\chi}^{-}\cdot\left(\frac{\sqrt{3}}{2}\cos\left(\theta\right)-\frac{1}{2}\sin\left(\theta\right)\right)=0$$

Simplifying and reorganizing the terms of (D.67), results in (D.68), which can be solved with respect to the phase angle θ as given by (D.69).

$$\sin\left(\theta\right)\cdot\left[\hat{\chi}^{+}\cdot\left(\sqrt{3}\sin\left(2\delta\right)-\cos\left(2\delta\right)\right)-k_p\cdot\hat{\chi}^{-}\right] \tag{D.68}$$
$$=\cos\left(\theta\right)\cdot\left[\hat{\chi}^{+}\cdot\left(\sqrt{3}\cos\left(2\delta\right)+\sin\left(2\delta\right)\right)-\sqrt{3}\cdot k_p\cdot\hat{\chi}^{-}\right]$$

$$\tan\theta=\frac{\sin\left(\theta\right)}{\cos\left(\theta\right)}=\frac{\hat{\chi}^{+}\cdot\left(\sqrt{3}\cos\left(2\delta\right)+\sin\left(2\delta\right)\right)-\sqrt{3}\cdot k_p\cdot\hat{\chi}^{-}}{\hat{\chi}^{+}\cdot\left(\sqrt{3}\sin\left(2\delta\right)-\cos\left(2\delta\right)\right)-k_p\cdot\hat{\chi}^{-}} \tag{D.69}$$

The phase angle θ corresponding to the maximum value of the *b*-phase current reference under the specified conditions is then given by (D.70).

$$\theta_{i_{p,b},\max}=\tan^{-1}\underbrace{\left(\frac{\hat{\chi}^{+}\cdot\left(\sqrt{3}\cos\left(2\delta\right)+\sin\left(2\delta\right)\right)-\sqrt{3}\cdot k_p\cdot\hat{\chi}^{-}}{\hat{\chi}^{+}\cdot\left(\sqrt{3}\sin\left(2\delta\right)-\cos\left(2\delta\right)\right)-k_p\cdot\hat{\chi}^{-}}\right)}_{\lambda},\quad 0\le\delta\le\frac{\pi}{3},\quad -1\le k_p\le 0 \tag{D.70}$$

To find the corresponding peak value of the *b*-phase current, the phase angle from (D.70) must be substituted back into (D.64), as given by (D.71).

$$i^{*}_{p,b,\max}=\frac{\overline{p}^{*}}{\hat{\chi}^{+^2}+k_p\cdot\hat{\chi}^{-^2}}\cdot\left(\hat{\chi}^{+}\cdot\sin\left(\theta_{i_{p,b},\max}+2\delta-\frac{\pi}{6}\right)-k_p\cdot\hat{\chi}^{-}\cdot\sin\left(\theta_{i_{p,b},\max}+\frac{\pi}{6}\right)\right) \tag{D.71}$$

The terms of this equation can be expanded as given by (D.72) and (D.73). The sine and cosine functions can also be expressed in terms of the intermediate variable λ defined in (D.70), as given by (D.74).

$$\sin\left(\theta_{i_{p,b},\max}+2\delta-\frac{\pi}{6}\right)=\frac{\sqrt{3}}{2}\sin\left(\theta_{i_{p,b},\max}+2\delta\right)-\frac{1}{2}\cos\left(\theta_{i_{p,b},\max}+2\delta\right)$$
$$\cos\left(\theta_{i_{p,b},\max}+\frac{\pi}{6}\right)=\frac{\sqrt{3}}{2}\sin\left(\theta_{i_{p,b},\max}\right)+\frac{1}{2}\cos\left(\theta_{i_{p,b},\max}\right) \tag{D.72}$$

$$\sin\left(\theta_{i_{p,b},\max}+2\delta\right)=\sin\left(\theta_{i_{p,b},\max}\right)\cdot\cos\left(2\delta\right)+\cos\left(\theta_{i_{p,b},\max}\right)\cdot\sin\left(2\delta\right)$$
$$\cos\left(\theta_{i_{p,b},\max}+2\delta\right)=\cos\left(\theta_{i_{p,b},\max}\right)\cdot\cos\left(2\delta\right)-\sin\left(\theta_{i_{p,b},\max}\right)\cdot\sin\left(2\delta\right) \tag{D.73}$$

$$\sin\left(\theta_{i_{p,b},\max}\right)=\frac{\tan\left(\theta_{i_{p,b},\max}\right)}{\sqrt{1+\tan^2\left(\theta_{i_{p,b},\max}\right)}}=\frac{\tan\left(\tan^{-1}\left(\lambda\right)\right)}{\sqrt{1+\tan^2\left(\tan^{-1}\left(\lambda\right)\right)}}=\frac{\lambda}{\sqrt{1+\lambda^2}}$$
$$\cos\left(\theta_{i_{p,b},\max}\right)=\frac{1}{\sqrt{1+\tan^2\left(\theta_{i_{p,b},\max}\right)}}=\frac{1}{\sqrt{1+\tan^2\left(\tan^{-1}\left(\lambda\right)\right)}}=\frac{1}{\sqrt{1+\lambda^2}} \tag{D.74}$$

The peak value of the *b*-phase current can then be expressed by (D.75).

$$i^*_{p,b,\max} = \frac{\bar{p}^*}{\hat{\chi}^{+^2} + k_p \cdot \hat{\chi}^{-^2}} \cdot \begin{matrix} \hat{\chi}^+ \cdot \left[\frac{\sqrt{3}}{2} \left(\frac{\lambda \cdot \cos(2\delta)}{\sqrt{1+\lambda^2}} + \frac{\sin(2\delta)}{\sqrt{1+\lambda^2}} \right) - \frac{1}{2} \left(\frac{\cos(2\delta)}{\sqrt{1+\lambda^2}} - \frac{\lambda \cdot \sin(2\delta)}{\sqrt{1+\lambda^2}} \right) \right] \\ - k_p \cdot \hat{\chi}^- \cdot \left[\frac{\sqrt{3}}{2} \frac{\lambda}{\sqrt{1+\lambda^2}} + \frac{1}{2} \frac{1}{\sqrt{1+\lambda^2}} \right] \end{matrix} \quad \text{(D.75)}$$

Simplifying this equation to the form given by (D.76), the detailed expression for λ from (D.70) can be re-introduced. The peak value of the *b*-phase current reference corresponding to a specified active power reference can then be expressed by (D.77).

$$i^*_{p,b,\max} = \frac{\bar{p}^*}{\hat{\chi}^{+^2} + k_p \cdot \hat{\chi}^{-^2}} \cdot \frac{1}{2} \cdot \frac{\begin{matrix} \hat{\chi}^+ \cdot \left(\sqrt{3} \sin(2\delta) - \cos(2\delta) \right) - k_p \cdot \hat{\chi}^- \\ + \left[\hat{\chi}^+ \cdot \left(\sqrt{3} \cos(2\delta) - \sin(2\delta) \right) - \sqrt{3} \cdot k_p \cdot \hat{\chi}^- \right] \cdot \lambda \end{matrix}}{\sqrt{1+\lambda^2}} \quad \text{(D.76)}$$

$$i^*_{p,b,\max} = \frac{\bar{p}^*}{\hat{\chi}^{+^2} + k_p \cdot \hat{\chi}^{-^2}} \cdot \frac{1}{2} \sqrt{\begin{matrix} \left[\hat{\chi}^+ \cdot \left(\sqrt{3} \sin(2\delta) - \cos(2\delta) \right) - k_p \cdot \hat{\chi}^- \right]^2 \\ + \left[\hat{\chi}^+ \cdot \left(\sqrt{3} \cos(2\delta) - \sin(2\delta) \right) - \sqrt{3} \cdot k_p \cdot \hat{\chi}^- \right]^2 \end{matrix}} \quad \text{(D.77)}$$

By expanding the square expressions in (D.77), and by applying trigonometric identities, this equation can be further simplified to result in (D.78).

$$i^*_{p,b,\max} = \frac{\bar{p}^*}{\hat{\chi}^{+^2} + k_p \cdot \hat{\chi}^{-^2}} \cdot \sqrt{\hat{\chi}^{+^2} - k_p \cdot \hat{\chi}^+ \cdot \hat{\chi}^- \left(\cos(2\delta) + \sqrt{3} \sin(2\delta) \right) + \left(k_p \cdot \hat{\chi}^- \right)^2} \quad \text{(D.78)}$$

$$0 \le \delta \le \frac{\pi}{3}, \qquad -1 \le k_p \le 0$$

From (D.78), the maximum average active power reference that can be allowed without the *b*-phase current exceeding a specified phase current limitation $i_{ph,lim}$ can be expressed as given by (D.79).

$$\left| \bar{p}^*_{\max} \right| = \frac{i_{ph,\lim} \cdot \left(\hat{\chi}^{+^2} + k_p \cdot \hat{\chi}^{-^2} \right)}{\sqrt{\hat{\chi}^{+^2} - k_p \cdot \hat{\chi}^+ \cdot \hat{\chi}^- \left(\cos(2\delta) + \sqrt{3} \sin(2\delta) \right) + \left(k_p \cdot \hat{\chi}^- \right)^2}}, \quad 0 \le \delta \le \frac{\pi}{3}, -1 \le k_p \le 0 \quad \text{(D.79)}$$

The maximum average active power reference can then be substituted back into (4.44) , to arrive at an expression for current reference calculation when operating under phase current limitation as given by (D.80).

$$\mathbf{i}^*_{p,\lim} = \mathbf{i}^{*+}_p + \mathbf{i}^{*-}_p = \frac{i_{ph,\lim} \cdot \mathrm{Sign}\left(\bar{p}^* \right)}{\sqrt{\left| \boldsymbol{\chi}^+ \right|^2 - k_p \cdot \left| \boldsymbol{\chi}^+ \right| \cdot \left| \boldsymbol{\chi}^- \right| \cdot \left(\cos(2\delta) + \sqrt{3} \sin(2\delta) \right) + k_p^2 \cdot \left| \boldsymbol{\chi}^- \right|^2}} \cdot \left(-\boldsymbol{\chi}^+_\perp + k_p \boldsymbol{\chi}^-_\perp \right), \quad \text{(D.80)}$$

$$0 \le \delta \le \frac{\pi}{3}, \qquad -1 \le k_p \le 0$$

The expressions given by (D.79) and (D.80) will only be directly valid for limiting the maximum phase currents as long as the specified conditions are fulfilled. For δ outside the range between 0°-60°, the equations must therefore be adapted accordingly. The derived equations for peak current, maximum allowable average active power reference and for current reference calculation when operating under phase current limitations can however still be used if the value of δ is shifted by a multiple of 60° so that it will stay within the specified range. The phase where the maximum current will occur and the corresponding adaptation required for applying the developed equations is listed in Table D-1.

Table D-1 Orientation of Virtual Flux trajectories and influence on equations for phase current limitation when −1≤kp≤0

Range of δ	Peak current in:	Lowest value of peak vector amplitude for	Expression for δ to be used in (D.78), (D.79) and (D.80)
$0 \le \delta \le \frac{\pi}{3}$	Phase b	$\delta = \frac{\pi}{6}$	$\delta' = \delta$
$\frac{\pi}{3} \le \delta \le \frac{2\pi}{3}$	Phase a	$\delta = \frac{\pi}{2}$	$\delta' = \delta - \frac{\pi}{3}$
$\frac{2\pi}{3} \le \delta \le \pi$	Phase c	$\delta = \frac{5\pi}{6}$	$\delta' = \delta - \frac{2\pi}{3}$
$-\pi \le \delta \le \frac{-2\pi}{3}$	Phase b	$\delta = \frac{-5\pi}{6}$	$\delta' = \delta + \pi$
$\frac{-2\pi}{3} \le \delta \le \frac{-\pi}{3}$	Phase a	$\delta = \frac{-\pi}{2}$	$\delta' = \delta + \frac{2\pi}{3}$
$\frac{-\pi}{3} \le \delta \le 0$	Phase c	$\delta = \frac{-\pi}{6}$	$\delta' = \delta + \frac{\pi}{3}$

The peak absolute value of the current in one phase will occur for both positive and negative values, and the orientation of the voltage or Virtual Flux trajectories will be symmetric with respect to the β-axis of the stationary reference frame. Thus, it is not relevant to consider values of δ outside the range of −90-90°. Additionally, the detection of the orientation angle δ by (D.28), will be limited within the range of 0-90°. The maximum average active power transfer, and the corresponding maximum current vector amplitude expressed as a function of the orientation angle δ will however be repeated for each interval of 60°, so this does not have any practical consequences. Thus, only the two first rows of Table D-1 will be necessary to consider for practical implementations

In case the maximum current vector amplitude coincides with the maximum current in one of the phases, equation (D.80) for current reference calculation can be significantly simplified. Considering for instance δ = 30° so that the maximum current vector amplitude will appear in phase *b*, and assuming $k_p = -1$, equation (D.80) is reduced to (D.81). This corresponds to active power control by the PNSC strategy with a limitation on the current vector amplitude as discussed in section 5.5.

$$\mathbf{i}_{p,\lim}^{*} = \mathbf{i}_{p}^{*+} + \mathbf{i}_{p}^{*-} = \frac{i_{ph,\lim} \cdot \mathrm{Sign}\left(\bar{p}^{*}\right)}{\left|\boldsymbol{\chi}^{+}\right| + \left|\boldsymbol{\chi}^{-}\right|} \cdot \left(-\boldsymbol{\chi}_{\perp}^{+} - \boldsymbol{\chi}_{\perp}^{-}\right) \tag{D.81}$$

The maximum allowable amplitude of the current vector will however occur for δ = 0° or any multiple of 60° with a fault condition of the grid given by $|\boldsymbol{\chi}^{+}| = |\boldsymbol{\chi}^{-}| = x$. The peak vector amplitude of the current reference will then be given by (D.82). This corresponds to the graphical illustration of the maximum allowable current vector amplitude for a specified phase current limitation as explained in section 5.2.

$$\left|\mathbf{i}_{p}^{*}\right|_{\max} = \frac{i_{ph,\lim}}{\sqrt{x^2 + x \cdot x + x^2}} \cdot \left(x + x\right) = \frac{i_{ph,\lim}}{x\sqrt{3}} \cdot 2x = \frac{2}{\sqrt{3}} \cdot i_{ph,\lim} \approx 1.15 \cdot i_{ph,\lim} \tag{D.82}$$

D.5.2 Operation with Reduction of Reactive Power Oscillations ($0 \le k_p \le 1$)

When the control objective is to reduce the reactive power oscillations, the orientation of the current reference trajectory will be aligned with the orientation of the voltage or Virtual Flux trajectories. For orientations within the range given by $-30° \le \delta \le 30°$, the maximum phase current will then occur in phase *a*. Since the *a*-phase current is equal to the α-axis current, it is expressed by (D.83).

$$i_{p,a}^{*} = i_{p,\alpha}^{*} = \frac{\overline{p}^{*}}{\hat{\chi}^{+^2} + k_p \cdot \hat{\chi}^{-^2}} \cdot \left(\hat{\chi}^{+} \cdot \cos\left(\theta + 2\delta\right) + k_p \cdot \hat{\chi}^{-} \cdot \cos\left(\theta\right) \right) \tag{D.83}$$

The phase angle corresponding to the maximum current in phase *a* can then be found by differentiation according to (D.84), resulting in (D.85) and (D.86).

$$\frac{d \cdot i_{p,a}^{*}}{d\theta} = \frac{\overline{p}^{*}}{\hat{\chi}^{+^2} + k_p \cdot \hat{\chi}^{-^2}} \cdot \left(\hat{\chi}^{+} \cdot -\sin\left(\theta + 2\delta\right) - k_p \cdot \hat{\chi}^{-} \cdot \sin\left(\theta\right) \right) = 0 \tag{D.84}$$

$$\hat{\chi}^{+} \cdot \left(\sin\left(\theta\right) \cdot \cos\left(2\delta\right) + \cos\left(\theta\right) \cdot \sin\left(2\delta\right) \right) + k_p \cdot \hat{\chi}^{-} \cdot \sin\left(\theta\right) = 0 \tag{D.85}$$

$$\tan\left(\theta\right) = \frac{\sin\left(\theta\right)}{\cos\left(\theta\right)} = \frac{-\hat{\chi}^{+} \cdot \sin\left(2\delta\right)}{\hat{\chi}^{+} \cdot \cos\left(2\delta\right) + k_p \cdot \hat{\chi}^{-}} \tag{D.86}$$

The resulting phase angle corresponding to maximum current in phase *a* is given by (D.87).

$$\theta_{i_{p,a},\max} = \tan^{-1}\underbrace{\left(\frac{-\hat{\chi}^{+} \cdot \sin\left(2\delta\right)}{\hat{\chi}^{+} \cdot \cos\left(2\delta\right) + k_p \cdot \hat{\chi}^{-}} \right)}_{\kappa}, \qquad -\frac{\pi}{6} \le \delta \le \frac{\pi}{6}, \qquad 0 \le k_p \le 1 \tag{D.87}$$

The maximum current in phase *a* is found by substituting the result from (D.87) back into (D.83), as given by (D.88).

$$i_{p,a,\max}^{*} = \frac{\overline{p}^{*}}{\hat{\chi}^{+^2} + k_p \cdot \hat{\chi}^{-^2}} \cdot \left(\hat{\chi}^{+} \cdot \cos\left(\theta_{i_{p,a},\max} + 2\delta\right) + k_p \cdot \hat{\chi}^{-} \cdot \cos\left(\theta_{i_{p,a},\max}\right) \right) \tag{D.88}$$

Applying the trigonometric identities from (D.73) and (D.74) the maximum current in phase a can be expressed by (D.89).

$$i_{p,a,\max}^{*} = \frac{\overline{p}^{*}}{\hat{\chi}^{+^2} + k_p \cdot \hat{\chi}^{-^2}} \cdot \left(\frac{\hat{\chi}^{+} \cdot \cos\left(2\delta\right) + k_p \cdot \hat{\chi}^{-} - \hat{\chi}^{+} \cdot \sin\left(2\delta\right) \cdot \kappa}{\sqrt{1 + \kappa^2}} \right) \tag{D.89}$$

Re-introducing the intermediate variable κ defined in (D.87) and simplifying, the maximum current in phase *a* can be expressed by (D.90) and further simplified into (D.91).

$$i_{p,a,\max}^{*} = \frac{\overline{p}^{*}}{\hat{\chi}^{+^2} + k_p \cdot \hat{\chi}^{-^2}} \cdot \sqrt{\left(\hat{\chi}^{+} \cdot \sin\left(2\delta\right) \right)^2 + \left(\hat{\chi}^{+} \cdot \cos\left(2\delta\right) + k_p \cdot \hat{\chi}^{-} \right)^2} \tag{D.90}$$

$$i_{p,a,\max}^{*} = \frac{\overline{p}^{*}}{\hat{\chi}^{+^2} + k_p \cdot \hat{\chi}^{-^2}} \cdot \sqrt{\hat{\chi}^{+^2} + 2 + k_p \cdot \hat{\chi}^{+} \cdot \hat{\chi}^{-} \cos\left(2\delta\right) + k_p^2 \cdot \hat{\chi}^{-^2}}, \qquad -\frac{\pi}{6} \le \delta \le \frac{\pi}{6}, \qquad 0 \le k_p \le 1 \tag{D.91}$$

The maximum average active power transfer that can be allowed within the phase current limitation $i_{ph,lim}$ can then be expressed by (D.92).

$$\left|\bar{p}^*_{\max}\right| = \frac{i_{ph,\lim}\cdot\left(\hat{\chi}^{+^2} + k_p\cdot\hat{\chi}^{-^2}\right)}{\sqrt{\hat{\chi}^{+^2} + 2 + k_p\cdot\hat{\chi}^{+}\cdot\hat{\chi}^{-}\cos(2\delta) + k_p^2\cdot\hat{\chi}^{-^2}}}, \qquad \frac{\pi}{6}\le\delta\le\frac{\pi}{6}, \qquad 0\le k_p\le 1 \quad \text{(D.92)}$$

Substituting (D.92) back into (4.44) results in the equation for active current reference calculation when operating under phase current limitation as given by (D.93) .

$$\mathbf{i}^*_{p,\lim} = \mathbf{i}^{*+}_p + \mathbf{i}^{*-}_p = \frac{i_{ph,\lim}\cdot\mathrm{Sign}\left(\bar{p}^*\right)}{\sqrt{\left|\boldsymbol{\chi}^+\right|^2 + 2\cdot k_p\cdot\left|\boldsymbol{\chi}^+\right|\cdot\left|\boldsymbol{\chi}^-\right|\cdot\cos(2\delta) + k_p^2\cdot\left|\boldsymbol{\chi}^-\right|^2}}\cdot\left(-\boldsymbol{\chi}^+_\perp + k_p\boldsymbol{\chi}^-_\perp\right), \qquad -\frac{\pi}{6}\le\delta\le\frac{\pi}{6}, \qquad 0\le k_p\le 1 \quad \text{(D.93)}$$

As explained for the case of $k_p < 1$, these equations can be made generally valid by shifting δ so that it will always be within the range from −30° to 30°. The corresponding information about the phase experiencing the maximum current amplitude and the required phase shifting of δ is listed in Table D-2. Also in this case, only the two first rows of the table will be relevant for practical implementation.

For $\delta = 0°$ and $k_p = 1$, it can easily be verified that (D.93) reduces to an expression for active power control by the AARC strategy when operating under vector current amplitude limitation as given by (D.94).

$$\mathbf{i}^*_{p,\lim} = \mathbf{i}^{*+}_p + \mathbf{i}^{*-}_p = \frac{i_{ph,\lim}\cdot\mathrm{Sign}\left(\bar{p}^*\right)}{\left|\boldsymbol{\chi}^+\right| + \left|\boldsymbol{\chi}^-\right|}\cdot\left(-\boldsymbol{\chi}^+_\perp + \boldsymbol{\chi}^-_\perp\right) \quad \text{(D.94)}$$

The maximum allowable amplitude of the current vector will however occur for δ = 30° of for any odd multiple of 30° and a fault condition characterized by $|\boldsymbol{\chi}^+| = |\boldsymbol{\chi}^-| = x$. The peak vector amplitude of the current reference will then be given by (D.95). This corresponds to the graphical illustration of the maximum allowable current vector amplitude for a specified phase current limitation as explained in section 5.2.

$$\left|\mathbf{i}^*_p\right|_{\max} = \frac{i_{ph,\lim}}{\sqrt{x^2 + 2\cdot x\cdot x\cdot\frac{1}{2} + x^2}}\cdot(x+x) = \frac{i_{ph,\lim}}{x\sqrt{3}}\cdot 2x = \frac{2}{\sqrt{3}}\cdot i_{ph,\lim} \approx 1.15\cdot i_{ph,\lim} \quad \text{(D.95)}$$

If the positive and negative sequence components of the Virtual Flux are given by $|\chi+| = |\chi-| = 0.5$, the resulting maximum power transfer while maintaining the objective of eliminating reactive power oscillations will be given by (D.96). In this particular condition, the average active power transfer can thus be increased by about 15 % compared to the 0.5 pu that could be transferred when operating under current vector amplitude limitation.

$$\left|\bar{p}^*_{\max}\right| = \frac{i_{ph,\lim}\cdot\left(\left(\frac{1}{2}\right)^2 + \left(\frac{1}{2}\right)^2\right)}{\sqrt{\left(\frac{1}{2}\right)^2 + 2\cdot\frac{1}{2}\cdot\frac{1}{2}\cdot\frac{1}{2} + \left(\frac{1}{2}\right)^2}} = \frac{i_{ph,\lim}\cdot\frac{1}{2}}{\sqrt{\frac{3}{4}}} = \frac{1}{\sqrt{3}}\cdot i_{ph,\lim} \approx 0.577\cdot i_{ph,\lim}, \qquad \delta = \pm\frac{\pi}{6}, \qquad k_p = 1 \quad \text{(D.96)}$$

Table D-2 Orientation of Virtual Flux trajectories and influence on equations for phase current limitation when 0≤kp≤1

Range of δ	Peak current in:	Lowest value of peak vector amplitude for	Expression for δ to be used in (D.91), (D.92) and (D.93)
$-\frac{\pi}{6} \le \delta \le \frac{\pi}{6}$	Phase a	$\delta = 0$	$\delta' = \delta$
$\frac{\pi}{6} \le \delta \le \frac{\pi}{2}$	Phase c	$\delta = \frac{\pi}{3}$	$\delta' = \delta - \frac{\pi}{3}$
$\frac{\pi}{2} \le \delta \le \frac{5\pi}{6}$	Phase b	$\delta = \frac{2\pi}{3}$	$\delta' = \delta - \frac{2\pi}{3}$
$\frac{5\pi}{6} \le \delta \le \pi$ $-\pi \le \delta \le \frac{-5\pi}{6}$	Phase a	$\delta = \pi$	$\delta' = \delta - \pi$ for $\frac{5\pi}{6} \le \delta \le \pi$ $\delta' = \delta + \pi$ for $-\pi \le \delta \le \frac{-5\pi}{6}$
$\frac{-5\pi}{6} \le \delta \le \frac{-\pi}{2}$	Phase c	$\delta = \frac{-2\pi}{3}$	$\delta' = \delta + \frac{2\pi}{3}$
$\frac{-\pi}{2} \le \delta \le -\frac{\pi}{6}$	Phase b	$\delta = \frac{-\pi}{3}$	$\delta' = \delta + \frac{\pi}{3}$

D.6 Derivation of Reactive Power Transfer Limitations and Current Reference Equations for Operation of Reactive Power Control Strategies under Phase Current Limitation

The starting point for the following derivations is the general reactive current reference equation from (4.45). By the definitions from the previous subsections, this current reference equation can be expressed by (D.97).

$$\mathbf{i}_q^* = \begin{bmatrix} i_{q,\alpha}^* \\ i_{q,\beta}^* \end{bmatrix} = \frac{\overline{q}^*}{\hat{\chi}^{+^2} + k_q \cdot \hat{\chi}^{-^2}} \cdot \begin{bmatrix} -\hat{\chi}^+ \cdot \sin(\theta + 2\delta) + k_q \cdot \hat{\chi}^- \cdot \sin(\theta) \\ \hat{\chi}^+ \cdot \cos(\theta + 2\delta) + k_q \cdot \hat{\chi}^- \cdot \cos(\theta) \end{bmatrix} \tag{D.97}$$

The derivations will be kept general by allowing the control parameter k_q to take any value between −1 and 1. The orientation of the current reference vector trajectory will however be aligned with the Virtual Flux trajectory when $k_q < 0$, while it will be perpendicular to the Virtual Flux trajectory when $k_q > 1$. The derivations must therefore be carried out separately for these two cases. The derivations will follow the same steps as presented for the case or active power control with phase current limitation, and therefore, fewer steps and explanations will be given here.

D.6.1 Operation with Reduction of Reactive Power Oscillations (−1≤k_q≤0)

For δ in the range of −30° ≤ δ ≤-30° the maximum peak value will occur in phase *a*, as given by (D.98).

$$i_{q,a}^{*} = i_{q,\alpha}^{*} = \frac{\overline{q}^{*}}{\hat{\chi}^{+^2} + k_q \cdot \hat{\chi}^{+^2}} \cdot \left(-\hat{\chi}^{+} \cdot \sin\left(\theta + 2\delta\right) + k_q \cdot \hat{\chi}^{-} \cdot \sin\left(\theta\right) \right) \tag{D.98}$$

Differentiation according to (D.99) results in (D.100), that can be solved as given by (D.101). Thus, the phase angle corresponding to the maximum current in phase *a* can be expressed by (D.102).

$$\frac{d \cdot i_{q,a}^{*}}{d\theta} = \frac{\overline{q}^{*}}{\hat{\chi}^{+^2} + k_q \cdot \hat{\chi}^{+^2}} \cdot \left(-\hat{\chi}^{+} \cdot \cos\left(\theta + 2\delta\right) + k_q \cdot \hat{\chi}^{-} \cdot \cos\left(\theta\right) \right) = 0 \tag{D.99}$$

$$\hat{\chi}^{+} \left(\cos\left(\theta\right) \cdot \cos\left(2\delta\right) - \sin\left(\theta\right) \cdot \sin\left(2\delta\right) \right) - k_q \cdot \hat{\chi}^{-} \cdot \cos\left(\theta\right) = 0 \tag{D.100}$$

$$\tan\left(\theta\right) = \frac{\sin\left(\theta\right)}{\cos\left(\theta\right)} = \frac{\hat{\chi}^{+} \cdot \cos\left(2\delta\right) - k_q \cdot \hat{\chi}^{-}}{\hat{\chi}^{+} \cdot \sin\left(2\delta\right)} \tag{D.101}$$

$$\theta_{i_{q,\alpha}\max} = \tan^{-1} \underbrace{\left(\frac{\hat{\chi}^{+} \cdot \cos\left(2\delta\right) - k_q \cdot \hat{\chi}^{-}}{\hat{\chi}^{+} \cdot \sin\left(2\delta\right)} \right)}_{\rho}, \qquad -\frac{\pi}{6} \le \delta \le \frac{\pi}{6}, \qquad -1 \le k_q \le 0 \tag{D.102}$$

The maximum current in phase *a* can then be expressed by (D.103), and expanded into (D.104). Re-introducing the expression for the intermediate variable ρ defined in (D.102) and simplifying the resulting expression, leads to (D.105).

$$i_{q,a,\max}^{*} = \frac{\overline{q}^{*}}{\hat{\chi}^{+^2} + k_q \cdot \hat{\chi}^{-^2}} \cdot \left(-\hat{\chi}^{+} \cdot \sin\left(\theta_{i_{q,\alpha}\max} + 2\delta\right) + k_q \cdot \hat{\chi}^{-} \cdot \sin\left(\theta_{i_{q,\alpha}\max}\right) \right) \tag{D.103}$$

$$i_{q,a,\max}^{*} = \frac{\overline{q}^{*}}{\hat{\chi}^{+^2} + k_q \cdot \hat{\chi}^{-^2}} \cdot \left(-\frac{\hat{\chi}^{+} \cdot \sin\left(2\delta\right) + \left[\hat{\chi}^{+} \cdot \cos\left(2\delta\right) - k_q \cdot \hat{\chi}^{-} \right] \cdot \rho}{\sqrt{1 + \rho^2}} \right) \tag{D.104}$$

$$i_{q,a,\max}^{*} = \frac{\overline{q}^{*}}{\hat{\chi}^{+^2} + k_q \cdot \hat{\chi}^{-^2}} \cdot -\sqrt{\left[\hat{\chi}^{+} \cdot \sin\left(2\delta\right) \right]^2 + \left[\hat{\chi}^{+} \cdot \cos\left(2\delta\right) - k_q \cdot \hat{\chi}^{-} \right]^2} \tag{D.105}$$

Equation (D.105) can be further simplified, to arrive at (D.106)

$$i_{q,\alpha,\max}^{*} = \frac{-\overline{q}^{*}}{\hat{\chi}^{+^2} + k_q \hat{\chi}^{-^2}} \cdot \sqrt{\hat{\chi}^{+^2} - 2 \cdot k_q \cdot \hat{\chi}^{+} \cdot \hat{\chi}^{-} \cdot \cos\left(2\delta\right) + k_q^2 \cdot \hat{\chi}^{-^2}}, \qquad -\frac{\pi}{6} \le \delta \le \frac{\pi}{6}, \qquad -1 \le k_q \le 0 \tag{D.106}$$

The maximum average reactive power transfer can then be expressed by (D.107), and the corresponding equation for current reference calculation when operating under phase current limitation is given by (D.108).

$$\left| \overline{q}_{\max}^{*} \right| = \frac{i_{ph,\lim} \cdot \left(\hat{\chi}^{+^2} + k_q \hat{\chi}^{-^2} \right)}{\sqrt{\hat{\chi}^{+^2} - 2 \cdot k_q \cdot \hat{\chi}^{+} \cdot \hat{\chi}^{-} \cdot \cos\left(2\delta\right) + k_q^2 \cdot \hat{\chi}^{-^2}}}, \quad -\frac{\pi}{6} \le \delta \le \frac{\pi}{6}, \quad -1 \le k_q \le 0 \tag{D.107}$$

$$\mathbf{i}_{q,\lim}^{*} = \mathbf{i}_{q}^{*_+} + \mathbf{i}_{q}^{*_-} = \frac{i_{ph,\lim} \cdot \mathrm{Sign}\left(\overline{q}^{*}\right)}{\sqrt{\left|\boldsymbol{\chi}^{+}\right|^2 - 2 \cdot k_q \cdot \left|\boldsymbol{\chi}^{+}\right| \cdot \left|\boldsymbol{\chi}^{-}\right| \cdot \cos\left(2\delta\right) + k_q^2 \cdot \left|\boldsymbol{\chi}^{-}\right|^2}} \cdot \left(\boldsymbol{\chi}^{+} - k_q \cdot \boldsymbol{\chi}^{-} \right), \qquad -\frac{\pi}{6} \le \delta \le \frac{\pi}{6}, \qquad -1 \le k_q \le 0 \tag{D.108}$$

The orientation of the current reference trajectory is in this case the same as for operation with active power control and reduction of double frequency reactive power oscillations. Thus, the derived equations have the same dependency on the phase angle δ, and the same table as presented in section D.5.2 can be applied to extend the validity of the equations outside the specified range.

D.6.2 Operation with Reduction of Active Power Oscillations ($0 \le k_q \le 1$)

If the orientation of the voltage or Virtual Flux trajectories under unbalanced conditions is within the range of $0 \le \delta \le 60°$, the maximum phase current will in this case occur in phase *b*. By starting from the current references in (D.97), the current in phase *b* can then be found as given by (D.109) and simplified to result in (D.110).

$$i_{q,b}^{*} = \frac{\overline{q}^{*}}{\hat{\chi}^{+^2} + k_q \cdot \hat{\chi}^{-^2}} \cdot \left(\frac{1}{2} \cdot \left(\hat{\chi}^{+} \cdot \sin\left(\theta + 2\delta\right) - k_q \cdot \hat{\chi}^{-} \cdot \sin\left(\theta\right) \right) + \frac{\sqrt{3}}{2} \cdot \left(\hat{\chi}^{+} \cdot \cos\left(\theta + 2\delta\right) + k_q \cdot \hat{\chi}^{-} \cdot \cos\left(\theta\right) \right) \right) \tag{D.109}$$

$$i_{q,b}^{*} = \frac{\overline{q}^{*}}{\hat{\chi}^{+^2} + k_q \cdot \hat{\chi}^{-^2}} \cdot \left(\hat{\chi}^{+} \cdot \cos\left(\theta + 2\delta - \frac{\pi}{6} \right) + k_q \cdot \hat{\chi}^{-} \cdot \cos\left(\theta + \frac{\pi}{6} \right) \right) \tag{D.110}$$

The phase angle corresponding to the maximum value of the current in phase *b*, can then be found by differentiation according to (D.111), resulting in (D.112).

$$\frac{d \cdot i_{q,b}^{*}}{d\theta} = \frac{\overline{q}^{*}}{\hat{\chi}^{+^2} + k_q \cdot \hat{\chi}^{+^2}} \cdot \left(\hat{\chi}^{+} \cdot -\sin\left(\theta + 2\delta\right) + k_q \cdot \hat{\chi}^{-} \cdot -\sin\left(\theta\right) \right) = 0 \tag{D.111}$$

$$\begin{aligned} \sin\left(\theta\right) \left[\hat{\chi}^{+} \left(\sqrt{3} \cdot \cos\left(2\delta\right) + \sin\left(2\delta\right) \right) + \sqrt{3} \cdot k_q \cdot \hat{\chi}^{-} \right] \\ + \cos\left(\theta\right) \left[\hat{\chi}^{+} \left(\sqrt{3} \cdot \sin\left(2\delta\right) - \cos\left(2\delta\right) \right) + k_q \cdot \hat{\chi}^{-} \right] = 0 \end{aligned} \tag{D.112}$$

The solution to (D.112) is given by (D.113), and the phase angle corresponding to the maximum current in phase *b* can be expressed by (D.114).

$$\tan\left(\theta\right) = \frac{\sin\left(\theta\right)}{\cos\left(\theta\right)} = \frac{\hat{\chi}^{+} \left(\cos\left(2\delta\right) - \sqrt{3} \cdot \sin\left(2\delta\right) \right) - k_q \cdot \hat{\chi}^{-}}{\hat{\chi}^{+} \left(\sin\left(2\delta\right) + \sqrt{3} \cdot \cos\left(2\delta\right) \right) + \sqrt{3} \cdot k_q \cdot \hat{\chi}^{-}} \tag{D.113}$$

$$\theta_{i_{p,b}\max} = \tan^{-1} \underbrace{\left(\frac{\hat{\chi}^{+} \left(\cos\left(2\delta\right) - \sqrt{3} \cdot \sin\left(2\delta\right) \right) - k_q \cdot \hat{\chi}^{-}}{\hat{\chi}^{+} \left(\sin\left(2\delta\right) + \sqrt{3} \cdot \cos\left(2\delta\right) \right) + \sqrt{3} \cdot k_q \cdot \hat{\chi}^{-}} \right)}_{\sigma}, \quad 0 \le \delta \le \frac{\pi}{3}, \quad 0 \le k_q \le 1 \tag{D.114}$$

The maximum current in phase *b* can then be expressed by (D.115). Expanding this equation and using the same trigonometric identities as explained in section D.5.1 results in (D.116).

$$i_{q,b,\max}^{*} = \frac{\overline{q}^{*}}{\hat{\chi}^{+^2} + k_q \cdot \hat{\chi}^{-^2}} \cdot \left(\hat{\chi}^{+} \cdot \cos\left(\theta_{i_{p,b}\max} + 2\delta - \frac{\pi}{6} \right) + k_q \cdot \hat{\chi}^{-} \cdot \cos\left(\theta_{i_{p,b}\max} + \frac{\pi}{6} \right) \right) \tag{D.115}$$

$$i_{q,b,\max}^{*}=\frac{\bar{q}^{*}}{\hat{\chi}^{+^2}+k_q\cdot\hat{\chi}^{-^2}}\cdot\frac{1}{2}\frac{\begin{array}{r}\hat{\chi}^{+}\cdot\left(\sqrt{3}\cos\left(2\delta\right)+\sin\left(2\delta\right)\right)+\sqrt{3}\cdot k_q\cdot\hat{\chi}^{-}\\ +\left[\hat{\chi}^{+}\cdot\left(\cos\left(2\delta\right)-\sqrt{3}\sin\left(2\delta\right)\right)-k_q\cdot\hat{\chi}^{-}\right]\cdot\sigma\end{array}}{\sqrt{1+\sigma^2}} \quad \text{(D.116)}$$

Re-introducing the expression for the intermediate variable σ defined by (D.114), the maximum current in phase *b* can then be expressed by (D.117) that can be further simplified to arrive at (D.118).

$$i_{q,b,\max}^{*}=\frac{\bar{q}^{*}}{\hat{\chi}^{+^2}+k_q\cdot\hat{\chi}^{-^2}}\cdot\frac{1}{2}\sqrt{\begin{array}{r}\left[\hat{\chi}^{+}\cdot\left(\sin\left(2\delta\right)+\sqrt{3}\cos\left(2\delta\right)\right)+\sqrt{3}\cdot k_q\cdot\hat{\chi}^{-}\right]^2\\ +\left[\hat{\chi}^{+}\cdot\left(\cos\left(2\delta\right)-\sqrt{3}\sin\left(2\delta\right)\right)-k_q\cdot\hat{\chi}^{-}\right]^2\end{array}} \quad \text{(D.117)}$$

$$i_{q,b,\max}^{*}=\frac{\bar{q}^{*}}{\hat{\chi}^{+^2}+k_q\cdot\hat{\chi}^{-^2}}\cdot\frac{1}{2}\sqrt{\hat{\chi}^{+^2}+k_q\cdot\hat{\chi}^{+}\cdot\hat{\chi}^{-}\cdot\left(\cos\left(2\delta\right)+\sqrt{3}\sin\left(2\delta\right)\right)+k_q^2\cdot\hat{\chi}^{-^2}}, \quad \text{(D.118)}$$

$$0\le\delta\le\frac{\pi}{3},\qquad 0\le k_q\le 1$$

The maximum average reactive power transfer when operating under a phase current limitation $i_{ph,lim}$ can then be expressed by (D.119).

$$\left|\bar{q}_{\lim}^{*}\right|=\frac{i_{ph,\lim}\cdot\left(\hat{\chi}^{+^2}+k_q\cdot\hat{\chi}^{-^2}\right)}{\sqrt{\hat{\chi}^{+^2}+k_q\cdot\hat{\chi}^{+}\cdot\hat{\chi}^{-}\cdot\left(\cos\left(2\delta\right)+\sqrt{3}\sin\left(2\delta\right)\right)+k_q^2\cdot\hat{\chi}^{-^2}}},\quad 0\le\delta\le\frac{\pi}{3},\quad 0\le k_q\le 1 \quad \text{(D.119)}$$

The equation for calculation of the reactive current reference when operating under phase current limitation can then be found as given by (D.120).

$$\mathbf{i}_{q,\lim}^{*}=\frac{i_{ph,\lim}\cdot\mathrm{Sign}\left(\bar{q}^{*}\right)}{\sqrt{\left|\boldsymbol{\chi}^{+}\right|^2+k_q\cdot\left|\boldsymbol{\chi}^{+}\right|\cdot\left|\boldsymbol{\chi}^{-}\right|\cdot\left(\cos\left(2\delta\right)+\sqrt{3}\sin\left(2\delta\right)\right)+k_q^2\cdot\left|\boldsymbol{\chi}^{-}\right|^2}}\cdot\left(\boldsymbol{\chi}^{+}-k_q\cdot\boldsymbol{\chi}^{-}\right), \quad \text{(D.120)}$$

$$0\le\delta\le\frac{\pi}{3},\qquad 0\le k_q\le 1$$

The orientation of the current reference trajectory is in this case the same as for operation with active power control and reduction of double frequency active power oscillations. Thus, the derived equations have the same dependency on the phase angle δ as the equations derived in section D.5.1, and the information given in Table D-2 can be applied to extend the validity of the equations outside the specified range of 0-60°.